UNIVERSITY OF OKLAHOMA

GRADUATE COLLEGE

MODELING RELATIONSHIPS BETWEEN BRAIN/MUSCLE ACTIVITY AND LOCOMOTIVE BEHAVIOR

A DISSERTATION

SUBMITTED TO THE GRADUATE FACULTY

in partial fulfillment of the requirements for the

Degree of

DOCTOR OF PHILOSOPHY

By

MONIQUE OLANIKE SHOTANDE

Norman, Oklahoma

2022

Downloaded from SHAREOK. Persistent Handle URL: https://hdl.handle.net/11244/336923

MODELING RELATIONSHIPS BETWEEN
BRAIN/MUSCLE ACTIVITY AND LOCOMOTIVE BEHAVIOR

A DISSERTATION APPROVED FOR THE
SCHOOL OF COMPUTER SCIENCE

BY THE COMMITTEE CONSISTING OF

Dr. Andrew H. Fagg

Dr. Lei Ding

Dr. Amy McGovern

Dr. David P. Miller

Dr. Thubi H. A. Kolobe

Dr. Carol P. Dionne

Dr. Sina Khanmohammadi

© Copyright by MONIQUE OLANIKE SHOTANDE 2022

All Rights Reserved.

Acknowledgements

I would like to thank a number of people for their part in assisting me with completing my dissertation. First I want to thank my advisor, Dr. Andrew H. Fagg. He has been an amazing mentor and role model to me. I have learned so much from him and continue to be inspired by his excitement and intrigue in interdisciplinary fields. His critical feedback has assisted in guiding and shaping this dissertation into its final form. It has been a profoundly educational experience to work under his tutelage and has helped me grow in preparation for my future endeavors.

Additionally, I would like to thank my committee members, Dr. Lei Ding, Dr. Amy McGovern, Dr. David Miller, Dr. Thubi H. A. Kolobe, Dr. Carol P. Dionne, and Dr. Sina Khanmohammadi, for all their guidance and feedback over these past few years. I greatly appreciate their patience with me during this process. It has been a great experience to learn from the unique perspectives and expertise of each of my committee members. They have all been instrumental in helping me formulate and shape my path forward as a researcher and, someday, a professor.

In addition, I would like to thank all the people I have collaborated with on these research projects. Dr. Kimberly P. Veirs, Jonathan Day, Dr. William J. J. Ertl for their instrumental roles in regard to the gait of individuals with osteomyoplastic transfemoral amputation (OTFA) and providing me with the data and background knowledge that I build upon in this work. I would like to thank Dr. Lei Ding, Dr. Ran Xiao, Dr. Guofa Shou, and Alejandro Patino, for their critical work on data collection and pre-processing of the infant EEG data

that I use in this work. I want to thank Daniel Brigance for helping me gets started and providing an initial code base for working with EEG and SVCs. I would like to thank Dr. Sesh Commuri, Dr. Anh Mai, Bhanu Prasad Kotamraju, and Ravi Soni for developing the OU-PAM and providing the initial code base for parsing and pre-processing the gait data. I would like to thank Jeremiah Yohannan for collaboration on initial exploration of analyses with the gait data and on resampling techniques. I would like to thank Zachary Muller for providing the first stage of applications of Markov Chains to the gait phenotypes. I did not have time to explore this path, however, Zachary has provided an initial implementation as a foundation for future work. I would like to thank Leonard Wilson for his academic and writing advice. I would like to thank Dr. Mustafa Ghazi for collaboration on work with the SIPPC and for academic and professional advice and resources.

I want to thank my friends, Uma Kaipa, Adi Narasimhan, Mel Wilson, Stephen Thung, and Kayla Foley, for their unfailing support and dynamic feedback. They have helped make Oklahoma feel more like home. I will never forget the many late nights, that turned into mornings, working on projects in the GA Lab together. I also want to thank my amazing friend back home, Desree Churaman, for our virtual work sessions motivating me to stay focused.

Lastly, I want to thank my family, for all their love and support throughout this process. To my wonderful sisters, Fatimat, Aisha, and Rawaa, thank you for inspiring me, believing in me and taking care of me during the last stages of this process.

Contents

List of Figures **x**

List of Tables **xxiii**

Abstract **xxiv**

1 Introduction **1**

2 Related Work **8**

2.1 Representation Learning 8

2.2 Dimensionality Reduction 11

2.2.1 Principal Component Analysis (PCA) 12

2.2.2 Autoencoders (AEs) 16

2.3 Support Vector Machines (SVMs) 21

2.4 Kernel Density Estimation (KDE) 25

2.5 Highest Density Regions (HDRs) 26

2.6 Model Hyper-parameter Selection 29

2.6.1 Leave Out Subject-wise Cross-Validation 30

2.6.2 Bayesian Optimization 31

2.7 Clustering 32

2.7.1 Gaussian Mixture Models (GMMs) 33

2.7.2 Hierarchical Clustering 36

2.7.3 Adjusted Mutual Information (AMI) 37

3 Bipedal Walking in Humans **40**

3.1 Muscles Above the Knee 41

3.2 Typical Walking Gait in Humans 42

3.3 Implications of Co-contraction 44

3.4 Performance of Healthy Men with Osteomyoplastic Amputation 46

3.4.1 Co-contraction within the Osteomyoplastic Residuum 49

3.4.2 Data Acquisition with the OU-PAM 50

4 Methods for Automated Stride Extraction and Analysis **53**

4.1 Data Pre-processing 54

4.2 Peak Identification 58

4.3 Stride Extraction 60

4.4 Stride Analysis 63

4.5 Muscle Behavior Analysis 65

4.6 Automated Gait Phenotype Identification 69

4.6.1 Data Representation 69

4.6.2 Compression Models 70

4.6.3 Model Validation 72

4.6.4 Automated Phenotype Extraction 72

5 Walking Behavior at Two Speeds **73**

5.1 Participant Selection 74

5.2 Continuous Data Overview 74

5.3 Distributions at each Time Slice During Gait 77

5.3.1 RSI Pressure Distributions 78

5.3.2 Foot Pressure Distributions 83

5.3.3 EMG Activity Distributions 85

5.4 Pressure and EMG Peak Timing . . . 95
5.4.1 Pressure Peak Times . . . 95
5.4.2 Muscle Activation Peak Times . . . 99
5.5 Co-activation of Muscle Groups . . . 103
5.5.1 OTFA Cohort . . . 103
5.5.2 Matched Intact Controls . . . 107
5.6 Gait Phenotypes . . . 110
5.6.1 Evaluation of Gait Reconstruction . . . 110
5.6.2 Extracted Top Level Phenotypes . . . 112
5.6.3 Extracted Top Level Phenotypes Co-contraction . . . 116
5.7 Discussion . . . 119
5.7.1 Pressure Distributions At Each Time Slice During Gait . . . 120
5.7.2 Peak Pressure Times . . . 121
5.7.3 Muscle Activation of Matched Intact Controls . . . 122
5.7.4 Muscle Co-Activation . . . 123
5.7.5 Gait Phenotypes . . . 126

6 Infant Locomotion 128

6.1 Infant Neurological and Motor Development . . . 129
6.1.1 Regional Brain Connectivity in Infants . . . 132
6.1.2 Acquisition of Crawling . . . 134
6.2 Cerebral Palsy (CP) . . . 135
6.3 Self-Initiated Prone Progression Crawler (SIPPC) . . . 136
6.3.1 SIPPC Protocol . . . 138
6.4 Measuring Relevance of EEG Representations for Predicting Limb Movements 140
6.4.1 Generation of Movement Labels . . . 140
6.4.2 Representing EEG Signals for Learning Models . . . 143
6.4.3 Classifier Construction . . . 145

6.4.4 Feature Importance 146
6.5 Results 147
6.5.1 Interactions Between Brain Regions 148
6.5.2 Correlates Between Spectral Power, Electrode Location and Limb Movements 151
6.5.3 Discussion 154

7 Conclusion and Future Work **160**
7.1 Walking Behavior of Individuals with OTFA 160
7.1.1 Potential Clinical Uses in Gait 162
7.1.2 Autoencoder Latent Space Topology 167
7.2 Functional Connectivity in Infants 167

Appendix **171**
A1 Gait Phase Duration 171
A2 Gait Phenotypes 172
A2.1 Hierarchical Clustering 176

List of Figures

1.1 A neuromusculoskeletal model of the human body during gait, modified from Figure 3 by Alamdari and Krovi (2017). 3

2.1 An illustration of PCA. (a) A transformation from the original measured space (left panel) into the new PC space (right panel). (b) Using PCA, the number of dimensions is reduced from two (left panel) to one (right panel). 15

2.2 An autoencoder (AE) neural network. (a) A simple compute node. (b) The autoencoder architecture. 17

2.3 1D convolutional block. (a) Illustrates convolution for a set of three input signals, using two convolutional filters (blue and orange). (b) A convolutional block where pooling (green) is performed after the convolution (blue). . . . 22

2.4 Support Vector Classifier from Figure by Boser et al. (1992). The decision boundary is defined by the support vectors that maximize the margin. 24

2.5 An illustration of 75% highest density regions (HDRs) compared to other common statistical intervals containing the same cumulative density of 75% (modified from Hyndman, 1996). The interval $\mu \pm k\sigma$ is a symmetrical interval $k\sigma$ units around the mean such that the cumulative probability within the interval is 75% where k is some constant to obtain the desired cumulative probability and σ is the standard deviation. The value c_q denotes the q^{th} quantile. 28

2.6 An illustration of 75% highest density regions (HDRs) for two skewed distributions. The top distribution has a lower spread than the bottom distribution. The red line indicates the 75% HDR and the black line indicates the interval $\mu \pm k\sigma$, where k is a constant scalar such that the interval contains 75% of the density. 29

2.7 Cross-validation using a subject-wise leave out approach. There are five subjects. The small squares inside the boxes for each of the subjects are their corresponding data instances. The best model and its corresponding hyper-parameters are selected based on the average validation performance and the average test performance over all the rotations is the generalization performance of the model. 31

2.8 A mixture of three Gaussians is fit to model the distribution of data instances that appears to have three categories, based on Figure 11.2 by Deisenroth et al. (2020). Each Gaussian $\mathcal{N}(x|\mu, \sigma)$ is defined my a mean μ and standard deviation σ. The complete probability density function (pdf) is $p(x|\theta) = 0.5\mathcal{N}(x|-2, 0.5) + 0.2\mathcal{N}(x|1, 2) + 0.3\mathcal{N}(x|4, 1)$ where Θ is the set of parameters for all three Gaussian components. 34

2.9 A dendrogram illustrating the hierarchy of clusters from an agglomerative approach. The horizontal axis is the number of data instances within the cluster branch. The vertical axis is the sum of squared differences within the clusters. The dashed gray line is the cluster distance threshold to determine an appropriate number of clusters. 38

3.1 The hamstrings (green) are on the back (posterior) of the thigh. The quadriceps (red) are on the front (anterior) of the thigh. The adductors (blue) are on the inner part of the thigh. 42

3.2 From Figure 1 of Alamdari and Krovi (2017). The gait cycle with the right limb. Gait begins with the heel-strike (HS) of the right foot. The direction and relative magnitude of the ground reaction force (GRF) is depicted with the yellow arrows. Just after the right HS, the toe-off (TO) of the left foot occurs. The right foot flat (FF) occurs around 20%. When the foot is flat, the GRF is near perpendicular with the ground and usually the entire body weight is supported on that leg. Just prior to 50% the right heel-off (HO) occurs. Double-support refers to moments during gait when both feet are in contact with the ground. 44

3.3 Sensor Placements (Shotande et al., 2022). Pressure and muscle activation data are simultaneously collected using the OU-PAM (Commuri et al., 2010). Sensor placements for individuals with OTFA are (a) two rings of pressure sensors are placed within the residuum socket at the 1/3-femur length (i.e., proximal) and distal femur levels. At each level, sensors were placed at the anterior, posterior, medial, and lateral positions, and (b) EMG sensors were placed on the respective external muscle bellies of the quadriceps, hamstrings and adductor muscle groups. The quadriceps are seen in the anterior view and the hamstrings in the posterior view. 51

4.1 Raw (blue) and pre-processed (red) data from an individual without amputation during self-paced walking. (a) The left heel pressure data from the individual. (b) The activity within the left quadriceps. 57

4.2 Stride extraction procedure for individuals with OTFA, from Shotande et al. (2022, in revision). The details of the RSI locations and abbreviations are in Figure 3.3. (panel a, row 1) Six of the eight RSI sensor values met our analysis inclusion criteria and are shown over a two-minute session. (row 2) The RSI sensor values show a periodic behavior, though each sensor has a distinct offset and scale. (rows 2 and 3) The mean of the selected normalized RSI sensor values and its inverse. (b) Gait events are chosen at the time that the mean RSI sensor value crosses a determined threshold. 61

4.3 Construction of stride heat maps using data from four strides for the DA (distal anterior) pressure sensor. The relative pressure is mapped to a color. The time within the gait cycle is the horizontal axis, and strides are stacked vertically, making the vertical axis the index of the stride. 64

4.4 95% HDRs for the DA (distal anterior) pressure sensor over all the strides from all individuals with OTFA from Shotande et al., in revision. (a) The heat map containing all the strides from the OTFA cohort. (b) Each vertical is a distribution of the activation over all the strides at a single time point. The 95% HDRs are shaded for each moment during gait. HDRs as a function of time in the gait cycle are in light-blue; mean pressure activity is depicted with the solid blue curve, with mean stance end is marked with the magenta triangle. (c) At 20% of the gait cycle, the pressure activity distribution and corresponding HDRs are shown. 65

4.5 Peak activation times for the left muscles of an intact control from both gait tasks. The blue distributions are from the brisk walking task. The magenta distributions are from the self-paced walking task. Two major modes are seen for each task and muscle. 66

4.6 Distances between muscle activation peaks during the same stride. Peak times for the left hamstrings are in the red cells. Peak times for the left quadriceps are in the blue cells. Distances in time between all pairs of peaks between the left hamstrings and quadriceps are in the white and yellow cells. The yellow cells indicate the pair of the closest peaks. 67

4.7 Peak matching between muscles during the same stride. Peaks within the left hamstrings and quadriceps are matched based on which pairs are closest in time. The relative locations within the gait cycle of each muscle peak are used to construct the scatter plot of co-activity between the muscles for the stride. This is done for all strides and pairings of muscle groups. The region along the diagonal of the scatter plot is considered evidence for co-contraction of the muscles. The points off the diagonal region are not co-contraction and contribute to momentum of the limb. 68

4.8 The EMG data $X \in \mathbb{R}^{N \times T \times C}$ are structured as a 3D tensor array for input into the AE model. There are N strides from all the participants, T normalized time samples which correspond to percent of the right/residual limb gait cycle, and there are C EMG channels for each of the muscles. Each row corresponds to a single stride. Each column corresponds to a single point in time and each rectangular depth slice corresponds to a single channel. For example, $X(1, 1, 1)$ indicates a single time sample from one stride and one EMG channel. The corresponding index for the stride is 1, the corresponding time sample index is 1 and the corresponding EMG channel is 1. 70

5.1 Log RSI pressure and EMG activity during eight seconds of brisk (a) and self-paced (b) walking, from visit two of an individual with OTFA (A06). Blue and red horizontal bars above each set of curves indicate the gait events and phases for the (blue) intact and (red) residual limbs, respectively. Black squares designate the start of the stance phase. Thin yellow horizontal lines designate the swing phase for the respective limb. Pressure abbreviations: distal anterior (DA), distal medial (DM), distal proximal (DP), distal lateral (DL), proximal anterior (PA), proximal medial (PM), proximal posterior (PP), and proximal lateral (PL). Sensor locations are shown in Figure 3.3. 75

5.2 Histograms are the distributions of stride and stance duration times in seconds for both the brisk and self-paced tasks. The stance duration is on average shorter for the intact limb than the residual limb, during both tasks ($p < 10^{-27}$). 76

5.3 Self-paced walking RSI pressure activity, from one visit, for all participants with OTFA. The heat maps in the first and third columns contain all the valid strides extracted from each of the six individuals with OTFA. The activity and time are normalized. Time is described as percent of the gait cycle. Each row in the heat map is activity from an individual stride. The red square indicates the end of the stance every twenty strides. The second and fourth columns display the distribution of activity, at each normalized time point. The 95% HDRs are designated by the light blue regions. The solid blue line is the mean activity. The shaded regions are the most likely pressures. 79

5.4 Brisk walking RSI pressure activity, from one visit, for all participants with OTFA. The heat maps in the first and third columns contain all the valid strides extracted from each of the six individuals with OTFA. The activity and time are normalized. Time is described as percent of the gait cycle. Each row in the heat map is activity from an individual stride. The red square indicates the end of the stance for each of the strides. The second and fourth columns display the distribution of activity, at each normalized time point. The 95% HDRs are designated by the light blue regions. The solid blue line is the mean activity. The shaded regions are the most likely pressures. 80

5.5 Self-paced walking foot pressure from one visit for all matched intact control participants. Kernel densities and HDRs are computed for each time slice of the gait cycle. 83

5.6 Brisk walking foot pressure from one visit for all matched intact control participants. Kernel densities and HDRs are computed for each time slice of the gait cycle. 84

5.7 Self-paced EMG Activity from one visit for all participants with OTFA. The heat maps in the first and third columns contain all the valid strides extracted from each of the six individuals with OTFA. The activity and time are normalized. Time is described as percentage of the gait cycle. Each row in the heat map is activity from an individual stride. The red square indicates the end of the stance for each of the strides. The second and fourth columns display the distribution of activity, at each normalized time point. The 95% HDRs are designated by the light blue regions. The solid blue line is the mean activity. 87

5.8 Brisk walking EMG activity, from one visit, for all participants with OTFA. Also see Figure 5.8 for details on the notations. 88

5.9 Self-paced EMG Activity from one visit, for all matched intact control participants. The heat maps contain all the valid strides extracted from each of the six matched controls. The activity and time are normalized. Time is described as percent of the gait cycle. Each row in the heat map is activity from an individual stride. The red squares indicate the end of the stance for each of the strides. The second and fourth columns display the distribution of activity, at each normalized time point. The 95% HDRs are designated by the light blue regions. The solid blue line is the mean activity. The shaded regions are the most likely activation. 91

5.10 Brisk EMG Activity, from one visit, for all matched intact controls. The heat maps contain all the valid strides extracted from each of the six individuals without OTFA. Also see Figure 5.9 for details on the notation. 92

5.11 Distribution of peak times for RSI pressure (a) and EMG activity (b) from an OTFA cohort of six and foot pressure (c) and EMG activity (d) from six intact matched controls (from Figure 1 by Shotande et al., 2022). Horizontal bars indicate the highest density regions (HDRs) with accumulated probabilities of 95% (diamond endpoints) and 75% (square endpoints) for brisk (blue) and self-paced (red) walking. (a) Eight RSI pressure sensors are placed at the proximal (P) and distal (D) levels, at anterior (A), posterior (P), lateral (L), and medial (M) positions (see Figure 3.3 for the sensor placements). 97

5.12 Comparison of peak muscle activation times within each stride from one visit for six OTFA participants and both gait tasks. Time zero corresponds to heel-strike of the corresponding limb. Muscle activation peak times for the adductors compared with the hamstrings, the adductors compared with the quadriceps and the hamstrings compared with the quadriceps within the intact and residual limbs for brisk and self-paced walking. Left two columns are for the intact limb; right two columns are for the residual limb. Different subjects are indicated by different colors. The diagonal line indicates points where peaks in the EMG of one muscle (e.g., hamstrings) and another muscle (e.g., quadriceps) occur simultaneously within the same stride, suggesting co-contraction. Points around the start and end of the stride can be considered a part of the same time cluster. 105

5.13 Distributions of matched muscle peak activation times between the adductors, hamstrings, and quadriceps muscle groups from six individuals with OTFA for the intact (a, c, and e) and residual (b, d, anf f) limbs. Individual points can be found in Figure 5.12. Time zero corresponds to heel-strike of the corresponding limb. Pairings that occur near or along the diagonal indicate co-contraction between muscle groups. The white cross indicates the mode of the distribution of the stance duration. Distributions of the stance duration are in Figure A1. The sub-figures depict the relative frequency of peak pairing times that occur during the gait cycle. Orange and red are within the 95% HDR. Red indicates points within the 75% HDR. Magenta are points with density equal to the 95% HDR threshold, f_{α_1}. For the intact limb, HDRs along the diagonal span most of the gait cycle. 106

5.14 Matched peaks from strides for the intact matched controls. Each point corresponds to a single stride. Time zero corresponds to heel-strike of the corresponding limb. Colors indicate a specific subject. Points along the diagonal indicate co-activation of the muscle pair. 108

5.15 Distributions of matched muscle peak activation times between adductors, hamstrings, and quadriceps muscle groups, from six matched controls for the left (a, c, and e) and right (b, d, and f) limbs. Individual points can be found in Figure 5.14. Time zero corresponds to heel-strike of the corresponding limb. Pairings that occur near or along the diagonal indicate co-contraction between muscle groups. The white cross indicates the mode of the distribution of the stance duration. The sub-figures depict the densities of peak pairings during the gait cycle. Orange and red indicate periods within the 95% HDR. Red indicates points within the 75% HDR. Magenta are time points with density equal to the 95% HDR threshold, f_{α_1}. 109

5.16 Training set reconstruction of EMG from the PC and AE latent spaces. . . 111

5.17 The high-level architecture for the trained AE model, consisting of the input layer, the encoder subnetwork (orange) and the decoder subnetwork (green). A single data input instance has 1400 time slices and 6 EMG channels. The encoder outputs the compressed representation as a 1D array with 98 features. The output of the decoder is the data reconstruction that is the same size as the original input. The full architecture design is in the Appendix. 113

5.18 Top level clustering on the training set in the PC and AE latent spaces. . . 114

5.19 95% HDRs for the top level clustering on the training set in the PC and AE latent spaces. 115

5.20 Co-activation time distributions for the top level clustering from PCA, on the training set. HDRs are for 95% and 50% most likely paired peak activities. Blue distributions are for the OFTA strides assigned to the cluster. The orange distributions are for the intact control strides assigned to the cluster. The purple distributions are the overall distribution for the muscle pair for the cluster. 117

6.1 The Self-Initiated Prone Progression Crawler (SIPPC) Robot 137
6.2 Electrodes over the Central Sulcus 139
6.3 Extrema Extraction and movement labels 141
6.4 Kolmogorov-Smirnov Distance between Cumulative Distributions of the Minimum and Maximum Speeds 142
6.5 Three Infants Weekly Correlation 150
6.6 Infant EEG Spatial and Spectral Feature Importance 152

A1 Distributions of stance duration in seconds and as a fraction of the gait cycle for both cohorts during brisk (blue) and self-paced (magenta) walking. Vertical dashed lines indicate the mode of the distributions. Horizontal red dashed lines indicate the threshold for the 95% HDRs. Green horizontal lines with diamond endpoints indicate the HDRs. *Mo* is short for mode of the corresponding distribution, and n indicates the number of strides extracted. 172

A2 The full architecture for the trained AE model. Each rectangle represents a layer. The left-most box contains the layer name prior to the semi-colon and the layer type after the semi-colon. The second box from the left is the data type of input and output of the layer. The right-most boxes indicate the input and output shapes of the layer. (a) The layers for the encoder. (b) The layers for the decoder. 173

A3 Co-activation time distributions for the top level clustering from AE, on the training set. HDRs are for 95% and 50% most likely paired peak activities. Blue distributions are for the OFTA strides assigned to the cluster. The orange distributions are for the intact control strides assigned to the cluster. The purple distributions are the overall distribution for the muscle pair for the cluster. The left three columns are the distributions for the intact/left muscles. The right three columns are the distributions for the residual/right muscles. 175

A4 Stride counts fof each participant within each top level cluster. (a) Strides for the top level clusters in the PC space. (b) Stride counts for the top level clusters in the AE latent space. 176

A5 Lower level clusters in the PC space. (a) The sub-clusters from the top level cluster 0. (b) The sub-clusters from the top level cluster 1. (c) The sub-clusters from the top level cluster 2. The top level clusters are in Figure 5.18. 179

A6 95% HDRs for the lower level clusters in the PC space. 180

A7 Lower level clusters in the AE space. (a) The sub-clusters from the top level cluster 0. (b) The sub-clusters from the top level cluster 1. The top level clusters are in Figure 5.18. 181

A8 95% HDRs for the lower level clusters in the AE latent space. 182

List of Tables

5.1 Demographic information for participants with OTFA and the matched controls. Two-tailed two sample t-tests were performed to assess the comparability of the demographic information between the groups. The two sample t-test was conducted since the participants come from independent groups. 74

5.2 Results of the KS tests, for the individuals with OTFA, comparing the shape of the distributions of peak times between brisk and self-paced walking for each pressure location (a) and muscle group (b), from Table S1 by Shotande et al. (2022). (a) The $\alpha = 0.05$ is corrected to 0.0064 for the RSI pressures to account for multiple comparisons (Šidák, 1967). (b) The $\alpha = 0.05$ is corrected to 0.0085 in for the muscle activation. Statistically significant differences are indicated by the *. 99

5.3 Results of the KS tests, for the matched controls, comparing the shape of the distribution of peak times between brisk and self-paced walking for each pressure location (a) and muscle group (b). (a) The $\alpha = 0.05$ is corrected to 0.013 for the foot pressures, to account for multiple comparisons (Šidák, 1967) of the foot pressures. (b) The $\alpha = 0.05$ is corrected to 0.0085 for the muscle activation. Statistically significant differences are indicated by the *. 100

5.4 Reconstruction performance based on average RMSE and FVAF. 112

Abstract

The dynamics of locomotion involve a fine-tuned, continuous feedback loop between processes in the brain, functioning of the muscles, and interactions with the environment. Neurological or motor disability can often disrupt this loop and alter muscle activation patterns and corresponding behavior. In order to maintain some level of function, the brain and body adopt atypical locomotive strategies that are often sub-optimal, which can have negative impacts on overall health and inhibit continued motor learning. Therefore, it is crucial to accurately and holistically characterize and diagnose motor behavior when providing interventions. In this dissertation, I propose an approach for comprehensively describing the variations in motor behavior within and across individuals, in addition to an approach for relating brain activity to motor behavior.

Many traditional locomotive analyses utilize subjective metrics derived from manually observed measures of the behavior, making it infeasible for high volumes of data with large numbers of trials or individuals. Additionally, broad summary statistics from a subset of the behavioral measures are typically used but fall short of capturing the full context or the inter-dependencies of the most important locomotive variables. In this work, I develop an approach to uncover the underlying characteristics defining distinct locomotive behaviors across multiple limbs and individuals, simultaneously. I apply higher order statistics, not utilized in standard gait analyses, to identify time-varying, multi-modal activation patterns for comprehensive descriptions and visualizations. With these methods, I describe muscle recruitment strategies during gait of individuals with and without osteomyoplastic

transfemoral amputation (OTFA) using pressure and electromyography (EMG) data and provide a robust approach for extracting, characterizing, and grouping the motor behavior across strides. I demonstrate the presence of muscle activity within the distal-residuum of multiple individuals with OTFA, which has not been shown before. I provide a novel perspective on co-contraction and compare the distributions of co-contraction timing between individuals with and without OTFA. Additionally, I provide quantitative descriptions of the distribution of pressures to objectively determine the quality of prosthetic fit. These results have potential implications for improving rehabilitation outcomes, prosthetic design, and reducing the risk of injury.

I also propose an approach for relating limb movements (from kinematic data) with brain activity (from electroencephalography, EEG) in infants during the acquisition of crawling. In this approach, I decompose the EEG signals into constituent frequency components and measure their relevance using machine learning models that predict movement from three developmental periods. This approach enables the examination of longitudinal changes in brain activity as infants are learning to crawl. I demonstrate that multiple frequency components of the EEG signals at distinct locations are relevant for predicting limb movements and I provide evidence for increasing functional connectivity at higher brain activation frequencies.

Chapter 1

Introduction

Human movement is deceptively complex. We often take for granted how much coordination goes into walking, or even just lifting a fork, until we observe infants learning these actions for the first time, or we receive an injury that requires us to relearn a motor task. Locomotive behavior results from a continuously tuning dynamic loop between the brain, the muscles, and the environment (Adolph & Franchak, 2017; Brattoli et al., 2021). Neurological or motor disability can often alter or inhibit this loop, resulting in compensatory locomotive behavior strategies in order to maintain some level of function (Atri et al., 2016; Bae et al., 2007; Damiano, 2009; Jaegers et al., 1996; Singh et al., 2019). These atypical strategies are often sub-optimal, can encumber motor skill acquisition and can have negative impacts on an individual's overall health. Therefore, it is crucial for analyses to accurately and holistically describe these motor behaviors to identify appropriate therapy techniques based on unique individual circumstances and to track real progress. In this work, I present a detailed custom approach for characterizing the variations in motor behavior within and across individuals, in addition to, an approach for relating characteristics of brain activation patterns to specific motor behavior.

Presently, it is a challenge to describe and interpret locomotive data due to the large number of continuous variables that are often taken from multiple locations on the body

and from multiple individuals. Broad summary statistics or linear models are often used in locomotor analyses but fall short of identifying the variation of the locomotor activity. It is an even greater challenge to characterize these dynamics across many individuals to distinguish common and unique behavioral patterns. Many locomotor analyses involve cumbersome manual annotation that is subjective and prone to human error (Arac et al., 2019; Berman, 2018; Horst et al., 2019). In addition, typical locomotion analyses focus on a narrow set of limited activities (e.g., reaching in defined directions; Berman, 2018; Wiltschko et al., 2015) and are localized to specific regions of the body (e.g., focusing on the legs while walking; Elsworth-Edelsten et al., 2017). For example, gait is defined as locomotion involving the feet (e.g., walking, running) leading many gait analyses to mostly or exclusively focus on aspects of the lower limbs despite the upper body also providing information about gait strategies (Elsworth-Edelsten et al., 2017). In Figure 1.1 is a neuromusculoskeletal model of the human body during a running gait. Motor commands are sent by the brain to the muscles. The electrical activity of the muscles is recorded using electromyography (EMG). In addition to the muscles within the legs, other muscles in the body, such as in the trunk and arms are involved in the production of gait.

For gait analyses, the movement of the legs, contraction of the leg muscles, and the ground reaction forces with the leg are often the phenomena of interest in many gait studies. Gait analyses commonly focus on scalar value metrics, such as average stride length or cadence. These metrics are indirect, single point measures of the actual time-varying phenomenon. Therefore on their own, these metrics provide incomplete descriptions about gait and are incapable of identifying distinct dynamic gait patterns (Berman, 2018). Other gait studies do monitor EMG to record the electrical activity of the muscles (Commuri et al., 2010; Dionne et al., 2015; Jaegers et al., 1996; Mai et al., 2013; Singh et al., 2019; Wentink et al., 2013; Winter, 1987). In many of these studies, the mean and standard deviation of the EMG activation across many strides are computed. However, the mean and standard deviation are incapable of identifying multiple, distinct patterns of behavior and are sensitive to outliers.

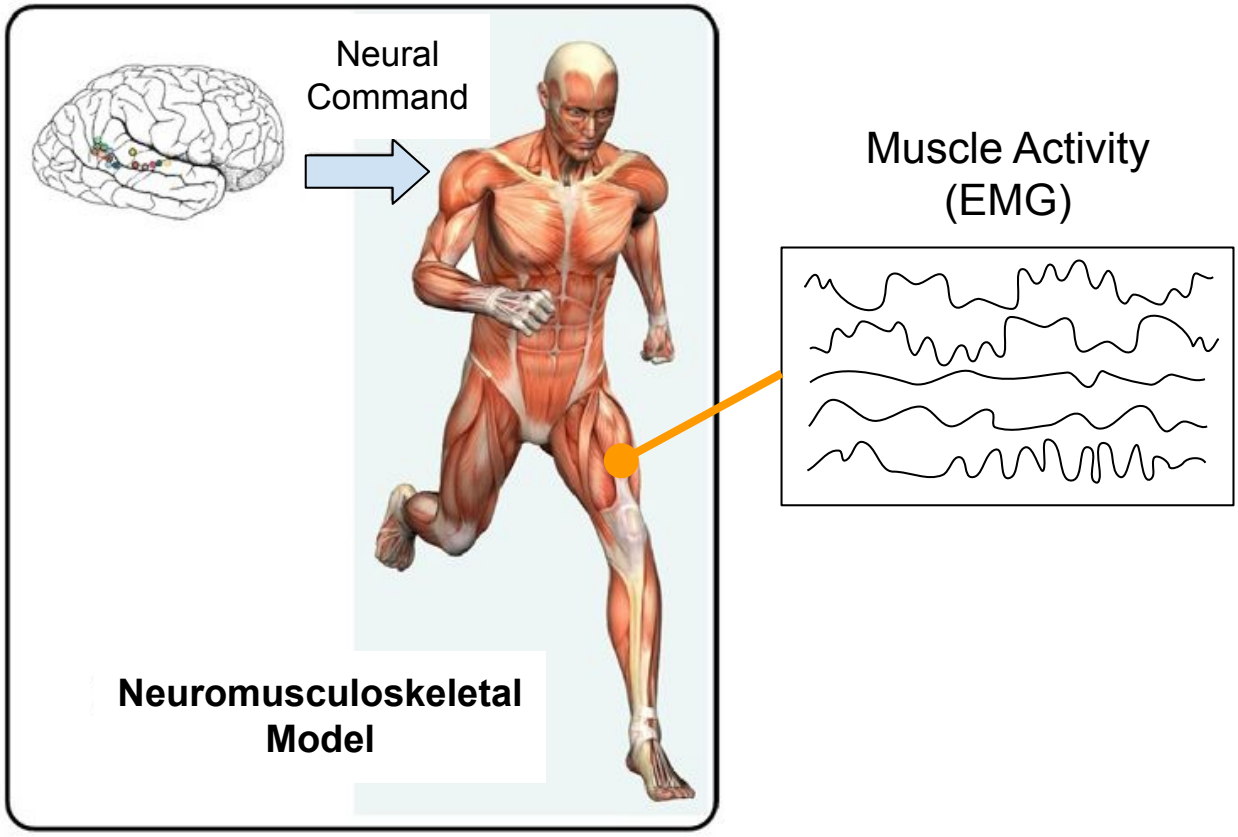


Figure 1.1: A neuromusculoskeletal model of the human body during gait, modified from Figure 3 by Alamdari and Krovi (2017).

Moreover, it is unlikely that a single muscle activation strategy is being employed across all strides from multiple individuals. Therefore, in this work, I apply higher order statistics that capture these unique behavioral patterns across multiple strides and individuals.

In particular, for individuals with amputation, many gait studies mainly divide amputees into two broad groups: above the knee (transfemoral), and below the knee (transtibial; Bae et al., 2007; Hong and Mun, 2005; Seyedali et al., 2012; Taylor and Poka, 2016; Wentink et al., 2013). However, there is large in-group variability (or heterogeneity) within these two demographics, due to factors such as the amputation reason (e.g., trauma, chronic condition) or the amputation surgical approach (i.e., traditional vs osteomyoplastic). Various combinations of these factors, in conjunction with holistic gait data, need to be examined thoroughly to understand precisely how these factors interact. For example, osteomyoplastic

amputation is an innovative surgical approach that aims to reconstruct distal muscles and salvage tissue within the amputated limb to provide function of the severed muscles and bear weight on the distal residuum for active prosthesis use (Ertl et al., 2010; Kahle et al., 2016; Taylor & Poka, 2016). In the presence of cadence asymmetry and greater perceived exertion, Dionne et al. (2017) still found comparable work performance during walking, lifting and carrying tasks in men with osteomyoplastic transtibial amputation (OTTA), as compared to intact controls. Therefore, Dionne et al. (2022) hypothesized similar results for those with osteomyoplastic transfemoral amputation (OTFA). However, they discovered that individuals with OTFA, on average, walked shorter overall distances at two speeds, had lower carry capacity, and reported greater pain during carry tasks than intact control counterparts. Therefore, more advanced approaches are needed to understand the complex differences in locomotive behavior, its causes, and strategies to effectively address motor deficits. Additionally, these approaches should provide the concise descriptions about the interactions of between numerous factors and locomotive measures. In this work, I employ machine learning techniques to objectively capture the complex relationships between the available locomotive measures.

Additionally, the presence of neurological motor disorders, such as Cerebral Palsy (CP), can negatively impact locomotive capabilities and learning. CP is a collection of developmental motor disorders in infants that can impact the progression of locomotion, cognition, perception, communication, and behavior (Bax et al., 2005). There is a wide variation in how CP can manifest in regard to different movement and postural limitations and can involve other secondary health conditions (Damiano, 2009). Physical therapy is a major tool to assist individuals with learning motor skills and tasks necessary for daily activities (Levac et al., 2009; Pomeroy et al., 2011). Many individuals with CP receive physical therapy to address motor disability (Damiano, 2009) and the therapists act as the mediators to their motor learning (Pomeroy et al., 2011). Therefore, the numerous factors involved with CP make it critical for therapists to have all relevant health and locomotive information, during therapy

sessions and throughout long term care. Moreover, early intervention is crucial due to the impacts of neural plasticity and neural pathway pruning in early childhood (Damiano, 2006, 2009; Morgan et al., 2016). The added challenge of communicating with infants adds to the necessity for analyzing large numbers of locomotive measures to ensure a detailed and accurate understanding of individual motor conditions and to evaluate learning progress for long-term improvements.

Crawling and walking are among the most complex behaviors humans learn, involving perceptual skill, postural control, muscular strength, and limb coordination (Adolph & Franchak, 2017; Winter, 1987). The acquisition of crawling can be critical for identifying and addressing neuro-motor deficits of infants with conditions, such as CP. In general, healthy walking strategies are important for injury prevention, especially for individuals with amputation or other motor conditions. Effectively analyzing these feature dense locomotor behaviors and understanding the specifics of how all the factors interact and vary over time demands more robust approaches for concisely and objectively representing them. Autoencoders (AEs) are powerful neural network models that are closely related to many commonly used approaches, such as principal component analysis (PCA; Bao et al., 2020; Champion et al., 2019; Hinton and Salakhutdinov, 2006; Plaut, 2018). I propose that, with AE inspired architectures, the learning of descriptive, compact locomotive representations can be automated, data driven, interpretable, nonlinear, and incorporate existing domain knowledge. To advance our understanding of locomotive behavior, nonlinear models that are capable of quantitatively describing and comparing continuous data streams recorded during real-world motor activities are needed (Berman, 2018). Typical locomotor analyses and therapy sessions occur in settings outside the home or regularly visited environments. According to Adolph et al. (2015), motor behaviors are best understood in their bodily, environmental, and social/cultural contexts. Additionally, individuals often perform relatively simple tasks such as reaching in one direction or walking in a straight line to simplify offline analyses for the experimenters (Berman, 2018). With more robust analyses that can process

large numbers of time-varying attributes, tasks performed during locomotor analyses can be less structured and closer to active daily activities. Therefore, machine learning models offer promising applicability to the domain of locomotor behavior analysis by providing high throughput automation to the data analyses (Arac et al., 2019; Brattoli et al., 2021).

In this work, I propose an approach to uncover the underlying characteristics defining diverse locomotive behaviors from multiple limbs and individuals, simultaneously. Additionally, I propose higher order statistics to quantify and identify multi-modal behavior patterns for comprehensive visualizations. Specifically, I use residuum socket interfacial (RSI), foot pressure and EMG data for discovering muscle recruitment strategies at two gait speeds of individuals, with and without osteomyoplastic transfemoral amputation (OTFA), and provide a robust automated approach for extracting, characterizing, and grouping the motor behavior strategies across strides from multiple individuals. I demonstrate the presence of muscle activity within the distal-residuum of multiple individuals with OTFA, which has not been shown before. I present a novel characterization of the differences in the distribution of co-contraction timing between individuals with and without OTFA. Additionally, I provide quantitative descriptions of the pressure distributions to objectively determine the consistency and quality of the prosthetic fit. These results have the potential implications for improving rehabilitation outcomes, prosthetic design and reducing risk of injury.

I also propose an approach for relating limb movements (from kinematic data) with brain activity (from electroencephalography, EEG) in infants during the acquisition of crawling by extracting relevant features from machine learning models. I describe the relationships between cortical brain regions over three periods of infant development. I extract movement labels for specific limbs to utilize for the construction of models. Through a feature importance approach, I demonstrate the significance of brain activation features at different regions across the cortex for predicting the movement of different limbs and provide evidence for increasing cortical connectivity at higher brain activation frequencies.

In the remainder of this dissertation, I review the details and advantages of higher-order

statistical tools for describing complex multi-modal distributions in Chapter 2. Chapter 2 also contains the definitions and descriptions of the machine learning tools and concepts I utilize for characterizing and identifying behavioral patterns. I introduce bipedal walking, the implications of the co-activation of muscles, and summarize gait analyses of individuals with osteomyoplastic reconstruction in Chapter 3. I discuss the details of my proposed approach for extracting strides from pressure data and comparatively visualizing and characterizing gait across multiple individuals and groups in Chapter 4. In Chapter 5, I present the results from the application of my approach on gait data from individuals with and without osteomyoplastic transfemoral amputation. I discuss infant neuro-motor development in Chapter 6. I provide the specific details of my approach for labeling movements and identifying significant brain activation patterns over the cortex. I discuss the results for identifying significant brain regions and activation frequencies using kinematic and EEG data from infants learning to crawl using an assistive crawling device. Lastly, I discuss conclusions and contemplate future directions for this work in Chapter 7. Additionally, some supplemental material is provided within the Appendix.

Chapter 2

Related Work

Locomotion is challenging to describe accurately and holistically due to the complex interdependencies between multiple systems of the body. Locomotor analyses are often performed in diagnostic settings to identify and evaluate motor disorders. The analyses typically involve slow subjective manual observations, single point summary statistics, or simple linear models. These factors limit the aspects of locomotive behavior that can be understood. Therefore, procedures that can provide more detailed contextualized information about complex locomotor actions can improve our general understanding of locomotion, diagnostic capabilities and overall quality of care for individuals.

In this chapter, I discuss the use of representation learning to address the challenge of modeling the complex nonlinear time-varying features of locomotion. I introduce relevant tools from the field of clustering to facilitate identification of distinct types of behaviors. Lastly, I describe statistical tools for quantitatively characterizing and visualizing large volumes of behavioral data.

2.1 Representation Learning

To advance our understanding of complex domains, such as human locomotion, we need well constructed representations of the observed systems. A well constructed representation can

be defined as one that is simple (i.e., understandable), conducive to building accurate models, and facilitates knowledge discovery (Bengio et al., 2013; Champion et al., 2019; Montavon et al., 2011). However, there is an innate trade-off between simplicity and accuracy as the complexity of a system increases. Simple descriptions will inherently remove details, making it more challenging to build representations that will yield the highest accuracies. Therefore, objective and efficient approaches are required to identify data representations that locate the appropriate balance between simplicity and performance.

For practical uses, principled approaches for constructing representations should also be automated to efficiently leverage information from large quantities of feature rich data. Current representation constructions can often involve manual, crafting making them less objective and less feasible for larger data sets. The more complicated the system is, the more challenging it becomes to identify the underlying relationships between the observed features. Some recorded variables might either partially describe the observed system, interact with multiple other variables, largely be overpowered by noise or be completely unrelated. Therefore, automated techniques for constructing well-formed representations should be robust to noise and superfluous information, to capture the meaningful relationships between the relevant features and yet effectively describe the data.

Representation learning can either be performed by a separate independent model or a jointly learned component to a larger model architecture. Depending on how information is represented, a task can become easier or harder impacting how well a model can perform or generalize (Bengio et al., 2013; Goodfellow et al., 2016). Therefore, it can be desirable to build representation transforms that are independent of any particular objective. Ideally, the learned representation transformation should be capable of taking amorphous, noisy, real-world inputs and describing the data at multiple levels of abstraction for application to any arbitrary task. Then, downstream models with specific objectives can simply query the representation transform for the optimal set of informative features specific to the model's objective.

Regardless of whether a separate upstream model (or individual) has transformed the data representation, task specific models still implicitly learn context-specific representations in the process of learning their objective. For example, deep neural network models for classification implicitly learn new data representations at each successive layer to produce an accurate, and typically simple, representation in the final layer (Bengio et al., 2013; Goodfellow et al., 2016; LeCun et al., 1998; Montavon et al., 2011; Rumelhart et al., 1986). Additionally, the goal of any semi-supervised or self-supervised learning model is to identify robust underlying data representations from a subset of labeled examples and effectively generate labels for large volumes of unlabeled or unseen instances (Bengio et al., 2013; Goodfellow et al., 2016; Sohn et al., 2015).

There are various high-level perspectives on the form of data representations. Data representations can describe the manifold upon which the data lie on or near, they can describe the decision boundaries partitioning the space around groups of data instances, or they can estimate the densities describing how the data are distributed throughout the space (Bengio et al., 2013). Manifolds can be described as low dimensional surfaces, or more generally, lower dimensional regions of a high dimensional space where the data are densely distributed. The approaches for learning these types of descriptions generally make assumptions about the abstract characteristics of the data and direct focus to a particular structure when building the new representation spaces. Various techniques, such as principal component analysis (PCA), independent component analysis (ICA), and various types of autoencoder (AE) architectures attempt to preserve global properties of the data when transforming it into new representations (Montavon et al., 2011). Global properties refer to the relative relationship between all pairs of points. For example, global approaches might explicitly act to preserve the relative magnitude of all the pair-wise distances or maintain the overall distribution of the points within the new representation space. Other representation learning approaches focus on preserving local traits of the data in the new representation space and often only make assumptions about the smoothness of the true data

manifold. Smoothness is defined such that given a function f and two nearby points x and y where $x \approx y$ then $f(x) \approx f(y)$ (Bengio et al., 2013). Smoothness is a useful characteristic that, unfortunately, on its own is not stable for high dimensional data since the quantity of non-smooth features of the target function grows exponentially with the number of dimensions. Additionally, by assuming that the lower dimensional manifolds are smooth, the locally focused techniques cannot adequately account for discontinuities or other complex structures within the data. Therefore, learned representations should focus on characterizing global traits or a combination of global and local attributes (Bengio et al., 2013).

2.2 Dimensionality Reduction

Accurately and concisely representing locomotion involves analyzing large quantities of time vary-ing data. Dimensionality reduction approaches provide an objective method for reducing locomotion data into smaller representations that still accurately describe the data. Dimensionality reduction and compression techniques are manifestations of representation learning that explicitly construct smaller representations. Unfortunately, more is not always better. When collecting large quantities of features, the true number of relevant features (i.e., the true dimensionality) that is necessary to accurately describe the underlying behavior of the data is likely to be significantly less (Champion et al., 2019; Hinton & Salakhutdinov, 2006; Shlens, 2014; van der Maaten et al., 2007). Moreover, large numbers of features can cause the computation times for building or executing models to explode and reduce our understanding of the models. There are many common approaches to representation learning that employ dimensionality reduction techniques to minimize the size of the representation while maintaining important characteristics of the data. Smaller or sparse representations are less computationally expensive and are typically assumed to be more interpretable. Moreover, larger representations are generally prone to erroneously mistaking noise for meaningful information.

Any subset of the features collected could be redundant, irrelevant, or dominated by noise. Therefore, numerous techniques for dimensionality reduction have been developed to identify the smallest set of informative features. The general approach can be framed by defining $X \in \mathbb{R}^{N \times D}$ to be a data set of N data instances with D features and the true dimensionality to be d (van der Maaten et al., 2007). Therefore, the aim of dimensionality reduction techniques is to identify the true dimensionality, d, such that $d \ll D$.

To determine an appropriate choice for d, some techniques will focus on directly selecting d of the measured features based on inter-feature correlation or strong correlation between the feature and the model output measure. More intricate techniques attempt to construct new features by computing lower dimensional embeddings of the original high dimensional data, such as PCA and AEs. These embedding techniques generally make assumptions about whether the lower dimensional features are linear or nonlinear and will either focus on retaining local or global structure when transforming the data into the reduced dimensional space. However, global dimensionality reduction approaches have been found to retain global and local data structure better and generalize well with the introduction of new data (van der Maaten et al., 2007). Additionally, many complex systems are expected to have nonlinear features (Bengio et al., 2013; Champion et al., 2019; Goodfellow et al., 2016; Hinton & Salakhutdinov, 2006; LeCun et al., 1998; Montavon et al., 2011; Shlens, 2014; van der Maaten et al., 2007).

2.2.1 Principal Component Analysis (PCA)

In this work, Principal Component Analysis (PCA) is used as a linear benchmark for constructing accurate reduced representations of locomotion. PCA constructs abstract linear features by determining the global axes accounting for the most amount of variation within the data (Bao et al., 2020; Plaut, 2018; Shlens, 2014; van der Maaten et al., 2007). These new axes or directions are referred to as the principal components (PCs). PCA essentially transforms the data X from the measured space into a new, "PC space" Y, where the features

are orthogonal, most of the variation is described, and the reconstruction error from reversing the transformation is minimized. PCA is formulated as:

$$Y = XP, \tag{2.1}$$

where the data X is a matrix of the form:

$$X = \begin{bmatrix} x_1 \\ \vdots \\ x_i \\ \vdots \\ x_N \end{bmatrix} \in \mathbb{R}^{N \times D} \; with \; x_i \in \mathbb{R}^{1 \times D}, \tag{2.2}$$

where N is the number of data samples and D is the number of observed features. The new representation Y is a matrix of the form:

$$Y = \begin{bmatrix} y_1 \\ \vdots \\ y_j \\ \vdots \\ y_N \end{bmatrix} \in \mathbb{R}^{N \times M} \; with \; y_j \in \mathbb{R}^{1 \times M}, \tag{2.3}$$

where M is the new dimensionality and is $M \leq D$. The matrix P containing the PC vectors (also the eigenvectors) defines the transformation into the new representation and is of the form:

$$P = \begin{bmatrix} p_1 & \dots & p_k & \dots & p_M \end{bmatrix} \in \mathbb{R}^{D \times M} \; with \; p_k \in \mathbb{R}^{D}, \tag{2.4}$$

where each column vector p_k is an eigenvector or PC. PCA assumes the PCs are orthogonal and unit vectors, making P an orthonormal matrix, therefore, when $M = D$ then $P^{-1} = P^T$.

The result of PCA reduces to a rotation aligning the maximal directions of variation along the PCs. The matrix P maps X to the new axes describing the most amount of variation and the reconstruction error is minimized using the objective function:

$$\begin{aligned} &\arg\min_{P} ||X - YP^{-1}||_2^2 \\ &= ||X - (XP)P^{-1}||_2^2, \end{aligned} \tag{2.5}$$

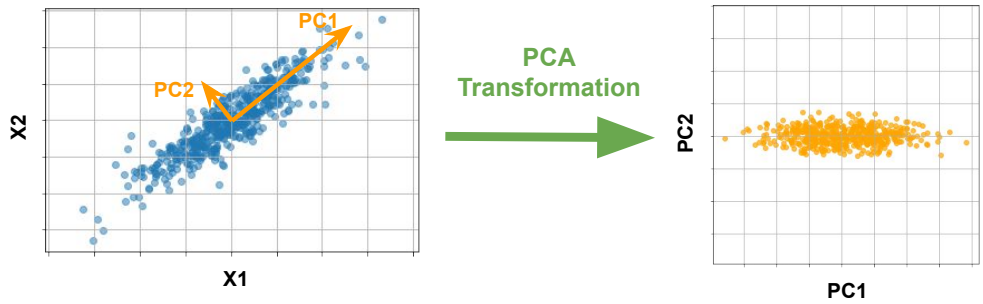
where P^{-1} is the inverse of P and $\tilde{X} = YP^{-1} \approx X$.

The eigenvectors of the covariance matrix C_X of the original data indicate the directions of largest variation within the data. The covariance matrix is computed as the product between all pairs of the feature vectors of X. Assuming X has a mean of zero, the covariance matrix is of the form:

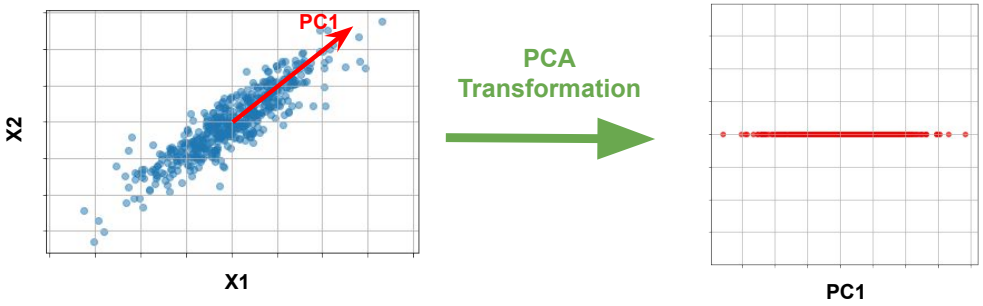
$$C_X = \frac{1}{N} X^T X = \frac{1}{N} \begin{bmatrix} x_1x_1 & x_1x_2 & \dots & x_1x_D \\ x_2x_1 & x_1x_2 & \dots & x_2x_D \\ \vdots & \vdots & \ddots & \vdots \\ x_Nx_1 & x_Nx_2 & \dots & x_Nx_D \end{bmatrix} \in \mathbb{R}^{D \times D}. \tag{2.6}$$

Then the transformation matrix P can be obtained using singular value decomposition (SVD) to compute the eigenvectors and the corresponding eigenvalues (Shlens, 2014; van der Maaten et al., 2007).

An example of the PCA transformation on a two-dimensional data set is shown in Figure 2.1a. In the left panel, two PCs are identified along the directions of greatest variance. In the right panel, is the result of the transformation of the data, resulting in a rotation. For data with a high number of dimensions, PCA can be used for compression by selecting a subset of PCs that account for the majority of the data variance. There are many strategies for selecting the number of PCs. The PCs are already ordered from highest to lowest variance accounted for (VAF). The VAF for each PC_i is the corresponding eigenvalue λ_i. One strategy



(a) PCA Transformation



(b) Dimensionality Reduction

Figure 2.1: An illustration of PCA. (a) A transformation from the original measured space (left panel) into the new PC space (right panel). (b) Using PCA, the number of dimensions is reduced from two (left panel) to one (right panel).

is to keep the PCs accounting for the most variance where the cumulative fraction of VAF (FVAF) is approximately some fraction such as 0.95. The FVAF for a single PC is:

$$\text{FVAF}_i = \frac{\lambda_i^2}{\sum_{j=1}^{M} \lambda_j^2} \ , \tag{2.7}$$

where λ_i is the eigenvalue or the standard deviation of the i^{th} PC and M is the total number of PCs. Another simple strategy is to remove the PCs with VAF below some threshold. Once the number $m < M \leq D$ of PCs is selected, a new transformation matrix $P' \in \mathbb{R}^{D \times m}$ containing the new number of PCs is used to transform the data using the formula

$$Y' = XP', \tag{2.8}$$

where $X \in \mathbb{R}^{N \times D}$ is the original data, $Y' \in \mathbb{R}^{N \times m}$ is the new lower dimensional data

representation, and

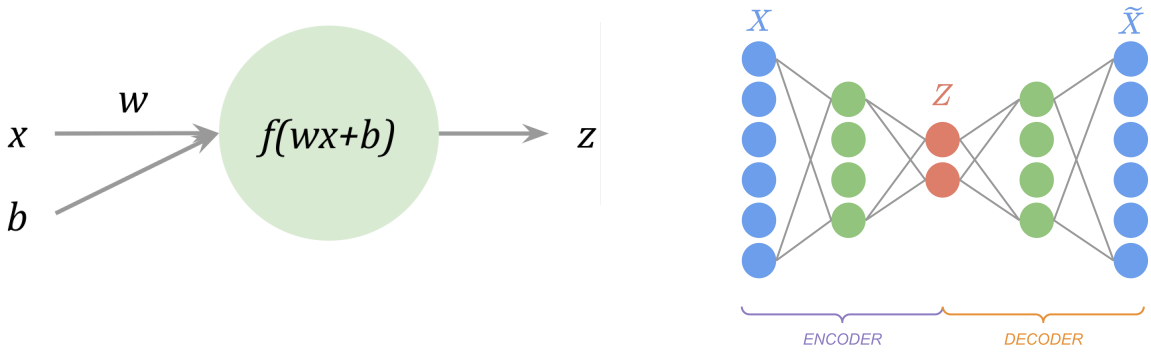
$$P = \begin{bmatrix} P' & p_{m+1} & \dots & p_M \end{bmatrix} \in \mathbb{R}^{D \times M}, \tag{2.9}$$

where p_{m+1} and $p_M \in \mathbb{R}^D$. An example of the dimensionality reduction from two to one dimension is shown in Figure 2.1b. In the left panel, one PC is selected along the direction with the greatest variance. In the right panel, is the result after applying the transformation and reducing the number of features. PCA often works well in practice, as its theoretical and mathematical foundations overlap with many other approaches. Therefore, it is often recommended as a starting point for constructing lower dimensional feature representations. However, there are likely nonlinear characteristics of the data that PCA does not capture, therefore, it is worth exploring the nonlinear alternatives.

2.2.2 Autoencoders (AEs)

In this work, I use autoencoders (AEs) to capture nonlinear relationships between locomotor measures. An AE is a type of neural network architecture that is typically used to construct meaningful compressed representations of data. Neural networks are models that can approximate complex nonlinear functions and are a generalized approach for modeling functions by connecting multiple computing units called *neurons* or *nodes* through multiple layers. Multiple nodes can be stacked into a layer and multiple layers can feed their outputs as inputs into subsequent layers. Figure 2.2a is an illustration of a singular node. Each node has multiple inputs $x \in \mathbb{R}$ from nodes in prior layers, with weight $w \in \mathbb{R}$, a single bias input $b \in \mathbb{R}$ and an output $z \in \mathbb{R}$ that can connect to multiple nodes in subsequent layers. At each node, the result of the weighted input plus the bias:

$$a = wx + b, \tag{2.10}$$



(a) Compute Node

(b) Autoencoder

Figure 2.2: An autoencoder (AE) neural network. (a) A simple compute node. (b) The autoencoder architecture.

is passed into a nonlinear activation function $f(a)$ with output z. The sigmoid function:

$$f(a) = \frac{1}{1 + e^{-a}}, \tag{2.11}$$

is an example of a nonlinear activation function in Figure 2.2a. Another common activation function is the exponential linear unit (ELU; Clevert et al., 2016). The ELU activation function is defined as:

$$f(a) = \begin{cases} a & \text{if } a > 0 \\ \alpha e^a - 1 & \text{otherwise} \end{cases}, \quad f'(a) = \begin{cases} 1 & \text{if } a > 0 \\ f(a) + \alpha & \text{otherwise} \end{cases}, \tag{2.12}$$

where a is the activation of the node, $\alpha > 0$ is a constant, and $f'(a)$ is the derivative of the node output. The node outputs are linear whenever $a > 0$ and exponential otherwise. ELUs can speed up the training process and help improve generalized model accuracy.

Using multiple compute nodes to build layers, multiple layers are stacked together to build larger neural network models such as AEs. AEs typically construct nonlinear lower dimensional representations of data by attempting to reconstruct the original input from an intermediate encoding, as shown in Figure 2.2b. The AE architecture is composed of two

connected sub-networks, the encoder and the decoder. The encoder is defined as:

$$Z = E_\theta(X), \tag{2.13}$$

where $X \in \mathbb{R}^{N \times D}$ is the original data, N is the number of data instances, D is the number of features, θ are the weights for the inputs of each layer, and $Z \in \mathbb{R}^{N \times d}$ is the lower dimensional representation where $d \ll D$. The decoder is defined as:

$$\tilde{X} = D_\beta(Z), \tag{2.14}$$

where $\tilde{X} \in \mathbb{R}^{N \times D}$ is the reconstruction of the original input and β are the weights for each layer of the decoder. The encoder transforms the data X and generates an informative lower dimensional or latent representation Z. The features of X are the inputs to the nodes of the first hidden layer of the encoder. The features of Z are the outputs of the encoder and the inputs to the nodes of the subsequent layer of the decoder. The latent representation Z is transformed by the decoder sub-network to produce the data reconstruction $\tilde{X}$ using the model parameters β as weights. To extend a single compute node to multiple data instances, weights are applied to each feature for each data instance:

$$f(A) = f(XW^T + b), \tag{2.15}$$

where $A \in \mathbb{R}^N$ is the intermediate output prior to applying the activation f and $W \in \mathbb{R}^D$ are the weights on each feature. The optimal parameters θ^* and β^* for the AE model are obtained by minimizing the reconstruction error between the original input and the output of the AE using the objective function:

$$\begin{aligned} \theta^*, \beta^* &= \arg\min_{\theta,\beta} ||X - \tilde{X}||_2^2 \\ &= \arg\min_{\theta,\beta} ||X - D_\beta(E_\theta(X))||_2^2, \end{aligned} \tag{2.16}$$

where $\tilde{X} = D_\beta(E_\theta(X))$. Then Equation 2.16 yields a set of values for θ and β such that the mean squared error (MSE) between the original data and the reconstruction is minimized. A set of values for θ and β that minimize the error are obtained over multiple iterations using the gradient of the MSE with respect to the weights in a process known as gradient descent. The global optimum is typically difficult to obtain, particularly, when the objective function (Equation 2.16) has many local minima. Gradient descent will typically find a set of parameter values that correspond to a local minimum.

Some advantages of AEs over PCA are nonlinear feature construction, model flexibility (e.g., various configurations of nodes and layers), and efficient scaling to large numbers of data instances. By simply changing the activation functions of the AE nodes, we can model linear or nonlinear relationships, whereas PCA can only model linear relationships. When the AE is a single layer network with linear activation functions at all the nodes, it effectively reduces to PCA (Plaut, 2018). The modularity of connecting various numbers of layers with various quantities of nodes with a variety of activation functions makes AEs very flexible for modeling characteristics of many data domains. In practice, PCA performs well in many applications, but still falls short when used for very complex nonlinear systems (van der Maaten et al., 2007) and is sometimes outperformed by AEs (Hinton & Salakhutdinov, 2006). Some disadvantages to AEs are long training times the larger the number of nodes and layers become. Additionally, the compressed representations are more difficult to directly interpret than that of PCA. After performing analyses within the AE latent space, the data are decompressed to understand the implications in the original data domain.

Layer Configuration

Part of the advantages of neural networks is the flexibility of their layer-wise configuration. Beyond stacking layers or adding nodes into layers, we can perform special operations such as convolution and pooling on temporal or spacial data with multiple signals or channels. Convolution and pooling are operations used for capturing time invariant signal patterns from

locomotor data within the compressed representations. Neural networks that use convolution operations are referred to as convolutional neural networks (CNNs).

Convolution in a CNN involves the point-wise multiplication of an input signal with a shorter signal, called a kernel or filter, at all offsets in time (or space). At each offset, τ, the point-wise weighted average of the input with the kernel is computed as:

$$g(\tau) = (X * K)(\tau) = \sum_{i=-\infty}^{\infty} x_i k_{\tau - i}, \tag{2.17}$$

where $X \in \mathbb{R}^{1 \times D}$ is the input signal with D time points, $K \in \mathbb{R}^{1 \times D}$ is the kernel function, and $x_i, k_i \in \mathbb{R}$. The kernel can also be applied to a set of input signals at each offset to compute a weighted average over the input signals and identify relationships between the signals over time. In the context of neural network architectures, multiple convolutional filters can be applied at each layer over the inputs to identify localized features and combine them across layers to produce higher order features (Bengio et al., 2013; LeCun et al., 1989, 1998). This process allows us to recognize more complex patterns and relationships between the original input signals. An advantage of convolution layers is that they are focused on recognizing localized time-varying structures or patterns that can occur at any time within the signal (LeCun et al., 1998).

The pooling operation, also referred to as sub-sampling, is similar to convolution. However, instead of two signals being weighted to together, typically, a max or average operation is performed on the input signal itself over the time interval to obtain a summary and is also time invariant for localized pattern recognition (Bengio et al., 2013). Max pooling is defined as:

$$g(\tau) = max(x_\tau, \ldots, x_{\tau+F}). \tag{2.18}$$

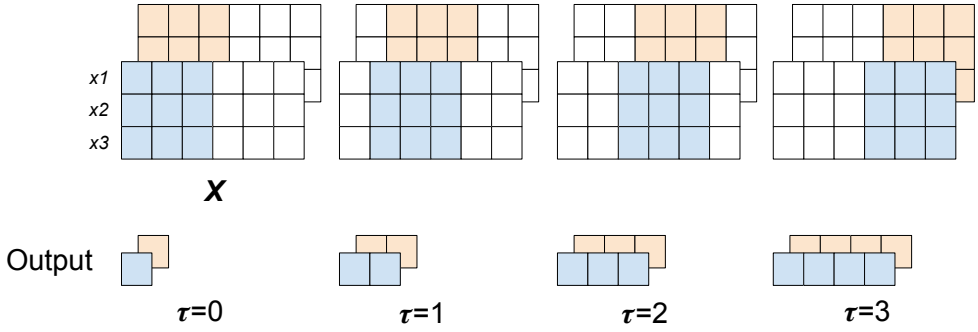
Layers that perform pooling reduce the number of parameters that a model has to learn while still identifying time invariant higher order features when composed together through multiple layers or, particularly, after convolutional layers (LeCun et al., 1998). Layers performing

convolution immediately followed by pooling are referred to as convolutional blocks. The convolutions identify the localized characteristics of patterns and pooling layers summarize those characteristics.

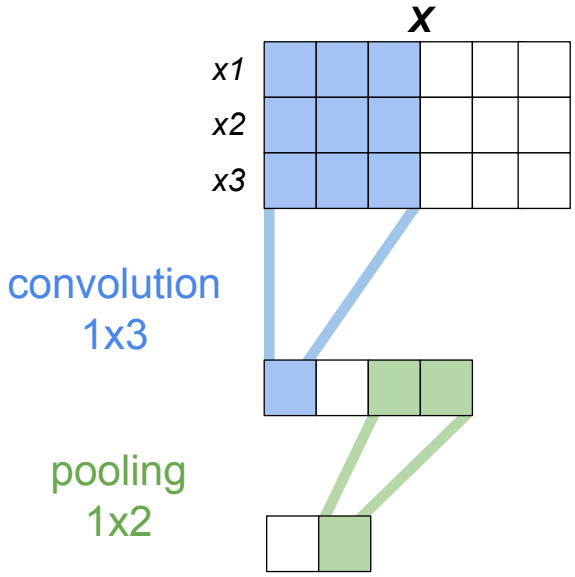
An example 1D (or time series) convolutional block is shown in Figure 2.3. The input $X \in \mathbb{R}^{n \times D}$ (Figure 2.3a) is a collection of $n = 3$ time series (or channels) where $D = 6$ is the number of time samples. All n times series are convolved using two filters (the blue and the orange samples) over a brief time interval containing 3 samples. The output produces a new set of time series from each convolution filter. Each output time series is colored based on the filter used to produce it. At each time offset τ, the filter is slid by one time sample to compute the next sample in the output. Pooling is performed on the outputs from each convolution filters, separately. The pooling on the output from the blue convolution filter is shown in Figure 2.3b. The pooling kernel and its output are in green and the pooling kernel is applied at non-overlapping time offsets containing 2 samples. Using convolutional blocks within AE architectures allows one to construct compressed representations that are based on multiple time-varying patterns and their relationships across multiple signals. Convolutional blocks for encoding time series data are shown in Figure 2.3. To use convolution for the decoding process, upsampling is used instead of pooling in between convolutional layers. Upsampling is performed by repeating each sample r times. For example, if $r = 2$ and $x = [1, 2, 3]$, then the result of upsampling is $x = [1, 1, 2, 2, 3, 3]$. After upsampling, convolution is performed to smooth the signal x.

2.3 Support Vector Machines (SVMs)

In this work, Support Vector Classifiers (SVCs) are used to predicting limb movements and evaluate the influence of specific brain regions and activation frequencies. SVCs compute an implicit hyper-surface to distinguish between two classes (Figure 2.4). The hyper-surface



(a) 1D Convolution



(b) 1D Convolutional Block

Figure 2.3: 1D convolutional block. (a) Illustrates convolution for a set of three input signals, using two convolutional filters (blue and orange). (b) A convolutional block where pooling (green) is performed after the convolution (blue).

(i.e., the decision boundary) is defined as:

$$y(x_i) = \sum_{f=1}^{D} \phi(x_{i,f}) w_f + b = 0, \tag{2.19}$$

where ϕ is a predefined transformation on the data $X \in \mathbb{R}^{N \times D}$, N is the number of data instances $x_i \in \mathbb{R}^{1 \times D}$, D is the number of features, $w_f \in \mathbb{R}$ is the weight for feature f, $W \in \mathbb{R}^D$ and $b \in \mathbb{R}$ are the parameters of the decision boundary y (Bishop, 2006; Boser et al., 1992; Chang & Lin, 2007). The class of the data instance x_i is computed using the rule:

$$+1 \quad \text{if } y(x_i) > 0 \tag{2.20}$$

$$-1 \quad otherwise. \tag{2.21}$$

The function ϕ is selected to construct a higher or infinite dimensional feature space that can produce nonlinear decision boundaries between the classes. The optimal values for the parameters are determined by minimizing the objective function:

$$\min_{W,b,\xi} \ \frac{1}{2}||W||^2 + C \sum_i \xi_i, \tag{2.22}$$

$$\text{subject to } t_i(\phi(x_i)W + b) \geq 1 - \xi_i, \ and \tag{2.23}$$

$$\xi \geq 0, \tag{2.24}$$

where $||W||^2$ controls the size of the margin between the decision boundary and the data, $C > 0$ is a regularization parameter and $\xi \geq 0$ is the slack variable used to control the amount of allowable misclassification. Additionally, ξ penalizes misclassification proportional to the distance from the margin boundary. The objective function is minimized under the constraints in Equation 2.23, where $t_i \in \{-1, 1\}$ is the class label for the data instance x_i. The decision boundary is defined such that $\phi(x_i)W + b > 0$ when $t_i = 1$ and $\phi(x_i)W + b < 0$ when $t_i = -1$.

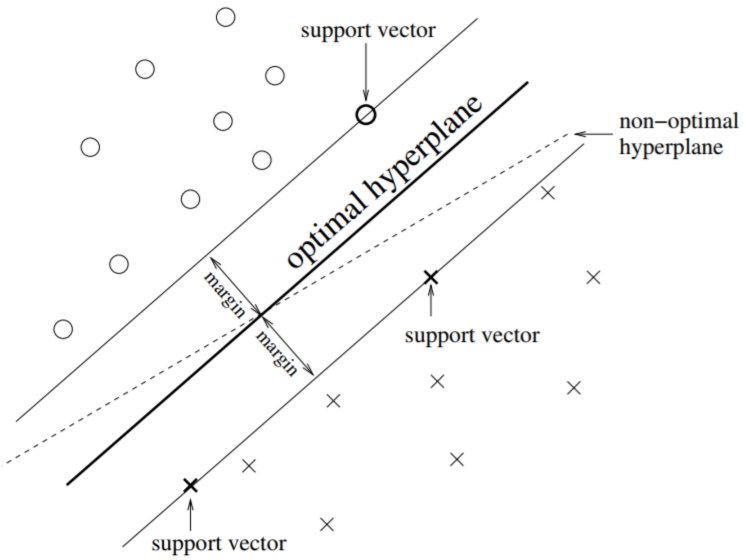


Figure 2.4: Support Vector Classifier from Figure by Boser et al. (1992). The decision boundary is defined by the support vectors that maximize the margin.

The Equations 2.22 and 2.23 balance maximizing the margins around the decision boundary and minimizing the classification errors. The closest training data instances on both sides of the decision boundary define the margin boundaries and are referred to as the support vectors (Figure 2.4). For all support vectors: $t_i y(x_i) = 1$ and $\xi_i = 0$.

In Figure 2.4, data instances from one class are the circles and data instances from the other class are the crosses. A non-optimal decision boundary that does not maximize the margins is shown as a dashed line. Data instances on or inside the margins on the correct side of the decision boundary satisfy $0 \leq \xi_i \leq 1$ so that $1 \geq t_i y(x_i) \geq 0$. Data instances on the decision boundary have $y(x_i) = 0$ and $\xi_i = 1$. For, data instances on the wrong side of the decision boundary $\xi_i > 1$ to indicate misclassification. The direction of the decision surface is determined such that the classification error is minimal, and the margin widths are maximal (Boser et al., 1992). Larger margins indicate greater relative distances between examples of the two classes and allow classification with higher confidence for greater class discrimination, improving generalization capabilities of the model (Besserve et al., 2011). SVCs incorporate a regularization parameter C to account for outliers and mitigate overfitting to improve generalization performance.

Additionally, non-linear decision boundaries are constructed at a low cost with a kernel function:

$$\kappa(x_i, x_j) = \phi(x_i)\phi(x_j)^T, \tag{2.25}$$

to implicitly map the feature data into higher dimensional spaces. A common kernel method is the Gaussian, or Radial Basis Function (RBF), $\kappa(x_i, x_j) = e^{-\sigma||x_i - x_j||^2}$ with scaling factor $\sigma > 0$. This kernel can produce rounded decision surfaces for more complex class separations. Other kernels include the linear kernel $x_i x_j^T$ that produces linear boundaries, polynomial kernel $(\sigma x_i x_j^T + r)^d$ of degree d with the offset r, and the sigmoid kernel $tanh(\sigma x_i x_j^T + r)$ (Pedregosa et al., 2011). The polynomial and sigmoid kernels produce curved boundaries. Optimizing Equation 2.22 is often difficult, therefore, it is reformulated using a dual formulation in terms of the kernel function and a sum over the support vectors. The reformulation makes it more efficient to compute the solution that maximizes the margins in higher dimensional spaces.

2.4 Kernel Density Estimation (KDE)

In domains, such as locomotor behavior, where parametric distributions do not adequately describe the distribution of some continous random variable or assumptions about the distribution shape are inappropriate, we can use non-parametric approaches to estimate the densities of the observed data (Silverman, 1998; Venables & Ripley, 2002). Kernel density estimation (KDE) is a common approach to non-parametric estimation of the true probability density and is represented using a set of samples from the unknown distribution. The probability density function (pdf) for the kernel density estimator is defined as:

$$\hat{f}_b(x) = \frac{1}{bN} \sum_{n=1}^{N} K\left(\frac{x - x_n}{b}\right), \tag{2.26}$$

where $\hat{f}_b(x)$ is the estimate of the pdf, $b > 0$ is the bandwidth, x is the random variable, N is the number of samples from the random variable, x_n is a sample, and $K(\bullet)$ is a kernel function (Silverman, 1998; Venables & Ripley, 2002). The kernel function is selected to have the properties:

1. Positive finite: $0 \leq K(u) < \infty$,
2. Symmetric: $K(u) = K(-u)$, and
3. $\int_{-\infty}^{\infty} K(u)du = 1$.

In practice, kernel functions are often selected to be a density function, such as the Normal distribution.

The choice of bandwidth, b, is among the most important decisions, next to the choice of the kernel function (Venables & Ripley, 2002). The bandwidth controls the smoothness of the estimated density. Setting the bandwidth too low results in under-smoothing and including too much noise into the estimation. Setting the bandwidth too high results in over-smoothing and eliminating meaningful details describing the shape of the distribution. There are many approaches to selecting theoretical values for the bandwidth provided certain assumptions hold or selecting data-derived values to minimize the number of assumptions in the estimation process. Additionally, a conservative estimate for the bandwidth can also be derived from the square-root rule $\sqrt{N}$ for selecting the number of bins (Dogan & Dogan, 2010), where N is the number of data samples. The bandwidth becomes $b = \frac{max-min}{\sqrt{N}}$, where the max is the maximum from the data, and min is the minimum.

2.5 Highest Density Regions (HDRs)

Traditionally, distributions or a set of samples from a distribution are summarized using the mean and standard deviation. This can misrepresent the true variation within locomotor behavior data, especially when the true distribution is not uni-modal or symmetrical.

Confidence intervals or intervals designated by percentiles are insufficient for describing the distribution shape, as they do not guarantee identification of all the most likely instances within the distribution (Figure 2.5). Therefore, we want an approach that can summarize the signal behavior by capturing multiple modes and all the most probable observations at each sample point, regardless of the shape of the distribution. Highest density regions capture multiple disconnected intervals containing local modes, are asymmetrical, and are guaranteed to contain all the most likely instances (Hyndman, 1996; Kruschke, 2015). Figure 2.5 is an example comparing multiple types of statistical intervals with cumulative densities of 75%. The 75% HDRs are the only approach capable of capturing both modes and ensuring all instances within the intervals are just as or more likely than the instances outside its intervals. Moreover, every instance within the HDRs is just as or more likely than any instance outside the HDRs. This is only true for confidence intervals when the distribution is uni-modal and symmetric.

The HDRs are defined as the shortest intervals consisting of the most likely values of a random variable X, whose set of likelihoods integrate to at least $(1 - \alpha)$ such that:

$$R(f_\alpha) = \{x : f(x) \geq f_\alpha\}, \tag{2.27}$$

where x is the domain of the random variable X, $f(x)$ is the pdf of the distribution of X, α is the probability that $x \notin R(f_\alpha)$, and f_α is the threshold density value (Hyndman, 1996). The value of f_α is the largest density value such that:

$$P(X \in R(f_\alpha)) \geq 1 - \alpha, \tag{2.28}$$

the total density of all the samples x from X, that are in $R(f_\alpha)$ and is at least $(1 - \alpha)$. The definition of f_α inherently yields the smallest set of intervals for the HDRs. The HDRs can be summarized concisely using f_α. The HDRs can also be summarized by the list of the pairs of the start and end points of each of the intervals $\{(s_1, e_1) \dots (s_i, e_i) \dots (s_n, e_n)\}$, where s_i

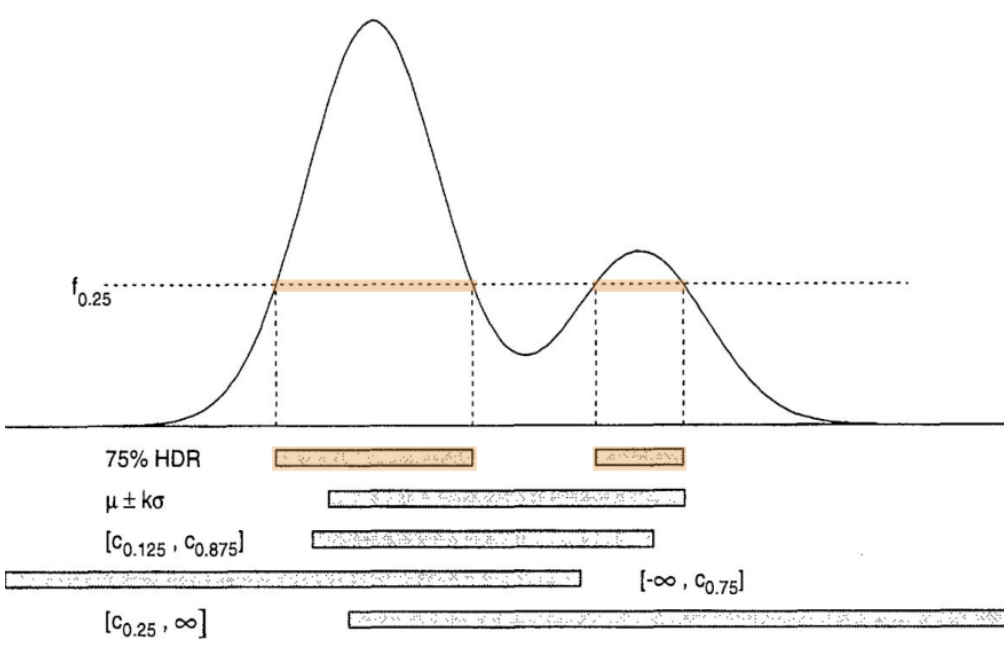


Figure 2.5: An illustration of 75% highest density regions (HDRs) compared to other common statistical intervals containing the same cumulative density of 75% (modified from Hyndman, 1996). The interval $\mu \pm k\sigma$ is a symmetrical interval $k\sigma$ units around the mean such that the cumulative probability within the interval is 75% where k is some constant to obtain the desired cumulative probability and σ is the standard deviation. The value c_q denotes the q^{th} quantile.

and e_i are the respective start and end points of the i^{th} interval and n is the number of intervals.

Moreover, HDRs are robust to skewed data. Figure 2.6 compares the 75% HDRs for two skewed distributions with different spreads to the interval $\mu \pm k\sigma$, where k is a scalar factor such that the density contained within the interval is approximately 75%. Despite the skewed shape of the data distribution, the HDRs are able to capture all the most likely instances. In contrast to the standard interval $\mu \pm k\sigma$, which contains instances less likely than those outside of its interval. Additionally, we can see that the length of the HDR increases with the spread of the data distribution.

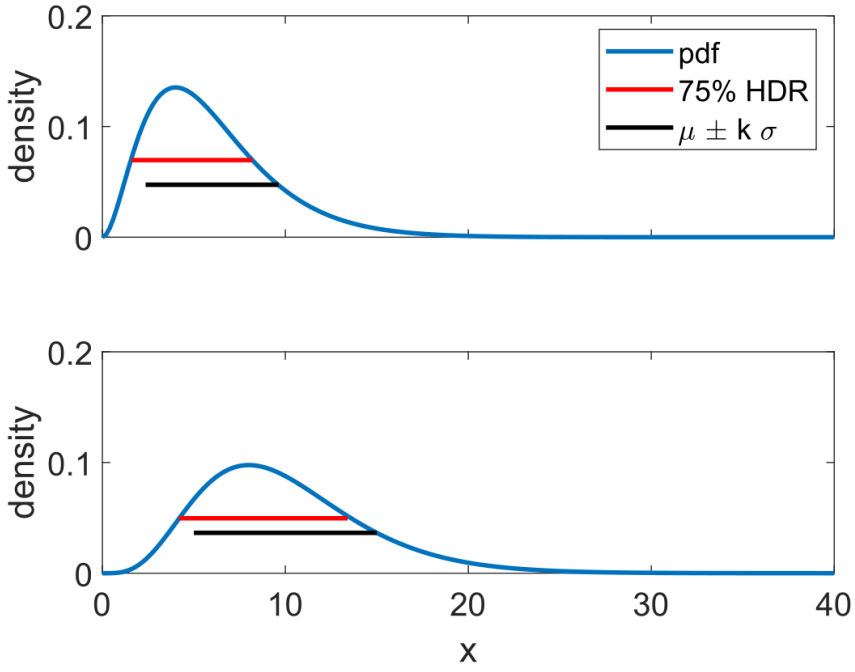


Figure 2.6: An illustration of 75% highest density regions (HDRs) for two skewed distributions. The top distribution has a lower spread than the bottom distribution. The red line indicates the 75% HDR and the black line indicates the interval $\mu \pm k\sigma$, where k is a constant scalar such that the interval contains 75% of the density.

2.6 Model Hyper-parameter Selection

Models used for constructing representations of locomotion have many configuration options. Hyper-parameters are high level configurations about a model's structure or learning process. The more sophisticated models become, the more options there are for configuring their hyper-parameters. Manually explore combinations of hyper-parameters is inefficient and naively selecting random combinations is less expedient. Furthermore, model and hyper-parameter selection are more challenging when it is costly to evaluate a single model (Bergstra et al., 2011). The difficulty can vary drastically by data set and model type. Therefore, efficient strategies are necessary to make informed decisions when selecting sets of hyper-parameters to examine.

2.6.1 Leave Out Subject-wise Cross-Validation

A model can easily perform well on the data it was trained with (Berrar, 2019; Isaksson et al., 2008). Therefore, training and evaluation sets are constructed to be as independent as possible to avoid information leaking between any of the sets and overestimating the generalization performance of the models (Arlot & Celisse, 2009; Berrar, 2019; Isaksson et al., 2008). Cross-validation is a set of re-sampling techniques for evaluating the generality of models by partitioning the data into independent subsets: training, validation and test (Isaksson et al., 2008). Given the data $X \in \mathbb{R}^{N \times D}$ where N is the number of instances and D is the number of features, the data can be partitioned into the sets $X_{train} \in \mathbb{R}^{A \times D}$, $X_{val} \in \mathbb{R}^{B \times D}$, and $X_{test} \in \mathbb{R}^{C \times D}$ such that:

$$N = A \bigcup B \bigcup C, \tag{2.29}$$

$$X_{train} \bigcap X_{val} = \varnothing, \tag{2.30}$$

$$X_{train} \bigcap X_{test} = \varnothing, \ and \tag{2.31}$$

$$X_{val} \bigcap X_{test} = \varnothing. \tag{2.32}$$

The goal of cross-validation is to estimate the generalization performance for hyper-parameter selection and model evaluation. The training, validation, and test sets are constructed by first segmenting the data into k independent collections of data instances called folds. One approach to constructing folds is by selecting individual groups of instances when the data instances are expected to have within group dependencies. Once the k folds are constructed, rotations are generated by sliding the folds through the training, validation, and test sets such that each fold is only used once for validation and once for testing. This maintains the independence between all subsequent validation sets across all the rotations and all the test sets across all the rotations to better assess generalization performance.

For example, in Figure 2.7 there are data from five subjects and each fold is the collection

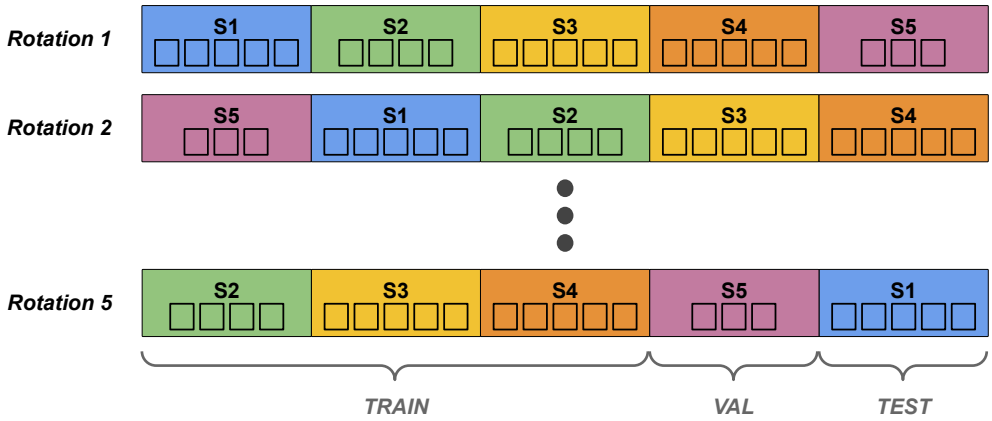


Figure 2.7: Cross-validation using a subject-wise leave out approach. There are five subjects. The small squares inside the boxes for each of the subjects are their corresponding data instances. The best model and its corresponding hyper-parameters are selected based on the average validation performance and the average test performance over all the rotations is the generalization performance of the model.

of data instances (small black boxes) from a single subject such that we obtain $k = 5$ folds. Then, rotations are constructed by moving the folds to the next position on the right and wrapping the last fold around to the front. In rotation 1, all the data instances from three subjects are allocated to the training set, one subject to the validation set and one subject to the test set. In rotation 2, all the data from subject 5 are moved to the training set, subject 3 is moved to the validation set and subject 4 to the test set. Once the models have been evaluated using all the $k = 5$ rotations, the training, validation, and test set average performances are computed over all k rotations. The model and its corresponding hyper-parameters, with the best average validation performance, is selected as the final model. The average test performance of this model is its generalization performance.

2.6.2 Bayesian Optimization

Bayesian Optimization (BayesOpt) is a flexible global optimization approach that uses Bayesian statistical inference to determine the best choice of hyper-parameters to examine by estimating the model performance over the space of possible hyper-parameters (Bergstra

et al., 2011; Frazier, 2018). BayesOpt balances exploring unknown hyper-parameter sets with exploiting knowledge gained from past explorations to determine a high performing choice for the hyper-parameters.

BayesOpt is advantageous for tuning when evaluating the model is expensive to compute. Additionally, BayesOpt provides a more objective and quantitative approach to making decisions about pre-processing choices and modeling architectures through the use of statistical inference. This lends itself to enhanced reproducibility and generality of results, which are often a challenge with machine learning (Bergstra et al., 2011). Lastly, any knowledge about the model is incorporated into the optimization process through the use of priors for statistical inference.

2.7 Clustering

Clustering provides a mechanism for quantifying and automating the extraction of distinct locomotor behavior patterns once useful and concise locomotor representations have been constructed. Clustering is the process of organizing (or grouping) similar data instances together. A clustering approach can be formalized as a function g that takes as input data $X \in \mathbb{R}^{N \times D}$, where N is the number of instances and D is the number of features, and a distance function $\boldsymbol{d}(x_i, x_j)$ to compute the distance between a pair of points $x_i \in \mathbb{R}^{1 \times D}$ and $x_j \in \mathbb{R}^{1 \times D}$ such that $\boldsymbol{d}(x_i, x_j) = \boldsymbol{d}(x_j, x_i)$ and $\boldsymbol{d}(x_i, x_j) = 0$ only when $x_i = x_j$. The clustering function f also outputs an assignment or partition $P = \{P_1 \dots P_K\}$ of the data where P_i is a cluster of similar data instances (Kleinberg, 2002). Depending on the clustering approach, pairs of similar instances where $\boldsymbol{d}(x_i, x_j) \approx 0$ are iteratively grouped together or pairs of dissimilar instances where $\boldsymbol{d}(x_i, x_j) \gg 0$ are iteratively split apart. Meaningful measures of distance between instances are difficult to determine in high dimensional spaces due to increasing sparsity of the volume of the higher dimensional spaces. Therefore, dimensionality reduction can be performed to help facilitate the comparisons.

2.7.1 Gaussian Mixture Models (GMMs)

One method for clustering is Gaussian Mixture Models (GMMs) or Mixtures of Gaussians (MoGs; Deisenroth et al., 2020; Dempster et al., 1977; Garcia et al., 2010; Goldberger and Roweis, 2004). Distributions that describe many complex phenomena, such as locomotion, often consist of multiple groups. These complex occurrences can be approximated by a combination of Gaussians to capture the underlying groups hidden within the data. Each group is assumed to be approximately Gaussian with the group center corresponding to the mean of one of the Gaussians.

GMMs are unsupervised parametric density estimation models that are composed by adding together multiple Gaussians and are useful for density estimation and clustering. The probability density function (pdf) for a single multivariate Gaussian is:

$$\mathcal{N}(x|\mu,\Sigma) = \frac{e^{-\frac{1}{2}(x-\mu)^T\Sigma^{-1}(x-\mu)}}{\sqrt{(2\pi)^d|\Sigma|}} \ , \tag{2.33}$$

where x is drawn from some distribution, d is the number of variables, $\mu \in \mathbb{R}^d$ is the mean vector, $\Sigma \in \mathbb{R}^{d\times d}$ is the covariance matrix, and $|\Sigma|$ is the determinant of the covariance matrix. The pdf for the composition of K multivariate Gaussians (or mixture components) is:

$$p(x|\Theta) = \sum_{k=1}^{K} \pi_k \mathcal{N}(x|\mu_k,\Sigma_k) \ , \tag{2.34}$$

where $\mathcal{N}(x|\mu_k,\Sigma_k)$ is the pdf for a single mixture component k, $\mu_k \in \mathbb{R}^d$ is the mean vector for the mixture component k, and $\Sigma_k \in \mathbb{R}^{d\times d}$ is the covariance matrix for mixture component k, and $\Theta = \{\Pi, M, S\}$ is the collection of all the mixture parameters such that $\Pi \in \mathbb{R}^K$ is the vector of all the mixture weights π_k, $M \in \mathbb{R}^{K\times d}$ contains the mean vectors of all the mixture components, and $S \in \mathbb{R}^{K\times d\times d}$ is the tensor containing the covariance matrices of all the mixture components. The mixing weights are defined such that $\sum_{k=1}^{K} \pi_k = 1$. Each constituent Gaussian is a mixture component where the mixture weight π_k represents the

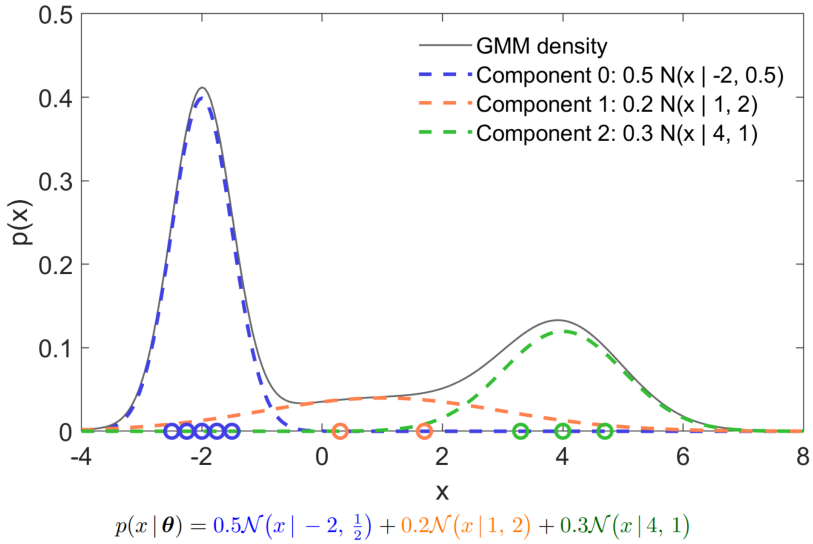


Figure 2.8: A mixture of three Gaussians is fit to model the distribution of data instances that appears to have three categories, based on Figure 11.2 by Deisenroth et al. (2020). Each Gaussian $\mathcal{N}(x|\mu, \sigma)$ is defined my a mean μ and standard deviation σ. The complete probability density function (pdf) is $p(x|\theta) = 0.5\mathcal{N}(x| - 2, 0.5) + 0.2\mathcal{N}(x|1, 2) + 0.3\mathcal{N}(x|4, 1)$ where Θ is the set of parameters for all three Gaussian components.

relative likelihood of the group described by the corresponding Gaussian.

An example Gaussian mixture distribution is shown in Figure 2.8. There are three mixture components $\mathcal{N}(x| - 2, 0.5)$, $\mathcal{N}(x|1, 2)$, $\mathcal{N}(x|4, 1)$ indicated by the dashed blue, orange, and green curves, respectively. The resulting mixture distribution is the black curve. KDEs that use a Gaussian kernel are a special case of GMMs where the number of mixtures is N with each data instance as the mean, the bandwidth b is the scale factor describing the variance, and the mixing weights are $\frac{1}{N}$.

The GMM parameters Θ can be estimated iteratively given a data set using Expectation Maximization (EM) algorithm, which successively updates the parameters (Deisenroth et al., 2020; Dempster et al., 1977). The objective is to determine the optimal parameters Θ^* of the GMM that maximizes the log likelihood of the full data set X:

$$\mathcal{L} = log\ p(X|\Theta) = \sum_{n=1}^{N} log\ p(x_n|\Theta) = \sum_{n=1}^{N} log \left(\sum_{k=1}^{K} \pi_k \mathcal{N}(x_n|\mu_k, \Sigma_k) \right) \tag{2.35}$$

where $x_n \in \mathbb{R}^d$ is a data instance from the data set $X \in \mathbb{R}^{N \times d}$ and N is the number of data instances. From Equation 2.35, the updates for each parameter is computed by taking the derivative of the log likelihood with respect to each parameter and then setting the derivative to zero. The resulting update formulas are

$$\mu_k \Leftarrow \frac{\sum_{n=1}^{N} x_n r_{nk}}{\sum_{n=1}^{N} r_{nk}}, \tag{2.36}$$

$$\Sigma_k \Leftarrow \frac{\sum_{n=1}^{N} (x_n - \mu_k)(x_n - \mu_k)^T r_{nk}}{\sum_{n=1}^{N} r_{nk}}, \ and \tag{2.37}$$

$$\pi_k \Leftarrow \frac{\sum_{n=1}^{N} r_{nk}}{\sum_{k=1}^{K} \sum_{n=1}^{N} r_{nk}}, \tag{2.38}$$

where the quantity:

$$r_{nk} = \frac{\pi_k \mathcal{N}(x_n | \mu_k, \Sigma_k)}{\sum_{j=1}^{K} \pi_j \mathcal{N}(x_n | \mu_j, \Sigma_j)} \tag{2.39}$$

is the probability of the n^{th} data instance being in the k^{th} mixture component (Deisenroth et al., 2020; Dempster et al., 1977).

For the EM algorithm, the parameters μ_k, Σ_k, and π_k are first initialized using heuristic guess. The EM algorithm has two main steps that are performed at each iteration that are guaranteed to monotonically increase the likelihood $\mathcal{L}$:

1. E-step: compute the responsibilities r_{nk} for each data instance x_n for each mixture component k, using the current parameter values for μ_k, Σ_k, and π_k (Equation 2.39), and

2. M-step: use the updated responsibilities r_{nk} to re-estimate the parameters μ_k, Σ_k, and π_k (Equations 2.36, 2.37, and 2.39).

In addition to density estimation, GMMs are flexible and powerful tools for data clustering (Goldberger & Roweis, 2004) and are a soft clustering approach that uses the mixture component probability of a data instance to determine its membership in one or more clusters.

The mixture component with the highest likelihood is the cluster assignment for the data instance. However, determining the best number of clusters for constructing the models is a trade-off between accuracy and simplicity (Garcia et al., 2010). Models that better capture the distribution shape of a given data set use a larger number of clusters but could poorly represent new data. Simpler models use fewer clusters and might not capture all the meaningful classes among the data instances. GMMs are useful tools for preliminary analysis to identify similarities within the data. An advantage of GMMs over simple Euclidean distances is that they use the Mahalanobis distance (Mahalanobis, 1936) instead, enabling GMMs to identify data distributed in ellipsoidal shapes based on the covariance matrix. Additionally, GMMs estimate the probability distribution of the data and can therefore be used for statistical inference. Using the probability distribution, we can predict likely behavioral patterns under specific conditions, such as surgical approach or rehabilitation method.

2.7.2 Hierarchical Clustering

Hierarchical clustering is a collection of methods for building levels of clusters and sub-clusters. Hierarchical clustering can be a useful tool for identifying multiple levels of similarity between data instances and describing variation within clusters. Higher cluster levels are sets of clusters formed prior to subsequent cluster splitting, with the highest leveling consisting of one cluster containing all the data instances. Higher levels group together more instances based on more general characteristics and the instances are less similar. The lower cluster levels of the hierarchy group together more similar instances based on more specific attributes.

There are two broad categories of hierarchical clustering: agglomerative and divisive (Garcia et al., 2010). Agglomerative involves starting with each data instance in its own cluster (i.e., elementary subsets). Then, the closest clusters are successively merged until a cluster remains that contains all the data instances. Divisive clustering works in the opposite direction, starting with one cluster containing all the data instances. The clusters are recursively

split until each data instance is within a cluster by itself.

The initial subset and how the subsets are merged or split are described by a tree like structure called a *dendrogram*. Each branch of a dendrogram is a split into a new cluster. Figure 2.9 is an example dendrogram. Starting from the top, all data instances are in the same cluster. As pairs of data instances are required to be closer together, sets of data instances get split into new sub-clusters. The number of clusters to stop splitting on is set to seven in Figure 2.9. However, the number of clusters to stop splitting on is optional and the full hierarchy can be computed such that each data instance is within its own cluster. The horizontal axis indicates the number of points within each branch. The dashed gray line is an adjustable threshold for the cluster distances to determine an appropriate number of clusters and indicates the flexibility to this approach. By adjusting the cut-off for the distance between clusters, we can determine a desirable number of clusters. In this example, $K = 4$ would be the chosen number of clusters based on the cut-off indicated by the gray line. The number of branches the gray line crosses indicates the number of clusters. Additionally, the branches leading to data instances within the same cluster are colored the same.

2.7.3 Adjusted Mutual Information (AMI)

When identifying distinct locomotor behavior patterns, the consistency of an approach is important for reliability, in addition to, reproducing and interpreting the results. Many clustering algorithms involve randomness and might yield different results upon subsequent executions. Therefore, special metrics have been developed to evaluate the consistency of a clustering approach. Mutual information (MI) is a metric that can be used to compare the similarity (or agreement) between two sets of label assignments for the same data (Pedregosa et al., 2011).

Let $U = \{U_1 \dots U_l\}$ be an assignment set of l clusters and $V = \{V_1 \dots V_m\}$ an assignment

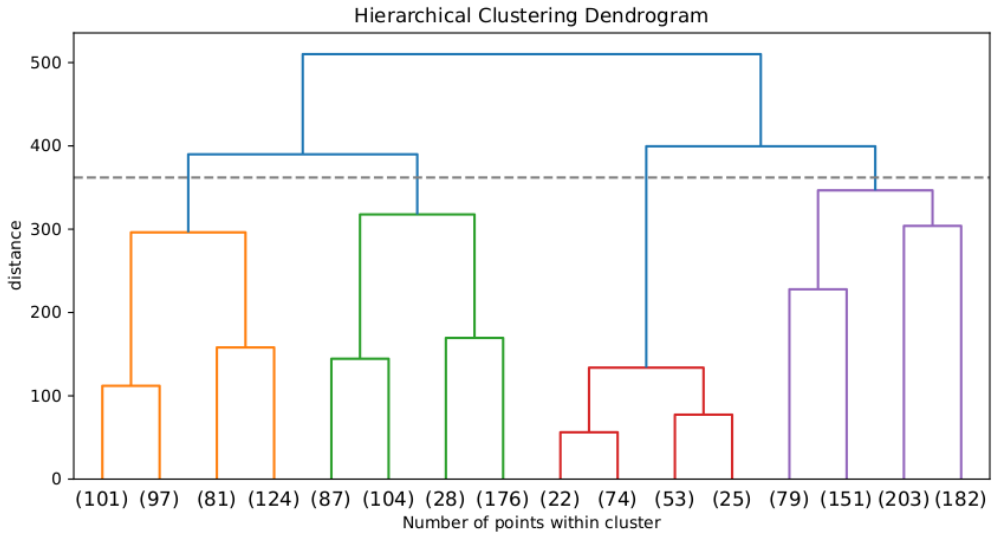


Figure 2.9: A dendrogram illustrating the hierarchy of clusters from an agglomerative approach. The horizontal axis is the number of data instances within the cluster branch. The vertical axis is the sum of squared differences within the clusters. The dashed gray line is the cluster distance threshold to determine an appropriate number of clusters.

set of m clusters, then:

$$MI(U,V) = \sum_{i=1}^{|U|}\sum_{j=1}^{|V|} \frac{|U_i \cap V_j|}{N} log \frac{N|U_i \cap V_j|}{|U_i||V_j|}, \tag{2.40}$$

is the mutual information or total amount of agreement or overlap between the cluster assignments U and V, where $|U_i|$ is the number of data instances within cluster U_i and $|V_j|$ the number of data instances within cluster V_j. The term $\frac{|U_i \cap V_j|}{N}$ is the overall probability of data instances being assigned to both clusters U_i and V_j. The term $\frac{|U_i \cap V_j|}{|U_i||V_j|}$ is the conditional probability that given the clusters U_i and V_j data instances will be assigned to both. The more likely data instances are to be assigned to the same sets of clusters, the greater the MI.

The MI score is robust to permutations of the cluster labels within U and V. Different models for a clustering algorithm could yield different label IDs for the same cluster in different assignment sets. Regardless of the exact name or label given to each cluster in the different assignment sets, the MI score will be the same when the same data instances are clustered together. However, a draw back to MI is that the greater the number of clusters,

the greater the MI score. Therefore, to account for this, an "adjusted-for-chance" MI (AMI) metric is computed by normalizing the MI score using the expected value of the MI between any random pair of cluster assignments (Pedregosa et al., 2011). This defines the AMI such that a score of 1 or close to 1 indicates perfect or near perfect agreement between the cluster assignments. Poor scores are a result of independent clustering assignments and have an AMI score ≤ 0. Specifically, random, uniform label assignments yield an AMI score close to 0, and worse than random scores are at the lowest at -1.

Chapter 3

Bipedal Walking in Humans

Locomotion requires complex, coordinated recruitment of multiple muscles. The loss of or damage to a limb alters how the muscles function and often results in compensatory behavior that can have adverse impacts on an individual's health (Atri et al., 2016; Bae et al., 2007; Jaegers et al., 1996). Gait is a particular form of locomotion that involves the feet, such as walking, running, or climbing stairs. In general, healthy gait strategies are important, especially for active prosthesis use after amputation surgery. Unfortunately, otherwise healthy individuals who have undergone amputation still risk injury, despite innovative prostheses and surgical approaches. Injury often prevents healthy individuals of working age, from participating within the work force (Dionne et al., 2022). Therefore, comprehensive gait analyses are necessary to understand the precise influences of various health factors and their impact on gait measures. In this chapter, I discuss human walking and the function of the muscles above the knee. I discuss the implications of the co-activation of muscles for understanding gait, and summarize analyses of the gait of individuals with osteomyoplastic amputation.

3.1 Muscles Above the Knee

Walking is an integrated activity involving numerous muscles acting across many joints throughout the body (Winter, 1987). However, typical gait analyses will mainly focus on the behavior of the legs. The femur (or thigh) is the segment of the leg from the hip to the knee. Amputation anywhere along the femur is referred to as *above the knee amputation* or *transfemoral amputation*. Amputation anywhere along the tibia, or below the knee, is *transtibial amputation*. The main muscle groups of interest within the upper leg for this work are shown in Figure 3.1. The muscle locations are:

- the quadriceps run along the anterior (or front) part of the thigh,
- the hamstrings run along the posterior (or back) of the thigh, and
- the adductors run along the medial (or inside) part of the thigh.

Contraction is the process of a muscle generating tension to produce force for manipulating the configuration (or angle) of one or more joints (Winter, 1987). Concentric contractions shorten the muscles while increasing tension. Eccentric contractions elongate muscles while increasing tension. Isometric contractions increase tension with the muscles without changing its length.

The adductors, hamstrings, and quadriceps groups contract to manipulate the hip and the knee joints in cooperation with other muscles groups. Most of the mass of these muscles is above the knee in order to manipulate both the hip and knee. Specifically, the quadriceps contract to flex the hip to bring the leg forward. Additionally, the quadriceps can contract to extend (straighten) the knee. The hamstrings contract to extend the hip to bring it backward and to flex (bend) the knee. The adductors largely contract to pull the leg inward toward the midline of the body. This action is known as adduction (Winter, 1995).

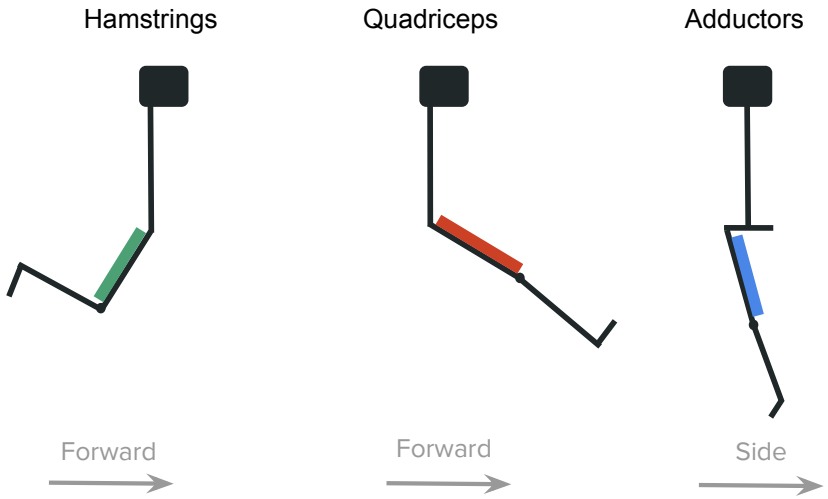


Figure 3.1: The hamstrings (green) are on the back (posterior) of the thigh. The quadriceps (red) are on the front (anterior) of the thigh. The adductors (blue) are on the inner part of the thigh.

3.2 Typical Walking Gait in Humans

Human walking is a cyclic behavior with each cycle referred to as a *gait cycle* or *stride*. A stride is defined as starting with the heel-strike of one limb and ending with the heel-strike of that same limb (Alamdari & Krovi, 2017; Winter, 1987). Throughout a stride, there are two major transitional gait events: heel-strike and toe-off. These gait events partition the gait cycle into two major phases: stance and swing as shown in Figure 3.2. The gait events occur in a consistent order and the gait cycle is typically described in terms of fraction or percent of the gait cycle instead of elapsed time. For example, there might be 1 second between the heel-strike and toe-off during one stride and .8 seconds between the events during the next stride. The percent of the gait cycle between the two events could still be 60% for both strides and the heel-strike always precedes the toe-off.

The stance phase is the beginning segment of the gait cycle, when the foot is on the ground, starting with the heel-strike (HS), or initial contact (IC), of the foot and ending with the toe-off (TO) of that same foot (Alamdari & Krovi, 2017; Winter, 1987). The push-off

(PO) is the last period of the stance. The PO begins when the heel initially comes off the ground and ends with the TO. The TO is the instant that the toe comes off the ground. The stance phase for walking is on average approximately 60% of the duration of the gait cycle. Double support is the period during stance when both feet are on the ground. Double support begins at the HS of the swinging foot at approximately 50% of the gait cycle (Alamdari & Krovi, 2017). Double-support ends after the TO of the supporting foot. The quadriceps reach average peak activity around the 10% point of the gait cycle to extend the knee during weight acceptance (Winter, 1987). On average, the adductor activity peaks during the typical stance to assist with weight acceptance. The knee joint is a crucial component of limb stability during stance, as it takes on the load from the entire weight and downward momentum of the body. The ankle contributes to shock absorption in the first half of stance and propels the body forward during PO.

The swing phase is the later portion of the gait cycle, when the foot is off the ground, beginning with the TO of the foot and ending with the HS of that same foot. The swing phase on average is approximately 40% of the duration of the gait cycle. On average, the hamstrings activity will peak around the 95% point of the gait cycle and into weight acceptance to decelerate the limb (Winter, 1987). The majority of the range of motion of the knee is required for progression during swing. The quadriceps eccentrically contract to elongate and facilitate the collapse of the knee into the beginning of the swing. Just after the TO, the quadriceps and adductors work together to flex (i.e., bend) the hip to bring the leg forward into swing. The quadriceps also extend the knee to control the speed of the limb. The knee reaches its highest angular velocities during the swing phase. Towards the end of swing, the hamstrings flex the knee to decelerate the swinging limb before contact with the ground. Additionally, the hamstrings extend the hip at the heel-strike to control the rotation of the thigh and stabilize the pelvis.

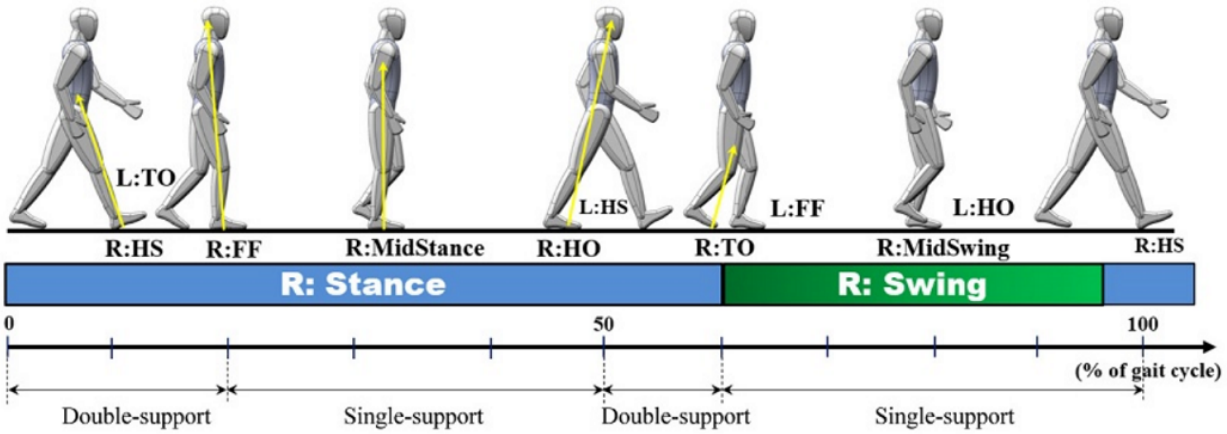


Figure 3.2: From Figure 1 of Alamdari and Krovi (2017). The gait cycle with the right limb. Gait begins with the heel-strike (HS) of the right foot. The direction and relative magnitude of the ground reaction force (GRF) is depicted with the yellow arrows. Just after the right HS, the toe-off (TO) of the left foot occurs. The right foot flat (FF) occurs around 20%. When the foot is flat, the GRF is near perpendicular with the ground and usually the entire body weight is supported on that leg. Just prior to 50% the right heel-off (HO) occurs. Double-support refers to moments during gait when both feet are in contact with the ground.

3.3 Implications of Co-contraction

Co-contraction occurs when a set of antagonistic muscles around the same joint simultaneously activate (Damiano, 1993; Darainy & Ostry, 2008; Huang et al., 2020; Jaegers et al., 1996; Rosa, 2015; Seyedali et al., 2012; Sharma et al., 2017; van der Krogt et al., 2012; Winter, 1987; Yuan et al., 2019). Individual muscles produce force in a single direction about a joint (Darainy & Ostry, 2008). Antagonistic muscles are a set of muscles that activate to contract in opposing directions (Chloca, 2018; Wing, 1978). The agonist muscle activation leads the movement of the joint in the main voluntary direction by contracting. The muscle that contracts in the opposing direction is the antagonist muscle that relaxes to facilitate the net movement in the desired direction. For example, the hamstrings and quadriceps are an antagonistic muscle pair that operate to manipulate the configuration of the hip and knee joints. The hamstrings will contract to flex the knee. The quadriceps will contract to

extend (or straighten) the knee. Both muscles activating equally and simultaneously stiffen the knee joint to limit the joint motion and maintain the present angle as much as possible. In reality, groups of antagonistic muscles simultaneously activate proportionally throughout the execution of a task to efficiently control movement and prevent injury. The value of the proportionality between the activation of the muscles varies throughout the task and is dependent upon numerous factors, such as environmental forces, movement direction, skill level, and health status.

Co-contraction is a typical control strategy employed by the nervous system to regulate movement under uncertainty or for compensatory adjustments (De Luca & Mambrito, 1987; Rosa, 2015). Darainy and Ostry (2008) found that the use of co-contraction can vary as a function of force magnitude and movement direction. Additionally, changes in co-activation of antagonist muscles occur during motor learning and in the presence of motor pathology (Damiano, 1993; Huang et al., 2020; Rosa et al., 2013; Seyedali et al., 2012; Sharma et al., 2017; van der Krogt et al., 2012; Yuan et al., 2019). Understanding the use of co-contraction during specific skilled tasks for healthy individuals defines a useful benchmark for characterizing deficits in pathological movement or skill progression. Excessive or atypical timing of co-contraction results from diminished coordination or inefficient motor strategies and can increase risk of injury or exacerbate motor conditions (Damiano, 1993; Darainy & Ostry, 2008; Rosa, 2015; Smith et al., 2019). Because co-contraction typically increases during early strategies of learning new tasks (Darainy & Ostry, 2008) and in the presence of motor dysfunction, it is crucial that clinical guidance on motor control have a detailed understanding of the nature of co-contraction behavior to promote healthy strategies and avoid further injury. Therefore, comparing muscle co-contraction strategies between groups and during various tasks is useful for characterizing inefficiencies in motor behavior and prescribing training objectives for rehabilitation.

3.4 Performance of Healthy Men with Osteomyoplastic Amputation

In the presence of lower extremity trauma or compromising medical conditions, amputation might be needed to address these concerns (Taylor & Poka, 2016). The amputation process has transitioned from simply a life-saving, traditional, guillotine-style approach to an innovative reconstructive osteomyoplastic procedure to create a functional residual limb (residuum) that expeditiously fits into a well-designed prosthesis (Ertl et al., 2010; Kahle et al., 2016; Taylor & Poka, 2016). A growing number of adults with amputation have undergone this innovative type of surgical amputation. The osteomyoplastic procedure aims to achieve active gait performance by salvaging as much of the residual muscles as possible and re-anchoring them around the distal end. The intent of the osteomyoplastic procedure is to yield a viable, reconstructed residuum for weight-bearing and reliable prosthetic fit and use. Active gait performance is the primary expected outcome.

For individuals with below the knee amputation, osteomyoplastic transtiblial amputation (OTTA) is preformed to reconstruct the distal anterior tibialis and gastrocnemius muscle groups for weight-bearing and dependable prosthesis utilization. For individuals with above knee amputation, osteomyoplastic transfemoral amputation (OTFA) is performed to reconstruct the distal adductors, hamstrings, and quadriceps muscle groups to enable distal muscle function during gait with a prosthesis. However, little is known about the roles of the distal-most residuum muscles or the pressures produced within the socket of the prosthesis during gait performance of individuals with osteomyoplastic amputation. Therefore, recent studies are interested in understanding whether muscles actually function at the distal end for individuals receiving osteomyoplastic amputation and the behavior of these muscles throughout the gait cycle (Dionne et al., 2022; Taylor & Poka, 2016).

Stable gait performance within the community is key to overall health and participation. Clinicians treating patients with osteomyoplastic amputation in rehabilitation and wellness

settings need to more fully understand the behavior of the distal-most muscles and residuum socket interfacial (RSI) pressures during active prosthesis use to obtain optimal outcomes. Currently, rehabilitation service providers for individuals with OTFA focus on proximal muscle (e.g., gluteus maximus) strengthening and direct little attention towards understanding the roles of residuum muscles distal to the hip (i.e., quadriceps, hamstrings or adductors; Dionne et al., 2009).

Despite the advances in prosthetic management and amputation surgical approach, otherwise healthy men with amputation still risk continued impairment and disability (Dionne et al., 2022; Jaegers et al., 1996). Frequent missteps and falls often result in painful residuum injury, yielding diminished participation by individuals with lower limb amputation (Hunter et al., 2017). It is paramount that individuals who have received the osteomyoplastic procedure following amputation are safely able to achieve and maintain gait stability once returned to the community. For this purpose, lower limb prostheses are designed to facilitate efficient biomechanical performance during walking. Proper fit of the prosthetic socket and the dynamics of the prosthetic component are key for patients to obtain similar gait performance to that before amputation. Improper design can result in pathological gait patterns that nefariously impact individual health and overall well-being. Furthermore, improper prosthesis design can subsequently result in developing health complications in otherwise healthy individuals.

Distinctions in gait performance between individuals with standard amputation and osteomyoplastic amputation have been sparsely studied. Mai et al. (2013) described novel muscle activity within the transtibial residuum following osteomyoplastic amputation and found evidence of active contribution to prosthesis control during gait by the distal-most muscles (i.e., anterior tibialis and gastrocnemius). Additionally, Dionne et al. (2015, 2017) found comparable work performance during walking, lifting and carrying tasks in men with OTTA to intact controls at two annual time points. Healthy individuals with OTTA demonstrated improved lift capacity and residuum anthropometric stability. The individuals

within the study received rehabilitation from the time of the amputation surgery and after initial receipt of a prosthesis. However, cadence asymmetry progressively worsened and perceived exertion increased for these healthy individuals with OTTA. The increasing asymmetry of the gait and increased exertion suggest further investigation is necessary to improve continued intervention and reduce the risk of residuum injury.

For individuals with OTFA, it is unknown what residuum muscle recruitment strategies are best for efficient gait and prosthetic control because few studies have focused on healthy individuals with OTFA. Because individuals with OTTA had comparable work performance to intact controls, Dionne et al. (2022) expected that men with OTFA would also perform similar to controls, despite missing a knee joint system, shank, ankle joint system, and foot (Hong & Mun, 2005). However, residuum tissue injury often occurs during active prosthetic use and work performance by healthy men with trauma-related TFA typically falls short of matched intact individuals (Dionne et al., 2022). They found individuals with OTFA walked shorter mean distances at two speeds, had lower carrying capacity, and reported greater pain during carry task than intact control counterparts.

Many existing studies of transfemoral amputation (TFA) have some limitations. Some TFA studies do not specify the amputation approach received by the participants within the study, such as Bae et al. (2007) and Wentink et al. (2013). Wentink et al. (2013) found low consistency in TFA walking patterns but did not measure the above-knee muscles of the intact limb. Additionally, the TFA cohort was not homogeneous, as there were broad inclusion criteria, making it difficult to isolate effects due to the amputation approach. Jaegers et al. (1996) did report how certain transfemoral muscles were cleaved or re-anchored and discovered longer activation times for hip muscles within the intact and residual limbs. However, results by Jaegers et al. (1996) were observed over a few strides, reducing the statistical power of the analysis. Additionally, the co-activity of the muscles were assessed only after averaging electromyography (EMG) activity across the strides, as opposed to assessing co-activity on a per-stride basis in the works by Jaegers et al. (1996) and Wentink et al. (2013). This makes it

unclear what the true co-activation patterns are within the TFA residuum. The limitations in the results of prior TFA studies indicate that additional investigation is needed to accurately understand residuum muscle recruitment behavior of individuals with OTFA and TFA in general. In this dissertation, I address these shortcomings by analyzing a large number of strides from a TFA cohort that have all received the osteomyoplastic procedure.

Moreover, the osteomyoplastic distal residuum muscles activity in relation to the pressures exerted at the RSI are not well understood (Hong & Mun, 2005). Further exploration is necessary to verify whether those with OTFA demonstrate distal residuum muscle activity for improved potential for enhanced functional gait performance. Additional exploration may help inform clinical decisions to better prepare individuals with OTFA for gait performance and community participation with reduced risk of residuum injury. To adequately understand the roles of distal residuum muscles and RSI pressure after osteomyoplastic amputation, investigators need to capture and analyze activation patterns in the muscles distal to the hip (i.e., quadriceps, hamstrings, and adductors) during functional activity performance in conjunction with other gait measures (e.g., RSI pressures, kinematics, kinetics, cadence, stride length) during work-related gait tasks for a holistic understanding of gait (Shotande et al., 2022, in revision).

3.4.1 Co-contraction within the Osteomyoplastic Residuum

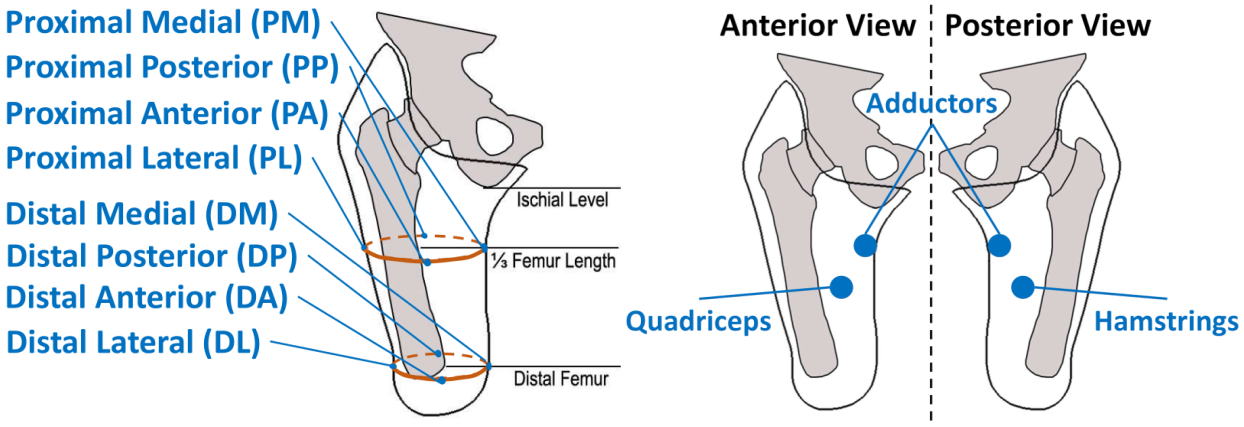
Co-contraction is the simultaneous activation of antagonistic muscles (e.g., hamstrings and quadriceps) and implements limb stabilization during weight-bearing or gait transitions (Huang et al., 2020; Jaegers et al., 1995; Rosa, 2015; Seyedali et al., 2012; Sharma et al., 2017; van der Krogt et al., 2012; Yuan et al., 2019). Therefore, characterizing co-contraction is useful in gait analyses for describing muscle recruitment behavior, understanding prosthesis use and evaluating rehabilitation progress. Many TFA studies that assessed co-activity describe muscle co-activity by comparing average EMG activity over a set of strides, as opposed to assessing co-activity on a per stride basis. Bae et al. (2007) quantifies co-activity

within strides, but computes cumulative ratios over the entire trial and do not describe precise co-activation times. Moreover, the amputation approach of the TFA cohort is not specified and co-activity is only described within the sound limb. Additional study is still necessary to better and more holistically understand gait behavior for individuals with and without osteomyoplastic amputation during a variety of active gait tasks (Shotande et al., in revision).

3.4.2 Data Acquisition with the OU-PAM

In a series of studies by Commuri, Mai, and Dionne, otherwise healthy men with and without osteomyoplastic amputation performed activity-based gait trials (Commuri et al., 2010; Dionne et al., 2009, 2015, 2017, 2022; Mai et al., 2012, 2013). The pressures and EMG data were recorded simultaneously using the University of Oklahoma Prosthetic Activity Monitor (OU-PAM) developed by Commuri et al. (2010) for individuals with and without osteomyoplastic amputation. The OU-PAM was developed as a portable data acquisition device that simultaneously captures foot and residuum socket interface (RSI) pressure, and muscle activity within both limbs. The OU-PAM can capture up to 16 analog input channels at 1kHz. The OU-PAM utilizes the STK525 and ATEVK525 (Microchip Technology, 1984) boards for data acquisition. Mai et al. (2013) used the device to study gait performance of participants with transtibial amputation (TTA). Work by Dionne et al. (2022) adapted the OU-PAM for participants with OTFA.

For individuals without amputation (i.e., the intact controls), pressure sensors were placed at the toe and ball of both feet to identify ground reaction forces and capture gait events. For individuals with OTFA, the pressure sensors were placed at eight locations within the RSI at the proximal and distal levels. The proximal sensors were placed at 1/3 the femur length, measured downward from the ischial level within the socket (Figure 3.3). At each level, sensors are placed at the anterior, posterior, lateral, and medial positions. In the study involving individuals with OTFA (Dionne et al., 2022), six surface EMG sensors were placed on the adductors, hamstrings, and quadriceps groups of both legs (Figure 3.3b) for



(a) RSI Pressure Sensors (b) EMG Sensors

Figure 3.3: Sensor Placements (Shotande et al., 2022). Pressure and muscle activation data are simultaneously collected using the OU-PAM (Commuri et al., 2010). Sensor placements for individuals with OTFA are (a) two rings of pressure sensors are placed within the residuum socket at the 1/3-femur length (i.e., proximal) and distal femur levels. At each level, sensors were placed at the anterior, posterior, medial, and lateral positions, and (b) EMG sensors were placed on the respective external muscle bellies of the quadriceps, hamstrings and adductor muscle groups. The quadriceps are seen in the anterior view and the hamstrings in the posterior view.

both participant groups. Differences in sensor placements between the OTTA cohort in the studies done by Dionne et al. (2017) and Mai et al. (2013) and the OTFA cohort in the study by Dionne et al. (2022) are: 1) two residuum EMG sensors are moved from the tibialis anterior and gastrocnemuis for the TTA studies to the adductors and hamstrings for the OTFA cohort (quadriceps are recorded for both cohorts), and 2) additional RSI pressures are also collected at the middle level for individuals with TTA. Gait performance was evaluated and compared between the participant groups using outcome measures such as cadence and stride length in conjunction with EMG. The RSI pressures were collected to juxtapose the quality of the prosthetic fit with the functionality of the gait performance. A good prosthetic fit is defined as the same distribution of pressure over all the RSI locations (Commuri et al., 2010; Dionne et al., 2022; Ertl et al., 2010; Mai et al., 2013; Taylor & Poka, 2016). Ertl et al. (2010) expected that a smooth residuum contour constructed with the osteomyoplastic procedure aids in the prevention of localized skin breakdown by reducing the potential for

localized pressure. Moreover, the reconstructed residuum should improve comfort within the RSI and functionality of the prosthesis (Commuri et al., 2010; Mai et al., 2012; Taylor & Poka, 2016).

Chapter 4

Methods for Automated Stride Extraction and Analysis

The objectives of the procedures described in this chapter are to understand likely muscle recruitment strategies, identify strategies unique to those with amputation, quantify the descriptions of distinct muscle strategies, and quantify the quality of the prosthetic fit.

Currently, rehabilitation service providers for those with osteomyoplastic transfemoral amputation (OTFA) focus little attention towards understanding the roles of the distal residuum muscles (i.e., quadriceps, hamstrings or adductors). Unfortunately, residuum tissue injury often occurs during active prosthetic use. Additionally, work performance of healthy men with TFA typically falls short of matched intact individuals (Dionne et al., 2022). There is limited knowledge about the behavior of the distal-residuum muscles and residuum socket interfacial (RSI) pressures for those with OTFA. A better understanding of gait strategies employed by those with amputation and practical gait strategies healthy for individuals with limb loss can inform healthcare professionals when providing resources and treatment to those with amputation. Gait analyses that consider all relevant health factors and locomotor measures can help inform long-term care to improve patient outcomes.

In this chapter, I explain the details of my proposed approach for extracting strides

from pressure data and comparatively visualizing and characterizing gait across multiple individuals and groups. I utilize highest density regions (HDRs), which have not been used in gait analyses, to identify and describe distinct pressure and muscle activation patterns across the strides of multiple individuals. The strides are extracted by first identifying peaks from the continuous pressure data to indicate the start and end of the strides. The distribution of pressure and EMG activity over all the strides is computed for each sensor location and gait task. Within each stride, the peak times are located for the pressure and EMG activity. The distribution of peak times from the pressures and EMG activity over all the strides is characterized for each sensor location and gait task. Within each of the strides, the EMG peaks are paired between muscles to examine co-activation patterns. The distribution of paired peaks from the EMG activity over all the strides is visualized for each pair of muscles and gait task.

After detailing a strategy for understanding the overall gait patterns, distinct types of muscle recruitment behaviors, referred to as phenotypes, are then automatically and explicitly separated using compression and clustering algorithms. Compression is an approach to remove the uninformative features and to facilitate the clustering of high dimensional data. The muscle activation patterns from the strides within and between the clusters are characterized and compared.

4.1 Data Pre-processing

Prior to extraction of the strides, the continuous pressure data are cleaned, using the general procedure outlined by Commuri et al. (2010). In this procedure, the pressure data are first trimmed to the period when the walking task is performed. The number of channels is C_p and T is the number of time samples, then the pressure data are stored within a matrix P of

the form:

$$P = \begin{bmatrix} P_1 \\ \vdots \\ P_c \\ \vdots \\ P_{C_p} \end{bmatrix} \in \mathbb{R}^{C_p \times T},\ and\ P_c \in \mathbb{R}^T. \tag{4.1}$$

Then each pressure channel P_c is normalized to a standard range using:

$$P_n = \frac{P_c - min(P_c)}{max(P_c)}, \tag{4.2}$$

and then filtered using a low-pass, first-order Butterworth filter (Butterworth, 1930), with a 3Hz cut-off frequency for participants with amputation and a 5Hz cut-off frequency for the participants without amputation. These cut-off frequencies are chosen to be consistent with Commuri et al. (2010). The low-pass, first-order Butterworth filter $B(\omega)$ with the appropriate cut-off frequency ω, is applied to each normalized data channel P_n using $P_b = P_n \circledast B(\omega)$, where $\circledast$ is the convolution operator defined as:

$$f(\tau) \circledast g(\tau) = \sum_{t=-\infty}^{\infty} f(t)g(\tau - t). \tag{4.3}$$

Lastly, a moving average is applied to the pressure data by computing the local average within a sliding window of length w:

$$\bar{p}_{b,k} = \frac{1}{w} \sum_{i=1}^{w} p_{b,k+i}\ , \tag{4.4}$$

where $\bar{p}_{b,k} \in \mathbb{R}$ is the average pressure computed for time k of the channel b. The resulting cleaned pressure data is of the form:

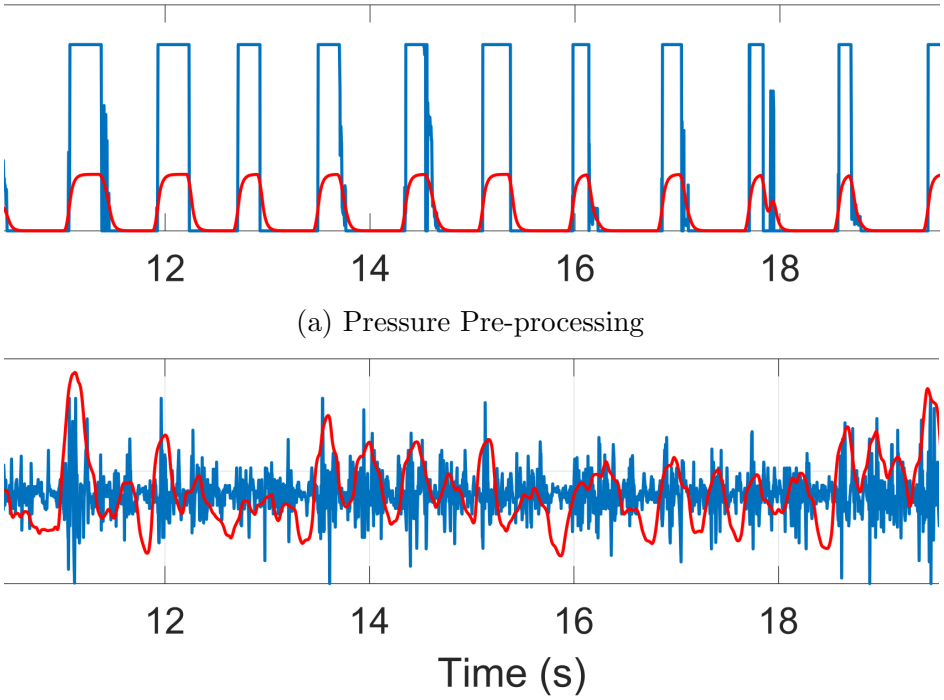
$$\bar{P} = \begin{bmatrix} \bar{p}_{1,1} & \cdots & \bar{p}_{1,T} \\ \vdots & \ddots & \vdots \\ \bar{p}_{C_p,1} & \cdots & \bar{p}_{C_p,T} \end{bmatrix} \in \mathbb{R}^{C_p \times T}. \tag{4.5}$$

The comparison between the raw left heel pressure and the final pre-processed output are shown in Figure 4.1a. The raw data are in blue and the pre-processed data are in red. The procedure removes noise artifacts such as that seen around 18s and smooths the onsets and offsets of the pressure peaks for more accurate peak and stride extraction. The onsets of the pressure peaks indicate the heel-strike of the foot and the start of the stride. The offsets of the peaks indicate the heel-off and the beginning of the push-off with the foot.

The procedure to clean the EMG removes the high frequency noise artifacts and captures the overall magnitude of the muscle activation. For the EMG data, C_e is the number of EMG channels and T be the number of time samples. The EMG data are stored within the matrix E with the following structure:

$$E = \begin{bmatrix} e_{1,1} & \cdots & e_{1,T} \\ \vdots & \ddots & \vdots \\ e_{C_e,1} & \cdots & e_{C_e,T} \end{bmatrix} \in \mathbb{R}^{C_e \times T}, \tag{4.6}$$
$$e_{c,t} \in \mathbb{R}, c = 1 \ldots C_e, \textit{ and } t = 1 \ldots T.$$

The EMG data are cleaned by first removing the DC offset $E_{offset} = E - d$, where $d \in \mathbb{R}$ is the offset. Then EMG is rectified to $E_r = abs(E_{offset})$, where the absolute value of the



(a) Pressure Pre-processing

(b) EMG Pre-processing

Figure 4.1: Raw (blue) and pre-processed (red) data from an individual without amputation during self-paced walking. (a) The left heel pressure data from the individual. (b) The activity within the left quadriceps.

matrix is defined as:

$$abs(E) := \begin{bmatrix} abs(e_{1,1}) & \dots & abs(e_{1,T}) \\ \vdots & \ddots & \vdots \\ abs(e_{C_e,1}) & \dots & abs(e_{C_e,T}) \end{bmatrix}, \ where \ e_{1,1} \in \mathbb{R}. \tag{4.7}$$

The signals are normalized to a standardized scale:

$$E_n = \frac{E_r - min(E_r)}{max(E_r)}, \tag{4.8}$$

and filtered using a low-pass, first-order Butterworth filter $B(\omega)$, with a cut-off frequency $\omega = 8$ for all participants, $E_b = E_n \circledast B(8)$. This cut-off frequency is also chosen to be consistent with Commuri et al. (2010) and captures the meaningful variation in the muscle activity.

Finally, the moving root mean square (RMS) of the EMG is computed as the signal power:

$$e_{b,k}^{RMS} = \sqrt{\frac{1}{w}\sum_{i=1}^{w} e_{b,i+k}^{2}}\ , \tag{4.9}$$

where $e_{b,k}^{RMS} \in \mathbb{R}$ is the RMS of the EMG computed for time k of the channel b and w is the window length. The comparison between the raw EMG activity of the left quadriceps and the final pre-processed output are shown in Figure 4.1b. The raw data are in blue and the pre-processed data are in red. The procedure removes the noise artifacts and captures the absolute changes in the magnitude of the muscle activation. For example, at about 11s the activity in raw data (blue) oscillates around the mean with high magnitude. The overall magnitude of the activity during this time is captured by the pre-processed EMG in red. Then at about 11.5s, there is less overall oscillatory activity than there is around 11s. This behavior is represented by the decrease in the activation of the red curve.

4.2 Peak Identification

Historically, redundant residuum soft tissue and inconsistent placement of the EMG and pressure sensors can reduce data collection quality during activity performance (Winter & Yack, 1987). These effects cannot always be addressed prior to data collection. The residuum soft tissue compounds the difficultly of detecting surface EMG. Therefore, robust processes are required to extract reliable data, regardless of the signal quality. To compensate for the missing or noisy data, I propose a robust, automated process for identifying heel-strike and toe-off events during each gait cycle, and for identifying peak activation times in pressure and EMG signals. The heel-strikes will then be used to designate the time basis of the strides and other gait events.

In typical walking, the maximum ground reaction force (GRF) within a stride occurs during stance (Alamdari & Krovi, 2017). Therefore, my algorithm locates the onset and

offset of this peak from the pressure data to determine the heel-strike and toe-off events, respectively. The heel-strike is the initiation of the peak in the heel pressure sensor. The toe-off event is the moment the pressure in the sensor on the ball of the foot is attenuated.

The mean RSI pressures $\tilde{P} \in \mathbb{R}^T$ also mimic the patterns of vertical GRFs observed during typical gait (Alamdari & Krovi, 2017); the mean RSI pressure is a stand-in for force and identifies the beginning and end of the stance phase for the residual limb. The signal quality of individual pressure sensors can vary. Therefore, on a per-trial basis, sensors containing many noise artifacts, or with little discernible variation after pre-processing, are excluded from the RSI pressure mean. The sensor selection process is done by visual inspection of the trial. The RSI mean is computed as:

$$\tilde{P} = \frac{\sum_{c=1}^{C_p} \alpha_c \bar{P}_c}{\sum_{c}^{C_p} \alpha_c}, \tag{4.10}$$

where $\bar{P}_c \in \mathbb{R}^T$ is one pre-processed RSI sensor and $\alpha_c \in \{0, 1\}$ is a binary scalar variable. When $\alpha_c = 1$ sensor $\bar{P}_c$ is selected, otherwise it is rejected and not used to compute the mean RSI $\tilde{P}$.

I define the time that the mean pressure initially rises above the data-derived threshold as the heel-strike (i.e., the stride start). The time that the mean falls below the threshold is the toe-off (i.e., the stance end). For individuals with amputation, the OU-PAM does not instrument pressure from the intact limb. While one limb is in stance the other limb is in swing, and vice versa (Alamdari & Krovi, 2017). Therefore, gait events are inferred for the intact limb by inverting (i.e., flipping vertically) the mean RSI pressure and then using the same extraction procedure. This procedure is illustrated in Figure 4.2 for an individual with OTFA during self-paced walking. In Figure 4.2a row 1, are the pressure from all the RSI channels. Figure 4.2a row 2 is a closer view of the data over the time interval $55 - 70$s. The distal anterior (DA), distal medial (DM), distal lateral (DL), posterior anterior (PA) and posterior medial (PM) sensors are used to compute the mean (blue curve). The mean is

flipped vertically, as seen by the red curve in Figure 4.2a row 3, to represent the pressures experienced by the intact limb. The formula for vertically flipping the mean is:

$$\tilde{P}_f = abs(\tilde{P} - max(\tilde{P})), \tag{4.11}$$

where $\tilde{P}_f$ is the flipped mean. Figure 4.2a row 4 shows the mean and flipped mean over the time interval $55 - 70$s.

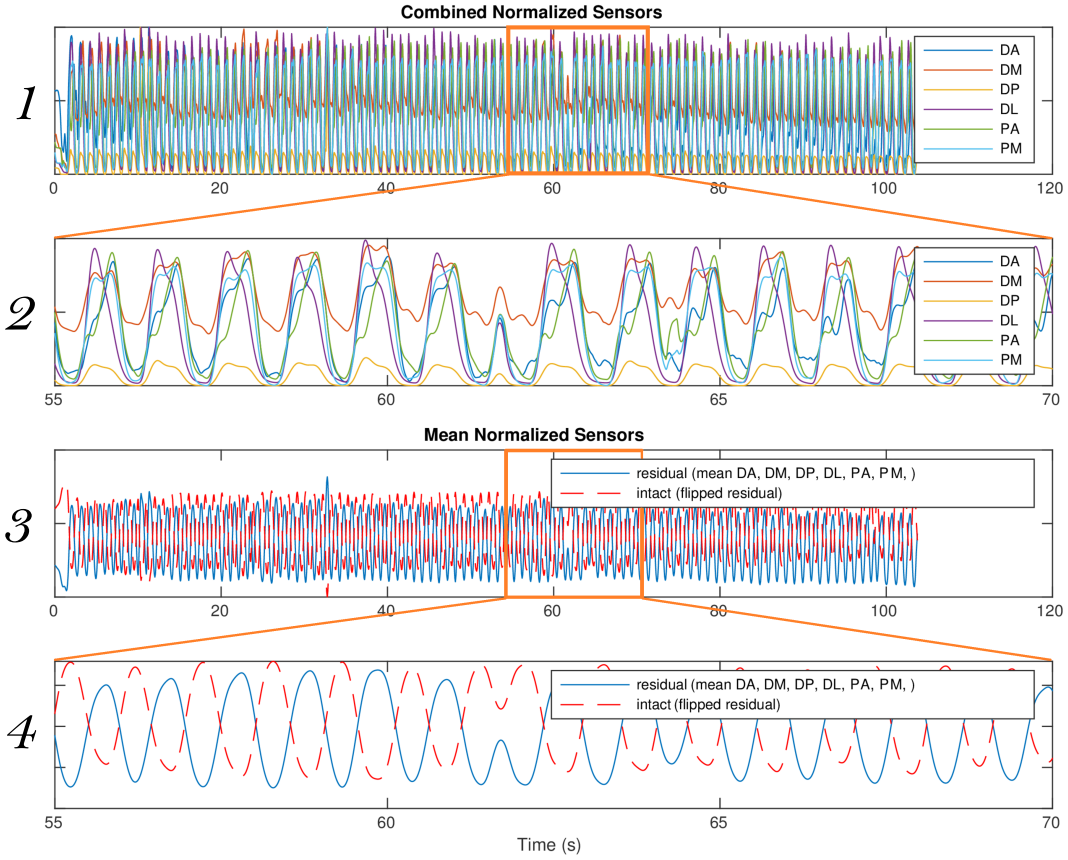
A similar detection procedure is used to identify peak times within both the pressure and EMG data. However, the EMG peaks are not identified until after the strides have been extracted. A peak is defined at time t if the following conditions hold:

1. the signal value is the largest during the range $[t - \delta, t + \delta]; ms$, where $\delta = 240\ ms$, and
2. the signal value is above a data-derived threshold ϵ.

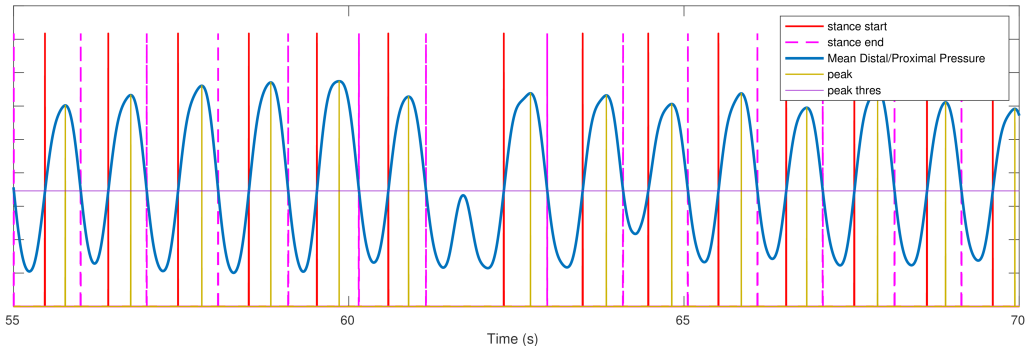
For preliminary analysis, data percentiles are selected for each subject for ϵ. The 64^{th}-percentile is used for the foot pressure peaks for individuals without OTFA. The 45^{th}-percentile is used for the RSI pressure peaks for 4 individuals with OTFA. The 35^{th} and 37^{th}-percentiles are used for the other two individuals with OTFA, respectively. The percentile used for the threshold for the foot pressure peaks are higher than the percentile for the RSI pressure peaks due to the brief duration of the foot pressure peaks. The 50^{th}-percentile is used for the EMG for all individuals. The general approach is modular such that other data-derived or statistically derived options can be computed instead. Occasionally, cases where a pressure or EMG sensor activation is saturated throughout a time range, the middle time of saturation is designated as the peak time.

4.3 Stride Extraction

Strides are extracted independently for each limb and defined as heel-strike to heel-strike with the same limb from the continuous data stream by identifying the gait events from available



(a) Sensor Selection and Averaging



(b) Step and Stance Time Determination

Figure 4.2: Stride extraction procedure for individuals with OTFA, from Shotande et al. (2022, in revision). The details of the RSI locations and abbreviations are in Figure 3.3. (panel a, row 1) Six of the eight RSI sensor values met our analysis inclusion criteria and are shown over a two-minute session. (row 2) The RSI sensor values show a periodic behavior, though each sensor has a distinct offset and scale. (rows 2 and 3) The mean of the selected normalized RSI sensor values and its inverse. (b) Gait events are chosen at the time that the mean RSI sensor value crosses a determined threshold.

pressure data (Figure 4.2b). For the control participants, the gait events are determined using the foot pressure data. The onset of the peak in the heel pressure determines the heel-strike and is designated as the start of the stride. The offset of the peak in the ball pressure determines the toe-off event, indicating the end of the stance.

The gait events for individuals with OTFA are located by examining the peaks from the mean of the available RSI pressure signals. The moment that the mean pressure initially rises above a data-derived threshold is defined as the heel-strike and designated the start of the stride. The time that the mean falls below the threshold is the toe-off, indicating the stance end. Strides whose peak pressures are below the data-derived thresholds are considered invalid and excluded from further analysis. Once the strides are extracted, I calculate the distribution of stride lengths and the corresponding 99% HDRs. Strides are excluded if their duration falls outside the continuous interval defined by the lower bound of the lowest 99% HDR and the upper bound of the highest 99% HDR. A general description of HDRs is provided in Chapter 2.5.

In Figure 4.2b is an illustration of the peak identification and the stride and stance extraction from the mean RSI pressure for an individual with OTFA during self-paced gait. The blue curve is the mean RSI pressure and the horizontal line is the peak detection threshold. The vertical yellow lines are the identified peaks, the red vertical lines designate the stride start times, and the vertical magenta lines designate the stance end times. At about 62s, there is a peak that is below the detection threshold. This results in the duration of the preceding stride (at about 61s) to almost doubling in length. Therefore, the final extraction step that filters out strides based on duration will omit the stride detected at about 61s from the analyses. Once the strides have been extracted, the peak activation times of the EMG are determined. Multiple peaks are considered since individual muscles can serve different roles throughout gait (Winter & Yack, 1987).

4.4 Stride Analysis

After the strides are identified and the invalid strides are excluded, gait performance is analyzed on a per stride basis. The re-sampled stride length is the median stride length over all the participants' strides. The strides are re-sampled such that they all have the same number of samples and can be compared directly. The median stride length is used to mitigate noise effects of re-sampling by minimizing the average difference in length between the original stride and the re-sampled strides. To re-sample the strides:

1. strides are padded at the beginning and end to better estimate the samples on the edges of the signal. Specifically, reflection padding is used to eliminate artifacts. The reflection is the reversed order of the samples (i.e., $reflection([s_1\ s_2\ s_3]) = [s_3\ s_2\ s_1]$).

2. Then a polyphase anti-aliasing filter is used to reduce noise and maintain the original stride shape (Crochiere & Rabiner, 1988; Harris & Constantinides, 1991). Strides are either:

    - down-sampled with a weighted moving average, or
    - up-sampled by linearly interpolating between samples at evenly spaced intervals.

I use heat maps to visualize the re-sampled strides for visual comparison of the activation timings. Figure 4.3 is an example of how the heat maps are constructed using four strides from a single RSI sensor. The horizontal axis of the heat map is the percent of the gait cycle. The vertical axis is the stride number. The color map indicates the relative pressure.

To quantify the variation in activity at each time point during gait, kernel densities for each time slice during gait are computed independently (illustrated in Figure 4.4). Kernel density estimation (KDE) is discussed in more detail in Chapter 2.4. Distributions of the pressure and EMG data are computed over all the strides within each participant group. The KDEs approximate the probability distribution of the sensor activity for a given time slice. For each kernel density, I use 95% HDRs to summarize the distribution at each time

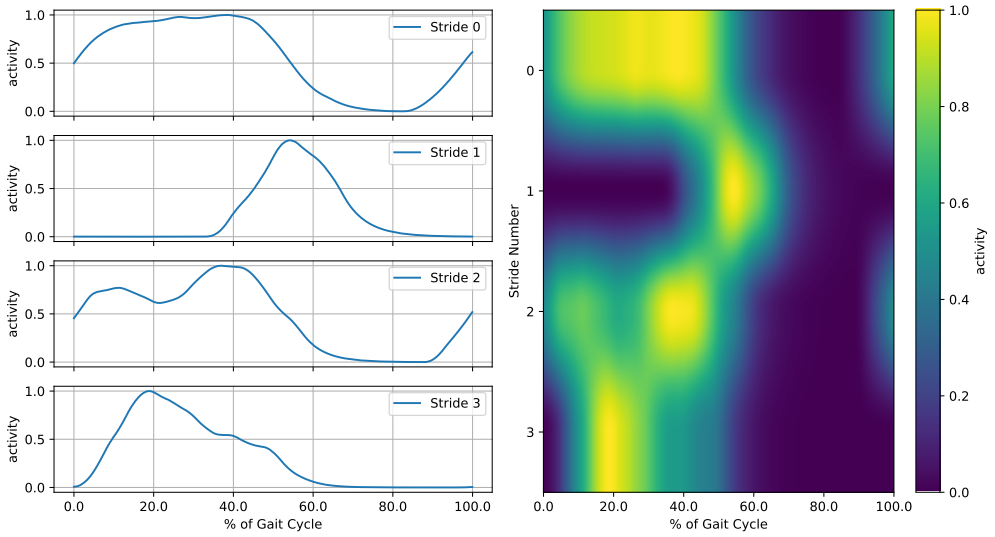


Figure 4.3: Construction of stride heat maps using data from four strides for the DA (distal anterior) pressure sensor. The relative pressure is mapped to a color. The time within the gait cycle is the horizontal axis, and strides are stacked vertically, making the vertical axis the index of the stride.

during the gait cycle. In standard gait analyses, pressure and muscle activity distributions are described using the mean and standard deviation. These measures are sensitive to outliers and do not adequately summarize distributions that are skewed or have multiple modes. The HDRs identify the most likely signal values and are guaranteed to capture all the modes within the data distribution.

Figure 4.4 is an example of the 95% HDRs at each time slice during gait at the DA (distal anterior) socket location and a kernel density at 20% of the gait cycle. HDRs identify the modes of the pressure distribution and distinct behavior patterns. In the left panel, the solid blue curve is the mean pressure over all the strides. The light blue regions indicate the 95% HDRs at each time point. The HDRs at 20% of the gait cycle are highlighted in red. In the right panel, is the kernel density and 95% HDRs (red lines) at 20% of the gait cycle. The dashed green line indicates where the endpoints between the left and right panels line up and indicates the DA pressure intervals that are most likely to occur 95% of the time.

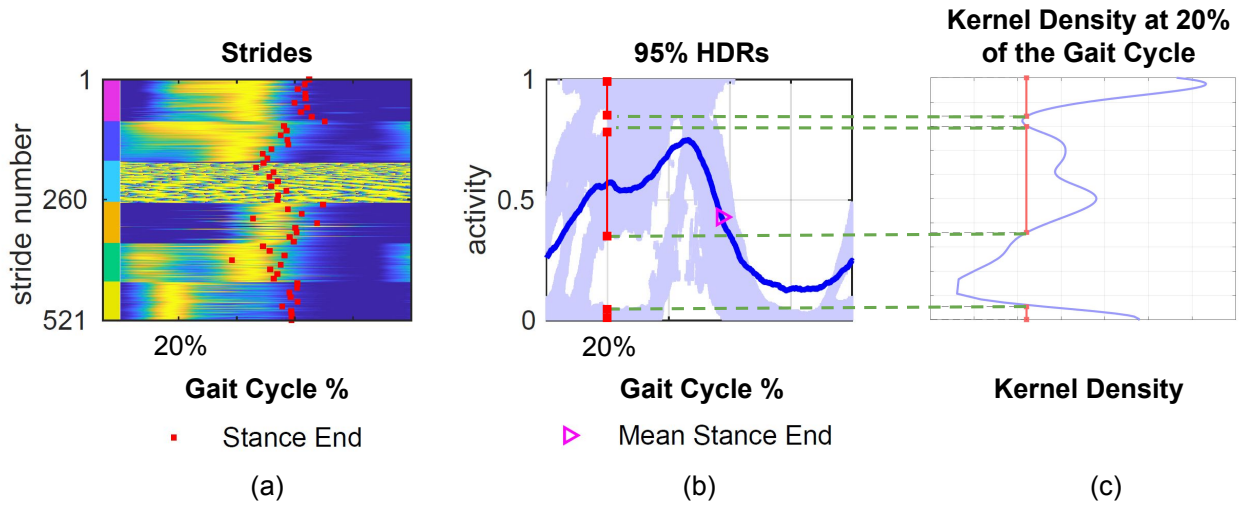


Figure 4.4: 95% HDRs for the DA (distal anterior) pressure sensor over all the strides from all individuals with OTFA from Shotande et al., in revision. (a) The heat map containing all the strides from the OTFA cohort. (b) Each vertical is a distribution of the activation over all the strides at a single time point. The 95% HDRs are shaded for each moment during gait. HDRs as a function of time in the gait cycle are in light-blue; mean pressure activity is depicted with the solid blue curve, with mean stance end is marked with the magenta triangle. (c) At 20% of the gait cycle, the pressure activity distribution and corresponding HDRs are shown.

4.5 Muscle Behavior Analysis

Peak EMG activation is the point where the muscle is imparting the locally maximal force. Therefore, I used the EMG peak times within each stride to characterize muscle recruitment and walking strategies. I quantify common muscle activation patterns by identifying the EMG peak activation time within each stride using my peak identification procedure. For a given stride, the procedure may identify zero or more peaks. I compute the distribution of muscle activation peak times across the strides for a given task. For example, the distributions for the peak EMG activation times for each of the left muscles and each task for a single intact control participant are shown in Figure 4.5. Blue distributions are for the brisk walking task and magenta are for the self-paced walking task. Two major modes are observed for each muscle and task. For example, the left adductors there are modes around 20% and 70% of

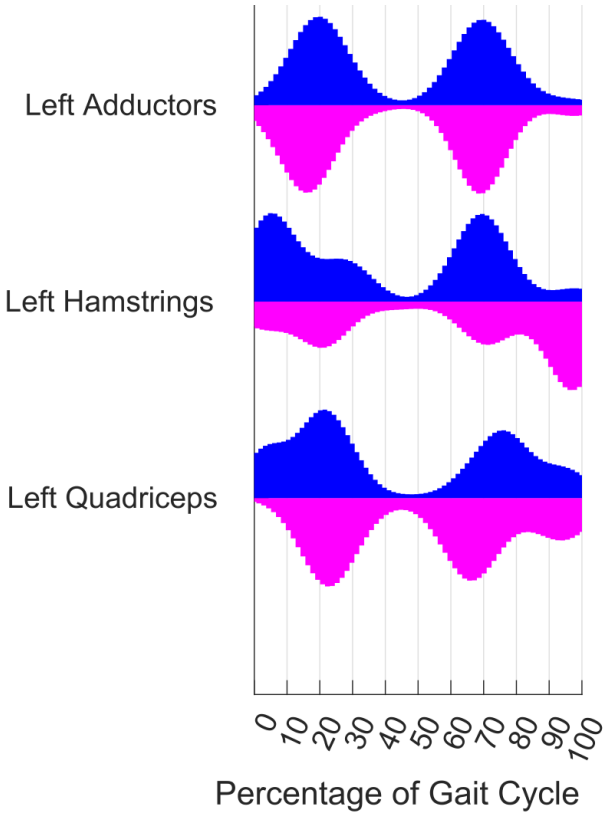
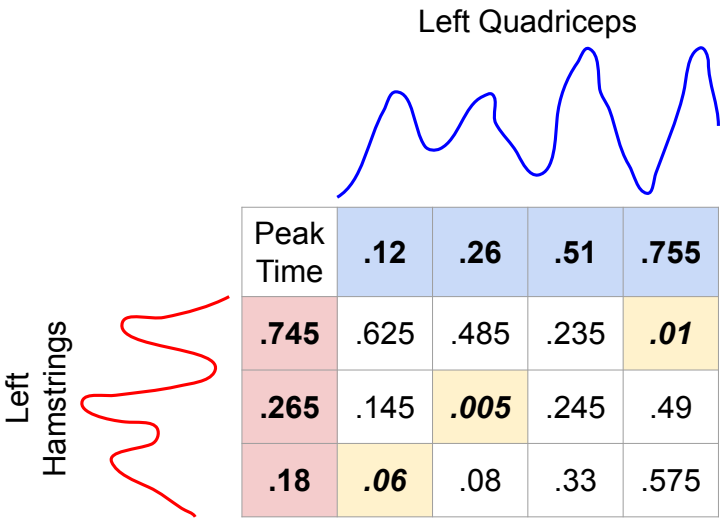


Figure 4.5: Peak activation times for the left muscles of an intact control from both gait tasks. The blue distributions are from the brisk walking task. The magenta distributions are from the self-paced walking task. Two major modes are seen for each task and muscle.

the gait cycle. Muscle activation peak times are further aggregated across the participants for each muscle group within the thigh (i.e., adductors, hamstrings, and quadriceps). Intervals with a high density of peaks indicate consistent periods during the gait cycle of high relative pressure or muscle activity.

To quantify co-activation timing, peaks during a stride from one muscle are matched with one or more of the closest peaks from another muscle (Figures 4.6 and 4.7). The matrix $A \in \mathbb{R}^{m_1 \times m_2}$ contains all the paired distances between muscle activation peaks for a pair of muscles, where m_1 is the number of peaks in muscle 1 and m_2 is the number of peaks in muscle 2. The minimum is computed along the longest dimension of A to locate the set of the closest pairs. Muscle activation peaks without matches are excluded from the analysis.



Peak Time	.12	.26	.51	.755
.745	.625	.485	.235	***.01***
.265	.145	***.005***	.245	.49
.18	***.06***	.08	.33	.575

Figure 4.6: Distances between muscle activation peaks during the same stride. Peak times for the left hamstrings are in the red cells. Peak times for the left quadriceps are in the blue cells. Distances in time between all pairs of peaks between the left hamstrings and quadriceps are in the white and yellow cells. The yellow cells indicate the pair of the closest peaks.

Co-occurrences of the EMG peaks across pairs of muscles are visualized using a scatter plot of paired peak times. An example matrix is shown in Figure 4.6. The muscle activation peak times for the left hamstrings are in red cells. The peak times for the left quadriceps are in the blue cells. The distances between the pairs of peaks are in the white and yellow cells and corresponds to the matrix A. The left hamstrings have the fewest peaks, therefore, the peak within the quadriceps closest to each of the peaks within the hamstrings are selected and shown in the yellow cells.

An illustration of the output of this approach can be found in Figure 4.7. The activity of the left quadriceps (blue) and hamstrings (red) are seen in the top panel of Figure 4.7. The peaks are indicated with stars. The points in the bottom panel of Figure 4.7 correspond to the matched peaks. The horizontal axis is the time during the gait cycle when the left quadriceps activate and the vertical is when the left hamstrings activate. Each peak in the muscle with the fewest peaks gets paired with a peak in the other muscle that is closest in time. Therefore, the peak around 50% in the gait cycle is not matched. Points near or along

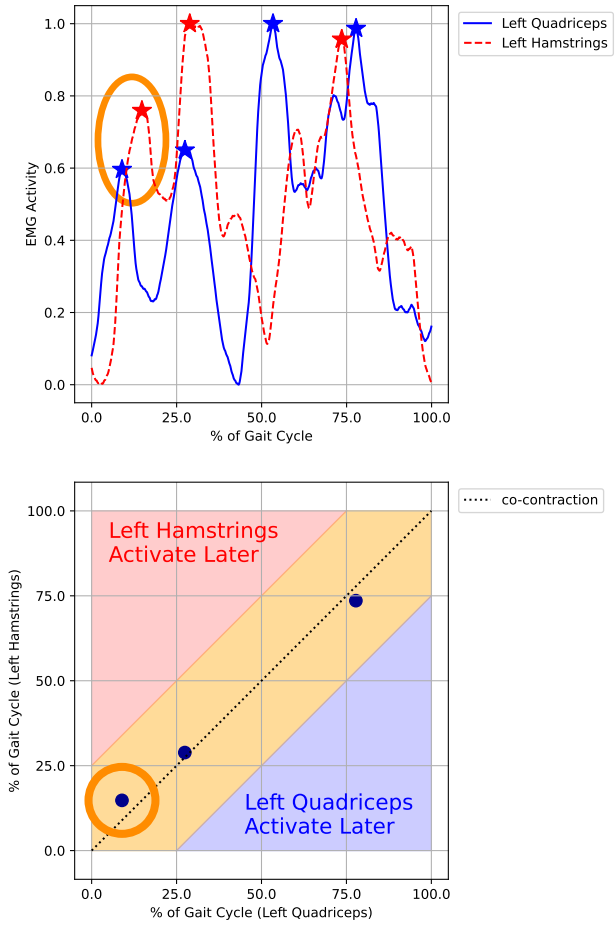


Figure 4.7: Peak matching between muscles during the same stride. Peaks within the left hamstrings and quadriceps are matched based on which pairs are closest in time. The relative locations within the gait cycle of each muscle peak are used to construct the scatter plot of co-activity between the muscles for the stride. This is done for all strides and pairings of muscle groups. The region along the diagonal of the scatter plot is considered evidence for co-contraction of the muscles. The points off the diagonal region are not co-contraction and contribute to momentum of the limb.

the diagonal are evidence for co-activation. All other points contribute to momentum of the limb since they are activating individually. For example, points within the blue triangular region of Figure 4.7 indicate that the left quadriceps activated later during the gait cycle than the hamstrings. The two peaks occurred at independent times.

4.6 Automated Gait Phenotype Identification

After the analysis performed thus far for understanding the overall gait patterns, the next step is to automatically and explicitly isolate the distinct types of muscle recruitment behavior. Here, I expand upon prior methods using compression and clustering algorithms. Compression is performed to remove redundant or noisy information and to speed up the clustering process. The latent features are constructed from the muscle activity of six muscles during valid strides. Ideally the compression model should preserve meaningful variance between and within groups of strides that utilize distinct muscle activation patterns (i.e., phenotypes).

After the strides have been clustered in the latent space, we can characterize and compare the muscle activation patterns of the strides within and between the clusters. The goals of my approach are to understand common muscle recruitment strategies, identify any strategies unique to those with amputation, and quantify the descriptions of these distinct muscle strategies.

4.6.1 Data Representation

The data are structured somewhat differently for this phase of the analysis. Instead of characterizing muscle activity of each limb individually, here, the muscle activity of both limbs are analyzed simultaneously, relative to the heel-strike of one limb. Strategies used by each limb are dependent upon what the other limb is doing. For individuals without OTFA, the heel-strike of the right limb is used to define the time basis of the gait cycle. For individuals with OTFA, the heel-strike of the residual limb is used to define the start and end of the gait cycle. The residual limb heel-strike is chosen as the time basis since we have direct measurements from the pressures within the residual limb; therefore the heel-strike times are more precise than for the intact limb.

The data are structured in a form such that all six muscles (i.e., adductors, hamstrings, and quadriceps of both limbs) across all participants (six with OTFA and six intact matched

controls) and both gait tasks (brisk and self-paced walking) are compressed using principal component analysis (PCA) or an autoencoder (AE) model described in Sections 2.2.1 and 2.2.2. There are N rows in the data array $X \in \mathbb{R}^{N \times T \times C}$ for each stride $X_i \in \mathbb{R}^{T \times C}$. There are T columns for each normalized time sample (or percent of the right/residual limb gait cycle) with D levels of depth for each EMG channel. The sample and channel dimensions are merged into one dimension resulting in an array with shape $X_{PCA} \in \mathbb{R}^{N \times F}$, where $F = T \times C$, for input into the PCA model. PCA can only perform the compression on 2D arrays and not 3D arrays (i.e., tensors), therefore, the data are reshaped from $N \times T \times C$ to $N \times F$. The 3D structure of the data is depicted in Figure 4.8.

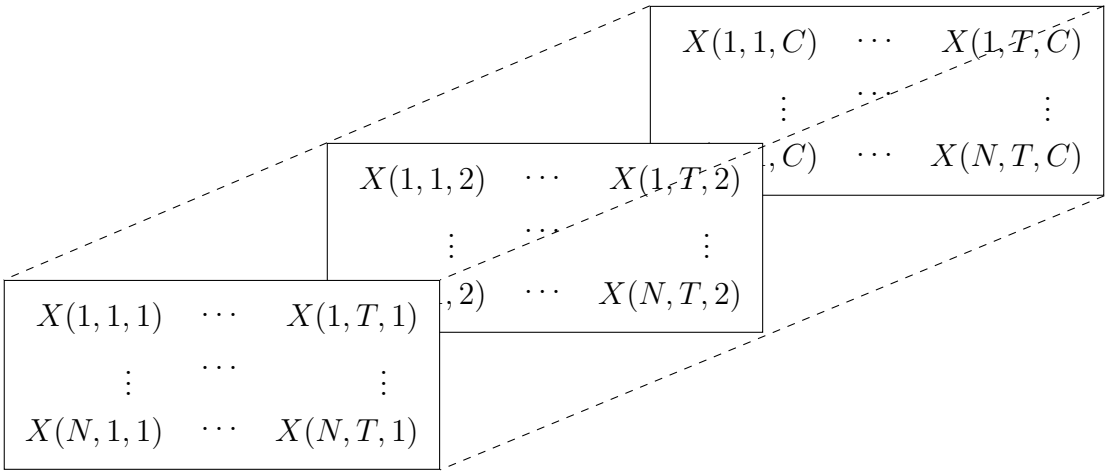


Figure 4.8: The EMG data $X \in \mathbb{R}^{N \times T \times C}$ are structured as a 3D tensor array for input into the AE model. There are N strides from all the participants, T normalized time samples which correspond to percent of the right/residual limb gait cycle, and there are C EMG channels for each of the muscles. Each row corresponds to a single stride. Each column corresponds to a single point in time and each rectangular depth slice corresponds to a single channel. For example, $X(1,1,1)$ indicates a single time sample from one stride and one EMG channel. The corresponding index for the stride is 1, the corresponding time sample index is 1 and the corresponding EMG channel is 1.

4.6.2 Compression Models

For compression, a 1D convolutional AE architecture is used to construct a nonlinear model that transforms the EMG activity from six muscles during a single stride into a lower

dimensional (latent) representation. The AE model as a whole is the function $f(X) = D_\beta(E(X))$. The encoder sub-network is represented by the function $Z = E_\theta(X)$ and the decoder sub-network is represented by the function $\tilde{X} = D_\beta(Z)$ where θ and β are the parameters for the encoder and decoder respectively. The input is $X \in \mathbb{R}^{N\times T\times C}$ and the latent representation is $Z \in \mathbb{R}^{N\times d}$, where d is the number of latent dimensions. The best set of parameters θ and β are obtained during the training by minimizing the reconstruction loss $||X - D_\beta(Z)||^2$ for the objective function. Additional details on AEs are in Chapter 2.2.2.

Compression is also performed using PCA, by minimizing $||X - ZP^{-1}||$, where Z is the compressed representation, X is the data and P performs the compression operation on X. The specific hyper-parameter details for PCA are provided in the Appendix. PCA is used as a linear benchmark for comparison. AEs are preferred to PCA for their ability to learn non-linear relationships. Within the latent space, the data are clustered into groups using a Gaussian Mixture Model (GMM). Activity and peak analyses are conducted within and across clusters to identify and compare muscle recruitment strategies.

To determine an optimal structure for the AE model, Bayesian Optimization (BayesOpt) is performed for hyper-parameter tuning. During this process, using a subset of the data, an appropriate number of nodes and layers within the encoder, decoder, and latent layers are determined. The configuration of nodes and layers is the set of hyper-parameters. BayesOpt computes a probability estimate of the performance function over a subspace of possible hyper-parameters. The probability estimate is referred to as the posterior probability. Using the posterior probability, an optimal selection for the hyper-parameters is identified. More details on BayesOpt are in Chapter 2.6.2.

For PCA, the optimal number of principal components (PCs) is chosen based on the fraction of variation accounted for (FVAF), defined in Equation 2.7, of the validation set. The smallest number, d, of dimensions (i.e., PCs) is chosen such that the total FVAF is approximately .95. Once d is determined, the PCA transformation is recomputed such that the number of output PCs is d. PCA is described in more detail in Chapter 2.2.1.

4.6.3 Model Validation

The model architectures are compared and validated using a participant-leave-out approach (described in Chapter 2.6.1). Specifically, I select two participants from each participant group to leave out from the training set and use their data in independent validation and test sets. The test set is used to determine generality of the model architecture to data not seen during training. The validation and test sets must contain examples independent of those in the training set to minimize any correlation with the training set and better access the performance quality of the model to unseen data. One participant from each cohort is allocated to the validation set and the other to test set. Models are trained using the training set and selected using the validation set. The model with the highest FVAF on the test set has the best generalization performance. The FVAF is chosen over root mean squared error (RMSE) since it is more interpretable in the context of normalized EMG voltages.

4.6.4 Automated Phenotype Extraction

After data compression with either PCA or the AE, the data are clustered using a Gaussian Mixture Model (GMM). GMMs are discussed in detail in Chapter 2.7.1. To automate the identification of distinct muscle recruitment phenotypes, I use GMMs for two-level hierarchical clustering. The data are initially broken into K clusters and then each cluster is further broken into C_k sub-clusters, where k is the cluster index. The number of clusters is determined using cross-validation based and the average adjusted mutual information (AMI) of the models. I use AMI to measure the consistency in the membership assignments across multiple executions of the model since stochasticity is involved in the training of the GMMs. The number of clusters from the model with the highest AMI score is used for K. For each of the K clusters, another round of clustering is performed, and each cluster may not necessarily have the same number of sub-clusters C_k. Then, peak and co-contraction analyses are performed for each cluster.

Chapter 5

Walking Behavior at Two Speeds

The gait performance of six men with OTFA and six matched intact controls from Dionne et al. (2022) are analyzed and compared. Approval for this study was obtained from the OU-HSC IRB (#4884). Gait pressures were collected at the heel and ball of each foot for the control participants. Eight RSI pressures were collected at the proximal and distal levels within the prosthetic socket, as seen in Figure 3.3. At each level, pressure sensors are placed at the anterior, posterior, medial, and lateral locations. For both participant groups, muscle activity is measured for the adductors, hamstrings, and quadriceps groups. In this chapter, I provide details of the results from applying the approach described in Chapter 4. I am able to show and describe the behavior of muscles within the distal residuum of those with OTFA, which has not been shown before. I provide an overview of an eight-second window of the continuous data. Then, I describe the distribution of pressure and EMG activity at each time slice during the gait cycle to determine likely gait patterns and assess the quality of prosthetic fit. I provide a comparative analysis of the distribution of the muscle co-activation times between the OTFA and intact controls. Lastly, I extract and compare gait phenotypes.

	Participants with OTFA	**Matched Controls**	p-value
age (years)	34.0 ± 15.0	27.2 ± 6.2	0.3367
height (m)	1.8 ± 0.1	1.8 ± 0.1	0.3391
weight (kg)	83.3 ± 16.4	87.3 ± 20.0	0.7125

Table 5.1: Demographic information for participants with OTFA and the matched controls. Two-tailed two sample t-tests were performed to assess the comparability of the demographic information between the groups. The two sample t-test was conducted since the participants come from independent groups.

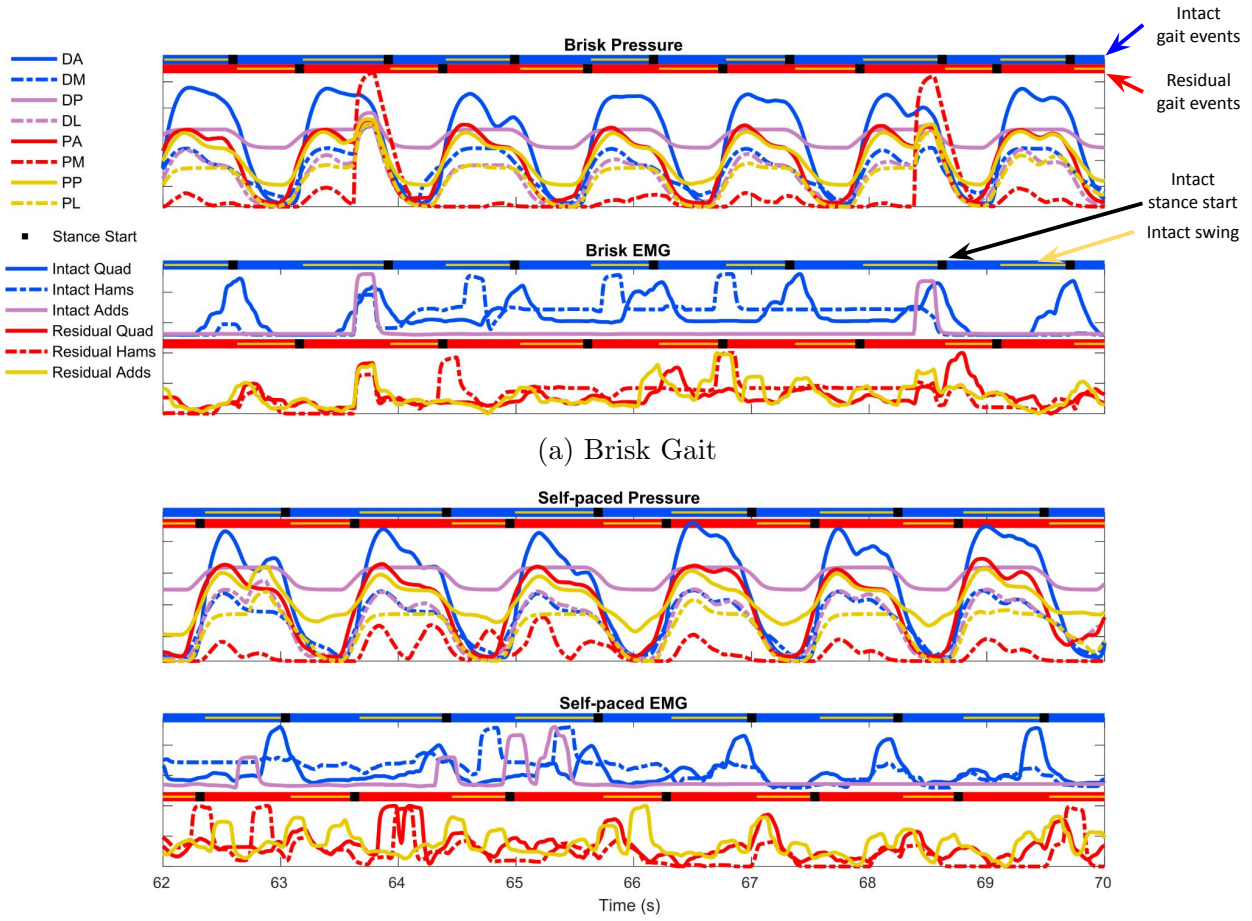
5.1 Participant Selection

The six matched intact control participants selected had no significant difference in their average age, height, or weight from those of the OTFA cohort. Two-tailed, two-sample t-tests, with $\alpha = 0.05$ are performed to assess the comparability of the demographic information (i.e., age, height, and weight) between the participants with and without OTFA to minimize sources of variation between the independent cohorts. The results of the tests along with the demographic details are shown in Table 5.1.

5.2 Continuous Data Overview

Using my proposed stride extraction procedure described in Chapter 4, after omitting invalid strides, over 67 strides per limb per individual are obtained. There are over 520 strides for each participant group during each walking task per limb. An eight-second snapshot of the continuous log RSI pressure and EMG activity during brisk (a) and self-paced (b) walking for an individual with OTFA (participant A06) are in Figure 5.1. Seven strides are observed during this time frame. Blue and red horizontal lines above each set of curves in each panel indicate the gait events and phases for the intact (blue) and residual (red) limbs, respectively. Black squares designate the start of the stance phase. Thin yellow horizontal lines designate the swing phase for the respective limb.

The log RSI pressures from the eight locations within the residuum socket are shown. There



(a) Brisk Gait

(b) Self-paced Gait

Figure 5.1: Log RSI pressure and EMG activity during eight seconds of brisk (a) and self-paced (b) walking, from visit two of an individual with OTFA (A06). Blue and red horizontal bars above each set of curves indicate the gait events and phases for the (blue) intact and (red) residual limbs, respectively. Black squares designate the start of the stance phase. Thin yellow horizontal lines designate the swing phase for the respective limb. Pressure abbreviations: distal anterior (DA), distal medial (DM), distal proximal (DP), distal lateral (DL), proximal anterior (PA), proximal medial (PM), proximal posterior (PP), and proximal lateral (PL). Sensor locations are shown in Figure 3.3.

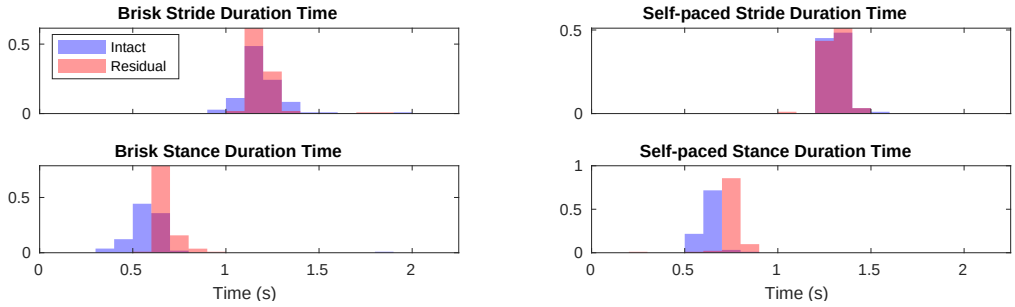


Figure 5.2: Histograms are the distributions of stride and stance duration times in seconds for both the brisk and self-paced tasks. The stance duration is on average shorter for the intact limb than the residual limb, during both tasks ($p < 10^{-27}$).

is evidence of consistency in the RSI pressures, during brisk (a) and self-paced walking (b), due to the regularity of the timing and shape of the peaks across the RSI locations. Just after the residuum heel-strike, as indicated by the black square on the horizontal red line, the RSI pressures begin to increase. Additionally, the RSI pressures are decreasing during push-off, prior to the start of the swing, indicated by the thin yellow line on the red line horizontal line. There is some exception for the posterior medial (PM, the dashed red pressure curve) location, where the pressures are relatively low for five of the strides and peak about halfway through the stance. However, the PM pressure peaks decrease during push-off as well.

For the EMG, some regular activation patterns are observed. For example, during both tasks the intact quadriceps (the solid blue EMG curve) consistently peak around the intact heel-strike, indicated by the black square on the horizontal blue line. Additionally, during both tasks the residual quadriceps (the solid red EMG curve) often peak around the beginning of swing. There is an exception during self-paced walking around 64s where the residual quadriceps peak in the middle of the stance. During brisk walking, the intact hamstrings (dashed blue EMG curve) peak in the early half of swing during the time frame from 64s to 67s. During self-paced walking for the intact hamstrings, after 66.5s, small peaks occur around the heel-strike during the same time as the peaks of the intact quadriceps (solid blue EMG curve). For brisk walking, the intact adductors (solid purple EMG curve) occasionally peak at 64s and 68.5s, just prior to heel-strike. The residual hamstrings (dashed red EMG

curve) during brisk walking, two major peaks occur at heel-strike around 64.5s and 66.8s, one smaller peak occurs during the end of stance around 63.8s, and one minor peak during early swing at 62.8s. During self-paced walking for the residual hamstrings, small peaks appear to occur during early swing. A larger peak for the residual hamstrings during the early swing occurs around 69.8s. For brisk walking, the residual muscles (red and yellow EMG curves) activate at similar times, with exceptions around 64.5s, 66-67s, and 68-69s.

The histograms in Figure 5.2 show the distributions of stride and stance duration times in seconds for both the brisk and self-paced tasks for the individual from Figure 5.2. Stride duration is the same for both limbs, during both tasks ($p < 0.67$). The stance duration is on average shorter for the intact limb than the residual limb, during both tasks ($p < 10^{-27}$).

However, examining only eight seconds from one participant is not enough to assess true consistency of the potential patterns. Therefore, I analyze the pressure and EMG activation distributions, across the strides at each time within the gait cycle of all the participants using the techniques described in Chapter 4.

5.3 Distributions at each Time Slice During Gait

Part of the strategy to understand gait behavior from the pressure and EMG data is to describe the distribution of the pressure and EMG data at each time slice during gait across all participant strides. In this section, I detail the results at each time slice of the gait and provide visualizations using the strides from both participant groups during both walking tasks. All the strides are combined into heat maps for visual comparison of the activation timing and to identify specific individuals. Strides from each participant are designated in the vertical axis and the percentage of the gait cycle is in the horizontal axis. The average stride and kernel density estimation at each time point are computed for each of the separate heat maps to quantify the variation in the activation at each time slice. The average time of the stance end is shown by the magenta triangle. Each sensor location has a heat map

and corresponding average and distribution plot. The estimated distributions are described using the 95% HDRs to identify the most likely pressure or EMG patterns that occur with the cumulative probability of 95%.

5.3.1 RSI Pressure Distributions

In addition to understanding gait behavior of those with amputation, we also want to understand prosthetic fit. Describing the distributions of the residuum socket interface pressures (RSI) at multiple locations allows us to better quantify the fit and its variation during tasks. The distribution of the pressure patterns within the prosthetic socket during the self-paced gait cycle are shown in Figure 5.3 and for brisk gait in Figure 5.4. Strides are taken from one visit, for each participant, since half of the cohort did not attend a second visit. The heat maps, in columns 1 and 3 of Figure 5.3, are constructed for all the RSI sensor locations, by taking the extracted strides and stacking them vertically. Strides from the same participant are grouped together and are indicated by the rectangular bars on the left of each heat map. Normalized RSI pressures are colored to indicate relative pressure and yellow indicates high pressure. Additionally, all the strides are normalized in time to describe the pressure at the percent of the gait cycle. The red squares indicate the stance end for every twenty strides. The stance ends on average at $\sim$58% of the gait cycle. Similar RSI pressure patterns occur across the strides and sensor locations for all the participants with OTFA.

The heat maps allow us to observe all the strides and general trends in RSI pressure within and across the participants. There is consistency within participants as seen by the abrupt horizontal shifts in the pressure as we move down the vertical axis of the heat map from one participant to the next. For example, the DL (distal lateral) location pressure peaks for participant A02 (blue bar) start closer to the heel-strike than the pressure peaks for A01 (magenta bar). For participant A03, data collected from the DA (distal anterior) and DP (distal posterior) sensors are invalid for many strides. Additionally, there are a few strides where the data collected from the PP sensor are also invalid.

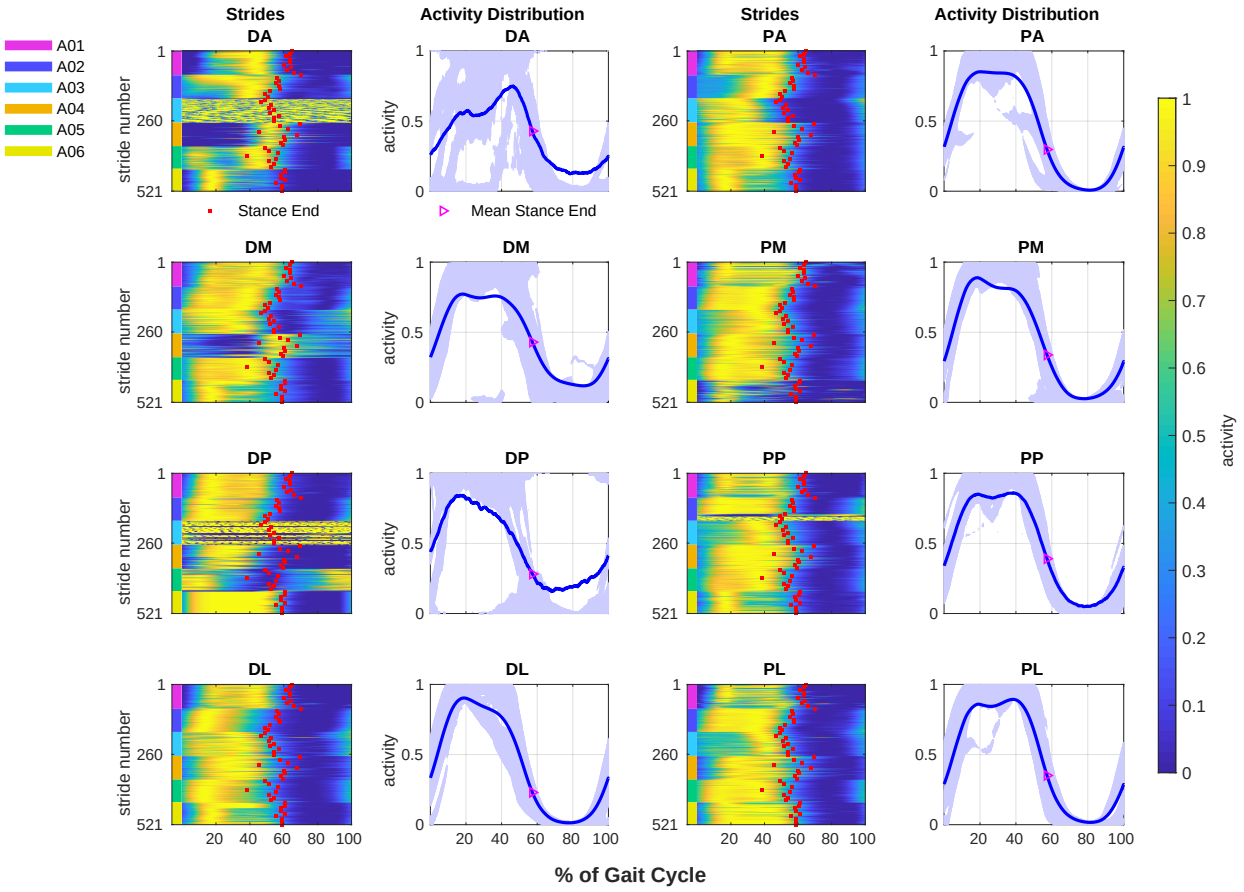


Figure 5.3: Self-paced walking RSI pressure activity, from one visit, for all participants with OTFA. The heat maps in the first and third columns contain all the valid strides extracted from each of the six individuals with OTFA. The activity and time are normalized. Time is described as percent of the gait cycle. Each row in the heat map is activity from an individual stride. The red square indicates the end of the stance every twenty strides. The second and fourth columns display the distribution of activity, at each normalized time point. The 95% HDRs are designated by the light blue regions. The solid blue line is the mean activity. The shaded regions are the most likely pressures.

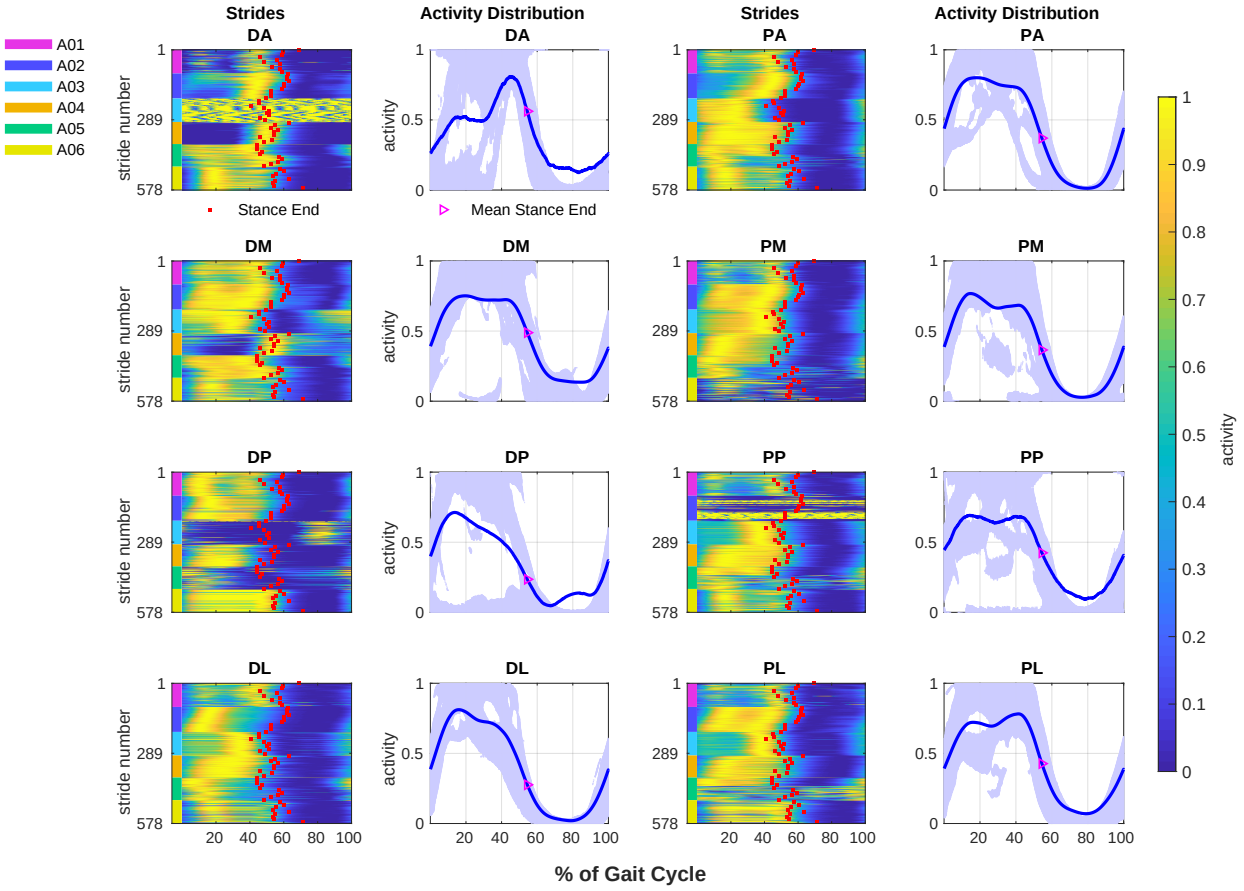


Figure 5.4: Brisk walking RSI pressure activity, from one visit, for all participants with OTFA. The heat maps in the first and third columns contain all the valid strides extracted from each of the six individuals with OTFA. The activity and time are normalized. Time is described as percent of the gait cycle. Each row in the heat map is activity from an individual stride. The red square indicates the end of the stance for each of the strides. The second and fourth columns display the distribution of activity, at each normalized time point. The 95% HDRs are designated by the light blue regions. The solid blue line is the mean activity. The shaded regions are the most likely pressures.

Despite some invalid readings, across all the sensor locations I can still identify broadly four types of pressure pattern. The first is when the pressure rises early in the gait cycle, prior to about 20%, and attenuates around approximately 60%. The second is similar to the first: the pressure rises early and attenuates around 60%. However, the difference is that during mid-stance (∼30%) there is a brief drop in the pressure. The third pattern is when the pressure peaks and drops early (prior to 50%). The fourth pattern is when the pressure peaks late (∼30%) and drops at approximately 60%. The first and second RSI pressure patterns are evidence for good prosthetic fit when present during the majority of strides across all the pressure locations. For these two patterns, the pressure is high throughout most of weight-bearing with the residual limb suggesting consistent and stable contact with the prosthetic socket. The later two pressure patterns might be evidence that the prosthetic fit requires some adjustments at one or more locations for an individual. With these two patterns, the pressure is low for half or more of the time spent during residuum weight-bearing. The low pressure at specific locations during weight-bearing suggests little to no contact with the socket at that location.

To the right of each heat map are RSI pressure distributions at each moment in the gait cycle for each sensor (columns 2 and 4 in Figures 5.3 and 5.4). The solid blue line is the mean pressure. The shaded regions are 95% HDRs of the pressures that are most likely at each time point over all strides. The magenta triangle indicates the average time that the stance ends. The pressure distributions are computed at each moment in the gait cycle and the pressures with probability above the corresponding threshold are selected such that the sum of these probabilities is 95% (concept visualized in Figures 2.5 and 4.4). Each time slice has a unique threshold since the distributions are computed independently. The HDRs are useful to identify disjointed pressure ranges that are most likely at any given time during gait. Individual regions are analogous to clusters and always contain the modes of the distribution. Additionally, variability in the data is directly proportional to the size of the HDRs. The closer the HDRs become to the mean, the less variation there is in the data and the more

accurately the mean represents the most likely activation patterns.

For both walking speeds (Figures 5.3 and 5.4), at all sensor locations the 95% HDRs during swing (between 60% and 100% of the gait cycle) are near zero. This indicates that is it most likely for the RSI pressures to be approximately zero during this period. Additionally, near zero pressure is observed for all four of the distinct pressure patterns. Prior to 60% (during stance), there are multiple HDRs over the pressure range. This indicates that there are multiple likely patterns of pressure activity during the stance phase. During stance for all the RSI locations, the HDRs contain one as part of the range of likely pressure patterns. For example, self-paced walking (Figure 5.3) for the DL, PA, PM, PP, and PL locations, have HDRs between 10% and 50% of the gait cycle are near one. This pressure behavior is consistent with the distinct pressure patterns where the peak pressure is high throughout stance with some overlap in the behavior where the pressure peaks later or attenuates earlier during the stance. For the DA, DP, and DM (distal medial) locations, there are some HDRs between 20 and 40% that are near zero. This pressure behavior is consistent with the distinct pressure patterns where the pressure peaks attenuate early or rise late during stance. For the DA location, there are also HDRs with pressure range from .4 to 1 prior to 60% of the gait cycle. This is a combination of the pressure peaks that rise late or attenuate early and pressures that rise to about .5 during the first half of the stance and then increase to about 1 midstance. Examples of this pressure behavior are seen for participants A01 and A02. When there are two or more distinct patterns, the mean crosses a path between the pressure patterns. For example, at the PL location for brisk walking at 20% of the gait cycle, there are two distinct pressure modes of similar likelihood and the mean misses both modes and the corresponding likely regions by taking the path halfway between the two modes.

During brisk walking (Figures 5.4), there is more variation in the pressures because the area covered by the HDRs is larger and spans additional regions of the pressure range. For example, HDRs for the PL (proximal lateral) socket location are larger for brisk walking during the time period between 10% and 60% of the gait cycle. For the PM (proximal medial)

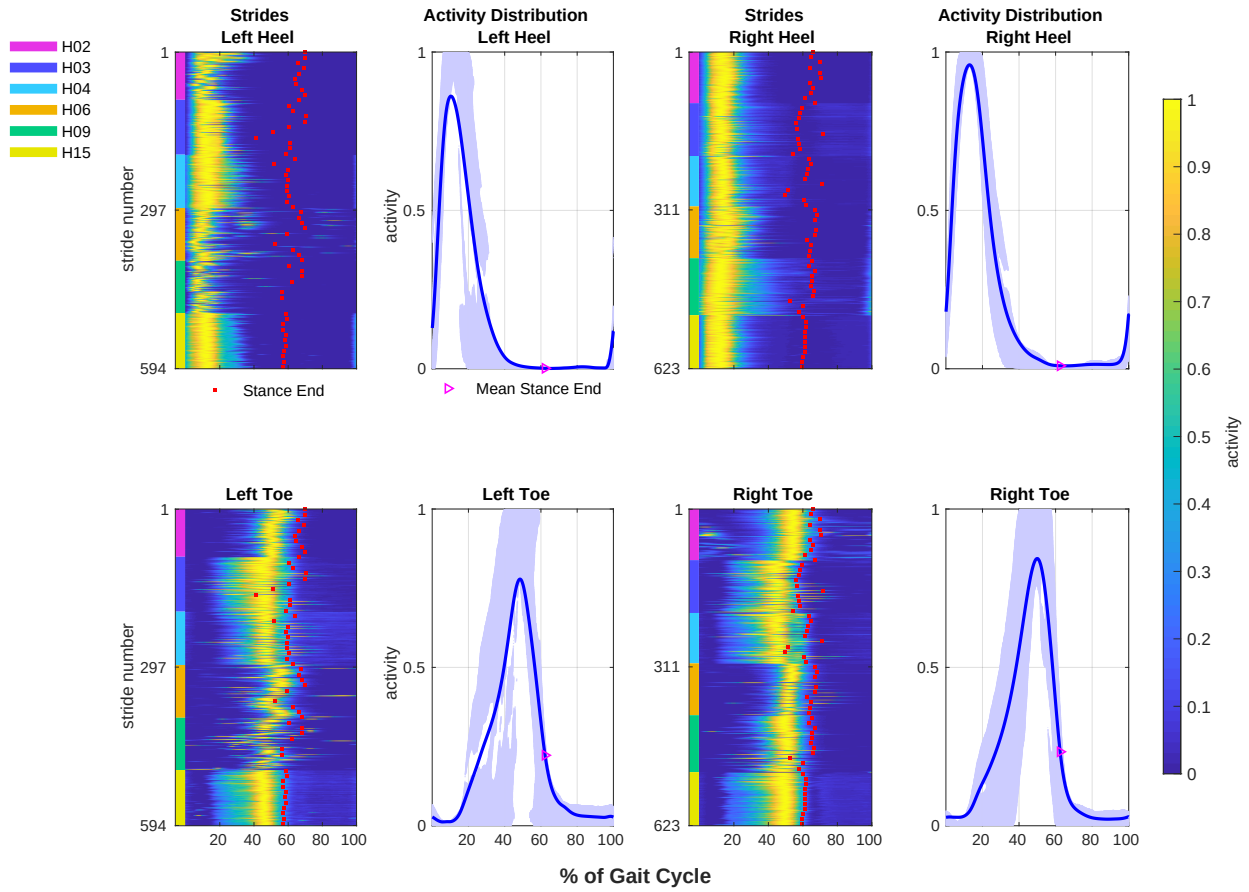


Figure 5.5: Self-paced walking foot pressure from one visit for all matched intact control participants. Kernel densities and HDRs are computed for each time slice of the gait cycle.

location, there are HDRs ranging from approximately .2 to .5 relative pressure, that are not present for self-paced walking. This indicates there is greater variability in the pressure patterns during brisk walking than self-paced.

5.3.2 Foot Pressure Distributions

The distribution of foot pressure patterns for the matched intact controls during the self-paced and brisk gait cycle are seen in Figure 5.5 and 5.6, respectively. The stance on average, ends at ∼61% of the gait cycle. There is not much variation in the pressures at the heel and toe-off the foot and there are typically only one to two regions of likely activation at each time point. Therefore, the HDRs more closely resemble the mean. Gaps between HDRs during the time

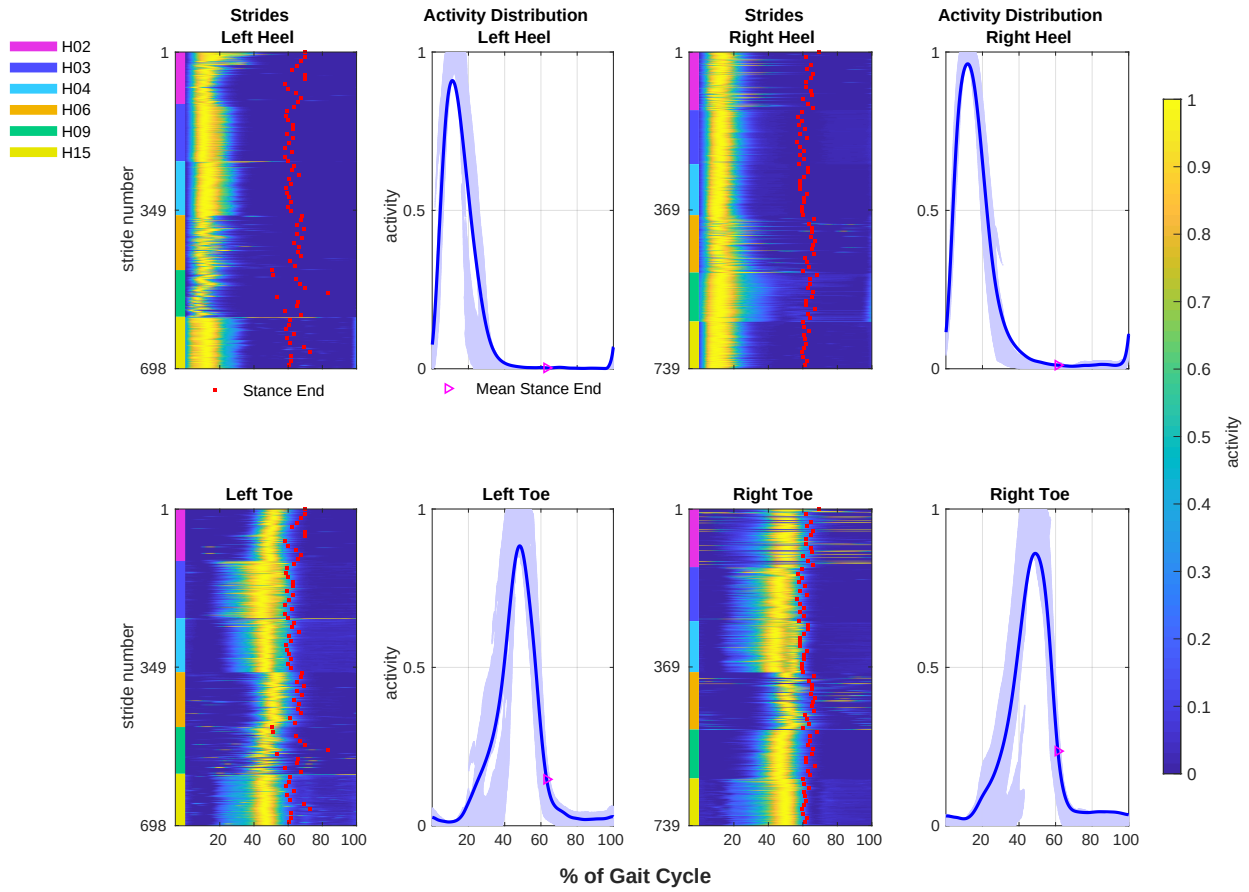


Figure 5.6: Brisk walking foot pressure from one visit for all matched intact control participants. Kernel densities and HDRs are computed for each time slice of the gait cycle.

period when the mean is rising are due to distinct onset times of the pressures. For example, during self-paced for the left toe between 20% and 40%, there are two distinct time periods for the pressure to start rising. This is exemplified by the corresponding heat map where participants H03, H04, and H15 have earlier pressure onsets than the other participants. Additionally, the participants with the peaks that rise earlier, have longer peak duration.

Similarly, when the mean is attenuating, gaps between HDRs indicate distinct pressure patterns, such as during self-paced for the left heel between 15% and 30%. In the corresponding heat map for participants H03, H04, and H15, the peak pressure typically attenuates later compared to the other participants. The gaps between HDRs that are more like "peninsulas", such as for the right toe during brisk walking around 40%, still indicate likely pressure

patterns and are a result of the HDRs at each time slice being computed independently of adjacent time slices. Additionally, the peninsulas indicate dramatic increases or decreases in the pressure between contiguous time slices. The foot pressure is most likely to be near the maximum pressure during the time period between 5% and 22% for the left and right heel with pressures most likely to be near zero after 40%. For the toe pressure, it is most likely for pressures to be near one between 38% and 60% of the gait cycle. Lastly, the toe pressures are most likely to be near zero in the time periods from 0% to 20% and 62% to 100%.

5.3.3 EMG Activity Distributions

OTFA Cohort

The distributions of EMG activation patterns during self-paced and brisk walking are in Figure 5.7 and Figure 5.8, respectively. The observed EMG activation patterns have high variability across the strides at many time periods throughout the gait cycle for each of the muscle groups. However, there are distinct patterns of deactivation within and across the participants that are identified from the HDRs. Additionally, there are general trends in the shapes of the distributions over time that indicate likely activation patterns. In particular, the size of the HDRs (i.e., the likely activity range) decreases during the time frame between 0% and 40% of the gait cycle for many of the muscles indicating decreasing variance in the likely activity over the strides. Additionally, the upper bound on the HDRs are lower indicating it is likely the muscle activation is decreasing during this time frame or likely to be lower towards the end of the time frame. For example, during self-paced walking prior to 12% for the intact quadriceps, the HDRs cover the majority of the activation range. After 12%, the range of the HDRs become more narrow with the activity range $\sim 0 - .35$. In the corresponding heat maps prior to 12%, some participants have the muscles activating during the heel-strike, of varying duration, and others at various times after the heel-strike. This is evidence for the large activation variability indicated by the HDRs.

For both walking tasks during early stance (prior to 20%), the muscles have two major ranges of likely activation, except the intact hamstrings and residual adductors during self-paced walking (Figure 5.7) where the HDRs span most of the activity range during much of the early stance. The intact adductors have two distinct HDRs, one near zero and another with the activity range $\sim.5-1$. This suggests two strategies, one where the intact adductors are not used during early stance ($0-20\%$), and another where the muscle is activated to assist with support just after heel-strike. For the quadriceps, there is an HDR with the activity range $0-.5$ during early stance and another small set of HDRs near one for the residual quadriceps. Strategies where the activation is near one indicate the muscle is a major contributor to controlling the limb during that time frame. Strategies where the activation is lower suggest a more supporting role of the muscles. In this particular instance, the quadriceps are often a major contributor after the heel-strike for stabilizing the knee to prevent the limb from over flexing and collapsing under the individual's weight. For the residual limb (where there is no knee joint), the quadriceps are activating to manage control of the prosthesis.

For both tasks and all muscle groups, between 20% and 40% of the gait cycle there is a high likelihood of lower muscle activation. For the residual quadriceps for brisk walking, this low activation time frame is shifted earlier (between 10% and 30% of the gait cycle). In the corresponding heat maps between $20-40\%$ or $10-30\%$, the periods of low activation appear as a blue river down the strides. During this time frame, the limb is likely done receiving and managing the full force from the body weight. The limb transitions into midstance (30%) where the center of mass of the body is at its highest and directly above the limb. Therefore, little energy is required from the muscles.

During the time frame between about 40% and 60%, the HDRs increase in size for all the muscles. To illustrate, within the residual hamstrings during self-paced walking (Figure 5.7), the HDRs initially cover narrow activation ranges between approximately 20% and 40% of the gait cycle. Then, after approximately 40% of the gait cycle, the HDRs increase to cover most

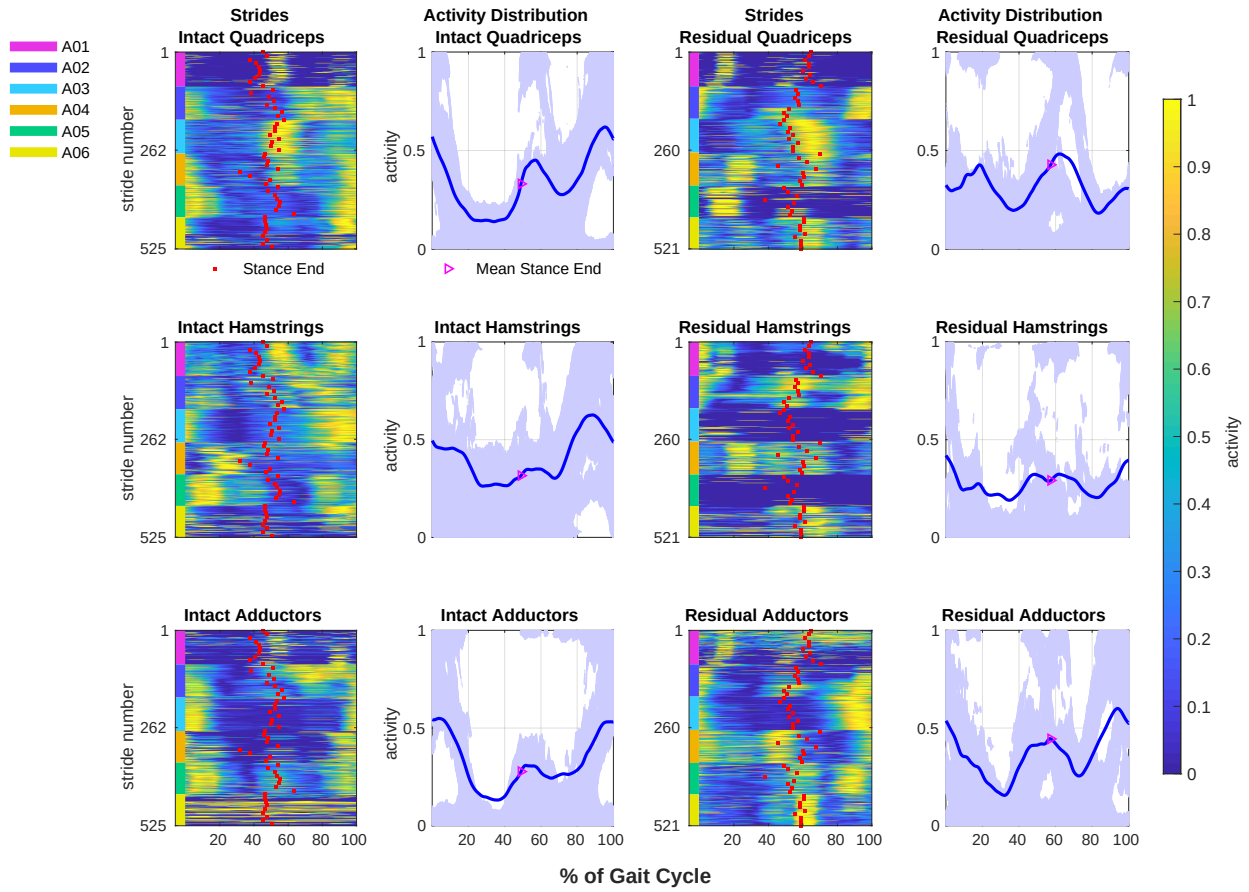


Figure 5.7: Self-paced EMG Activity from one visit for all participants with OTFA. The heat maps in the first and third columns contain all the valid strides extracted from each of the six individuals with OTFA. The activity and time are normalized. Time is described as percentage of the gait cycle. Each row in the heat map is activity from an individual stride. The red square indicates the end of the stance for each of the strides. The second and fourth columns display the distribution of activity, at each normalized time point. The 95% HDRs are designated by the light blue regions. The solid blue line is the mean activity.

of the activation range (0−.8). During 20% and 40% of the gait cycle, the leg is supporting the body weight and the knee is kept relatively straight throughout this period. Therefore, the muscle activity is likely to be low for many strides with little variation since the knee experiences little change in angle or force. During 40% and 60% of the gait cycle, the lower limb begins preparation for push-off (∼50−60%) by propelling the body forward. Therefore, the muscles increase in activity to generate force to accelerate the limb and stabilize the knee. During the push-off when the heel is off the ground, the hamstrings activate to bend

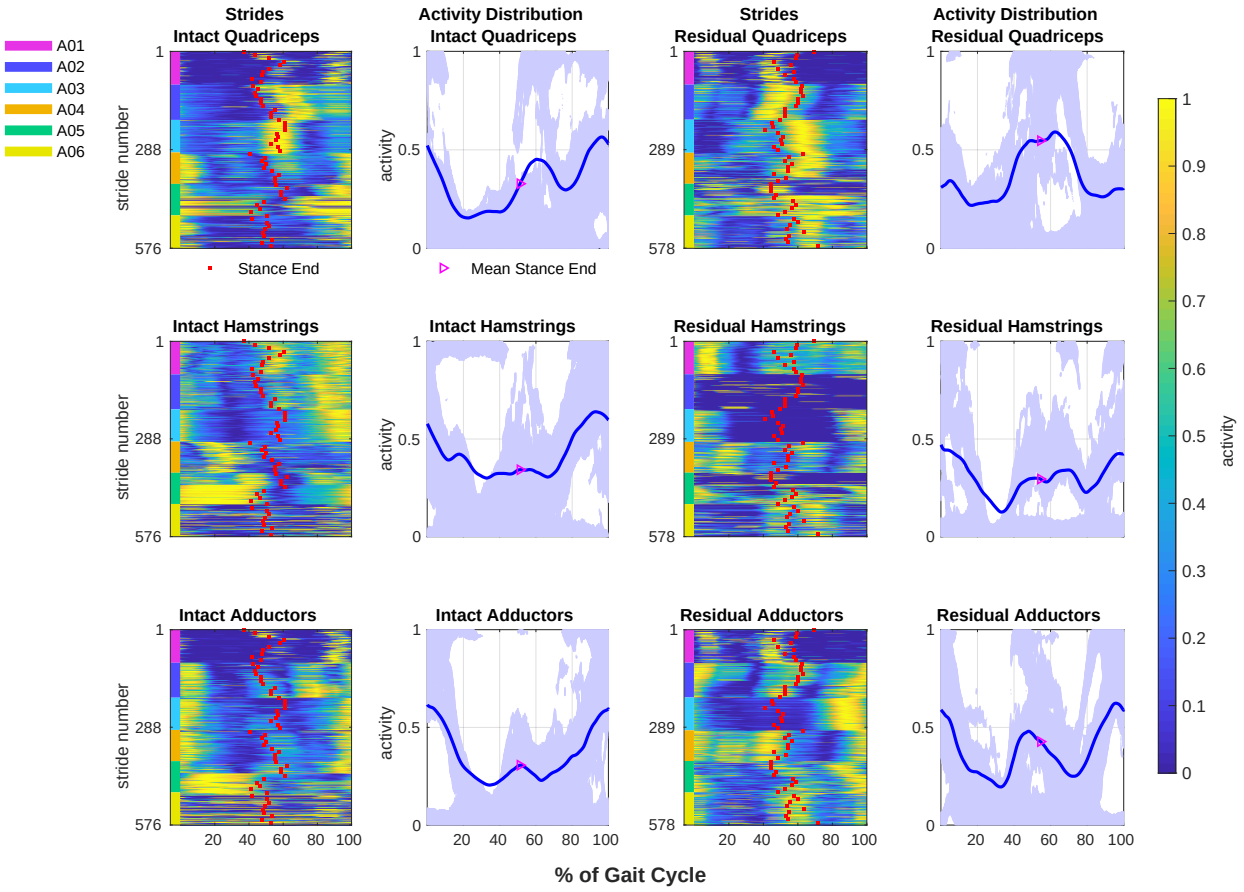


Figure 5.8: Brisk walking EMG activity, from one visit, for all participants with OTFA. Also see Figure 5.8 for details on the notations.

the knee, the quadriceps activate to control the amount of knee flexion, and the adductors activate to bring the limb slightly inwards for balance. Despite the missing knee joint in the residual limb, similar patterns of muscle behavior are observed between the two limbs. However, there is greater variation in the residual adductors than the intact adductors for both walking tasks. The residual adductors are also more likely to have higher activation than the intact adductors, indicated by the HDRs above .5 activity during 40% and 60% of the gait cycle. These differences might be due to the added weight and general difficulty of controlling the prosthesis and preparing to lift it into swing.

Between 60% and 80% (initial swing), muscles such as the residual quadriceps have two

modes of likely activation where both modes are missed by the mean EMG activation curve during that time frame. For example, the residual quadriceps during self-paced walking have two distinct recruitment strategies: one where the activity is near one and the muscles play a major role in controlling the swinging limb, and another where the muscles are used to a minor extent. However, the two strategies have similar likelihoods resulting in the mean curve missing both modes entirely.

During self-paced walking (Figure 5.7) for the end of stride (after 80%), all muscles except the intact hamstrings, have two major regions of likely activation. The intact hamstrings have one major region with small gaps in the activation range. Between 80−98%, it is unlikely for the intact hamstrings to be near zero activation. For both walking speeds, HDRs also increase in size and activation range during terminal swing (90−100%) for the intact quadriceps, hamstrings, and both adductors. This is consistent with the high variability in activation seen at the beginning of the stride where some muscles will often activate at varying levels towards the end of the stride to decelerate the limb in anticipation of the heel-strike and often remain active throughout the heel-strike. For some strides, the muscles will finish peaking prior to the heel-strike and remain inactive or have a low activation through the heel-strike.

Matched Intact Controls

The distribution of EMG activation patterns for the matched intact controls during the self-paced gait are seen in Figure 5.9 and brisk gait in Figure 5.10. For each muscle, it is most likely for the activity to be near zero during terminal stance (30−55%), with some exception for the left quadriceps for self-paced walking and both quadriceps for brisk walking. For the left quadriceps for self-paced walking, the upper bound of the likely activity (.4) is higher during terminal stance when compared to the other muscles during this time frame. For the right quadriceps during brisk walking, the period when the muscle is most likely to be near zero is during swing (∼75%). For the left quadriceps for brisk walking, the HDRs span most of the activity range, with some gaps, prior to 75% of the gait cycle, suggesting

a wide variety of strategies for this particular muscle and gait speed. In the corresponding heat maps, different participants activate the left quadriceps during brisk walking at varying times during stance. Participant H03 does not activate the left quadriceps after about 20% during the stance. The activation peaks for the left quadriceps are progressively shifting later in the stance, from participant H04 through to H09. Participant H02 activates the left quadriceps for a subset of the strides between 40% and 50%. The longest timeframe where it is unlikely for the left quadriceps to be near maximum activation is during the latter half of swing (75−100%). During this time frame, activation below .5 is most likely, indicating that for most strides, the left quadriceps often have a minor role when controlling the limb through the latter half of swing.

For self-paced walking (Figure 5.9), the time frame when the muscles have low activation is shifted to later within the gait cycle for the left limb, compared to the right. The left quadriceps are unlikely to have activation near 0 for a brief time period between approximately 15% and 22%. During this time frame the quadriceps activate to extend the knee to provide clearance for the contra-lateral limb to swing forward. For the hamstrings, there are two likely activation ranges during the first half of stance (0−30%). This is the time frame of weight acceptance when the limb transitions from initial contact to maximum knee flexion at the load response (∼10−12%) into single support on the limb (∼10−12). The two ranges indicate distinct strategies where the hamstrings are utilized by most participants for most strides, such as the right hamstrings by participant H09, while not utilized by other participants, such as the left hamstrings by H04.

During self-paced swing (60−100%), the hamstrings have three likely activation ranges, indicating three strategies which are seen in the corresponding heat maps. For example, one strategy involves the left hamstrings for participants H03 and H15, where activation peaks around 80% during the midswing when the knee flexion is maximal to bring the limb under the body and to start decelerating the limb. Another strategy involves participants H02 and H06, where minor activation peaks rise at varying times across the strides during the swing

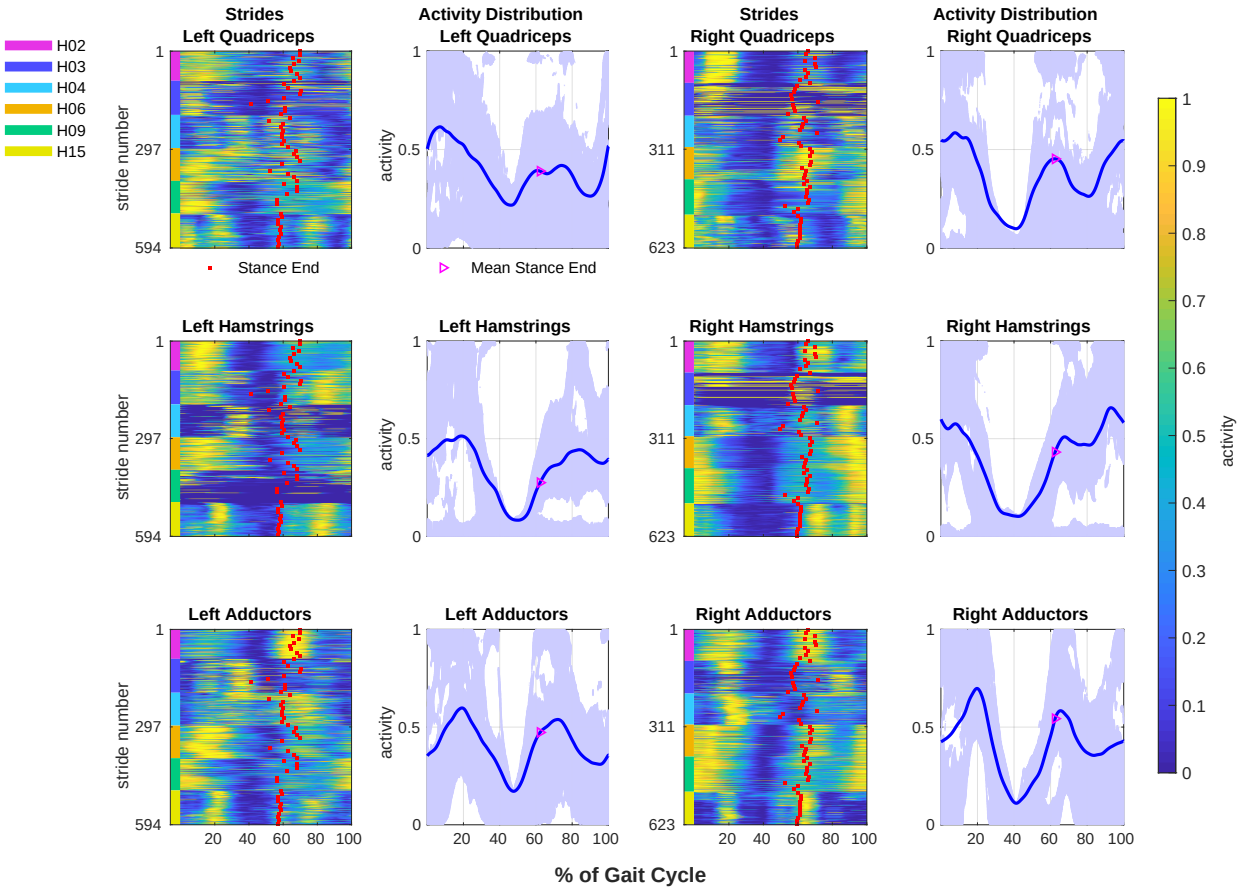


Figure 5.9: Self-paced EMG Activity from one visit, for all matched intact control participants. The heat maps contain all the valid strides extracted from each of the six matched controls. The activity and time are normalized. Time is described as percent of the gait cycle. Each row in the heat map is activity from an individual stride. The red squares indicate the end of the stance for each of the strides. The second and fourth columns display the distribution of activity, at each normalized time point. The 95% HDRs are designated by the light blue regions. The solid blue line is the mean activity. The shaded regions are the most likely activation.

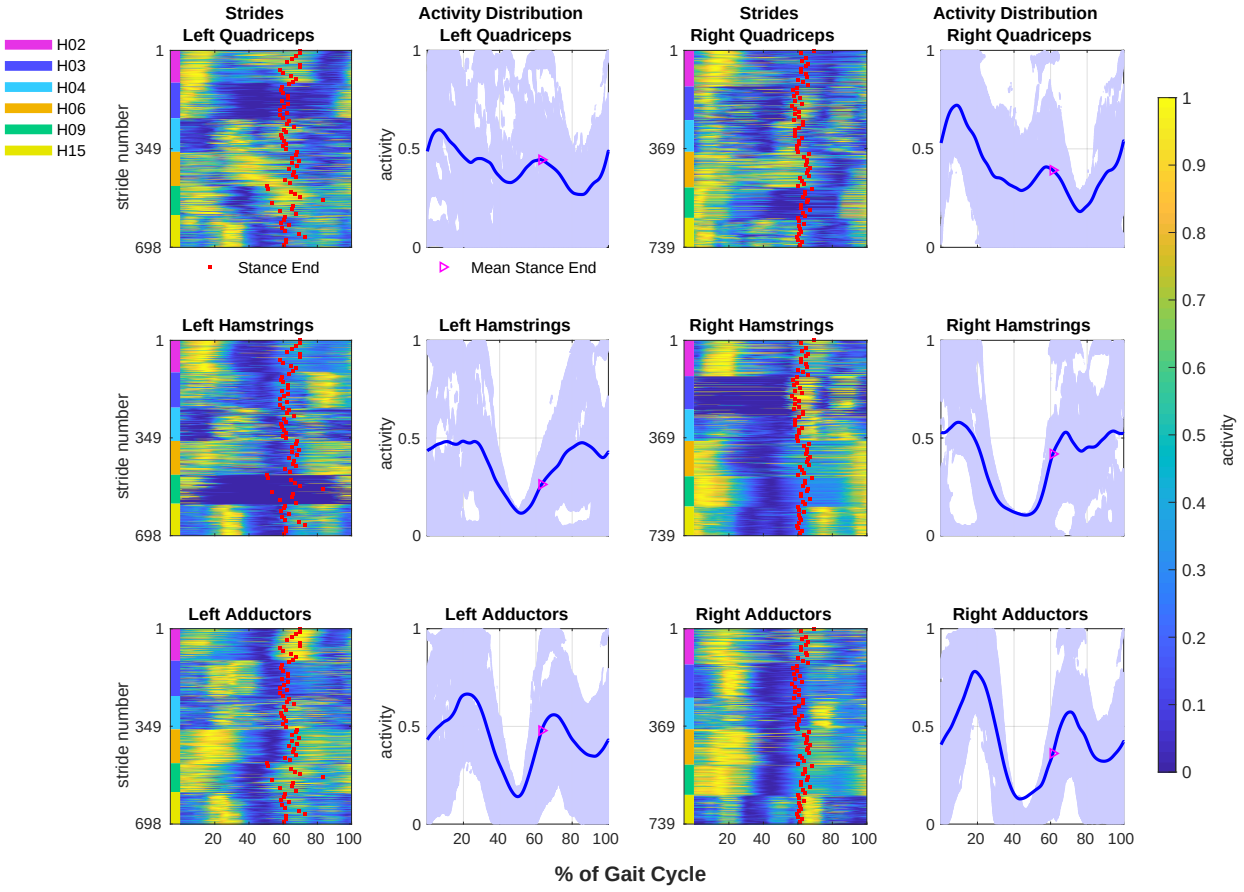


Figure 5.10: Brisk EMG Activity, from one visit, for all matched intact controls. The heat maps contain all the valid strides extracted from each of the six individuals without OTFA. Also see Figure 5.9 for details on the notation.

until the end of swing (about 95%) when major activation peaks consistently begin to rise into and through the heel-strike. This second strategy might be due to the individuals using the current momentum to continue the swing of the limb without much deceleration and mainly focusing on preparation for the heel-strike towards the end of the swing. The third strategy involves little to no activity of the hamstrings, such as for participants H04 and H09. It is possible this third pattern is the result of an issue with the sensor calibration, as little to no activity is observed throughout most of the gait for most of the strides for the left hamstrings for participants H04 and H09. This is an advantage of the HDRs over the mean and standard deviation as these potentially degenerate strides are distinguished from the others.

During self-paced walking for each of the adductors, there are two periods during the stride where it is unlikely for the muscle to have activation near zero. The left adductors are unlikely to be near zero in the ranges $\sim 12-30\%$ and $\sim 70-81\%$. The right adductors are unlikely to be near zero in the ranges $\sim 15-25\%$ and $\sim 65-70\%$. This suggests the adductors are usually active during and after the load response $(10-12\%)$ and likely to assist with balance by keeping the body centered during the transition from double support to single support and from early to midswing $(65-81\%)$ to keep the swinging limb towards the center of the body.

For both walking speeds, there are distinct periods during the stride when maximum muscle activity is likely for each muscle. Within all the muscle groups, activity near one is likely prior to 40% of the gait cycle. For all muscles (except right quadriceps during brisk walking), activation near one is likely during periods of swing. The adductors are likely to reach activity near one between $58-80\%$ and $90-100\%$. Activation near one is also likely to occur within the left hamstrings between $75-90\%$. For the right hamstrings during both walking tasks, and the right quadriceps for self-paced, activation near one is likely during most of the swing $(60-100\%)$. There is a brief period around 80%, where activation near one is unlikely for these muscles. For the left quadriceps, there are brief periods during swing

when it is likely for muscle activity to be near one. The most consistent muscle activation pattern across the strides is during the latter period of stance (40−60%) when it is unlikely for the majority of muscles to activate, except for the left quadriceps during brisk walking. In the heat maps this is a river of blue down the strides between 40% and 60%. The high likelihood of muscle deactivation is in part due to forces being produced by the hip and shin muscles (not recorded) for momentum instead. After this period of deactivation, the muscles increase in activation throughout the beginning of swing (60−80%) and peak at various times throughout the swing.

There is a high level of agreement between the HDRs of the two gait tasks. However, the quadriceps behave differently between the two tasks. For the left quadriceps during self-paced walking, activation above .7 is unlikely between 30−70% of the gait cycle, except for small regions around 35% and 60% where an activation of near one is likely. However, during brisk for the left quadriceps most of the activation range is likely between 30−70%. This is a result of the varying strategies for utilizing the left quadriceps across the participants. Different participants might use the quadriceps differently to propel the body forward and control the amount of knee flexion when pushing the limb off the ground into swing. For the right quadriceps in the time frame 0−20% for brisk walking, near zero activation is unlikely. At the faster gait speed, the quadriceps are likely activating to provide force to extend the knee and counter excessive knee flexion under the added forces at higher speeds during the weight acceptance phase (0−20%). Additionally, the upper bound on the HDRs is higher between 25−50% for brisk walking. This might be to continue to counter excess knee flexion as needed. During swing (60−100%), near activation maximum is unlike for brisk walking. The added momentum to the limb from walking at higher speeds might reduce the need for added forces from the quadriceps while swinging the limb. Additionally, other muscles at the hip and shin (not recorded) also play a role in the momentum of the swinging limb. The causes of asymmetry between the left and right quadriceps are not fully understood and might be impacted by limb dominance or morphological differences between the muscles (Sadeghi

et al., 2000).

5.4 Pressure and EMG Peak Timing

For gait data, characteristics at each time are influenced by the characteristics of the prior window of time, therefore, each time slice should not be treated independently. The distributions of the pressure and EMG data above describe the strides at each time slice as though they are independent, however, they are insufficient to completely characterizing gait. Additional analysis is required to further describe the pressure and muscle behavior relative to prior time samples. Therefore, after describing the patterns at each time slice during gait, I characterize the specific timing of the activation peaks. The peak identification procedure is detailed in Section 4.2. The peaks are defined as the largest signal value within a window of time and above a data-derived threshold. Once the peaks are identified, I can describe the stride behavior based on the distribution of peak times over the entire gait. The distributions of the peak times and the HDRs for the pressure and EMG are visualized using the violin plots in Figure 5.11. The violin plots are constructed using code based on functions by Jonas (2009).

5.4.1 Pressure Peak Times

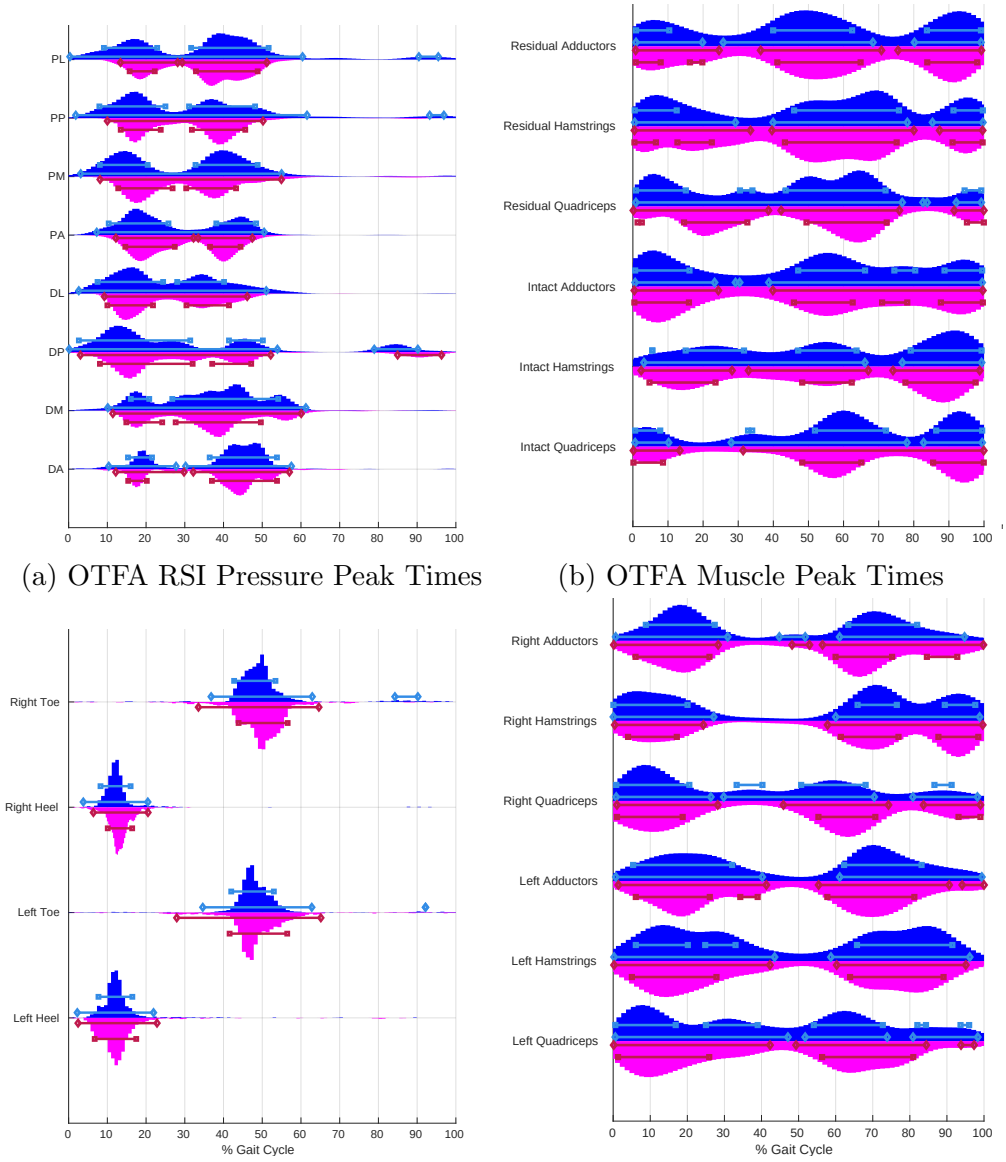
OTFA Cohort

The distributions of peak RSI pressure times for the strides from the individuals with OTFA at brisk (blue) and self-paced (magenta) walking speeds, are shown in Figure 5.11a. The HDRs with accumulated probabilities of 95% (diamond endpoints) and 75% (square endpoints) are depicted with horizontal bars drawn above (brisk) or below (self-paced) the line corresponding to the respective sensor. These distributions are multimodal, with the HDRs comprising multiple time segments. The 95% and 75% HDRs of RSI pressure peaks are predominately prior to 61% of the gait cycle, at all RSI locations. Additionally, RSI pressure peaks are

likely to occur between 90.5-95.5% at the PL location for brisk walking, 93.3-96.9% at the PP location for brisk walking, 78.9-90.2% at the DP location for brisk walking and 85.0-96.3% at the DP location for self-paced walking. The 95% HDRs are longer for brisk walking than self-paced, at all RSI locations. These time periods start later in the gait cycle for self-paced than brisk walking, and end earlier for self-paced. This suggests that maximum pressure within the residuum socket likely occurs later into the stance and for a shorter duration for self-paced walking compared to brisk.

During the stance phase (prior to 60% of the gait cycle) there are two periods, indicated by the 75% HDRs, at each socket location, when peaks are most likely to occur. These periods split the stance into two major intervals corresponding to weight acceptance (between $0-30\%$) and to push-off (between $30-60\%$). The period of time that peak pressures occur during early stance is shortest at the DM and DA locations, compared to the other locations. During push-off, the distribution of peak times at the DM location is the longest compared to other locations. The long HDRs during push-off at the DM location suggest greater variation in the timing of peak pressures at this location when attempting to generate force to accelerate the prosthetic limb off the ground.

Two-sample Kolmogorov-Smirnov (KS) tests are conducted for each pressure location to test the null hypothesis of whether the peak times for brisk and self-paced walking are from a distribution with the same shape. The $\alpha = 0.05$ was Šidák-corrected to account for multiple comparisons (Šidák, 1967). There are significant differences in the shape of the distributions of peak times between the two walking tasks for the RSI locations except for the DA location (Table 5.2a). Despite overlaps in the HDRs, there are differences in duration. Moreover, there are shifts in peak times where a corresponding region for one task might be earlier or later, compared to the other task. For example, at the PM location, the HDRs during early stance for self-paced walking start later than the regions for brisk walking. This indicates peaks are more likely to occur closer to the heel-strike during a brisk gait than a self-paced gait. Additionally, peaks during self-paced are likely to have a shorter duration



(a) OTFA RSI Pressure Peak Times (b) OTFA Muscle Peak Times

(c) Controls Foot Pressure Peak Times (d) Controls Muscle Peak Times

Figure 5.11: Distribution of peak times for RSI pressure (a) and EMG activity (b) from an OTFA cohort of six and foot pressure (c) and EMG activity (d) from six intact matched controls (from Figure 1 by Shotande et al., 2022). Horizontal bars indicate the highest density regions (HDRs) with accumulated probabilities of 95% (diamond endpoints) and 75% (square endpoints) for brisk (blue) and self-paced (red) walking. (a) Eight RSI pressure sensors are placed at the proximal (P) and distal (D) levels, at anterior (A), posterior (P), lateral (L), and medial (M) positions (see Figure 3.3 for the sensor placements).

before attenuating earlier during the stance. These are consistent with the higher variation in pressure at each time during brisk gait seen in Figure 5.4 when compared to self-paced gait in Figure 5.3.

Matched Intact Controls

The distributions of peak times for the foot pressure from the matched controls at both gait speeds, are shown in Figure 5.11c. Approximately 95% of pressure peaks at the heel occur between 2−22.9%. The HDRs for the peak times of the heel pressures are consistent with the activity distributions in Figures 5.5 and 5.6 where the HDRs containing one occur between 5% and 22%. However, the distributions of peak times (Figure 5.11c) are specific to when the peaks actually occur during the gait cycle. The pressure distributions (Figures 5.5 and 5.6) look at the pressure at each time independently. Approximately 95% of pressure peaks at the toe occur between 27.9−65.2% during the gait cycle. Additional toe pressure peaks with lower likelihoods within the 95% HDRs for brisk walking also occur during brief periods between $84.2 - 90.2\%$ for the right toe and $92.1 - 92.2\%$ for the left toe. The time period when the toe pressure (Figures 5.5 and 5.6) is most likely to be one is between 38% and 60%, which is a subset of the HDRs for the peak time distributions. Pressures $> .1$ are unlikely during swing when looking at the pressure distribution at each time independently. However, when focusing specifically on peaks over the entire gait, there are brief time periods during swing when toe pressure peaks are still likely to occur.

Results of the KS tests indicate there are significant differences in the shape of the distributions between the two walking speeds for the foot pressures (Table 5.3a). These results suggest there are distinct differences in likely muscle recruitment strategies between gait speeds that yield different foot pressure patterns. While the HDRs are similar, there are differences in duration and shifts in time where corresponding regions for one task might be earlier or later, compared to the other task. For instance, HDRs for the toe are longer relative to the normalized time for self-paced walking than for brisk walking. Additionally,

RSI Location	p-value
DA	0.15
DM	0.0010*
DP	6.0e-06*
DL	0.00013*
PA	4.5e-05*
PM	4.4e-08*
PP	6.3e-05*
PL	5.0e-06*

(a) RSI Pressure

Muscle	p-value
Intact Quadriceps	0.00043*
Intact Hamstrings	0.0019*
Intact Adductors	0.72
Residual Quadriceps	5.5e-08*
Residual Hamstrings	0.0056*
Residual Adductors	0.026

(b) Muscle Activation

Table 5.2: Results of the KS tests, for the individuals with OTFA, comparing the shape of the distributions of peak times between brisk and self-paced walking for each pressure location (a) and muscle group (b), from Table S1 by Shotande et al. (2022). (a) The $\alpha = 0.05$ is corrected to 0.0064 for the RSI pressures to account for multiple comparisons (Šidák, 1967). (b) The $\alpha = 0.05$ is corrected to 0.0085 in for the muscle activation. Statistically significant differences are indicated by the *.

toe pressure peaks are likely to occur after 84% (i.e., 92.1−92.2% and 84.2−90.2%) only for brisk walking. The wider HDRs for the toe pressure during self-paced indicate greater variability in the initiation time and duration of the push-off. This is greater variability in the self-paced foot pressures is consistent with the time slice HDRs from Figure 5.5 (self-paced) and 5.6 (brisk).

5.4.2 Muscle Activation Peak Times

OTFA Cohort

The distributions of peak times for the EMG activation from the participants with OTFA at both gait speeds are shown in Figure 5.11b. The 95% HDRs of peak times in the EMG activity are separated into two or three time segments depending on the muscle and gait task. For example, during brisk walking within the residual hamstrings, 95% of the most likely peaks occur during early stance (∼0.9−28.2%), terminal stance to midswing (∼39.3−78.8%), and terminal swing (∼85.9−99.1%). For the intact hamstrings during brisk walking, the 95% most likely peak times are throughout stance into early swing ($\sim 1.9 - 65.7\%$) and the latter

Foot Location	p-value
Left Heel	0.001843*
Left Toe	0.003233*
Right Heel	7.00E-17*
Right Toe	1.62E-06*

(a) Foot Pressure

Muscle	p-value
Left Quadriceps	0.0005250*
Left Hamstrings	0.001357*
Left Adductors	0.008107*
Right Quadriceps	1.53E-21*
Right Hamstrings	2.23E-06*
Right Adductors	0.0001259*

(b) Muscle Activation

Table 5.3: Results of the KS tests, for the matched controls, comparing the shape of the distribution of peak times between brisk and self-paced walking for each pressure location (a) and muscle group (b). (a) The $\alpha = 0.05$ is corrected to 0.013 for the foot pressures, to account for multiple comparisons (Šidák, 1967) of the foot pressures. (b) The $\alpha = 0.05$ is corrected to 0.0085 for the muscle activation. Statistically significant differences are indicated by the *.

half of swing ($\sim$77.8$-$99.1%). The 75% HDRs of peak times for the EMG activity are separated into three to four time segments. For all muscles and tasks, peaks are most likely to occur throughout load response ($\sim$10% of the gait cycle), pre-swing ($\sim$55$-$60%), and terminal swing ($\sim$90$-$100%). During load response, the full weight of the body is transferred onto the standing limb as the contralateral limb is now in swing (Kharb et al., 2011). During pre-swing, the limb is in the process of generating forces necessary to lift the ipsilateral limb into swing. In the terminal swing phase, the limb is anticipating heel-strike and decelerating the limb. Each of these periods involves a transition for the limb in terms of accepting forces or producing forces to change momentum. There are also shorter time segments only during early stance, such as for the residual adductors for self-paced ($\sim$17.1$-$19.1%), or only during mid-swing, such as for the intact adductors for the brisk walking task ($\sim$73.8$-$80.9%). The adductors activate to pull the limb inwards. During early stance the residual adductors might be activating to maintain balance as weight has being transferred onto the standing limb and the contralateral limb is swinging. During mid-swing the swinging limb is opposite the standing limb, the intact adductors might be puling the limb in closer under the body for better balance and control during this time. For the OTFA cohort, the 95% HDRs are wide

often extending throughout most of the stance and swing for both tasks. This indicates high variability in muscle activation strategies among the cohort.

According to the results of the KS tests, there are significant differences in the shape of the distributions between the two walking speeds, for the EMG muscle groups (Table 5.2b) indicating differences in likely muscle recruitment strategies between the gait tasks. Despite similar patterns between tasks, the HDRs do not start and end at the same times. For instance, the 75% HDR near the start of push-off (around 50%) for brisk walking with the intact quadriceps, occurs earlier for self-paced than brisk walking. This period is typically where the quadriceps activate to absorb energy and provide minor knee extension to control the amount of knee flexion during the push-off (Winter, 1987). The push-off might be more likely to begin earlier during gait for self-paced walking than brisk walking.

Intact Matched Controls

The distributions of peak times for the EMG activation from the matched controls are shown in Figure 5.11d. The HDRs of peak times in the EMG activity occur during two time segments designated by two 95% HDRs for each muscle during both gait tasks. These segments are divided into sub-intervals by the 75% HDRs. During early stance, the 95% HDRs for the right limb muscles are $0-30.9\%$ and the 75% HDRs range is $0-27.4\%$. This indicates the muscles are most likely to reach peak activation at various times during the initial weight acceptance (0%), into the transfer of the full body weight onto the limb for single support ($\sim 10-12\%$), and into midstance when the body center of mass is over the standing limb ($\sim 30\%$). There is an additional 75% HDR for the right quadriceps for brisk walking from 33.3% to 40.3%. This is during the time frame the limb reaches maximum extension driven by the quadriceps and then begins preparation to continue moving the body forward. The quadriceps might be activating to control the amount of knee flexion after transitioning from maximum extension.

During early stance for the left limb, the 95% HDRs are longer, $0-47.1\%$ compared to the right limb. The corresponding 75% HDRs are within the range $0-39.0\%$. For the hamstrings

and quadriceps for brisk, and the adductors for self-paced, there are two modes of likely peak times during stance indicated by the 75% HDRs. The first mode is around the load response ($\sim$10$-$12%) where the greatest forces are experienced during early stance and begins the single support for the left limb (Alamdari & Krovi, 2017). The quadriceps and hamstrings might co-activate more during this time to stabilize the limb. The hamstrings activate to absorb most of the force from the load by flexing the knee. The quadriceps might activate to control the amount of knee flexion to prevent the limb from collapsing under the weight. The 95% HDRs end later for the left limb than for the right limb. The shorter HDRs for the right limb compared to the left limb indicate more consistent muscle activation strategies for the right limb during stance. This asymmetry might be related to a combination of factors such as limb dominance, morphological differences between the limbs, and differences in neurological processing. Additionally, the individuals rounding covers during the study might also have an impact (Akiyama et al., 2018).

In the time frame 60$-$100% (swing), there is one 95% HDR for both tasks for both hamstrings and right adductors muscle groups. Additionally, there is one 95% HDR for the left adductors for brisk walking. Muscle groups with two 95% HDRs during swing, have an early interval that extends throughout half or more of the swing, and starts either during pre-swing prior to the toe-off (55$-$60%) or initial swing just after the toe-off (60$-$75%), except the right quadriceps for brisk walking, where the interval begins at 29.9% (mid-stance) and extends into the swing, ending at 71.1%. The second interval starts after 80% (mid-swing) after the knee is typically at maximum flexion, such as with the right quadriceps, or after 90% with the left adductors during self-paced gait. For all the muscles, peak activity is likely more than half of the swing. This might be partly due to generating necessary forces to control the speed of the swinging the limb. During swing, the limb has to lift into the air, change its trajectory mid-swing, and prepare for the impact of the next heel-strike.

The result of the KS tests indicate significant differences in the shape of the distributions between walking speeds for the EMG muscle groups (Table 5.3b). The HDRs differ in

duration and some do not overlap between gait speed, such as the right quadriceps during mid-stance between 30−40% during which there are 95% and 75% HDRs for brisk, that are not present for self-paced. During this time frame the heel is accelerating. The greater forces necessary for acceleration during brisk walking might result in the right quadriceps activating more often.

5.5 Co-activation of Muscle Groups

Co-contraction is a useful metric to monitor factors such as disease progression, limb stabilization and joint function (Damiano, 1993; Hodges et al., 2015; Schmitt & Rudolph, 2008). To properly understand co-contraction, we cannot compare the aggregate muscle activity distributions or the aggregate distributions of peak times, which is typical performed in analyses on amputee gait. Rather, we need to first identify and match the peak activations within individual strides, and then examine the distribution of matched peaks. In this section, I demonstrate a unique perspective of co-contraction by defining co-contraction based on the matched peak activation times within the strides. Then, I compute the distribution over the co-activation times and examine them using my approach described in Chapter 4.5.

5.5.1 OTFA Cohort

Co-activation Peak Times

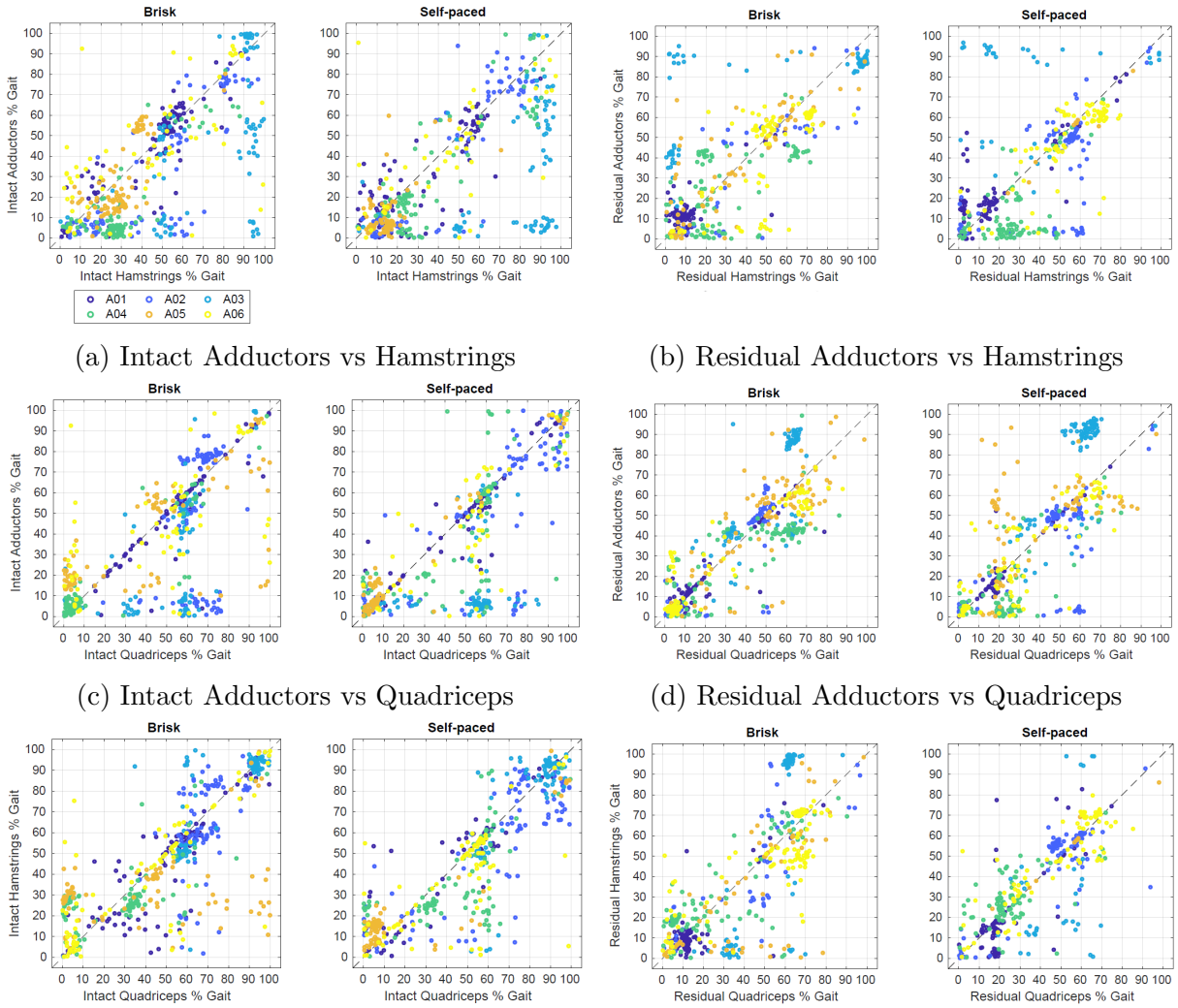
Once the peak activation times have been determined and the distributions of individual peak times described, we can match peaks between pairs of muscles within strides to identify co-contraction. The comparisons of peak times between each pair of muscles within a given limb for each stride from all OTFA participants and both gait tasks are shown in Figure 5.12. A single point corresponds to the peak activation time for a pair of muscles in a single stride. Points are determined by matching the closet peaks in time between two muscles within the same limb, during the same stride. Therefore, all the peaks presented in Figure 5.11 are not

necessarily within Figure 5.12. Points along the diagonal indicate the co-occurrence of muscle peaks and suggest co-contraction between the muscles. It is possible that two peaks from one muscle might be closest to the same peak within another muscle; these cases result in horizontal or vertical clusters. Time zero is the heel-strike of the corresponding limb. Points from different participants are indicated by different colors. Dense clusters of co-activation occur around heel-strike (0%) and toe-off (60%) for all pairs of muscles, within both limbs.

Compact clusters of points indicate consistent activation patterns. For all pairs of intact muscles, co-activation clusters spread throughout stance and swing suggesting an inconsistent role of the intact muscles across the strides. For the residual limb, clusters spread prior to 80%, except the clusters for one of the individuals (A03) prior to heel-strike. Terminal swing clusters for A03 within the residual muscles are typically off-diagonal, except for the residual adductor-hamstring peaks. Points that are far off the diagonal indicate paired muscle activity that occurred at distinctly different times during gait and each muscle likely contributes to momentum by generating a uni-directional force (Darainy & Ostry, 2008) as opposed to stability or control. For participant A03, the residual quadriceps often activate around 60% during both tasks independent of the other two muscles. This could be evidence of a strategy A03 consistently implements to propel the prosthesis forward into swing.

Distribution of Co-activation Peak Times

The density of peak times between pairs of residuum muscles from all OTFA participants for brisk (left) and self-paced (right) walking are seen in Figures 5.13b, 5.13d, and 5.13f. The corresponding data points within the distributions are seen in Figure 5.12. The HDRs for 75% (red) and 95% (orange and red), are the most likely time periods for peak activation between muscles to be matched. Regions shaded in magenta have likelihoods equal to the 95% HDR threshold, f_{α_1}. The white cross indicates the mode of the distribution of the stance duration (Figure A1). The HDRs near or along the diagonal are the most likely co-contraction times and occur prior to 80% of the gait cycle, with the subregions $0-30\%$ and $40-80\%$. The



(a) Intact Adductors vs Hamstrings

(b) Residual Adductors vs Hamstrings

(c) Intact Adductors vs Quadriceps

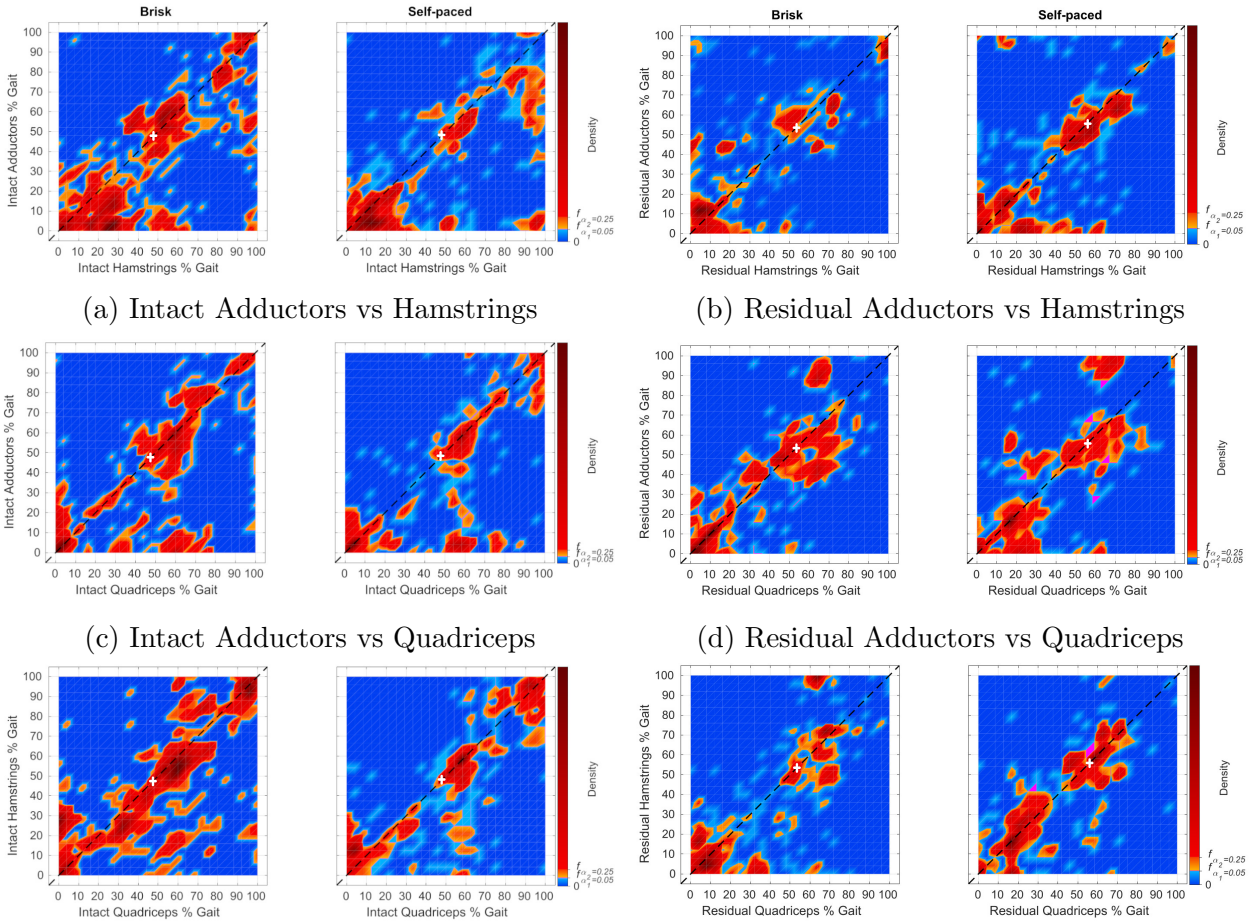
(d) Residual Adductors vs Quadriceps

(e) Intact Hamstrings vs Quadriceps

(f) Residual Hamstrings vs Quadriceps

Figure 5.12: Comparison of peak muscle activation times within each stride from one visit for six OTFA participants and both gait tasks. Time zero corresponds to heel-strike of the corresponding limb. Muscle activation peak times for the adductors compared with the hamstrings, the adductors compared with the quadriceps and the hamstrings compared with the quadriceps within the intact and residual limbs for brisk and self-paced walking. Left two columns are for the intact limb; right two columns are for the residual limb. Different subjects are indicated by different colors. The diagonal line indicates points where peaks in the EMG of one muscle (e.g., hamstrings) and another muscle (e.g., quadriceps) occur simultaneously within the same stride, suggesting co-contraction. Points around the start and end of the stride can be considered a part of the same time cluster.

subregion 0−30% corresponds to weight acceptance and ends at mid-stance when the center of mass of the body is over the standing limb. There is no knee to stabilize for the residual limb.



(a) Intact Adductors vs Hamstrings

(b) Residual Adductors vs Hamstrings

(c) Intact Adductors vs Quadriceps

(d) Residual Adductors vs Quadriceps

(e) Intact Hamstrings vs Quadriceps

(f) Residual Hamstrings vs Quadriceps

Figure 5.13: Distributions of matched muscle peak activation times between the adductors, hamstrings, and quadriceps muscle groups from six individuals with OTFA for the intact (a, c, and e) and residual (b, d, anf f) limbs. Individual points can be found in Figure 5.12. Time zero corresponds to heel-strike of the corresponding limb. Pairings that occur near or along the diagonal indicate co-contraction between muscle groups. The white cross indicates the mode of the distribution of the stance duration. Distributions of the stance duration are in Figure A1. The sub-figures depict the relative frequency of peak pairing times that occur during the gait cycle. Orange and red are within the 95% HDR. Red indicates points within the 75% HDR. Magenta are points with density equal to the 95% HDR threshold, f_{α_1}. For the intact limb, HDRs along the diagonal span most of the gait cycle.

However, the distal muscles are still co-activating, likely to manage control of the prosthesis while the residuum is bearing weight within the socket. The subregion $40-80\%$ corresponds to terminal stance until mid-swing. During the terminal stance, the limb is preparing for the beginning of the push-off (50%). During the initial swing, the muscles are managing

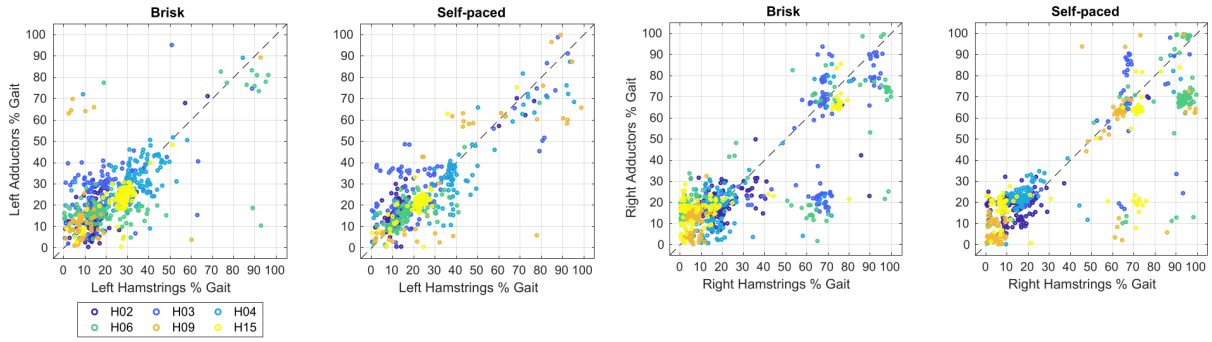
the velocity of the leg. Normally the knee would be flexed prior to mid-swing to obtain clearance under the body for the swinging limb. However, bending the knee is not possible with the residual limb. Therefore, the residual limb has to identify a strategy to control of the prosthesis and typically activates all three muscle groups simultaneously. For residual adductors-hamstrings at both speeds (Figure 5.13b) and the residual adductors-quadriceps at the self-paced speed (Figure 5.13d), there is also an HDR on the diagonal after 90% of the gait cycle. Late swing co-activity can be considered part of the cluster at the heel-strike, as peaks during the end of swing often continue into the start of the next stride. The off diagonal HDRs are not co-contraction and contribute to momentum of the leg and not its stability.

The density of co-contraction times for the intact limb muscles are in Figures 5.13a, 5.13c, and 5.13e. The HDRs for the intact muscles near or along the diagonal extend throughout the entire gait cycle, with small gaps (less than 10% in width). This indicates high inconsistencies in the use of these muscles. The intact muscles might be co-activating often to assist with managing control of the prosthesis.

5.5.2 Matched Intact Controls

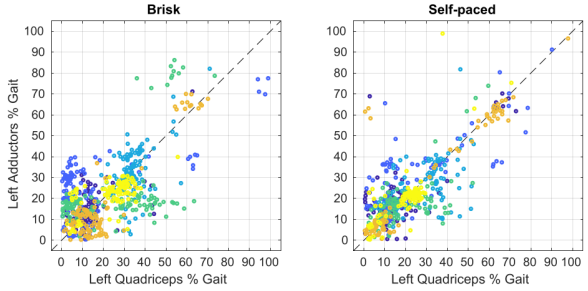
Co-activation Peak Times

Comparisons of peak times between each pair of muscles within a given limb for each stride, from the matched control participants, and both gait tasks, are shown in Figure 5.14. For all muscle pairings, there is a large cluster along the diagonal containing strides from all the control participants during most of the stance. There are much smaller groups of points scattered during the swing for the left limb. For the right limb, there are smaller compact clusters along the diagonal during swing that contain strides from a subset of participants. The clusters during stance, are spread farther along the diagonal for the left limb than the right. We can better understand the bounds of these clusters by examining the HDRs in the

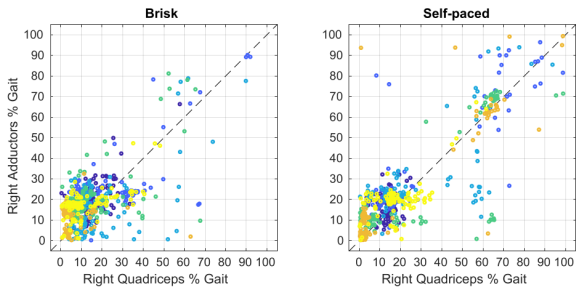


(a) Left Adductors vs Hamstrings

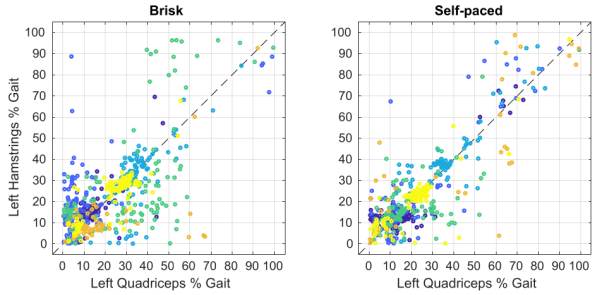
(b) Right Adductors vs Hamstrings



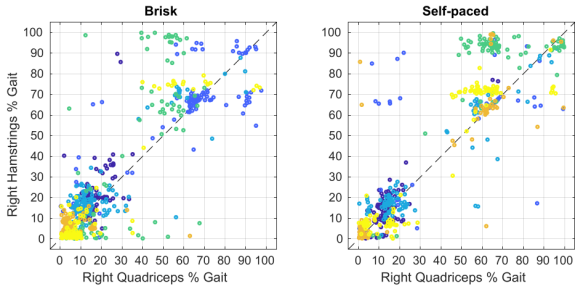
(c) Left Adductors vs Quadriceps



(d) Right Adductors vs Quadriceps



(e) Left Hamstrings vs Quadriceps



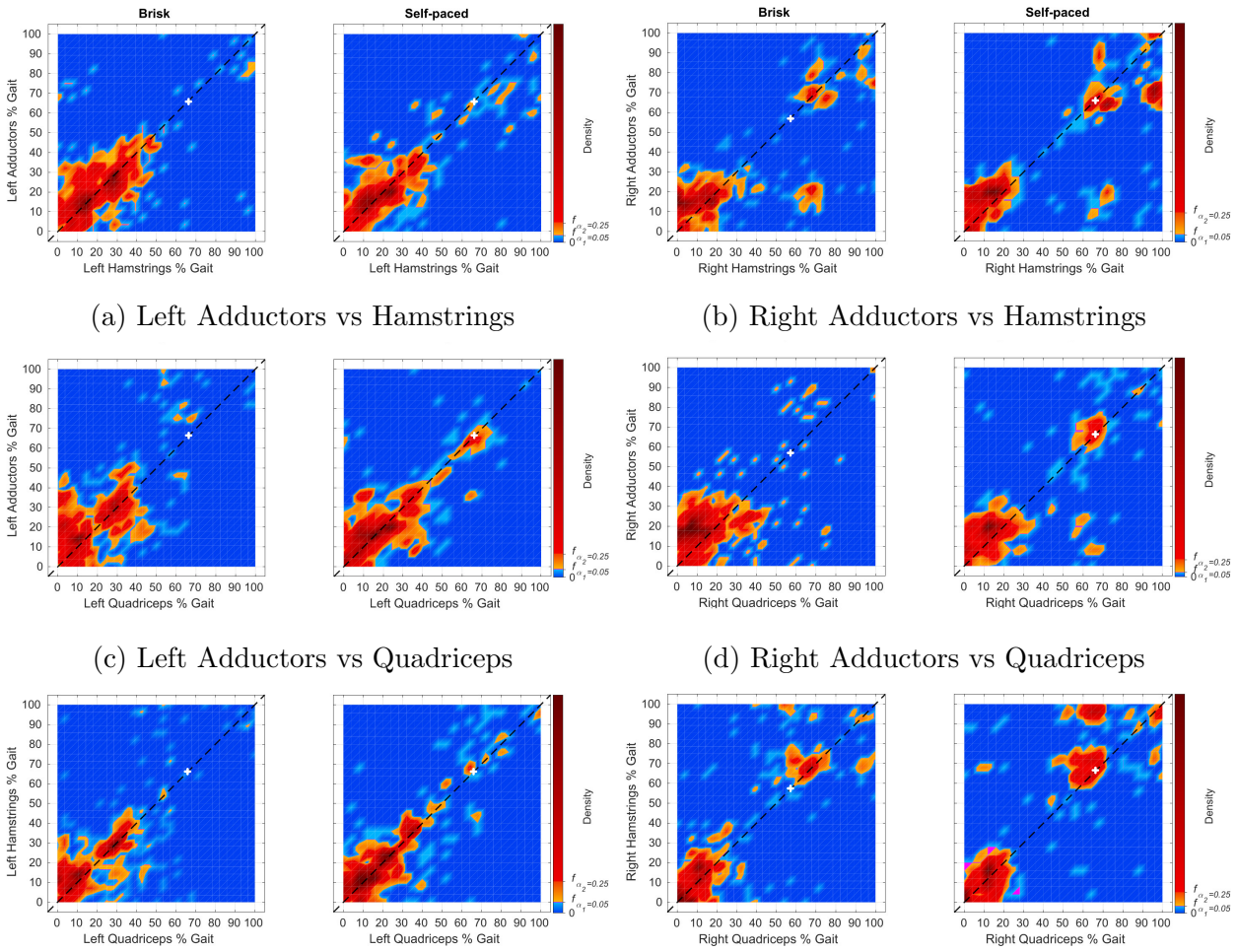
(f) Right Hamstrings vs Quadriceps

Figure 5.14: Matched peaks from strides for the intact matched controls. Each point corresponds to a single stride. Time zero corresponds to heel-strike of the corresponding limb. Colors indicate a specific subject. Points along the diagonal indicate co-activation of the muscle pair.

following sections.

Distribution of Co-activation Peak Times

For the matched controls, the density of peak activation times between pairs of muscles for each limb are shown in Figure 5.15. The corresponding data points within the distributions are seen in Figure 5.14. Large HDRs for co-contraction are during stance (prior to 60%) for all muscle pairs within the left (Figures 5.15a, 5.15c, and 5.15e) and right (Figures 5.15b,



(a) Left Adductors vs Hamstrings

(b) Right Adductors vs Hamstrings

(c) Left Adductors vs Quadriceps

(d) Right Adductors vs Quadriceps

(e) Left Hamstrings vs Quadriceps

(f) Right Hamstrings vs Quadriceps

Figure 5.15: Distributions of matched muscle peak activation times between adductors, hamstrings, and quadriceps muscle groups, from six matched controls for the left (a, c, and e) and right (b, d, and f) limbs. Individual points can be found in Figure 5.14. Time zero corresponds to heel-strike of the corresponding limb. Pairings that occur near or along the diagonal indicate co-contraction between muscle groups. The white cross indicates the mode of the distribution of the stance duration. The sub-figures depict the densities of peak pairings during the gait cycle. Orange and red indicate periods within the 95% HDR. Red indicates points within the 75% HDR. Magenta are time points with density equal to the 95% HDR threshold, f_{α_1}.

5.15d, and 5.15f) limbs of the matched controls. For the right limb, HDRs along the diagonal prior to 60% are shorter than those within the left limb. For the right limb the diagonal HDRs are between 0% and 35% of the gait cycle. This indicates the time of co-activation during stance has more variation within the left limb.

Additionally, there are periods within the 95% and 75% HDRs after 60% along the diagonal,

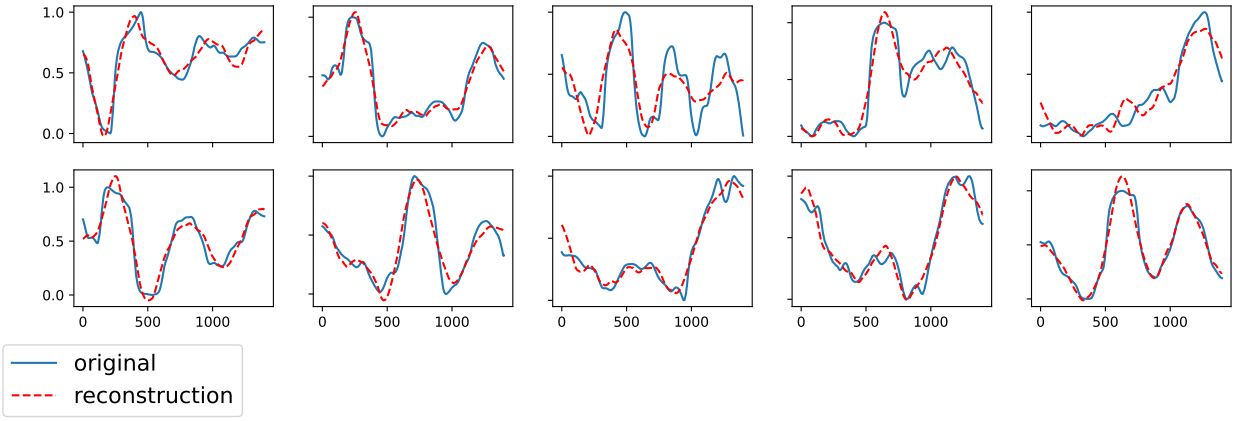
within the right limb. Small HDRs also occur during swing for self-paced walking within the left limb for adductors-hamstrings, adductors-quadriceps, and hamstrings-quadriceps pairings and during brisk walking for adductors-hamstrings pairings. These co-activation peaks occur during early or mid-swing and might be due to control of the trajectory of the swinging limb.

5.6 Gait Phenotypes

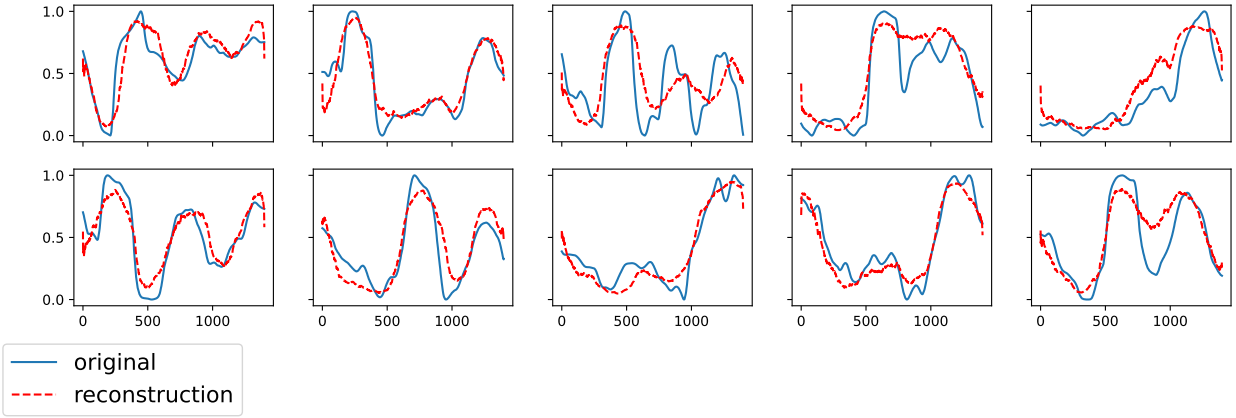
After obtaining an understanding of the overall gait patterns, it is useful to further quantify and automate the extraction of the distinct types of muscle recruitment behaviors or phenotypes. The data are compressed to remove redundant or noisy features and to speed up the extraction procedure. All six muscles from both limbs are used to generate the compressed features. Additionally, strides from both gait tasks are used to train the compression models. Each of the extracted phenotypes are characterized and compared using the general approach seen above and detailed in Chapter 4.

5.6.1 Evaluation of Gait Reconstruction

Examples of the reconstruction quality for PCA (a) and the AE (b) models are shown using activity of the adductors from ten strides from the validation set in Figure 5.16. For PCA, the best number of components is 50 with an average validation FVAF ≈ 0.923. For the AE, the best number of latent components discovered is 98 with an average validation FVAF ≈ 0.937. A compact diagram of the AE architecture model is shown in Figure 5.17. The full architecture diagram is in the Appendix in Figure A2. The AE model has 11 overall layers. The encoder and decoder subnetworks each have five layers not including the latent layer. I use the exponential linear unit (ELU) activation function t each node except for the output layer. The sigmoid activation function is used for the output layer to reconstruct the output within the standardized activation range. The models using the ELU activation function performed better than the models that used a linear activation function on the output layer.



(a) PCA Reconstruction



(b) AE Reconstruction

Figure 5.16: Training set reconstruction of EMG from the PC and AE latent spaces.

Table 5.4 contains the average reconstruction RMSE and FVAF. Both models did well reconstructing the general shape of the data and is evidence for the compressed representations capturing relevant features of the gait activity. Occasionally the reconstructions miss exact extrema (i.e., peaks or valleys), especially when the extrema are relatively close together in time, or where there are small bumps close together in time. An example of these are seen after time sample 1000 in the third column.

	PCA	AE
train	0.069	0.074
val	0.088	0.081
test	0.089	0.088

(a) Average RMSE

	PCA	AE
train	0.956	0.948
val	0.923	0.937
test	0.923	0.923

(b) Average FVAF

Table 5.4: Reconstruction performance based on average RMSE and FVAF.

5.6.2 Extracted Top Level Phenotypes

Clustering is performed at two levels. The top level clusters are in Figure 5.18 with the corresponding 95% HDRs in Figure 5.19. For PCA (Figure 5.18a), the number of clusters at the top level is three. For the AE (Figure 5.18b), the number of clusters at the top level is two. Each row of heat maps is for a distinct cluster. Each column of heat maps is for a particular muscle. Muscles for the left and intact limb are in the left three columns for the left. Muscles for the residual and right limb are in the right three columns for the cluster. To the left of each individual heat map is the indicator of the participant group the stride is from, with red indicating the control group and blue indicating the OTFA group. To the right of each heat map is the indicator of the gait task the stride comes from, with orange being for brisk and magenta for self-paced. The percent of the gait cycle is relative to the residual or right limb. Consecutive strides from the same participant are contiguous. Horizontal shifts moving down the strides within a heat map indicate transitions between either participants, participant groups, or gait tasks.

General similarities are seen between the muscles within the clusters. For example, the intact/left hamstrings in cluster C0 for PCA (Figures 5.18a and 5.19a). This particular cluster has no strides from individuals with OTFA suggesting a gait strategy only utilized by the matched intact controls. For the majority of the strides, the left hamstrings are peaking between 30% and 40% (mid-stance to terminal stance of the right limb) and then remain relatively active until terminal swing of the right limb after approximately 90%. During the start of this time frame (30%), the left limb is swinging and passes the standing right limb.

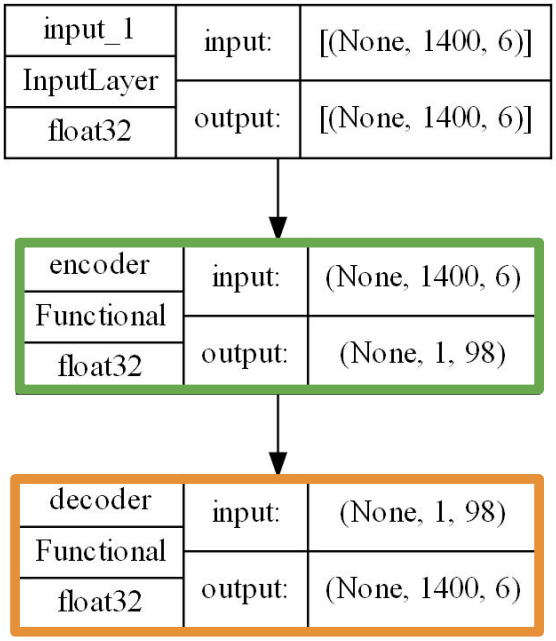
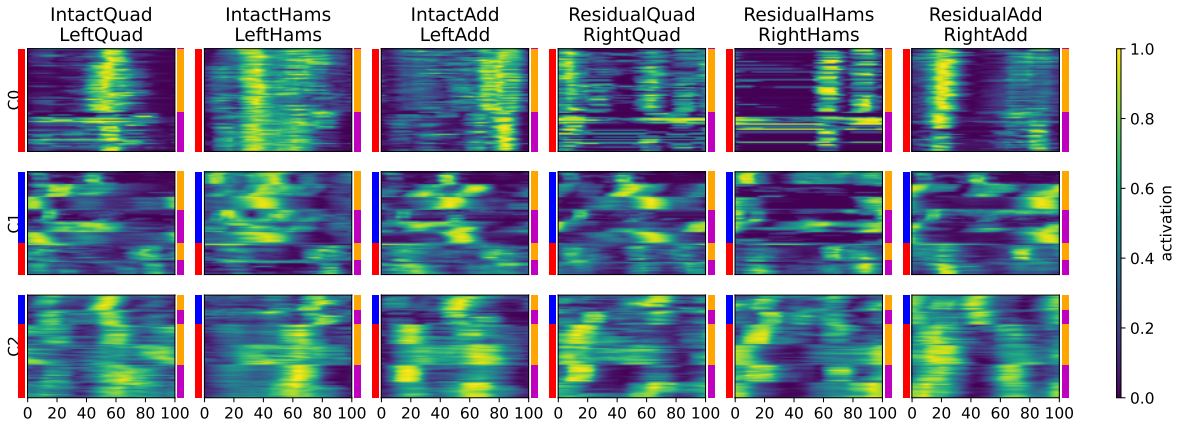
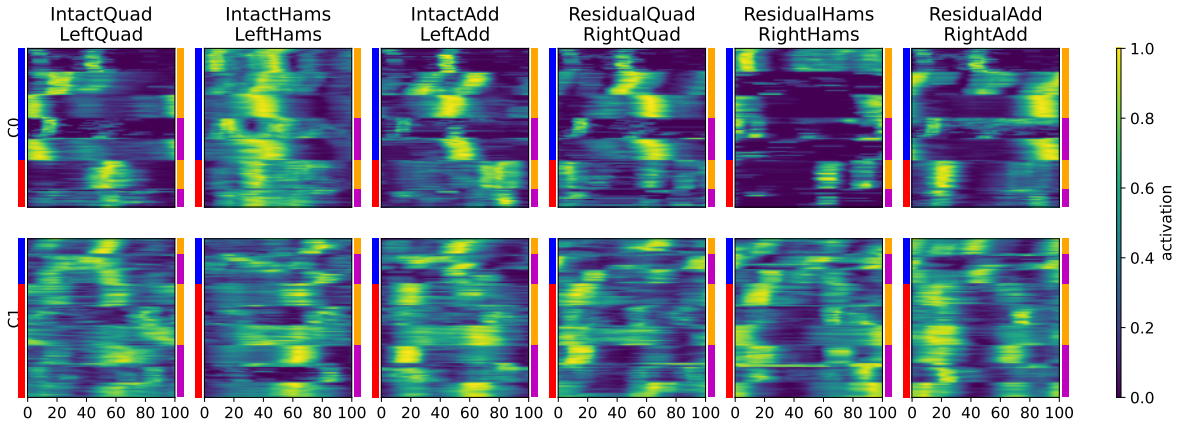


Figure 5.17: The high-level architecture for the trained AE model, consisting of the input layer, the encoder subnetwork (orange) and the decoder subnetwork (green). A single data input instance has 1400 time slices and 6 EMG channels. The encoder outputs the compressed representation as a 1D array with 98 features. The output of the decoder is the data reconstruction that is the same size as the original input. The full architecture design is in the Appendix.

The left hamstrings are likely flexing the knee to provide clearance under the body. During this time within the right limb, it is unlikely for the right hamstrings to activate and there is high variability in the activity of the right adductors and quadriceps. This suggests the roles of the right adductors and quadriceps during this time might be optional coming out of mid-stance. Additionally, the HDRs for the right adductors and quadriceps are decreasing in size and the upper bound is also decreasing after about 35%. Activity is also unlikely for the right adductors and quadriceps between $\sim$40$-$60%, indicating they are unlikely to be used or play a minor in propelling the body forward when using this particular muscle recruitment strategy. Closer to 90% of the gait with the right limb, the left limb is coming from terminal stance and transitioning into push-off. During this time the left hamstrings are most likely to have activation near zero. Within the right limb, the entire activation range is likely for the adductors and quadriceps indicating they have an inconsistent and potentially optional



(a) PCA Top Level Cluster

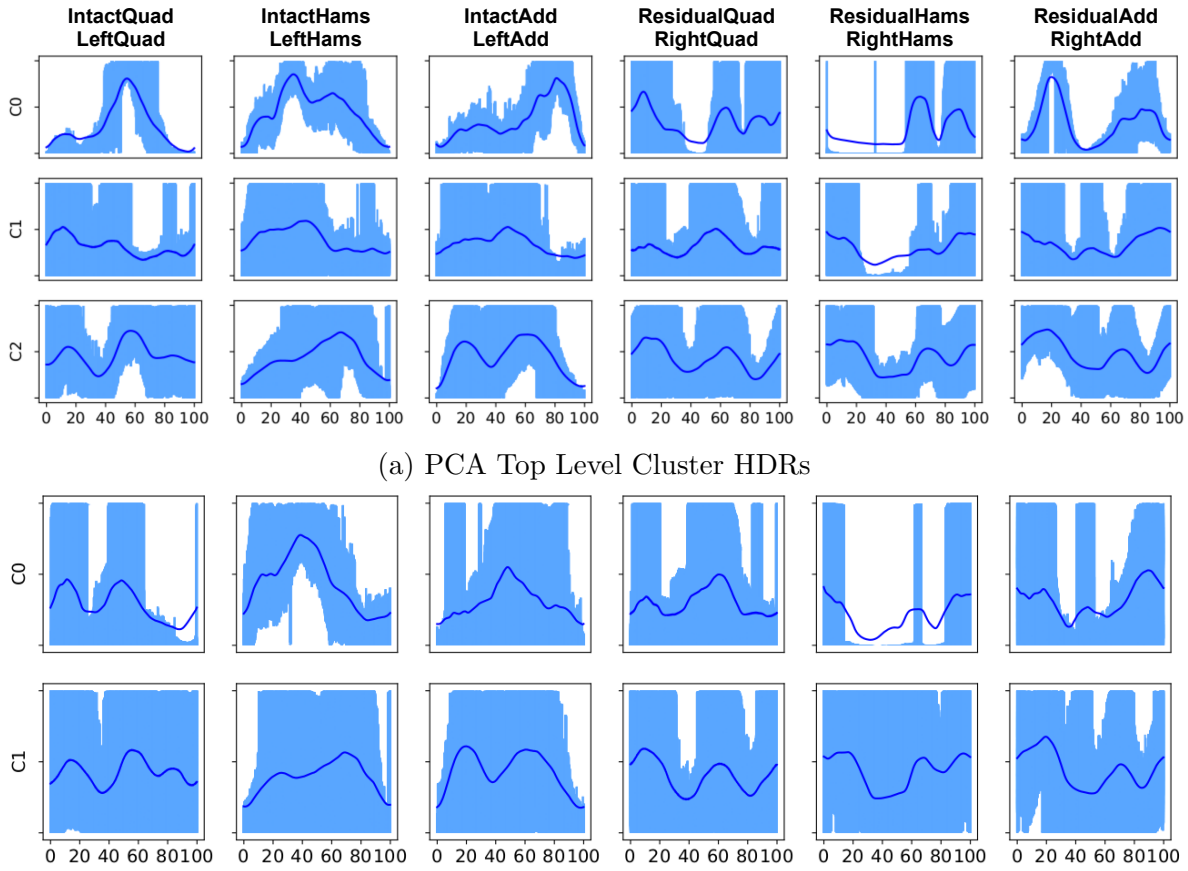


(b) AE Top Level Cluster

Figure 5.18: Top level clustering on the training set in the PC and AE latent spaces.

role during this time.

The different clusters have distinct HDRs indicating they identify differing muscle recruitment strategies. For example, in cluster C0 for the AE (Figure 5.18b and 5.19b), the residual/right hamstrings are unlikely to activate 20% and 40%, indicating these muscles are not utilized during this time with this particular recruitment strategy. However, in cluster C1 for the AE, the muscles are likely to have any activation during this time, suggesting multiple roles are performed with these muscles over the strides using this second strategy. The time frame 20−40% is centered around mid-stance (30%), where the residual/right limb is extended and the body's center of mass (COM) is directly over the standing right limb



(a) PCA Top Level Cluster HDRs

(b) AE Top Level Cluster HDRs

Figure 5.19: 95% HDRs for the top level clustering on the training set in the PC and AE latent spaces.

and the COM is at its highest. For the first strategy (C0), the residual/right hamstrings are not needed. The major activity is to extend the limb, which is predominantly done by the quadriceps. In the second strategy (C1), sometimes the residual/right hamstrings are used, likely to stabilize the knee by co-contracting with the quadriceps to prevent over extension.

Cluster C1 constructed from in the PC space contains many of the same OTFA strides as cluster C0 constructed in the AE latent space. This is evidenced by the peak activity prior to 20% within the intact/left quadriceps, in addition to, the peak activity around 30% within the intact/left hamstrings. A partial overlap between the clusters suggests the different types of strategies identified have common characteristics. Specifically, the intact/left hamstrings

activity around 30% is more consistent across the strides in cluster C0 from the AE, than in cluster C1 from the PC features. From the HDRs of these clusters (Figure 5.19), the intact/left hamstrings are unlikely to have activation near between 20% and 60% of the gait cycle for both strategies. However, for cluster C1 for PCA in Figure 5.19a, zero activation is also likely, which is unlikely in C0 for the AE in Figure 5.19b.

Despite the overall similarities observed for each muscle, it is unclear exactly how each pair of muscles is cooperating together at each time within the individual strides. Therefore, to better understand the relationship between the muscles within a cluster, co-contraction is described using the distribution of co-activation peaks between the muscle pairs within each cluster.

5.6.3 Extracted Top Level Phenotypes Co-contraction

The distribution of the co-activation times for the top level clustering, using the PC features, on the training set are shown in Figure 5.20. The HDRs are for 95% and 50% most likely paired peak activities and are shown for each cohort assigned to the cluster, as well as, the overall distribution (purple) for all the muscle pairs within the cluster. Every three rows are for a single cluster. The blue distributions are for the strides from individuals with OTFA that are assigned to the cluster. The orange distributions are for the strides from the intact controls that are assigned to the cluster. The purple distributions are the overall distribution from all the strides assigned to the cluster. The 0% is relative to the residual or right limb for all distributions.

The first cluster has no strides from individuals with OTFA, therefore, the distribution is empty in the top row. The more narrow the distributions are along the diagonal, the more consistent the co-contraction behavior is across the strides within the cluster. These more consistent co-activation pairs might be the behavior of interest defining the cluster and the corresponding muscle recruitment strategy. Sub-sets of muscles are likely more important for a particular strategy, rather than all the muscles. Less important muscles can

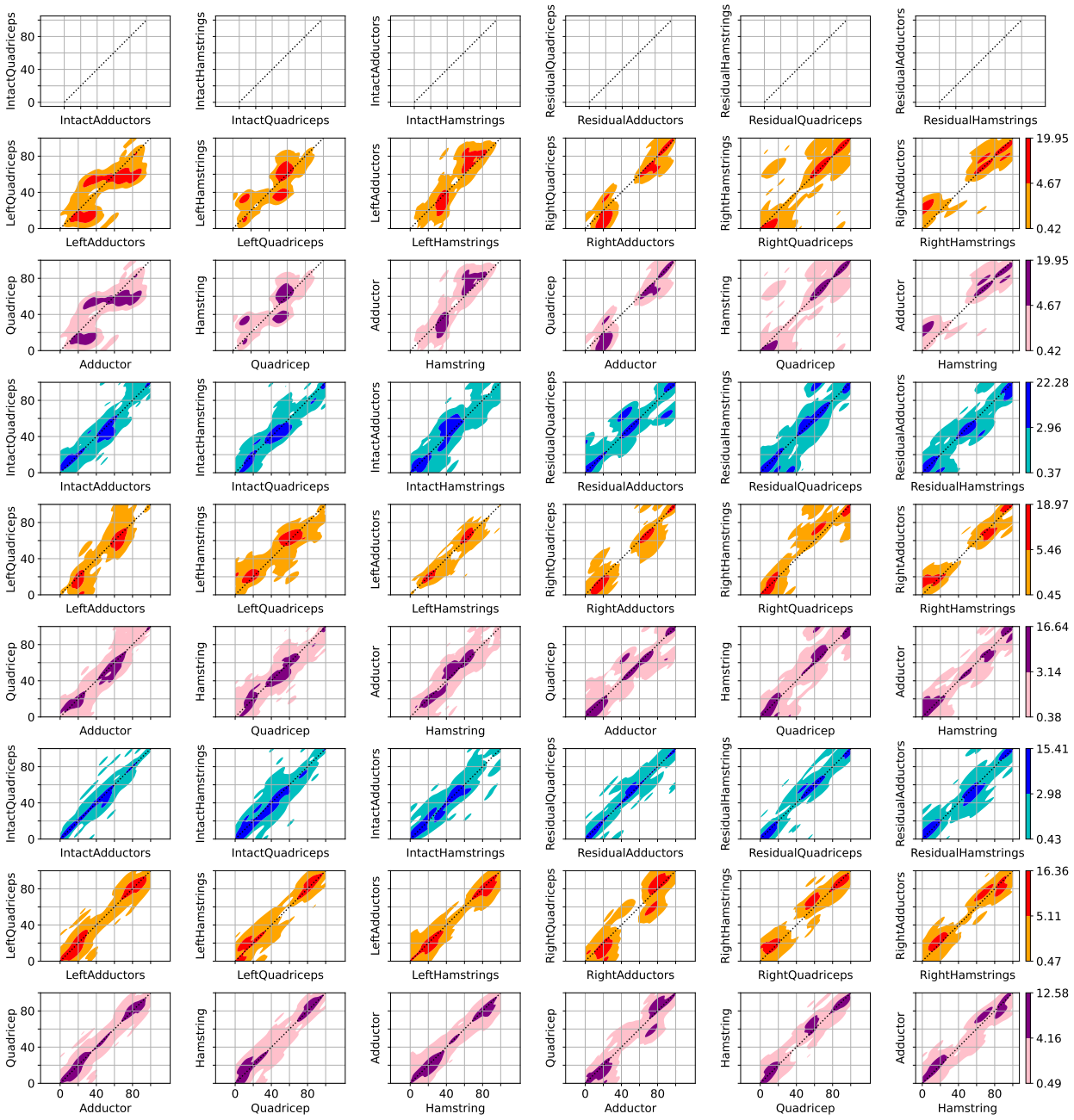


Figure 5.20: Co-activation time distributions for the top level clustering from PCA, on the training set. HDRs are for 95% and 50% most likely paired peak activities. Blue distributions are for the OFTA strides assigned to the cluster. The orange distributions are for the intact control strides assigned to the cluster. The purple distributions are the overall distribution for the muscle pair for the cluster.

have an optional or varying roles throughout the strides within the cluster. For example in the first cluster (C0, rows 1 to 3), from the overall distribution (purple) for the right

adductors-quadriceps, the most likely peaks occur prior 40% and after 50%, as indicated by the 95% HDRs in light purple. The 50% HDRs are in the time frames 0−20%, ∼60−80%, and ∼90−100%. During the time frames 0−20% and ∼90−100%, peaks are considered part of the same cluster since activity that occurs late during swing often continues into the heel-strike and attenuates during early stance. Muscle activity during this time frame is likely to control the velocity of the swinging limb into the heel-strike and assist with managing the impact from weight acceptance by preventing excessive knee flexion. During the time frame ∼60−80%, the right limb is in initial swing where the limb is accelerating and being pulled inwards by the adductors and excess knee flexion and limb speed are being controlled by the quadriceps. Right hamstrings-quadriceps co-contraction is also likely during this time frame since the hamstrings are flexing the knee.

In the second cluster (C1, rows 4 to 6), the intact/left adductors-quadriceps and the residual/right hamstrings-quadriceps are muscle pairings with the most similarity between the two cohorts within the cluster. For the intact/left adductors-quadriceps, both cohorts have 50% HDRs around 20% and 60% of the residual/right gait cycle. Around 20%, the intact/left limb is in the initial stage of its swing phase. The adductors likely active to bring the limb inwards towards the body and the quadriceps are co-contracting with the hamstrings to control the knee flexion and the limb's velocity. Intact/left hamstrings-quadriceps co-activation is also likely during this time. Around 60%, the left/intact limb is in its load response phase where it is receiving the full weight of the body as the residual/right limb begins its swing phase. The intact/left adductors-quadriceps involves the adductors assisting to propel the body forward and the quadriceps control excess knee flex to prevent the collapse of the limb under the full weight of the body.

Across the co-activation distributions, peaks off the diagonal are less likely. This might be due to the fact that strides where independent muscle activation peaks occur are dispersed across the clusters and less likely since clusters are formed based on correlates between the activation patterns. Additional results for the AE and the second level clusters are in the

Appendix.

5.7 Discussion

Combining the results of the various analyses above allows us to get a better understanding of the muscle behavior of individuals with OTFA, as well as the matched intact controls. Moreover, comparison with the matched controls informs us of potential deviations in performance strategies between the two participant groups. For example, greater inconsistency in co-contraction timing is observed in the OTFA cohort when compared to the matched intact controls. This is evidenced by the longer HDRs along the diagonal for the OTFA cohort in Section 5.5. Even among control participants, there are multiple likely muscle activation patterns that can occur throughout the gait cycle. Gait analyses that only monitor average muscle activation tend to over simplify the rich dynamics in the muscle recruitment behavior. In standard gait analyses, averages or distributions of singular muscles across the strides are compared and inappropriately describe co-activation. In this work, I provide a novel perspective of co-contraction and muscle behavior by describing the patterns of co-occuring muscle activation peaks within the strides and identify multiple muscle recruitment strategies. For example, the distribution of left hamstring activity at independent moments during self-paced gait have a high likelihood of being near zero between 40% and 60% (Figure 5.9). However, there is a brief interval among the 95% HDRs near the diagonal between 40% and 60% for the distribution of co-occurring peaks between the left hamstrings and quadriceps in Figure 5.15e, suggesting that co-contraction between these two muscles is likely during this time frame despite activation of the left hamstrings individually being unlikely. Therefore, it is crucial to expand gait analyses with various perspectives on the data and multiple gait measures.

5.7.1 Pressure Distributions At Each Time Slice During Gait

One goal of the osteomyoplastic procedure is to reconstruct the residuum for an efficient fit into the prosthesis for distal weight-bearing to promote operative gait performance (Ertl et al., 2010; Kahle et al., 2016; Taylor & Poka, 2016). The presence of bi-modal and wide RSI pressure peak patterns at all RSI locations across most strides for an individual is evidence for good prosthetic fit. Similar RSI pressure patterns are also observed when comparing behavior between walking tasks, suggesting robustness of the prosthetic fit to the gait speed. These RSI pressure patterns mimic vertical ground reaction forces (GRFs) found during typical gait (Alamdari & Krovi, 2017). The bi-modal peak pressures result from stable increases in force during the load response and push-off events. A single wide, flat peak during the stance phase indicates consistent contact of the residuum with the socket for the majority of weight-bearing during the residual stance phase. For example, at the DA (distal anterior) location in Figure 5.1a between $62 - 64$s during self-paced walking, the bi-modal RSI pressure peaks occur after heel-strike and before toe-off. An example of a single wide peak is seen between 62-64s during brisk walking. On the contrary, the RSI pressure peaks that begin and end late or begin and end early during stance might suggest that some improvement to prosthetic may be necessary. From the heat maps, we can identify which participants have a prosthetic socket that might need adjustments and at which locations the adjustments should be made. For example, the DA location may require some modifications to the fit for participants A01, A02, and A04. For brisk walking these individuals often experience peak pressure only after 30% of the gait cycle. Pressures are relatively higher later during the stance for these individuals at the DA location for both gait tasks. The DA location is the lower front position of the socket. During the first half of the stance (prior to 30%) much of the pressure is distributed to the back and sides of the socket until these individuals start to bring their weight over and in front of the limb before push-off into swing.

Despite imperfections in the sensors, the HDRs are robust to atypical signal activations

and capture multiple, distinct patterns. For example, the DA sensor for participant A03 mostly captures noise (Figure 5.3). However, the HDRs still capture distinct pressure patterns exhibited by the other participants such as the wide peaks and peaks that start late during the stance phase. The less variation there is across the strides and individuals, the closer the HDRs become to the mean gait activity when looking at the distributions of pressure or EMG activity at each moment during gait (Figures 5.3 and 5.4). For instance, the region of space covered by the HDRs for the DL and PM locations for self-paced walking closely follow the path of the mean pressure.

5.7.2 Peak Pressure Times

The distributions of peak times for the RSI pressure (Figure 5.11a) have similar patterns to the foot pressure distributions of the controls (Figure 5.11c). A set of HDRs for the RSIs span prior to 30% of the gait cycle. This is comparable to the HDRs for the heel-strike of the controls, also spanning prior to 30%. However, the HDRs for the controls' heel pressures are narrower. The peaks during this time frame prior to 30% are due to the load response after heel-strike, when more of the body weight is on the corresponding limb (Alamdari & Krovi, 2017). The second set of HDRs after 30% are comparable to the controls' toe pressure distributions. However, the HDRs for the toes end later than those of the RSI pressures. The peaks during this time frame after 30% are due to the force required to initiate and finish pushing the foot off the ground into swinging the leg and propelling the individual forward. Moreover, the RSI pressure peak distributions mimic the pattern of vertical ground reaction forces observed by Alamdari and Krovi (2017) because the RSI pressures peak most often during residual limb load response and into push-off. The set of sensors shows similar peak pressure times, further supporting distributed spatial contact with the prosthetic socket for a good prosthetic fit.

5.7.3 Muscle Activation of Matched Intact Controls

The average muscle activation patterns for the matched intact controls I found during self-paced walking (Figure 5.9) are consistent with that described by Winter (1987). Similarly, I identify peak average muscle activation just before and after heel-strike for the three muscles groups. Additionally, for the adductors, we both identify average peaks around the toe-off. However, a difference between our findings is that Winter (1987) found the average activation peaks around the toe-off to be minor for the hamstrings and quadriceps. These peaks were less than .3 of the average peak activation. Whereas, in my work I found the average activation peaks around the toe-off to have similar activations to that of the peaks around the heel-strike. This difference could be a result of the difference in cohort size and/or the number of strides. I compute the average over 6 individuals, however, I use over 590 strides. Whereas, Winter (1987) uses at least 10 strides per participants for 11 to 17 participants for each muscle.

Additionally, Winter (1987) states that the hamstrings and quadriceps have variable roles in manipulating the hip and knee to produce a net extension of the leg and that these muscle groups dynamically alternate in leading the net leg extension. However, this is not captured by his summary statistics. With the HDRs in Figure 5.9, I am able to show the high variability over the activation domain of these muscles and capture the distinct modes of likely activation patterns at each time during the gait cycle. The peaks in the average muscle activation do not necessarily coincide with the most likely times of the peaks or the most likely times of co-occuring peaks between pairs of muscles. My work is unique from prior gait analyses, especially regarding amputee gait, by describing the distribution of peak times (Figure 5.11) and co-occuring peak times within the strides (Figures 5.13 and 5.15). I found that the distributions of co-occuring peaks indicate that muscle pairs such as the hamstrings and quadriceps are most likely to occur prior to 50% of the gait cycle for the left limb and brief periods during early swing for self-paced walking. The average activations provided by Winter (1987) do not inform us of the likelihood of peaks or co-occuring peaks

during normal gait.

5.7.4 Muscle Co-Activation

Excessive or ill-timed co-contraction can have negative influences on individual health (Bae et al., 2007; Hodges et al., 2015; Schmitt & Rudolph, 2008). The analysis describing the gait of the current OTFA cohort revealed increased rates of adductor-hamstrings-quadriceps co-contraction throughout the gait cycle within the intact limb and at times of residuum weight transference. In Figure 5.13, the 95% and 75% HDRs are seen for each muscle pair for the OTFA cohort. The HDRs for muscle peaks near or along the diagonal indicate co-contraction. All other peaks offset in time likely contribute to the momentum of the leg and not its stability. The HDRs of co-contraction for the intact limb occur at most times during the gait cycle and have high variance of peak time, suggesting increased reliance on the intact limb for stability during all gait phases regardless of pace (Figures 5.13a, 5.13c, and 5.13e). The HDRs for co-contraction within the residuum are during weight acceptance, push-off, and the first half of swing (Figures 5.13b, 5.13d, and 5.13f). All three residuum muscle groups are co-activated at initial contact, pre-swing, and initial swing to obtain control of the prosthesis. In the control group in Figure 5.15, the 95% and 75% HDRs of muscle co-activation peaks predominately occur during stance for both paces. During self-paced walking, shorter HDRs of muscle peaks also occur during pre-swing and initial swing. The HDRs are longer within the left limb than within the right limb. HDRs are also present during swing with the right limb regardless of gait speed. Gait asymmetry is observed among the healthy intact individuals, however, the causes are not fully understood. Some combination of asymmetries in morphology and neural processes likely contribute to asymmetrical gait measures (Seeley et al., 2010). Sadeghi et al. (2000) found that gait asymmetry reflects natural functional differences between limbs related to each limb's contribution to propulsion and control and varies by gait task. Additionally, asymmetry observed in this study might also be impacted by participants rounding corners (5 left and 1 right) during data collection (Akiyama et al.,

2018). Because video was not a part of the protocol, it is unknown which strides occurred while rounding corners.

The longer diagonal co-activation HDRs of the OTFA group compared to the control group indicate greater variation in the co-contraction timing. Additionally, co-contraction is likely within the intact limb of individuals with OTFA during most of the swing. Co-contraction during swing is unlikely for the left limb of the control group and likely for only short periods of swing within the right limb. Co-contraction involves two or more muscles around the same joint that operate to move the joint in opposing directions to stiffen the limb and control its movement (Damiano, 1993). When executed proficiently, co-contraction is a strategy for performing skilled movements. However, exorbitant amounts of co-contraction signify inefficiency in managing the movement of the limb and improper timing of co-contraction indicates poor control and instability while moving (Damiano, 1993; Huang et al., 2020; Seyedali et al., 2012; Sharma et al., 2017; van der Krogt et al., 2012; Yuan et al., 2019). Therefore, the increased variation in co-contraction for both limbs of the OTFA group demonstrates diminished control of both limbs. In contrast, the control group demonstrated more consistency within the co-activation patterns and consequentially more control. For example in Figure 5.15, the control group's most likely muscle co-activation peaks, in red or orange, are largely along or near the diagonal during stance or briefly during swing. Some differences in co-contraction between participants with OTFA might also be impacted by residuum length (Bae et al., 2007). Theoretically, more residuum muscle mass would increase motor performance capacity with greater potential to generate forces and perform more similarly to the control group. Future analyses should incorporate studying the influences of residuum length as part of understanding the distributions of gait patterns.

Typically, medial muscle co-contraction is positively correlated with the progression of medial knee osteoarthritis (OA) and lateral muscle co-contraction is negatively correlated with protection against exacerbating OA (Hodges et al., 2015). Additionally, Schmitt and Rudolph (2008) found that increasing medial co-contraction led to an ineffective walking

strategy that was harmful to joint integrity in individuals with unstable medial knee OA. The results of these studies suggest too much or inappropriate co-contraction has adverse impacts on individual health. Therefore, efficient use of the distal residuum muscles during gait to reduce contraction within the intact limb may improve OTFA outcomes.

I found high variance in the co-activation time of the adductors, hamstrings and quadriceps. This is evidence of the contribution by the distal-most residuum muscles to control the OTFA residuum within the prosthetic socket, similar to what was found in healthy men with OTTA by Mai et al. (2013). The higher variance in the EMG activity and the increased reliance on the intact limb are also consistent with results by Wentink et al. (2013) from a heterogeneous TFA cohort. Similarly, Jaegers et al. (1996) found longer average hip muscle activation times within the intact and amputated limbs, indicating compensatory behavior by individuals with TFA.

However, in contrast to my work, the study by Wentink et al. (2013) did not specify the amputation approach of the participants. Both Jaegers et al. (1996) and Wentink et al. (2013) examined hip muscles of the amputated limb. I examine the knee muscles of individuals who have specifically received osteomyoplastic amputation to access the impacts of the surgical approach on the functionality of the distal residuum muscles and overall gait performance. Additionally, the TFA cohort examined by Wentink et al. (2013) was not homogeneous and had no inclusion criteria. Some individuals they collected data from used a walking aid or had vascular disease, which were amongst the exclusion criteria for the OTFA cohort I examined. The heterogeneity among the TFA cohort examined by Wentink et al. (2013) makes it unclear how the amputation influenced the gait performance of the individuals they examined. Moreover, of the few studies on TFA, most do not specify the amputation approach (Bae et al., 2007; Hong & Mun, 2005; Wentink et al., 2013).

Another difference between this dissertation work and prior TFA studies, such as Hong and Mun (2005), Jaegers et al. (1996), and Wentink et al. (2013), is the approach used to describe co-contraction. The prior TFA studies measure muscle co-activation after averaging

the muscle activations over the strides. For the current study, I assess the distributions of co-activation peak times between muscles during the same stride to verify muscle co-activity and improve the accuracy in the co-contraction descriptions. Bae et al. (2007) quantifies co-activity within strides for a TFA cohort, however, the cumulative ratios over the entire trial are computed. They do not describe precise co-activation timing and only measure the average co-contraction behavior of the muscles within the intact limb. These prior TFA studies also report fewer than 24 strides per subject. For the current study, I use more than 67 strides per participant per trial to increase the statistical power of the analyses.

Moreover, to my knowledge, no studies on TFA have identified multiple muscle recruitment strategies. Prior TFA studies discuss the average behavior and compare those averages to that of the controls. Muscles have multiple roles and trade-off these roles from stride to stride (Winter, 1987). Therefore, in this dissertation, I have identified and extracted likely sets of muscle recruitment behaviors that are utilized by individuals with and without OTFA.

5.7.5 Gait Phenotypes

Some amount of overlap between clusters found in the PC and AE latent spaces is expected, in part, due to randomness and the small number of clusters between the two approaches. However, for the clusters C1 in the PC space and C0 in the AE space, there is a high amount of overlap in the OTFA strides between these clusters. The generalized reconstruction performance for PCA and the AEs were similar and high (FVAF$\approx$.923), indicating that both approaches capture informative characteristics of the data. Ideally, informative representations should maintain within and between class variance. Therefore, another factor that likely influences the overlap between the clusters is that fundamentally similar strides are consistently grouped together when using accurate, informative representations. Additionally, the activation function $f(a)$ used for the AE is the exponential linear unit (ELU) from Equation 2.12 and is described in more detail in Chapter 2.2.2. The node outputs from the ELU are linear whenever the node activation $a > 0$ and exponential otherwise. This might

explain why the majority of overlapping strides are from individuals with OTFA. Perhaps these strides correspond to the portion of the domain that is linear, resulting in similarities between the PCA and the AE approaches. Future work should investigate the impacts of activation functions and characteristics of the input space on the latent representations and cluster assignments.

The current top level clusters are able to extract more general, high-level feature similarities between the strides. However, additional clustering levels are likely necessary to more accurately group strides to identify more precise strategies. The clusters are able to group similar strides within each cohort, however, the muscle activation patterns often deviated between the cohorts within a cluster, suggesting additional sub-clusters will separate the more unique strategies and lower level clusters are presented in the Appendix.

Chapter 6

Infant Locomotion

The goal of this chapter is to understand relationships between neurological and locomotor development in infants. Crawling is an interesting stage of development when many infants experience a variety of changes that facilitate learning of coordinated movement and spatial perception. Neurological or motor conditions, such as Cerebral Palsy (CP), can disrupt this dynamic neuro-motor learning process and have lifelong consequences. We want to understand how CP changes functional connections within the brain at each developmental stage for better prevention, earlier diagnosis, and more personalized care. Therefore, describing typical, functional and structural changes throughout infant development can assist in understanding deficits caused by neuro-motor conditions.

In this chapter, I summarize the neuro-motor development of infants and the significance of crawling. I provide a description of CP and its impact on infant development. I discuss the Self-Initiated Prone Progression Crawler (SIPPC) robot for assisting infants at risk of CP during the acquisition of crawling. Additionally, I describe a preliminary approach and results for understanding typical changes in infant brain activity and locomotion during the acquisition of crawling using the SIPPC.

In my approach, first I characterize functional connections using correlations between electroencephalography (EEG) frequency bins across multiple scalp locations. As infants

learn new motor skills, they explore and experiment with more complex and coordinated movements (Adolph & Franchak, 2017). These exploratory movements are facilitated by structural and functional changes within the brain where distinct brain regions activate in coordinated ways to produce new motor actions. Therefore, I hypothesize that functional connections will increase longitudinally, and that this increase will result in increasing correlations between the frequency bins at different EEG electrode locations.

In the second part of my approach, I construct and examine movement prediction models to measure the relevance of specific frequency bins at each electrode location for predicting limb movements. Ipsilateral activity stabilizes early in life, while contralateral activity progressively developments until adulthood (Nevalainen et al., 2008). Therefore, I hypothesize that the number of ipsilateral features that are important will be constant throughout development, and the number of important contralateral features will increase.

6.1 Infant Neurological and Motor Development

The morphological and physiological relationships between the brain and behavior are more easily studied and better understood for adults than in infants (Paterson et al., 2006). More investigation is necessary to properly elucidate the complex set of trajectories for the typical brain development of infants. A non-invasive approach for studying brain activity is electroencephalography (EEG). EEG involves placing a set of electrodes over the scalp that detect the net electrical activity over the surface of the brain. Despite the fact that EEG is susceptible to various noise sources (e.g., eye movement, external muscle activity), it can provide many insights into the function of various brain regions. Some artifacts from these various noise sources are mitigated with pre-processing techniques, allowing us to capture significant components of the brain activation patterns.

The strength of the frequency components that comprise the EEG signal is referred to as the power spectrum. Various frequency ranges are associated with particular functions (e.g.,

movement generation) and distinct spatial distributions. The power spectrum is useful for describing functional relationships between brain regions within different frequency bands. Different frequency bands are associated with certain brain states, regions, and functions. These bands are typically delineated as delta (.5−4 Hz), theta (4−7 Hz), alpha and mu (8−12 Hz), beta (13−30 Hz), and gamma (>30 Hz) in EEG analyses (Britton et al., 2016; Nayak & Anilkumar, 2022; Newson & Thiagarajan, 2019). The power in the delta and theta bands are relatively more dominant during resting states in infants when compared to adults (Britton et al., 2016; Stroganova & Orekhova, 2007; Xiao et al., 2017). Additionally, the frequency ranges for the delta, theta, and alpha/mu bands are lower in infants and progressively increase to the adult ranges over time. For example, Xiao et al. (2017) found that, with maturation, the average frequency boundaries between the delta-theta and theta-alpha bands shifted towards higher frequencies. Understanding these EEG activation patterns, which brain regions produce them, and when they occur during development can provide insights into the underlying neurological pathways of infant development and assist in understanding the impacts of developmental neuro-motor conditions.

In regard to locomotion, activity in the primary motor cortex and primary somatosensory cortex play a major role in representing and producing movement. Alpha band activity within these brain regions is also related to movement. Generally, movement that involves the arms, hands, and more dexterous actions is generated by neural activity in the lateral primary motor regions. The activity involving the movement of the lower extremities and less dexterous actions occurs in the central-medial regions of the primary motor cortex (Cheyne et al., 1991). Activity on each side of the motor regions has a dominate role in movements of the contralateral limbs (Cheyne et al., 1991; Chouinard & Paus, 2006). Sensory information from the skin, muscles, tendons, and joints activate neurons in the primary somatosensory cortex and allow us to perceive the position (i.e., proprioception) and movement (i.e., kinesthesia) of the parts of our bodies (Chouinard & Paus, 2006; Kaas, 2015; Tuthill & Azim, 2018; Webb, 2017). For example, stretch receptors within the muscles measure a combination of muscle

length, stretch velocity and force. Additionally, sensory receptors within the joints often peak in activation at the joint position boundaries to provide feedback and avoid exceeding joint limits.

In EEG analyses, the mu rhythm is when power within the frequency range 8−12 Hz at the primary motor and somatosensory regions desynchronize (or attenuate) during movement, imagined movement, or somatosensory stimuli (Britton et al., 2016; Garcia-Rill, 2015; Marcuse et al., 2016; Marshall & Meltzoff, 2011; Marshall et al., 2013; van Elk et al., 2008). The mu rhythm also demonstrates bilateral behavior upon movement of the arms or legs, resulting in power decreasing bilaterally in the motor regions.

In infants, Xiao et al. (2017) described developmental changes in the frequency range, power and location of the mu rhythm in resting infants during the first year of life. In particular, they identified that increases in the relative peak power and the corresponding mu rhythm frequency are correlated with the onset of crawling. However, this study did not examine changes in the mu rhythm during locomotion. Other studies have found that the mu response is impacted by an infant's personal experience with particular actions and their processing of the actions of others (Marshall & Meltzoff, 2011; Marshall et al., 2013; van Elk et al., 2008). Marshall et al. (2013) found subtle hemispheric differences at central EEG electrodes when infants observed reaching, grasping, and lifting of heavy and light objects that they had personal experience with lifting. Infants were given time to lift color-coded objects of varying weight. When infants observed others perform actions with the heavier objects, power at the right electrodes decreased while power at the left electrodes increased. Additionally, the reverse was found when infants observed the same actions with the lighter objects. This effect could be related to infants preparing, associating, and imagining different plans of action based on an object's weight. However, further investigation is still needed since the roles of additional factors, such as perspective and the color-coding of the object weights, are not fully understood.

Another study that examines the mu rhythm during infant locomotion, found that mu

desychronization in infants is stronger in response to specific auditory stimuli that have been related to a specific action (Paulus et al., 2012). The infants in the study trained for a week with a rattle that made a specific action related sound. Compared to familiar non-action related sounds and unfamiliar sounds, there was significantly more mu desynchronization in response to the action related sound. Additionally, the average difference between the mu desychronization for the action-related response and the other sound conditions was greater the longer the infant trained with the action-related sound. This is evidence that infants are able to learn and understand the effects of unique actions. Training time also has an influence on these abilities. However, it is unclear exactly when or how these capabilities develop and what their impacts are on locomotive proficiency.

6.1.1 Regional Brain Connectivity in Infants

Neurological functions, such as movement generation and visual processing, produce complex electrical activation patterns. These electrical signals arise from changes in the electrical potential of neurons which propagate from one neuron to neighboring neurons via synapses. Alterations in synaptic connections produce circuits that are able to produce complex sensorimotor behavior and solve numerous problems.

Co-occuring activation patterns captured by EEG electrodes at different locations on the scalp indicate functional and possible effective or structural connectivity (Chouinard & Paus, 2006; Friston, 2011; Shaw, 1984; Thatcher, 1994). *Effective connectivity* describes the underlying casual relationship between a pair of neurons or populations of neurons and is conditioned on structural connections (Eickhoff & Müller, 2015; Friston, 2011). Effective connectivity describes the actual direction, strength, and timing of the connections between neurons. The effective connections between neurons are the underlying mechanisms that produce observed functional connections. *Functional connectivity* is a non-directional linear correlation between co-occuring activation patterns. Functionally connected regions are not necessarily connected directly by synapses. The functional correlations between two regions

can be mediated by multiple synapses driven by a common source directly or indirectly. Although we cannot determine precise synaptic connections from measurements of functional connectivity alone, it is useful for understanding high level brain activity and predicting individual characteristics, such as disease classification.

Volume conduction is the result of the activity of a single neuron spreading to nearby tissue via electromagnetic fields, resulting in sets of EEG electrodes detecting activity from overlapping populations of neurons (Chorlian et al., 2009; Holsheimer & Feenstra, 1977). The amplitude of the neural activity detected by the electrodes decreases with increasing distance between the neuron and the electrodes. Volume conduction does not actually describe neural connectivity and biases measures of functional connectivity. Fortunately, the influence of volume conduction on these measures is mainly a concern for electrodes within a 7 cm radius and can be mitigated with various techniques, such as spatial filters or ICA (Corbetta et al., 2014; Thatcher et al., 1987).

Coherence is a standard metric that measures the functional relationship between a pair of co-occuring activation patterns and can be defined as the magnitude squared correlation between the corresponding frequency profiles of the signals (Shaw, 1984; Thatcher, 1998). Coherence is related to a combination of the number of functional neural connections, the strength of these connections, and the distance between the electrodes. Therefore, if the effects of volume conduction are not addressed, coherence is biased between nearby electrode pairs. In conjunction with measures of neurological structure and physiology, coherence measures provide more insight into the mechanisms of the functional connections within the brain, than coherence would on its own. Longitudinal increases in coherence might indicate synaptic growth or strengthening and longitudinal decreases in coherence might indicate synaptic pruning (Thatcher, 1998). In this dissertation, I measure average functional connections at one second time scales for periods of three weeks to describe aspects of typical infant development while learning to crawl.

Foundational work by Hudspeth and Pribram (1990), Matousek and Petersén (1973), and

Thatcher (1998) describes and models developmental changes in neural connections during childhood. Thatcher (1998) found an overall exponential increase in mean resting state coherence in children ages 1.5 to 16 years old. Additionally, they identified periodic changes in mean EEG coherence and power that coincide with stages or cycles in cognitive development. These stages spanned 2 to 4 years and often exhibited anatomical organization along the anterior-posterior or medial-lateral directions. For example, they observed sudden increases in mean coherence in the theta band (3.5−7.0 Hz) between parietal and frontal electrodes between the ages of 5 and 7 years old. The increases in mean EEG coherence observed over development reflected potential increases in the number of synapses and decreases reflected stages of synaptic pruning. They also identified evidence that greater variance during decreases in mean coherence (i.e., pruning stages) were correlated with the variability of the environmental factors, such as location and interactions with their caregivers. In regard to the development of hemispheric communication within the brain, Thatcher (1998) observed different developmental trajectories for intra-hemispheric mean coherence in the delta (0.5−3.5 Hz), theta (3.5−7.0 Hz), alpha (7.0−13.0 Hz), and beta (13−22 Hz) bands between the left and right hemispheres. More work still needs to be done to understand the mechanisms that influence or give rise to specific developmental changes in coherence and how they impact motor learning and capacity.

6.1.2 Acquisition of Crawling

Studying the acquisition of crawling is useful for identifying approaches to managing the impacts of neuro-motor conditions. Crawling is a profound developmental milestone for most infants, impacting muscular strength, motor coordination, and cognitive development. Skilled locomotion is not reflexive or hardwired, but is a creative and adaptive learning process for infants to learn control of their bodies (Adolph & Franchak, 2017). Locomotion is a creative process since there are many ways for infants to recruit muscles and limbs to solve the same problems.

Typically, infants progress through multiple stages during the acquisition of crawling. The loop between action and perception makes locomotion functional for effective maneuvering. As infants lay in a prone position, they will progressively move more of their body (Adolph et al., 1998). Infants will lift their head higher and for longer to observe their surroundings and identify objects of interest worth moving towards. Additionally, they obtain more control over the movement of their limbs, while building muscular strength to move onto their hands and knees. Infants will also try to grasp objects before eventually learning control and coordination to advance towards interesting objects and finally crawl. The precise functional and structural neurological mechanisms corresponding to each of these stages are not yet fully understood.

During each of these stages, infants learn through exploratory movements for enhancing perception and cognition (Adolph & Franchak, 2017). These advancements facilitate the identification of better strategies for handling the physical and spatial constraints of their environment and its relation to their body. Unfortunately, developmental motor disorders can make locomotive exploration more challenging and delay or prevent infants from expanding their motor capabilities and expanding the associated neurological functions (Damiano, 2009; Morgan et al., 2016).

6.2 Cerebral Palsy (CP)

Cerebral Palsy (CP) is a collection of developmental motor disorders in infants that can impact the progression of locomotion, cognition, perception, communication, and behavior (Bax et al., 2005). Infants with CP have reduced motor control and coordination, making the motor learning process more challenging and leading to delayed or missed developmental milestones, such as crawling (Damiano, 2006; Morgan et al., 2015, 2016).

Typically, infants experiment with a variety of movements while learning to crawl and will achieve intrinsically motivating results from their motor exploration (Adolph & Franchak,

2017). However, as a result of reduced motor coordination or strength, infants with CP typically generate less productive, atypical actions (Graessle, 2018). Depending on the form of CP, atypical actions might involve an over-dependence on one side of the body or rapid, imprecise movements while reaching or crawling. During the first year of life, these atypical strategies influence the changes in neural structure and function. Various studies have found that individuals with CP to demonstrate decreased mu responses over centrally located electrodes, in addition to atypical topography (Démas et al., 2020; Inuggi et al., 2018; Kukke et al., 2015; Kulak & Sobaniec, 2005; Kułak & Sobaniec, 2003; Pihko et al., 2014). Additionally, decreases in inter-hemispheric coherence have been found in the delta, theta, alpha, and beta bands in older children (6 to 15 years old) with CP compared to a control group (Kulak & Sobaniec, 2005; Kułak & Sobaniec, 2003). For the alpha band, less inter-hemispheric coherence was observed over the central, parietal, and occipital regions. These functional differences, particularly, in the alpha and beta bands likely contribute to continued motor deficits in individuals with CP. Further investigation is still necessary to understand the mechanisms that yield these functional and structural changes and their relationship to neural plasticity and motor learning during infancy.

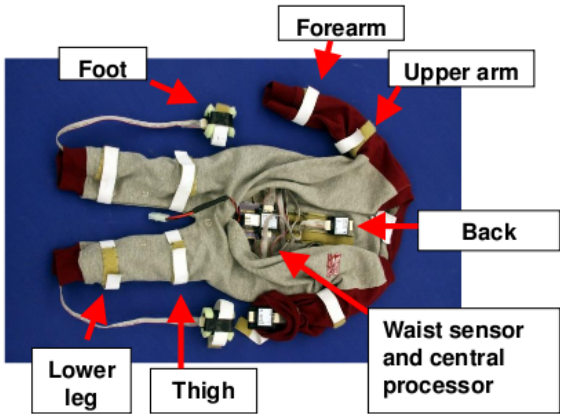
6.3 Self-Initiated Prone Progression Crawler (SIPPC)

Presently, CP has no cure, however, there is evidence that crawling training for infants with or at risk of cerebral palsy improves motor skill, cognitive and language functions, intelligence, memory and attention (Bai & Gao, 2022; Kolobe & Fagg, 2019). Many individuals with CP receive physical therapy to assist with learning motor skills for tasks necessary for daily activities (Damiano, 2009; Levac et al., 2009; Pomeroy et al., 2011). The complexity of the effects of CP make it important for therapists to have all relevant health and neuro-motor information, during therapy sessions and throughout long term care.

The Self-Initiated Prone Progression Crawler 3 (SIPPC3) robot is an assistive crawling



(a) SIPPC Robot



(b) SIPPC Suit

Figure 6.1: (a) A training session where the infant is using the Self-Initiated Prone Progression Crawler 3 (SIPPC3; Fagg et al., 2012). The infant makes crawling like motions to move the robot and reach toys. The infant is outfitted with a kinematics capture suit. (b) The infant kinematics motion capture suit is constructed as an infant onesie containing 12 Inertial Measurement Units (IMUs) for easy application onto the infant to track trunk and limb positions and movements (Southerland, 2012).

robot designed to promote movement learning in infants with locomotor delays, in particular, CP (Kolobe & Fagg, 2019) by offering an array of crawling-based movement strategy options (Figure 6.1a). The SIPPC is a unique avenue of intervention and support that provides robot-assisted locomotion for infants with motor delays to practice skills that would otherwise be too difficult for the infants to obtain independently. In Figure 6.1a, above the platform of the SIPPC is a force-torque sensor that detects the ground reaction forces (GRFs) generated by the infants. A motion capture suit (Figure 6.1b) tracks the limb movements to enable the robot to respond to crawling-like gestures generated by infants even when they are unable to produce sufficient GRFs to move the robot. The robot has three wheels to the left, right and back of the infant. Above each wheel is a camera recording the infant's actions. Additionally, EEG is collected from the infants to examine the relationship between motor behavior and neurological changes.

A key feature of the SIPPC is its ability to assist the infant through augmented locomotion contingent upon the movements and forces produced by the infant. The SIPPC possesses a

user interface (UI) for therapists to control aspects of the robot-assisted training. Infants lay prone on the robot to access motor skills relevant to crawling. Moreover, a variety of control modes, with variable levels of assistance, are available to allow the infant to explore and practice actions that move the robot. During training sessions, the robot measures the infant's performance in real-time using kinematics and GRFs to detect and promote a wide array of actions. Actions that are otherwise difficult for the infant are augmented by the robot's response to encourage continued exploration. Successful robot movements intuitively communicate with the infant the knowledge of results (e.g., whether they reached or got closer to the toy) and implicit objectives (e.g., how to move certain limbs to progress forward).

Additionally, the device provides the therapist with feedback that can be used to adjust the robot's responses and further guide learning. The therapist can guide the infant's learning by altering the feedback to either decrease difficulty to motivate the infant or increase the challenge to prevent dependency on the assistance. As the infant's skill level and capacity improves, the SIPPC can be adjusted intentionally to continue to challenge the infant and shape motor learning. The ability to adjust difficulty is crucial to prevent dependency on the robot-assistance and ensure that progress translates to daily life (Damiano, 2006; Kitago & Krakauer, 2013). The therapist can control feedback from the robot in real-time through the UI. The UI exposes the robot control mode parameters and sensitivity thresholds to the therapists. Adjusting the control modes and thresholds enables the therapists to increase or decrease the amount of feedback from the robot and, consequentially, the difficulty level of the therapy session. The ability to adjust the robot's response makes it applicable to a wide array of infants with various types and severity of injury, disability, or motor skill.

6.3.1 SIPPC Protocol

In a set of studies by Kolobe, Fagg, Ding, and Miller (Ghazi et al., 2016; Kolobe & Fagg, 2019; Patino et al., 2017; Xiao et al., 2017), typically and atypically developing infants engaged in sessions three times a week for 12 weeks prior to the onset of crawling. During the sessions,

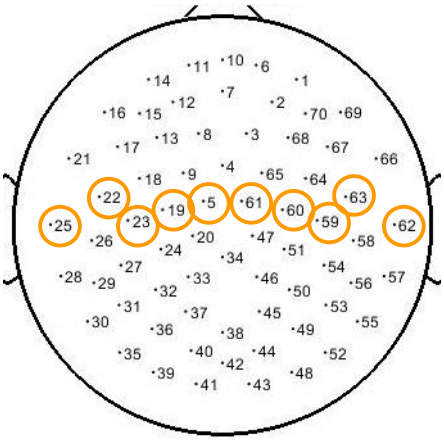


Figure 6.2: EEG electrodes over the central sulcus (modified from Figure by Xiao et al., 2017, personal communication).

infants rested for 5-minutes prior to a 15-minute robot-assisted crawling session with the SIPPC.

During the beginning of the session, calm state EEG is captured to observe the effects of structural and functional changes in infants prior to the onset of crawling (Xiao et al., 2017). The infants were seated upright on their parent's lap to capture EEG activity while the infants were calm. The infants were shown a rattle app, with the phone beyond their reach, to keep them relaxed. The EEG net cap (EGI's Geodesic EEG System 300) recorded brain activity during the session at 124 locations on the scalp at 1 kHz (Figure 6.2). Videos were recorded and synchronized to the EEG through EGI's Netstation software.

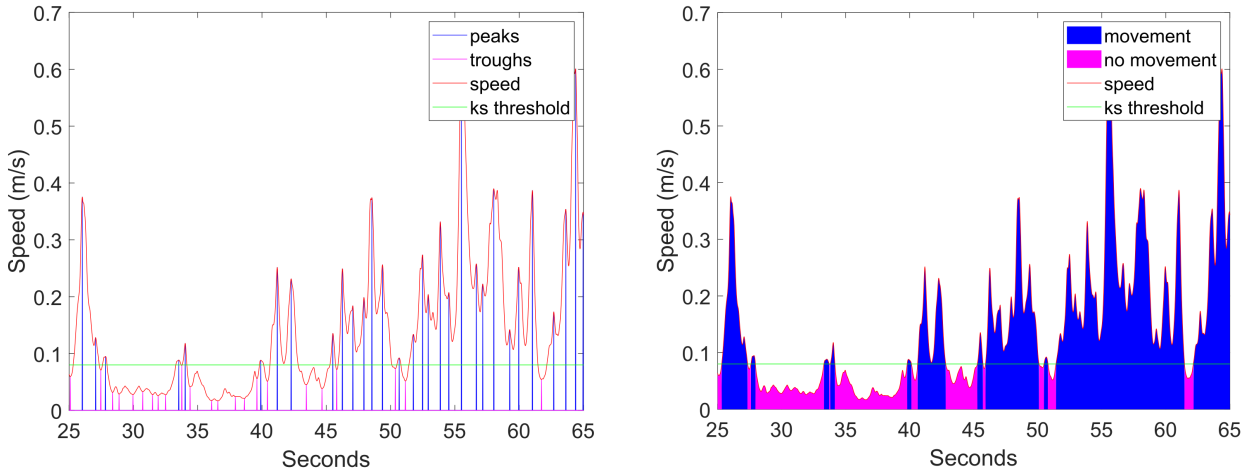
For the robot-assistance, with the EEG net cap on the infant's head, the motion capture suit (Figure 6.1b) containing 12 Inertial Measurement Units (IMUs) was placed onto the infant's arms, trunk, legs, and feet before placing them onto the robot platform. The suit records the kinematic data at a sampling rate of 50 Hz. The force-torque sensor detects the GRFs produced by the infant and the rotational velocity of the wheels are recorded during the sessions to measure how the infant's actions control the SIPPC. These data provide multiple perspectives for characterizing and understanding infant locomotor development during the acquisition of crawling.

6.4 Measuring Relevance of EEG Representations for Predicting Limb Movements

Monitoring infants during the acquisition of crawling can provide useful insights into the maturation of the brain and how it relates to the development of locomotion. Examining crawling can also facilitate our understanding of neuro-motor developmental conditions. Therefore, we want to know how changes in brain activity captured by EEG relate to motor behavior during crawling acquisition. To investigate this relationship, I provide a preliminary approach for measuring the relevance of EEG electrodes and frequency bins for predicting limb movements during the acquisition of crawling. Models that are able to accurately determine whether a limb is moving based on patterns within the EEG data may identify meaningful information in order to successfully predict characteristics of the limb behavior. Therefore, I examine these models that predict the limb movements from the EEG. I describe a custom process for generating the movement labels for the models using the kinematic data, the procedure for constructing EEG representations and the construction and selection of the models. Lastly, I describe how the models are examined to measure the relevance of the spatial and frequency attributes of the EEG for movement prediction.

6.4.1 Generation of Movement Labels

My approach is to construct machine learning-based models to predict limb movements from EEG. Then I identify the electrodes and frequency bins that are most relevant in making the predictions. In this section, I describe my approach for assigning movement labels from kinematic data by defining voluntary movements performed by the infants based on relatively high limb speeds. A one second period is defined to contain movement if the peak or average speed exceeds a data-derived threshold. The movement labels are extracted by first identifying the local extrema (i.e., maxima and minima) from the speed of each limb. The maxima are



(a) Extrema

(b) Movement Labels

Figure 6.3: (a) Extrema extracted from the speed (red curve) of the left wrist. The KS threshold is in green, blue spikes indicate the maxima, and the magenta spikes indicate the minima. (b) Final output from a movement labeling procedure for the left wrist using a time window less than one second. Blue regions are identified as movement. Magenta regions are identified as no movement.

located using the same peak extraction procedure described in Section 4.2. The peak speed is at time t where:

1. the speed is the largest during the range $[t - \delta, t + \delta]$ ms, where $\delta > 0$, and

2. the speed is above a data-derived threshold ϵ.

A similar procedure is used for the minima, except troughs are identified below the threshold ϵ. Figure 6.3a contains an example of the output from the extrema extraction using the speed from the left wrist. The maxima (blue spikes) below the data-derived threshold are ignored and not considered intentional goal-directed movement. Similarly, the minima (magenta spikes) that are above the data-derived threshold are ignored.

To obtain the threshold that distinguishes between intentional movement and no movement, I use the speed that corresponds to the Kolmogorov-Smirnov (KS) distance (Massey, 1951). The KS distance is the largest distance between the cumulative distributions for the speed

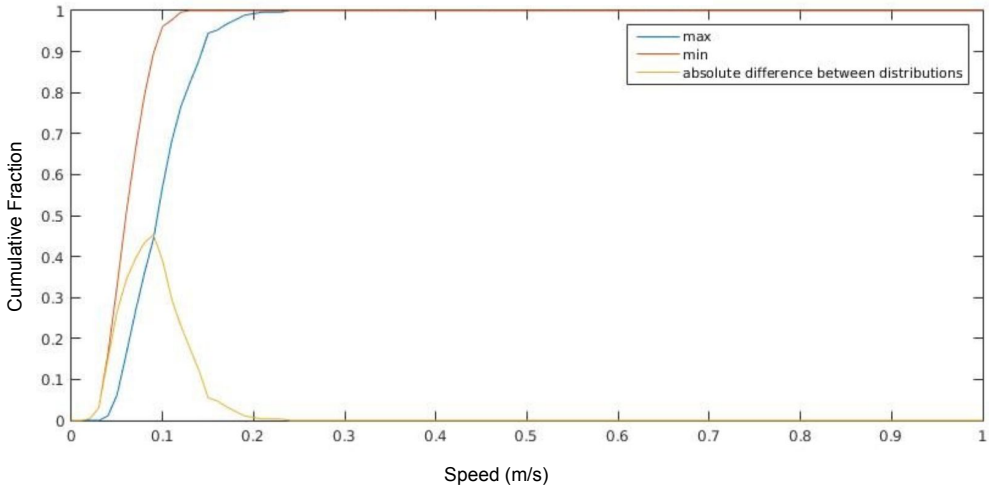


Figure 6.4: The cumulative distribution of the maximum speeds is the blue curve. The cumulative distribution of the minimum speeds is the red curve. The absolute distance between the distributions is the orange curve.

peaks and troughs and is defined as:

$$d = arg\max_{s} |P(s) - Q(s)|, \tag{6.1}$$

where P is the cumulative distribution of the speed from the speed peaks, Q is the cumulative distribution of the speed from the speed troughs, and s is the domain of the speed. An example of the cumulative distributions and the distance curves are shown in Figure 6.4, with the cumulative distribution for the maxima in blue and the minima in red. The absolute difference between the two distributions is the orange curve. The speed with the greatest absolute difference is the threshold for the corresponding limb for the infant.

The extrema identified using the KS threshold are used to label the time intervals of movement. Non-overlapping intervals of one second are used to capture the full duration of voluntary movements from the infants. Intervals where speed peaks are located and that have no speed troughs are labeled as *movement*. Intervals that contain a speed trough but no speed peaks are labeled as *no movement*. Time intervals that contain neither peaks or troughs are labeled as movement if the average speed is above the threshold, otherwise, they are labeled as *no movement*. Time intervals that contain both speed peaks and troughs are

labeled as movement if the average speed is above the threshold, otherwise, they are labeled as *no movement*. An example of a final result from the movement labeling process using a time window of less than one second, is shown in Figure 6.3b. The blue regions indicate time windows that are designated as movement and the magenta regions are *no movement*.

6.4.2 Representing EEG Signals for Learning Models

To measure the relevance of specific EEG electrodes and frequency bins for predicting limb movements, EEG representations are constructed as the input to the movement prediction models. I build EEG representations using ten locations arrayed along the central sulcus region (seen in Figure 6.2). The EEG data are segmented into one second time frames that correspond to the time frames for each of the movement labels generated using the procedure described in Section 6.4.1.

Spectral power analysis is a standard approach for decomposing EEG signals into constituent frequency bins and examining activation patterns (Lindsley, 1939; Smith, 1938a, 1938b; Stroganova & Orekhova, 2007). Computation of the spectral power is defined over an infinite range, however, I am examine the EEG over one second windows. This causes power from the dominate frequencies to leaky across the frequency domain. A standard approach to address this power *leakage* is to apply a window function to the EEG intervals. Therefore, prior to the spectral decomposition, each one second time window of EEG activity is passed through a 25% Tukey window (Tukey, 1967) to taper the EEG to reduce the power leakage between the frequencies (Harris, 1978). The Tukey window is applied pointwise using the formula:

$$\tilde{E}_t = E_t W_t, \tag{6.2}$$

where $E_t \in \mathbb{R}$ is a time sample from an EEG segment $E \in \mathbb{R}^{1\times T}$ of length T from a single electrode, and $W_t \in \mathbb{R}$ is the corresponding weight from the Tukey window $W \in \mathbb{R}^{1\times T}$. The EEG signals are decomposed into constituent frequencies in the range $0-26$ Hz using the

Discrete Fourier Transform (DFT):

$$X_f = \sum_{t=1}^{T} \tilde{E}_t e^{-2\pi i f \frac{t}{T}}, \ f = 0, \ldots, 26, \tag{6.3}$$

where $\tilde{E}_t$ is the tapered EEG at time t and f is the frequency (Bracewell, 1986). The power of each frequency is computed as the magnitude of the DFT:

$$P_f = |X_f|. \tag{6.4}$$

Then, the average power for a frequency bin is computed as:

$$P_B = \frac{1}{|B|} \sum_{f \in B} P_f, \tag{6.5}$$

where B is the set of frequencies for the bin and $|B|$ is the size of the bin. Xiao et al. (2017) observed large fluctuations in power mainly in the frequency range $2-9$ Hz in infants while calmly seated on their parent's lap. Frequencies above 9 Hz were not examined by them. However, there is a possibility of emergent beta ($13-30$ Hz) activity during the first one to two years of life (Britton et al., 2016). Therefore, I examine sub-intervals in the delta, theta, alpha, and beta bands for this work. Specifically, I use the bins: DC, 1, 2, 3-5, 6-8, 9-11, 12-14, 15-17, 18-20, 21-23, and 24-26 Hz. Lastly, the power for each electrode and frequency bin are normalized over the training set data instances to a standard normal distribution:

$$\hat{P_B} = \frac{P_B - \bar{p}_B}{s_B}, \tag{6.6}$$

where $\bar{p}_B \in \mathbb{R}$ is the mean power of the frequency bin B over all the data instances, and $s_B \in \mathbb{R}$ is the standard deviation of the frequency bin B over the data instances.

6.4.3 Classifier Construction

To investigate the relationship between the EEG and limb movements, I construct Support Vector Classifiers (SVCs) that predict movements of the arms and feet from average power over the frequency bins captured by each EEG electrode. SVCs generate implicit hyper-surfaces in high dimensional feature spaces to partition the space into two classes (Boser et al., 1992). The higher dimensional features are constructed using a kernel function $\kappa(x, x')$, where x and x' are pairs of data instances. The kernel function, κ, computes a new feature representation by measuring the similarity between the pairs of data instances (Schölkopf et al., 1998).

Models that successfully predict movement at high rates are the most useful for assessing the relevance of the EEG electrodes and frequency bins. I use cross-validation (described in Section 2.6.1) to identify the models with the best generalized prediction performance. Cross-validation splits the data into training, validation, and test sets, each comprised of independent sub-sets of data instances called folds. The cross-validation folds are stratified, meaning that approximately the same ratio of *movement* to *no movement* labels is used within each fold. I use the Peirce Skill Score (PSS) to measure model performance or skill level by evaluating the relative rate of correct and incorrect movement predictions. PSS is preferred over accuracy since it provides meaningful performance estimations when there are significantly more data instances of *no movement* compared to *movement*. The PSS is defined as:

$$\begin{aligned} PSS &= TPR - FPR, \text{ where} \\ TPR &= \frac{TP}{FP + FN}, \text{ and} \\ FPR &= \frac{FP}{FP + TN}, \end{aligned} \tag{6.7}$$

and where TP is the number of true positive predictions, FP is the number of false positive predictions, FN is the number of false negative predictions, and TN is the number of true negative predictions (Jolliffe & Stephenson, 2011; Peirce, 1884). The TPR is the true positive

ratio and measures the fraction of correctly predicted movements. The FPR is the false positive ratio and measures the fraction of *no movement* time frames that are incorrectly predicted as movement. PSS is the difference between the TPR and FPR and is adept at evaluating the skill level of models in scenarios where the movement events are unlikely. For example, if an infant is rarely moving, a model could have a high accuracy from predicting the *no movement* most of the time, but a low PSS from incorrectly predicting the few intentional movements made by the infant. If the model correctly detects most of these rare movement events, then the model is considered skilled.

6.4.4 Feature Importance

I assess which EEG electrodes and frequency bins are most pertinent for predicting specific limb movements by corrupting each feature individually within an independent validation data set (Pedregosa et al., 2011). A feature is defined by an EEG electrode and frequency bin. The corruption is performed by randomly shuffling the values between the data instances within a feature. Shuffling is used to ensure the corrupted values are within the domain of the feature while disrupting the relationship between the feature and the predicted value. Corrupting features that are most relevant to the model for predicting the output class are likely to reduce the model prediction performance (Altmann et al., 2010; François et al., 2006; Pedregosa et al., 2011). Therefore, the relevance (or importance) score is computed as the difference between the prediction score before and after corruption. The larger the difference is between the PSS values, the more important the feature is likely to be to the model.

After a model is trained using a training data set, I shuffle each feature k times within the validation set to estimate the average importance. To statistically evaluate the feature importance, I use bootstrap re-sampling to test the null hypothesis that a feature has the same average importance as all the other features. Prior to shuffling any features, the PSS, p_0, is computed on the validation set. Then each feature f is shuffled k times and the PSS, $p_{k,f}$, is computed for each shuffle. I compute the performance difference as $i_{k,f} = p_0 - p_{k,f}$, such

that the value is positive for important features. Then, I draw n of the importance values, $i_{k,f}$, over all the features, with replacement, and compute the mean of this sample distribution. I perform this sampling process r times to obtain the bootstrap sampling distribution of the overall mean feature importance. The bootstrap sampling distribution is mean shifted to zero prior to computing the p-value corresponding to the mean importance of each feature. I use the p-values to evaluate the relevance of each feature and Šidák-correct (Šidák, 1967) the p-values to account for 110 multiple comparisons (one for each feature).

6.5 Results

While learning new motor skills, Bell and Fox (1996) and Corbetta et al. (2014) observed increasing resting state functional connectivity with locomotor experience prior to skill acquisition. Therefore, I would expect to observe increasing connectivity during the execution of crawling-based activities as well. In this section, I examine the preliminary results of my approach applied to the EEG and kinematic data from three typically developing infants, ages 4 to 8 months during a 9 week period of crawling-related activities with the SIPPC. The infants attended weekly sessions following the protocol described in Section 6.3. Limb movements of the infants were recorded using kinematics and their brain activity was recorded using EEG. Approval for this study was obtained from the OU-HSC IRB (#5120).

During crawling acquisition, infants will progressively reach more, in addition, to coordinating more movements between both arms (Adolph & Franchak, 2017; Adolph et al., 1998). Therefore, correlations between the frequencies at lateral electrodes are currently of focus because activity in the lateral sensorimotor regions is related to movement of the upper limbs, as well as more dexterous actions (Chouinard & Paus, 2006). Additionally, lateral electrodes have the largest maximum distances from other electrodes, reducing the potential influences of volume conduction on the correlations between the distant electrodes. Thus, I hypothesize that with development there will be increasing correlation between activity at

contralateral electrodes. I also examine the relevance of the EEG electrodes and frequency bins for predicting the limb movements. The movement of the limbs are predicted during three developmental time frames. Ipsilateral activity in the brain is established early in infancy and generally persists throughout the remainder of one's life span (Nevalainen et al., 2008; Salamy et al., 1985). Whereas contralateral activity is progressively developing throughout childhood before stabilizing in adulthood. Therefore, I hypothesize that the ratio of the number of relevant contralateral features to the number of important ipsilateral features will increase, over the developmental period. Additionally, I hypothesize that the number of important features at the medial electrodes will increase for predicting feet movement. Lastly, I hypothesize that the important features will be in the frequency range $3-8$Hz since it contains the range of mu rhythm frequencies observed in infants ages 4 to 8 months old (Marshall et al., 2013; Xiao et al., 2017).

6.5.1 Interactions Between Brain Regions

Specific co-occuring activation patterns across multiple brain regions could be the result of functional neural communication and may present distinct coherence behaviors throughout maturation. Longitudinal increases in coherence could suggest general increases in related synaptic connections or the strength of these connections. The correlation between the spectral power of different EEG signals is mathematically analogous to coherence (Guevara & Corsi-Cabrera, 1996; Thatcher, 1998). Therefore, I use a correlation analysis to describe the EEG activity over the course of the study to establish a general understanding of the relationship between the EEG electrode location and frequency bin of this infant cohort. These correlations describe potential functional relationships between different brain regions based on spectral power averaged over one second time intervals across three weeks. These results could be used for descriptive comparisons with infants at risk for CP, in addition to describing the impacts of different activity-based rehabilitative approaches.

Using data from all the infants, I compute the Pearson correlation between the spectral

power at EEG electrode locations for three developmental time periods during crawling-based trials. Infants only participated in one EEG session a week. Therefore, each time period contains three weeks to increase the number of trials within the developmental periods. I compute the correlations on one second time scales across three infants for each three week period. In Figure 6.5 are two sets of correlation maps. Electrodes 22 and 63 are discussed here to observe the longitudinal changes in lateral EEG activity since lateral activity is associated with movement of the arms. The top row of correlation maps are the correlations between the average power at electrode 63 in the bin $3-5$ Hz to all the other locations and frequency bins for the three developmental time periods. Each column of heat maps is for a set of three weeks. Within each correlation map in Figure 6.5, the horizontal axis is the EEG electrode and the vertical axis is the frequency bin. There is an overall increase in correlation between the average power at electrode 63 in the $3-5$ Hz bin and the different locations and frequency bins, over the three time periods. For example, in the first 3 weeks above 12 Hz at each of the EEG electrodes the correlation is below .3. During the last 3 weeks, the correlations for these same features are greater than or equal to .3. This could suggest more average synchronization of lateral activity with the activity at the other locations and frequency bins over time. These increases could be related to the production of more or stronger synaptic connections between the corresponding brain regions (Thatcher, 1998). Similarly, in the bottom row, the correlations with electrode 22 in the frequency bin $3-5$ Hz are increasing over time. During each developmental period, higher correlations are seen contralaterally, medially, and in the lower frequency ranges at the immediate neighbors. Correlations between the immediate neighbors may also be influenced by volume conduction. However, these correlations might be small since they decrease rapidly with increasing frequency bin at the adjacent electrodes during earlier developmental periods.

In the first three weeks, higher correlations are also seen medially for the power at both electrodes 22 and 63 in the $3-5$ Hz range. This would indicate higher medial-lateral functional connectivity. The increasing medial-lateral functional connectivity might indicate improving

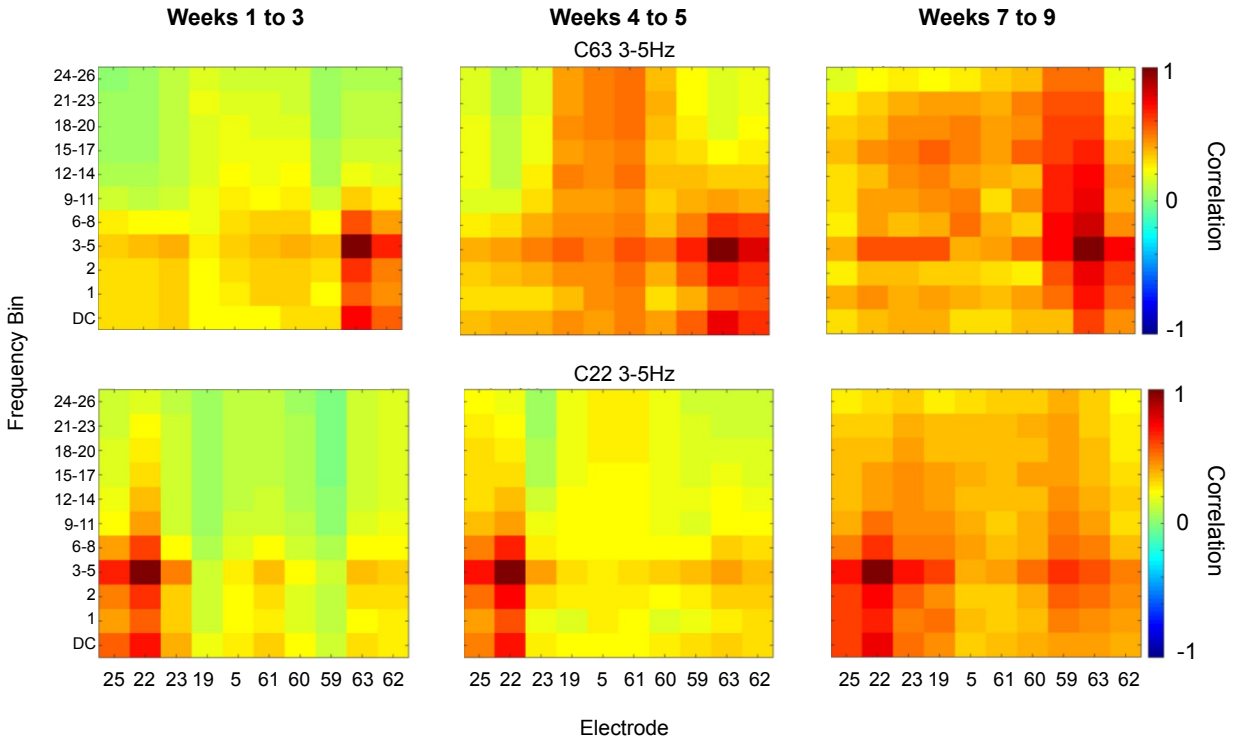


Figure 6.5: Correlation of the 3−5Hz frequency bin at electrodes 22 (bottom row) and 63 (top row) to all the other features for the three infants.

coordination between the feet and arms. Additionally, high correlations are seen in lower frequency bins at electrodes 22 and 63; however, these features might be more impacted by some power leaking between the adjacent frequency bins below the 3−5 Hz bin since they are more narrow bins than those at the higher frequencies. Despite electrode 22 and 63 being directly contralateral to each other, the trend in correlation is not completely symmetrical between the two. For example, during the second developmental period, the average power correlation is higher medially in the upper frequency ranges with the power at electrode 63 than with electrode 22. This asymmetry may indicate the difference in specialized functions performed by each of the hemispheres. Although high correlations are present in these results, I have not accounted for multiple comparisons which could also be a factor. Corrections for multiple comparisons should be performed in future expansions to this work, along with regression analyses to quantify the significance of these longitudinal correlation trends.

6.5.2 Correlates Between Spectral Power, Electrode Location and Limb Movements

As infants mature, their brains experience a variety of regional and interregional changes. For example, Xiao et al. (2017) found increasing power of the mu rhythm frequency over multiple central locations while infants rested prior to the onset of crawling. A set of these changes are impacted by infant motor behavior. Therefore, to identify which EEG electrode locations and frequency bins are most predictive of specific limb movements, I construct and examine several models using the methods described in Section 6.4. I expect with maturation, the ratio of the number of contralateral-to-ipsilateral important features will increase in the frequency range 3−8 Hz.

Figure 6.6 contains a set of results from three SVC models, each detecting the movement of a different set of limbs, over three developmental time periods. Each row of feature importance heat maps corresponds to a different set of limbs. The feature importance measures how relevant an electrode-frequency pair is to the model for prediction. The feature importance for predicting limb movement is determined by testing the hypothesis that a feature has the same average importance as all the other features. The most relevant features are identified based on their Šidák-corrected p-values from the hypothesis tests. The p-values are indicated by color. The features in light to dark red have a $p-value \leq .05$. I refer to these features as important, indicating they have a mean importance significantly greater than that of the other features.

All the models use the linear kernel function. For 8 of the 9 models, the average test PSSs for the three-week time periods are in the range .01 to .12. These models are able to correctly predict movement but with low generalized skill. The model for predicting right arm movements in the last three-week period has no skill with a PSS of −.09.

Ipsilateral brain activity develops early in infancy and contralateral brain activity gradually increases during childhood (Nevalainen et al., 2008; Salamy et al., 1985). Therefore, I expect

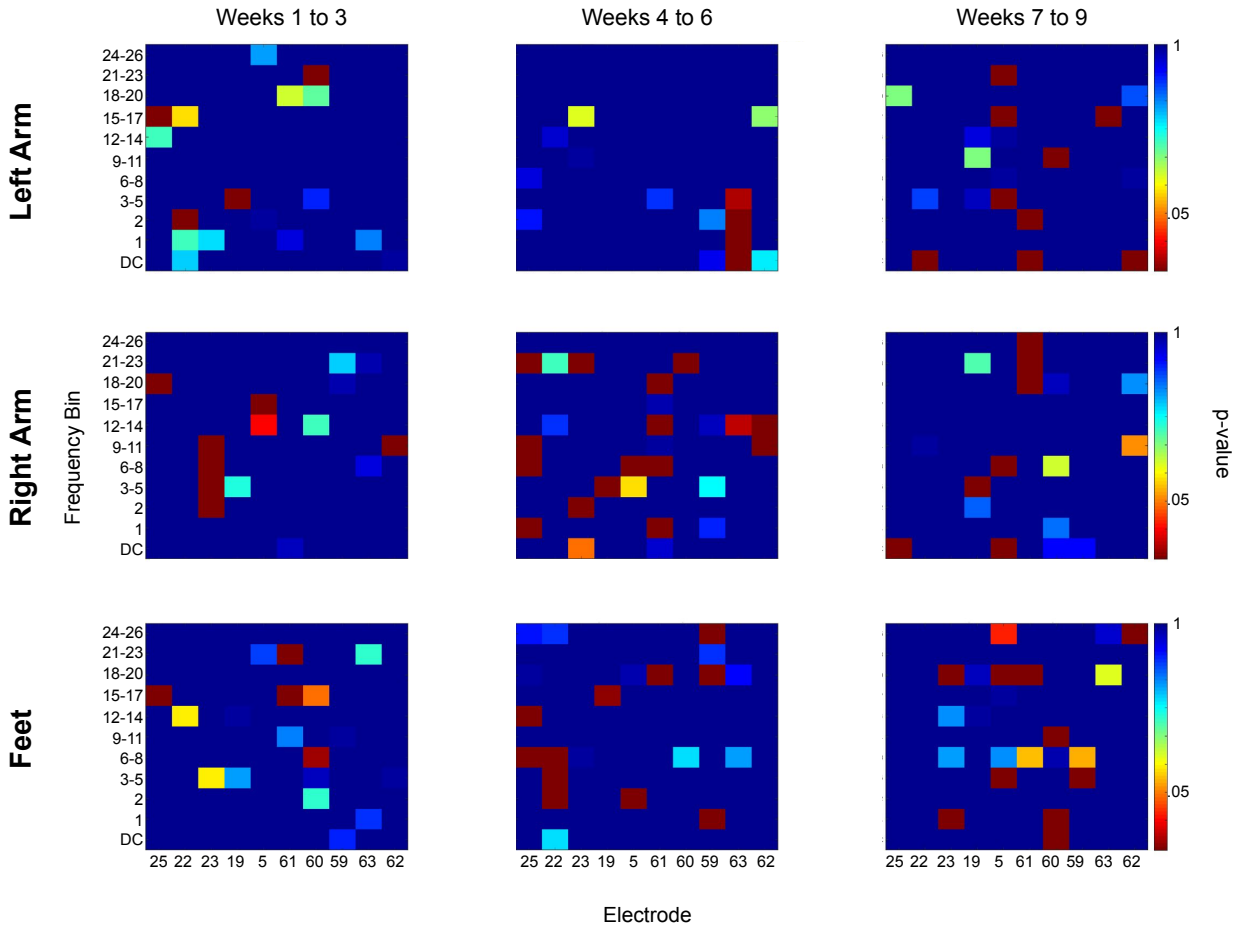


Figure 6.6: Spectral and spatial features most relevant for predicting limb movements at electrodes over the central sulcus. Features colored in red have an average feature importance significantly greater than the other features. The EEG electrode is the horizontal axis and the frequency bin is the vertical axis.

the number of important contralateral features to increase between successive developmental periods and the number of important ipsilateral features to remain constant. Examples of contralateral features relevant for predicting left arm movement are seen in weeks 4 to 6 and 7 to 9. In weeks 4 to 6, the contralateral activity occurs at electrode 63 in the frequency range 0 to 5 Hz. During this period, the frequency range 0 to 5 Hz might be related to functional changes in the boundaries of the delta-theta and theta-alpha bands observed by Xiao et al. (2017). In the last set of weeks, the significant contralateral features are at electrode 63 for 15-17 Hz and electrode 62 for the DC band. Additionally, there are significant

features that are medial and on the right at electrode 61 for the DC and 2 Hz bands and at electrode 60 for 9−11 Hz. These features might be related to the exploration of a variety of movements with the limb while learning to crawl with the SIPPC. The significance of the 9−11 Hz bin might be related to the infants exploring more intricate brain functions to produce complex, coordinated actions with the limb.

Contralateral activity is further supported by the larger quantity of significant features on the left when predicting right arm movement. In Figure 6.6, the number of significant features suggesting contralateral activity for the left arm movement overall increases from the first developmental period to the last. Additionally, there are relevant frequency bins at ipsilateral electrode locations during the first and last developmental periods. Similar to what has been observed in other studies, ipsilateral activity is most relevant at early ages, and becomes dominated by the development of contralateral activity at later ages (Nevalainen et al., 2008; Salamy et al., 1985). However, my results show the developmental change in the ratio of relevant contralateral-to-ipsilateral features is nonlinear.

For the feet, I expect most of the significant features to be at the more medial electrodes (i.e., 19, 5, 61, 60), which is seen during the first and last set of weeks. However, during the weeks 4 to 6, most of the significant features are dispersed over both sides. This could indicate that lateral regions are also involved in aspects of generating foot movements.

Different sets of features are found to be significant during each developmental period, with less than five overlapping features between the periods. This could be related to different sets of brain functions beginning to develop during the different stages of maturation. Additionally, there could be developmental changes that occur on weekly time scales that are missed by the current analysis since it observes development on longer, 3 week time scales. However, one common observed patterns for each set of limbs and across time is that multiple frequencies from the same electrode are found given the current models. Examples of this pattern are seen when detecting left arm movement, at electrode 63 during the second developmental period and at electrode 5 during the last time period. This could mean that multiple neural

functions are performed at the corresponding regions of the central sulcus and are relevant for predicting the left arm movements.

6.5.3 Discussion

Implications of Correlation Analysis

Combining the preliminary results of the analyses above provides a stepping stone for future investigation of specific regions and frequencies during infant locomotion. Performing the same analyses for atypically developing infants can assist with identifying differences in brain development and potential impacts on motor behavior. To illustrate, a comparative correlation analysis between typical and atypical infants could indicate potential topographic and functional connectivity differences between these groups while learning to crawl. These longitudinal differences could indicate differing patterns of increasing or strengthening synaptic connections and pruning. The longitudinal differences can also be correlated with measures of locomotor performance. This could allow clinicians to identify motor repertoires for infants with CP that could have the potential to more directly address their functional brain connectivity pertinent to locomotive capacity.

In children with CP, I would expect lower inter-hemispheric correlations in the alpha and beta bands during locomotion and slower increases over the developmental period. I expect reduced inter-hemispheric correlations because lower inter-hemispheric coherence have been observed in older individuals with CP during resting states and the magnitude of the reduction is related to the severity of the brain injury (Kulak & Sobaniec, 2005; Kułak & Sobaniec, 2003). Infants with CP are delayed in obtaining various developmental motor milestones, therefore, it is plausible this might also be related to slower changes in functional connections.

In general, most studies on coherence describe resting state activation patterns in adults or older children (Chorlian et al., 2009; Corbetta et al., 2014; Forman et al., 2022; Guevara

& Corsi-Cabrera, 1996; Koeda & Takeshita, 1998; Kukke et al., 2015; Kulak & Sobaniec, 2005; Kułak & Sobaniec, 2003; Meijer et al., 2016). Bell and Fox (1996) perform one of a few studies that focus on infants. However, they focused on resting state coherence and did not examine longitudinal coherence changes. They compared resting state coherence between groups of infants with varying amounts of crawling experience. They found higher intra-hemispheric coherence in novice crawlers compared to prelocomotor and experienced crawlers. They concluded this may be due to an over production of synapses in anticipation of skilled locomotion. Therefore, once an infant is skilled at crawling, the superfluous connections are pruned. However, very few studies have described longitudinal developmental changes in coherence during locomotor activities, or compared these longitudinal changes to those of infants with CP. My preliminary work is the first step to comparing longitudinal changes in functional connectivity between typical infants and those with CP during crawling acquisition, by initially characterizing coherence during typical infant locomotion.

The current correlation analysis identified potential evidence for increasing average functional communication between the lateral regions of the central sulcus and the medial and contralateral sites during the acquisition of crawling. This is consistent with my hypotheses and could be related to more information being exchanged within and between the hemispheres to coordinate certain types of actions during crawling-based activities. Whilst higher correlations between the adjacent electrodes are expected to be partly impacted by volume conduction, the correlations at the left and right neighbors do not appear to be identical, especially during the first 3 weeks for electrode 63 (top row). If these differences are significant, it could be related to non-uniform distributions of the local synaptic connections around the electrode of focus. Since distinct frequency ranges are related to specific functions in specific regions, correlations between these would suggest simultaneous recruitment of these functions to perform more complex tasks. For example, the frequency bins above the 12-14 Hz range have high correlations between the electrodes 63 and 59, especially in the last 3 weeks. This might be a result of an increase in functional diversity of the local brain region

and coordinating these neural processes to produce new types of movements in order to learn and practice crawling-based actions.

My preliminary results potentially extend observations by Bell and Fox (1996). They observed increasing resting state intra-hemispheric coherence prior to experienced crawling in 8-month-old infants. These results suggest increasing synapse production to facilitate learning various pre-crawling motor skills. This is also consistent with work by Corbetta et al. (2014) that found that during novice motor learning stages in infancy, coherence consistently increases. However, these studies examined only resting state intra-hemispheric coherence and in the frequency range 6-9 Hz. Additionally, they compared coherence between groups of infants as opposed to examining the developmental trajectories of the infants. In this work, I examine the coherence longitudinally during the locomotor task of interest.

Similar to what Thatcher et al. (1987) identified in resting state intra-hemispheric coherence, I identified differing developmental rates between the left and right hemispheres in my preliminary results while infants perform crawling-based activities. These differing rates may be indicative of the specialized roles of the hemispheres (Krashen, 1976; Meijer et al., 2016). During the second developmental period, higher correlations are observed between electrode 63 and the medial electrodes (top row), than what is observed between electrode 22 and the medial electrodes (bottom row). If these correlations are significant, this could be related to hemispheric specialization. However, on its own, correlation is insufficient information to verify the neurophysiological factors that generate the observed activity (Chorlian et al., 2009) and should be corroborated with other neurological measures.

An unexpected observation in the correlation results is that the vast majority of the correlations are positive. Very few correlations are less than zero. The few correlations that are less than zero are very small negative values greater than $-.06$. The precise cause of this positive bias in the correlations is unclear. Volume conduction could be contributing to the bias in the activity between the neighboring electrodes but is less likely to impact the more distant pairs. However, in future work, volume conduction should be explicitly addressed to

verify its influence (Chorlian et al., 2009; Holsheimer & Feenstra, 1977). Another possible factor that should be investigated, is the impact of computing the correlation over all the one second intervals from all three weeks of the three infants within each development period. This might heavily skew the data results towards positive values. A third factor that should be investigated, is the impact of the feature normalization I used, defined in Equation 6.6. Power spectra are typically normalized over the frequency domain within a single time frame and individual. However, in machine learning, features are normalized over all the data instances. In my preliminary approach, I normalize over the data instances which consists of the power spectra over all one second intervals from all three weeks within each development period. A fourth potential influence could be high autocorrelation. This could potentially bias the power computations and should be examined in future work.

The conclusions that I have drawn have several limitations that should be addressed in future work. First, corresponding p-values for each correlation should be computed. Future work should compute the statistical significance of the correlations, the hemispheric differences, and the longitudinal trends. Additionally, the longitudinal correlations should be examined between the EEG electrode locations and the frequency bins in conjunction with other neurological measures. To statistically verify the slope or shape of the longitudinal trends in the correlations, a regression analysis can be performed, with time as the independent variable and correlation as the outcome measure. Additionally, Kolmogorov-Smirnov (KS) tests can be performed to compare the distribution of correlations between contralateral electrode pairs such as electrodes 22 and 63, to evaluate hemispheric symmetry in the correlations. The KS test can also be used when comparing the correlations between infants with and without CP.

Implications of Feature Importance Analysis

The feature importance analysis is part of my generalized approach to understand the activity at distinct brain regions and their potential functional changes during crawling acquisition. A feature is defined as an electrode-frequency bin pair. Results for the feature importance

analysis can be compared between typical infants and those with CP. Mutual information can be used to statistically evaluate the differences between the sets of important features between the infant groups. Differences in the relevant EEG electrodes and frequency bins for predicting specific limb movements indicate potential functional differences in the production of those limb movements. These differences can be correlated with motor performance to identify specific underlying brain activation patterns that might be related to the generation of atypical limb movements by infants with CP. Unilateral brain injuries are common in infants with CP (Kulak & Sobaniec, 2005), often leading to these infants depending heavily on the unaffected side (Graessle, 2018). Therefore, I would expect many of the relevant features to be on the side contralateral to the brain injury, when this analysis is performed using data from infants with CP.

Despite a general increase in the number of relevant contralateral features for predicting arm movement from the first developmental period to the last, the results are inconsistent with my hypothesis. The overall trend is non-monotonic, which is more consistent with observations of oscillatory developmental changes in mean coherence made by Thatcher (1998). Additionally, contrary to my hypothesis, the relevant frequency bins are not bound between 3 and 8 Hz. This suggests functional activity corresponding to other frequency ranges are also related to predicting limb movements.

The sets of EEG electrodes and frequency bins most relevant to the models for predicting the limb movements change at each developmental period. This might reflect functional and structural changes that occur during each period of maturation. The important features are typically distributed over the frequency bins, with some localization over sets of electrodes, such as at electrode 61 for the right arm during weeks 4 to 6. Multiple important frequency bins at a single electrode could indicate several functional purposes of the corresponding brain region throughout the trials when moving the limb. However, more precise developmental changes might be observed at finer developmental time scales and should be examined in future work.

However, conclusions using the current models should be made with caution since the current models have low predictive performance on independent data sets, in addition to one model having a PSS of less than 0. PSS values lower than 0 indicate the model has a higher FPR (incorrectly labeled *no movement*) than TPR (correctly labeled movement) and is not reliable for movement prediction, especially, for trials when infants rarely move. Constructing models with higher generalized PSS values will increase the statistical power of the results (Altmann et al., 2010; François et al., 2006; Pedregosa et al., 2011). The low skill of the current models suggest that inaccurate relevance values might be used for some features, resulting in poor movement prediction. Models with high skill would likely identify different EEG electrodes and frequency bins as important in order to boost the performance. Additionally, different kernels for the SVCs yield different sets of important features, in part due to the differences in the shape of the classification boundary. The current models use a linear kernel and might not capture all the meaningful complex characteristics necessary to distinguish movement and *no movement*.

Lastly, the current feature importance technique does not directly measure important correlations between pairs or sets of electrodes and frequency bins. The feature importance is computed by corrupting a singular feature, independent of the other features and is not guaranteed to identify sets of correlated features. Less computationally efficient approaches to the feature importance could simultaneously corrupt sets of features to identify relevant relationships between sets of electrodes and frequency bins for predicting specific limb movements. Further advancements to this work will aim to improve the skill and consistency of the models, incorporate more infants and locomotor measures, and extract more precise details of the relationships between sets of features.

Chapter 7

Conclusion and Future Work

Motor behavior is a dynamic sequence of posture changes, the result of complex coordinated neural processes (Brattoli et al., 2021), and encompasses every type of action from reflexive to goal-orientated, for every combination of limbs (Adolph & Franchak, 2017). Traditional locomotive analyses typically use broad summary statistics that likely over simplify the rich complexity of locomotion. Additionally, these analyses often use labor-intensive manual examination that inhibits processing data from large numbers of trials and individuals.

In this dissertation, I propose an approach to elucidate some of the complexity in motor behavior through unique multimodal characterizations of distinct time-varying patterns from available gait measures from individuals with and without osteomyoplastic transfemoral amputation (OTFA). Moreover, I identify distal residuum muscle activity in individuals with OTFA that should be targeted in rehabilitation to reduce further risk of injury. In this chapter, I discuss the implications of the results, future expansions, and contemplate potential applications for this work.

7.1 Walking Behavior of Individuals with OTFA

Individuals with OTFA still risk injury after amputation surgery and the behavior of their distal residuum muscles is not well understood. My proposed approach applies higher

order statistics to comprehensively characterize multiple distinct motor behavior patterns of individuals with and without OTFA. Prior to the work in this dissertation, the functionality of the distal residuum muscles of individuals with OTFA had not been verified. I show that the distal residuum muscles are actively used during the gait cycle and characterize multiple muscle recruitment behaviors. I show that individuals with OTFA co-activate their muscles with greater inconsistency than intact controls, indicating instability throughout gait. Presently, the state of the art in OTFA rehabilitation does not target these muscles. My results show that these muscles should be targeted to reduce risk of injury.

In traditional gait analyses, gait performance is typically described in terms of broad summary statistics that do not capture multiple behavior strategies. For example, the mean and standard deviation are often used. These metrics are not robust to outliers and are incapable of capturing multiple behavior patterns. My proposed approach use highest density regions (HDRs; Hyndman, 1996) of the muscle activation and clustering techniques to produce comprehensive, automated summaries of gait behavior that describe multiple muscle recruitment strategies. Additionally, prior studies on TFA, such as Hong and Mun (2005), Jaegers et al. (1996), and Wentink et al. (2013), described co-contraction by comparing activation patterns between averages of the muscle activity. This inaccurately represents within-stride co-activation patterns. Bae et al. (2007) quantify co-activity within-strides for a TFA cohort, for the intact limb. However, they did not compute co-activation timing or describe the behavior within the residual limb. In contrast, my approach offers a unique perspective on co-contraction in individuals with OTFA by identifying within stride co-activation peaks and summarizing the distribution of co-activation peak timing, within both limbs, to characterize co-contraction behavior. I show that the co-contraction within the intact limb of individuals with OTFA is the most inconsistent compared to the residuum limb or the limbs of the intact controls. This indicates that compensation for the missing limb and weight of the prosthesis largely falls onto the intact limb. Rehabilitation approaches should address these alterations in muscle behavior and leverage the distal residuum muscles

to improve gait performance of the OTFA cohort.

7.1.1 Potential Clinical Uses in Gait

Distributions at Time Slices During Gait

For objective holistic descriptions of behavior, it is necessary to quantify and capture the full duration and scale of the actions under real-world conditions from multiple limbs to understand the full nature of locomotion (Berman, 2018). My work focuses on just the lower limbs during gait, however, the methods utilized here have the potential to be applied to analyses with more locomotor variables and to other tasks or domains. I am able to comprehensively extract multiple time-varying behavior patterns across multiple individuals, from two unique groups, during two distinct gait tasks. In Chapter 5.3, I present distributions at each time slice during the gait cycle for the different tasks and participant cohorts. This stage of the analysis provides a compact and salient visual representation for observing the consistencies found in EMG activation patterns from all the consecutive strides and highlights deviations in activation or deactivation times. In conjunction with the HDRs, we can quantitatively assess the consistency of patterns based on whether its path falls into a 95% HDR. Therapists could use this approach to assess which muscles consistently deviate from the desired behavior and the timing of those deviations. This approach can be used to objectively evaluate and describe gait consistency beyond energy expenditure metrics (Abu-Faraj et al., 2015). Additionally, unlike the mean and standard deviation used in standard gait analyses, my approach using HDRs allows us to identify multiple likely patterns of behavior and is robust to outliers. My approach is easily scalable in terms of the number of strides and individuals by appending more strides to the data structure. Moreover, by progressively collecting a corpus or database of strides from healthy, intact control individuals during gait tasks of interest, therapists can compare activation patterns of an individual to the EMG activation distributions of the control group. The HDRs can be

interpreted directly based on overlap. If certain muscle activation patterns are too likely (i.e., parts of HDRs overlap with undesired activation levels) or there is too much variation (i.e., large HDRs) then therapists can work with individuals to address the use of those muscles.

Additionally, my approach provides more precise detail about prosthetic fit and use. Prosthetists predominately rely on broad, subjective reporting from the individuals for determining the quality of the prosthetic fit. Individuals cannot provide exact locations or quantify the amount of adjustment necessary. Prosthetists have collected pressures from within residuum sockets for analysis (Commuri et al., 2010), however, these analyses examine average pressures and standard deviations, which are incapable of identifying multiple modes of activation and result in inaccurate assessments of the true dynamic fit. My proposed approach presents prosthetists with a method for understanding the quality of the fit from all the strides and quantifying the consistency to make more refined adjustments, in conjunction with the comfort assessments from the individuals by using the HDRs of the pressures.

Additionally, the distributions at each time slice during gait in Chapter 5.3 provide a general description of the likely activation values at each time point, independent of the prior time slices. However, events at each time during gait influences the set of time samples after it. Therefore, a simple expansion to this analysis stage is to instead compute 2D densities and then calculate the HDRs to obtain planes instead of intervals consisting of the most likely patterns (or paths) of activity. Construction of 2D HDRs are more precise when attempting to identify activation paths through space (i.e., the activity) and time. However, individual muscles do not exist in a vacuum independent of other muscles. Analysis of singular muscles is best contextualized in relation to other muscles operating around the same joint. Therefore, when making decisions about modifications to muscle recruitment strategies it is better to explicitly identify co-occurring peaks within the same stride and not compare independent aggregate behavior between muscles.

One reason I use Gaussian Mixture Models (GMMs) for clustering to extract gait phenotypes in Chapter 5.6, is that they are also probability density estimators of the data.

Therefore, they can also be used to generate plausible RSI pressures and muscle recruitment strategies under specific conditions. In future expansions to this work, the GMMs could be useful for predicting the impacts of combinations of surgical approaches, prosthesis designs, and rehabilitation methods. This could provide healthcare providers with additional details about the possible outcomes to different patient-care plans prior to their implementation.

One draw back in my current approach is the preliminary decision to manually set the detection threshold percentiles and select the RSI sensors for computing the mean to identify the OTFA stride events. This decision was made early in the exploratory phases of developing the approach and has potential to impact the timing of the activation patterns when inappropriate values are set. In the future, evaluating the distribution of the signal-to-noise ratios (SNRs) of the pressure sensors to determine which pressures to use for computing the mean RSI would further improve the robustness of the approach to low quality data. Additionally, HDRs of the continuous pressure and EMG signals prior to stride extraction can also be used for objectively determining threshold cut-offs based on activation likelihoods. Nevertheless, the threshold and sensor selection are modular components to the overall approach, therefore, they can easily be replaced with different statistical methods. In my current approach, the exact threshold value has less impact with increased consistency across many strides since the same threshold is used for all the strides within a subject. Any false positives in the stride detection, as a result of the threshold being too low, would yield strides that were too short and would be omitted from the analyses. Any strides that are missed by the stride detection, as a result of the threshold being too high, would become part of the previously detected stride, making that stride too long and would be omitted from the analyses.

Contextualizing Co-contraction

In Chapter 5.5, I examined muscle co-activation of the distal adductors, hamstrings and quadriceps groups within the OTFA residuum concomitantly with the contralateral intact

limb. In addition, I examined the RSI pressures during brisk and self-paced gait in a homogeneous OTFA cohort. I demonstrated the presence of distal residuum muscle activity for individuals with OTFA, in addition to characterizing co-contraction timing. The distal residuum muscle activity is a significant finding, since these muscles are not functional for individuals with traditional amputation surgery and thus generally not targeted by clinicians during therapy for those with osteomyoplastic amputation (Dionne et al., 2022; Taylor & Poka, 2016). Instead, clinicians typically target the hip muscles during therapy sessions for individuals with OTFA. The evidence I have shown can motivate more exploration into the distal motor capacity of those with OTFA and promote rehabilitative training of the distal residuum to assist in improving health care outcomes for individuals with OTFA. Despite the osteomyoplastic approach being invented about a century ago, little is known about the precise motor capabilities of those with osteomyoplastic amputation and how these capabilities change relative to factors such as residuum length, comorbidity, and prosthetic utility (Dionne et al., 2022; Taylor & Poka, 2016). Clinicians can use my proposed gait analysis approach to assist with determining appropriate postoperative protocols for personalizing care for individuals with OTFA.

Comparing Individuals with and without OTFA In Chapter 5.5, I show evidence for inappropriately timed and likely excessive co-contraction within both limbs of the individuals with OTFA. The co-contraction is likely to occur within each of the limbs of the OTFA cohort for at least 80% of the gait. This suggests diminished control and an increased dependency on the intact limb to compensate for the missing limb segment below the knee of the residual limb. Compared to the matched intact controls, individuals with OTFA are inconsistently using co-contraction within the intact limb. This increased dependency on the intact limb might place an unhealthy burden onto this limb and should be further investigated in future studies. Jaegers et al. (1996) found that the moment of knee flexion is often unstable for most with TFA due to challenges with weight-bearing on the residuum. The

osteomyoplastic approach aims to address this instability by reconstructing the weight-bearing end of the residuum. Additionally, activity found within the distal-muscle groups of those with OTFA suggests they have improved distal-muscular capacity over their traditional amputation counterparts. Therefore, future work should analyze specific modifications to OTFA distal residuum muscles recruitment strategies and assess their impact on motor control and performance.

Additionally, some differences in co-contraction between participants with OTFA and the intact controls might in part be impacted by residuum length. According to Bae et al. (2007), more residuum muscle mass increases motor performance capacity as a result of the greater potential to generate forces. Future work should include the residuum length as part of understanding the distributions of co-contraction times. Using my approach, the individuals can be grouped by residuum length prior to computing the distributions of co-contraction times. This level of analysis can offer surgeons more insights into the impacts of available salvaged tissue. Additionally, therapists are provided with insights into the precise muscle recruitment strategies and potential motor capacity of individuals receiving therapy based on more specific conditions such as the residuum mass.

Future analyses should compare co-contraction with the locomotor measures such as neural activity, upper body dynamics, kinematics and kinetics to improve the contextualization and interpretation of the results. Although the size of the OTFA and intact control cohorts are small, limiting what we can conclude about the larger overall populations, I am able to obtain a large quantity of strides for each individual to assess likely co-contraction strategies employed on a per individual basis. This is useful for personalized care in contexts such as prosthesis design and therapy. Moreover, my approach has the potential to scale with more strides and participants to expand current understanding of the dynamics of locomotion for various populations.

7.1.2 Autoencoder Latent Space Topology

Another direction for expansion is to incorporate more knowledge about the locomotor measures into the compressed representations through the AE architecture. AEs have numerous options for constraining or identifying global and local structure onto the data in the compressed space (Bao et al., 2020; Bengio et al., 2013; Champion et al., 2019; Kingma et al., 2014; Plaut, 2018; Zhou et al., 2020). For example, Kingma et al. (2014) and Zhou et al. (2020) imposed multimodal distributional representations onto the latent space to facilitate classification via statistical inference by including a penalty term into the reconstruction error. Additionally, Champion et al. (2019) imposed simplicity to minimize the size of the latent representations with sparsity constraints. Champion et al. (2019) also incorporated physical dynamics into the compressed representations, using general knowledge about physical dynamics to design an additional reconstruction penalty. In this application, including statistical inference for recognizing the number of modes (i.e., locomotor phenotypes) would allow the compressed representation and class distributions to be optimized jointly.

7.2 Functional Connectivity in Infants

I propose an approach for identifying relevant regions of the cortex and characteristic frequency bins for predicting limb movements of infants during the acquisition of crawling in Chapter 4. Prior studies on functional connectivity in infants, such as Bell and Fox (1996), Corbetta et al. (2014), and Thatcher (1998), focus on changes during resting states. Moreover, only the study conducted by Thatcher (1998) directly observed developmental changes of each of the infants. In this dissertation, I show preliminary evidence for developmental changes in functional connectivity during crawling-based activities in typically developing infants. This work is a stepping stone for comparisons to infants with CP, or other developmental neuro-motor conditions, and for assessing the longitudinal impacts of rehabilitative activities on changes in functional connectivity in infants when learning to crawl.

From the preliminary correlation analyses in Section 6.5.1, I show potential increases in correlation between activation patterns of neighboring and distant cortical regions, over three time periods that cover the acquisition of crawling for three infants. This could be due to increasing functional connectivity and suggests synaptic strengthening and/or growth with maturation. Since these correlations are observed during locomotion, they suggest that these increasing functional connections are utilized during motor activities.

The superposition of electrical activity of neighboring groups of neurons results in activity captured by an EEG electrode being highly correlated with neighboring electrode activation and is not as informative for understanding functional activation patterns. However, the longitudinal increase in correlation between distant brain regions could be a result of increasing effective connectivity. More precise relationships between the specific locomotor behavior (i.e., left arm moved) and the cortical activity are necessary to more comprehensively understand infant neuro-motor development and mechanisms of the neurological implications of any interventions. I begin to address this by constructing models that predict specific limb movements based on EEG power spectral density (PSD) captured by multiple electrodes over the cortex, and then examine the models for the most relevant features. The correlation analyses can also be expanded using regression analysis to quantitatively determine the shape and strength of the correlation trends over development.

One unexpected result of the correlation analysis is the large positive bias in the values, in spite of the average powers being normalized (procedure described in Chapter 6.4.2). The source of this result is unclear and should be examined in future work. Possible factors could be related to the shape of the distribution of the power spectra over all the infants within each three week period. The distribution might be largely skewed towards higher powers. Additionally, the autocorrelation within the data could be high and contribute to increasing the average power over all the frequency bins. The impact of these potential factors on the correlation distribution should be examined in future work.

In this dissertation, I examined the movement of three groups of limbs, of three infants: the

left wrist, right wrist and feet. In future work, I want to expand analyses to the entire body and corroborate my automatically generated movement labels with therapist assessments of movement. My current results suggest that it is possible to identify electrodes and frequency bins that are relevant for the production of specific limb movements. Overall, I show increasing quantities of significant features on the left when predicting right arm movement, suggesting contralateral brain activity. For the feet, I found features over central electrodes to be significant to the model for the first and last set of time periods. However, further work is necessary to verify whether features significant to the model have true biological significance. In addition, using skilled models, comparisons between the sets of important features for the different developmental periods and groups of infants can be statistically assessed using Mutual Information to quantify the degree of overlap. This would quantitatively describe potential differences in the functional behavior of distinct brain regions over time and between different clinical conditions. Differences in the sets of important features could be used to compare rehabilitation approaches to access differences in their influences on infant development.

However, further model exploration for the feature importance analysis is warranted. The statistically significant features are also dependent on the structure of the model. My prior exploration with SVCs that use other kernels exhibited different and inconsistent results, along with low generalized skill. I expect with more skilled and intricate models, consistency in the feature importance results can be improved. Specifically, prediction with well constructed convolutional models has yet to be fully explored such that additional EEG characteristics beyond frequency information can be leveraged more effectively to understated infant locomotor behavior and development. Convolutional models can allow us to identify more specific co-occuring patterns at multiple time scales, simultaneously. Finally, longitudinal resolution of the time periods should be increased to more precisely capture neuro-motor developmental trends. Currently, the 9 weeks are segmented into three time periods, potentially missing crucial developmental milestones and trends.

In regard to OTFA gait and infant crawling, during therapy sessions, it can be useful

to have access to concise summaries of locomotor performance in real-time to provide the individuals with more precise feedback on how to modify specific motor actions. With further refinement of my approach, incorporating it into current real-time therapy systems could be useful for therapists and individuals receiving therapy.

Appendix

This Appendix contains additional figures describing the gait of individuals with and without OTFA. In this section I provide additional details about the muscle recruitment strategies extracted in the AE latent space. Additionally, the results of the hierarchical clustering using GMMs are examined within the PC and AE latent spaces.

A1 Gait Phase Duration

The stance end times are also extracted using the procedure described in Chapter 4.2. The distributions of the stance duration for the individuals with and without OTFA are shown in Figure A1. The stance duration are measured terms of seconds and fraction of the gait cycle for brisk (blue) and self-paced (magenta) walking. The mode of each distribution is indicated by a vertical dashed line and specified as *Mo*. The horizontal red dashed lines indicate the likelihood threshold for the 95% HDRs and the green horizontal lines with diamond endpoints indicate the HDRs. The number of extracted strides are indicated by n. The distributions of stance duration are consistently narrower and start later for the control group compared to the OTFA group, as evidence by the HDRs. The narrower HDRs for the distributions for the intact controls indicate greater consistency in the stance duration for the control group.

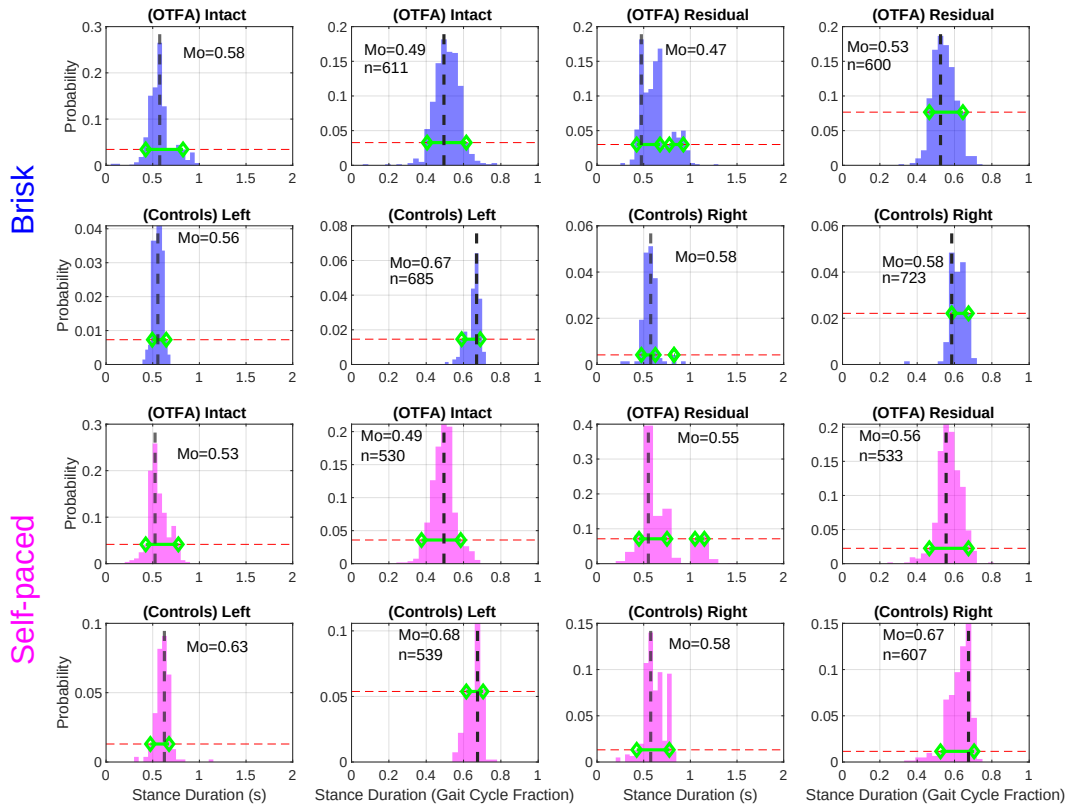
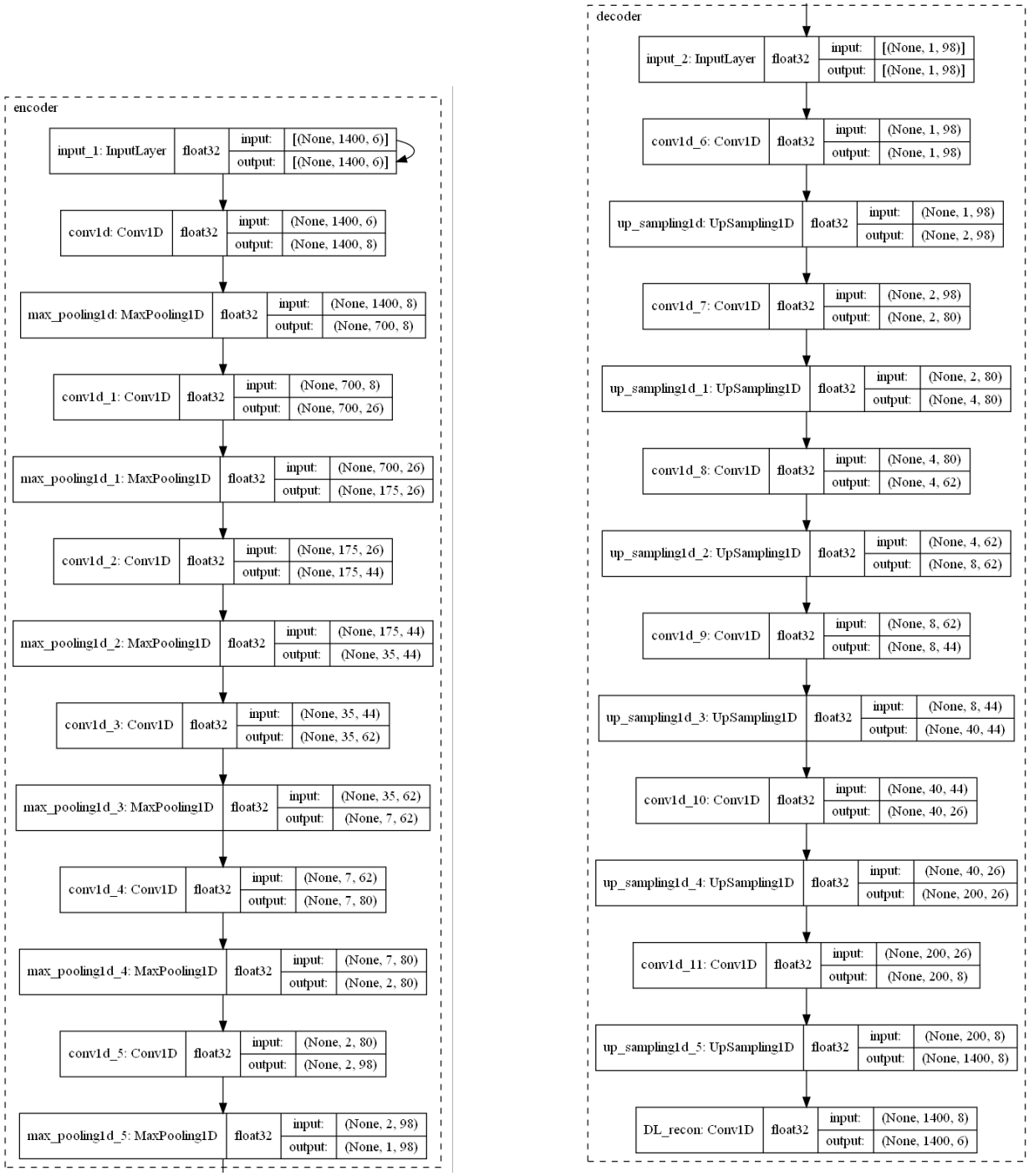


Figure A1: Distributions of stance duration in seconds and as a fraction of the gait cycle for both cohorts during brisk (blue) and self-paced (magenta) walking. Vertical dashed lines indicate the mode of the distributions. Horizontal red dashed lines indicate the threshold for the 95% HDRs. Green horizontal lines with diamond endpoints indicate the HDRs. *Mo* is short for mode of the corresponding distribution, and n indicates the number of strides extracted.

A2 Gait Phenotypes

The complete architecture diagram for the AE trained in Chapter 5.6 is shown in Figure A2. Each layer is represented by a rectangle that contains the layer name, the layer type, the data type of layer input and output, and the input and output shapes of the layer. A single data input instance has 1400 time slices with 6 EMG channels and is represented by the first



(a) Encoder (b) Decoder

Figure A2: The full architecture for the trained AE model. Each rectangle represents a layer. The left-most box contains the layer name prior to the semi-colon and the layer type after the semi-colon. The second box from the left is the data type of input and output of the layer. The right-most boxes indicate the input and output shapes of the layer. (a) The layers for the encoder. (b) The layers for the decoder.

layer in the encoder (a) and the output of the last layer in decoder (b). The compressed representation is a 1D array with 98 features represented by the last layer of the encoder and the first layer of the decoder. Additionally, ELUs are used as the activation function for all nodes except for the output layer where the sigmoid activation function is used.

In Figure A3 are the 95% and 50% HDRs of co-activation times for the top level clusters in the AE latent space that are shown in Figure 5.18. The regions in lighter colors correspond to the 95% HDRs and the darker colored regions correspond to the 50% HDRs. The heel-strike for all the muscles pairs is relative to the heel-strike of the residual or right limb. The three columns on the left are the distributions for the intact/left muscles. The three columns on the right are the distributions for the residual/right muscles. The first three rows correspond to C0. The last three rows correspond to C1. The row with the blue distributions are the distributions of the co-activation peak times between each pair of muscles for the individuals with OTFA, within the cluster. The orange correspond to the co-activation distributions for the matched intact controls within the cluster. The purple corresponds to the overall co-activation distribution for all the individuals within the cluster.

Ideally, I would expect the HDRs for at least one pair of muscles between the participant groups within a cluster to be similar. The pair of muscles with the most consistency between the participant groups would suggest that pair of activations could be one of the defining characteristics of the cluster. For example, the 50% HDRs in C1 for adductor-quadriceps co-activation have similar timing between the two cohorts around 20% and 60%. The adductors and quadriceps activating together around 20% could be part of a strategy after load response to maintain balance on the single standing limb by pulling the leg inwards with the adductors while extending the knee.

The number of strides for each participant within each top level cluster for PCA and AE are in Figures A4a and A4b, respectively. Each bar indicates the total strides for an individual. The number of strides for a participant that are placed into a cluster are indicated by color. The table below the participants contains the exact counts per cluster for the participant.

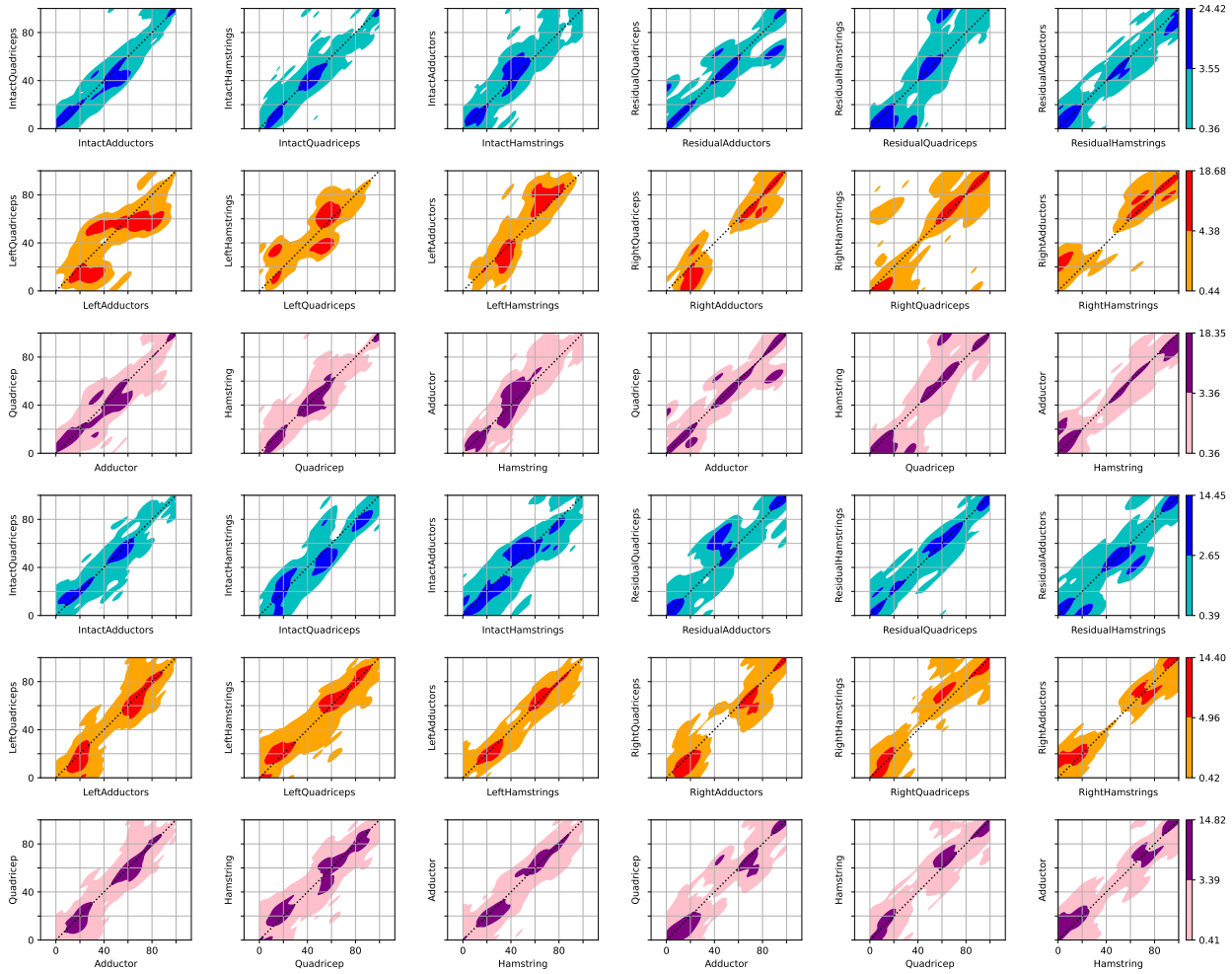
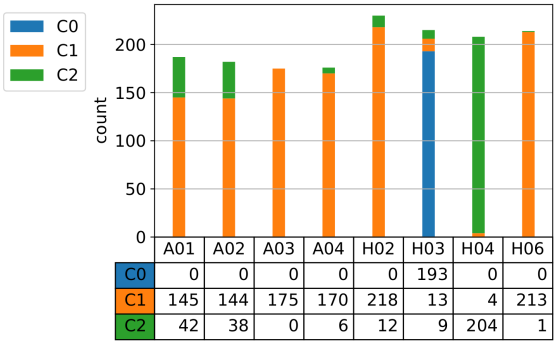


Figure A3: Co-activation time distributions for the top level clustering from AE, on the training set. HDRs are for 95% and 50% most likely paired peak activities. Blue distributions are for the OFTA strides assigned to the cluster. The orange distributions are for the intact control strides assigned to the cluster. The purple distributions are the overall distribution for the muscle pair for the cluster. The left three columns are the distributions for the intact/left muscles. The right three columns are the distributions for the residual/right muscles.

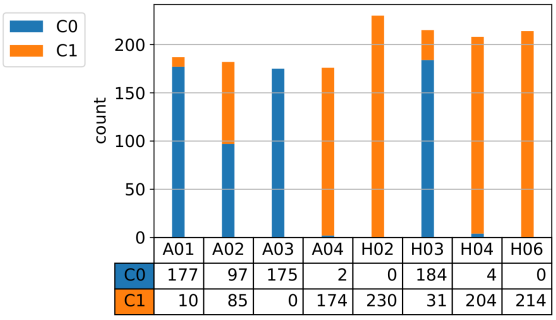
Participant codes prefixed with "A" are individuals with amputation. Participants with the "H" prefix are the intact controls.

In Figure A4a, cluster C0 (blue) in the PC space only contains strides from one participant (H03) without OTFA. This is the main reason reason C0 has a high amount of consistency across the strides. In general, participants exhibit within class consistency. Cluster C2 (green) also has the majority of its strides from a single participant without OTFA (H04). However,



	A01	A02	A03	A04	H02	H03	H04	H06
C0	0	0	0	0	0	193	0	0
C1	145	144	175	170	218	13	4	213
C2	42	38	0	6	12	9	204	1

(a) PCA Top Level Cluster Stride Counts



	A01	A02	A03	A04	H02	H03	H04	H06
C0	177	97	175	2	0	184	4	0
C1	10	85	0	174	230	31	204	214

(b) AE Top Level Cluster Stride Counts

Figure A4: Stride counts fof each participant within each top level cluster. (a) Strides for the top level clusters in the PC space. (b) Stride counts for the top level clusters in the AE latent space.

cluster C1 (orange) is the most general cluster since most of the strides within it come from multiple participants with and without OTFA. This might indicate an overlap between their likely muscle recruitment strategies.

In the AE space, two clusters are extracted. In Figure A4b, cluster C0 contains more strides from individuals with OTFA and cluster C1 contains more strides from individuals without OTFA. The larger amount of OTFA strides within C0 might suggest that this muscle recruitment strategy is less typical for healthy gait and not used as often by most individuals without OTFA. However, most of the strides for one intact control participant are also within this cluster. This could suggest an additional level of clustering is necessary to better distinguish the strategy used by the OTFA cohort from the strategy used by the intact control individual. The cluster with most of its strides from individuals without OTFA (C1) suggests it represents a more typical muscle recruitment strategy that is occasionally employed by the individuals with OTFA.

A2.1 Hierarchical Clustering

Hierarchical clustering is useful for identifying multiple levels of similarity between the strides and describing variation within muscle recruitment strategies. Specifically, I use divisive

hierarchical clustering to obtain a second level of clusters using GMMs. Within each of the top level clusters, I use cross-validation to identify an appropriate number of sub-clusters in the PC and AE latent spaces.

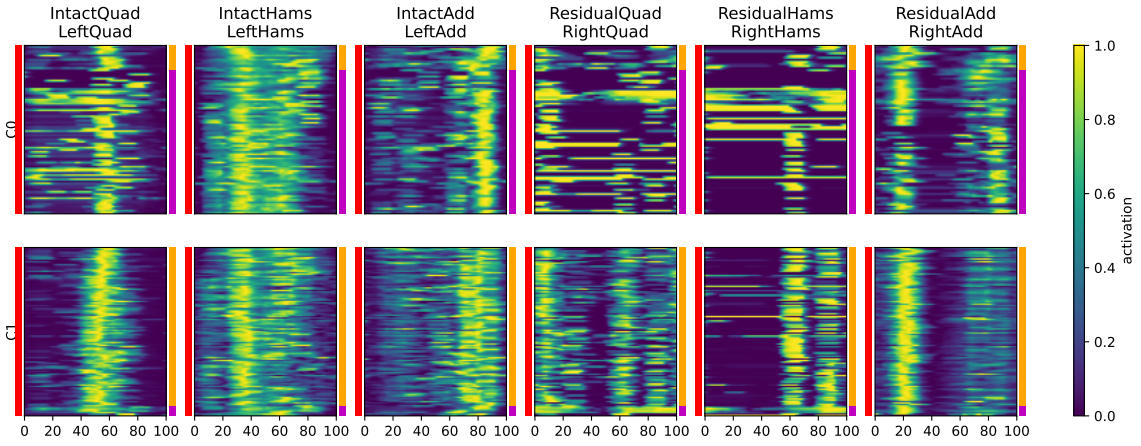
PC Space

In Figure A5 are the second level clusters in the PC space constructed from the top level clusters discussed in Chapter 5.6. These second level clusters show increased consistency across the strides, when compared to the top level clusters in Figure 5.18. The clusters are also becoming more homogenous in terms of participant group. For example, in top level cluster C1, sub-cluster 1, the vast majority of strides come from individuals without OTFA. The peak activation times are also more consistent than within the top level cluster, especially for the residual/right adductors.

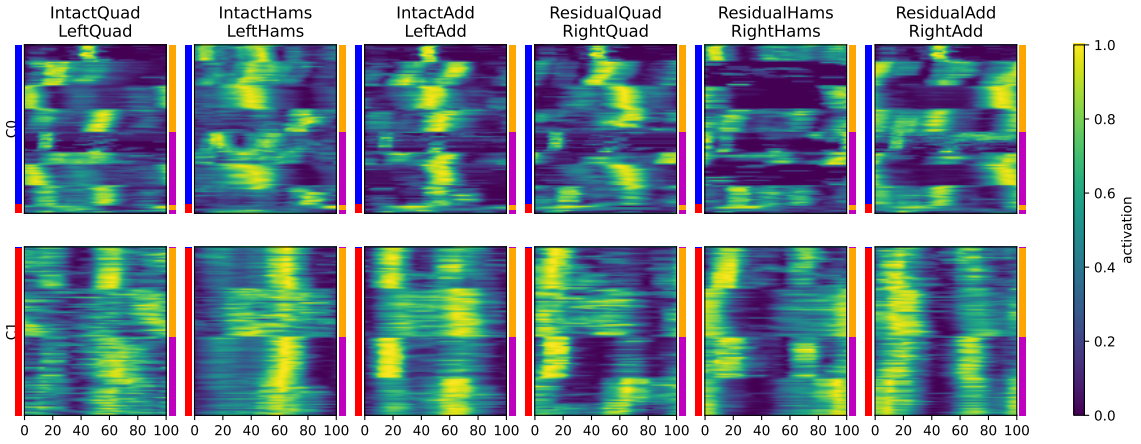
The 95% HDRs for the PC sub-clusters are shown in Figure A6. In cluster 0, sub-cluster 0, the intact/left quadriceps demonstrate a high amount of variability during most of the strides. This suggests these muscles might play an optional role in this muscle recruitment strategy for most of the gait cycle. During the residuum/right terminal swing (85−100%), the intact/left limb is in terminal stance and the intact/left quadriceps are unlikely to be used for this particular strategy. The intact/left hamstrings are likely to have activation greater than .5 between 10% and 90% of the residuum/right gait cycle, suggesting that they consistently contribute to movement during this time. Around 10% is the residuum/right load response, therefore, the intact/left limb is beginning the swing phase. This indicates these muscles consistently contribute to the toe-off. In cluster 1, sub-cluster 1, the 95% are more narrow for the intact/left hamstrings, residual/right hamstrings, and the residual/right adductors, indicating high consistency in the behavior of these muscles across the strides.

AE Latent Space

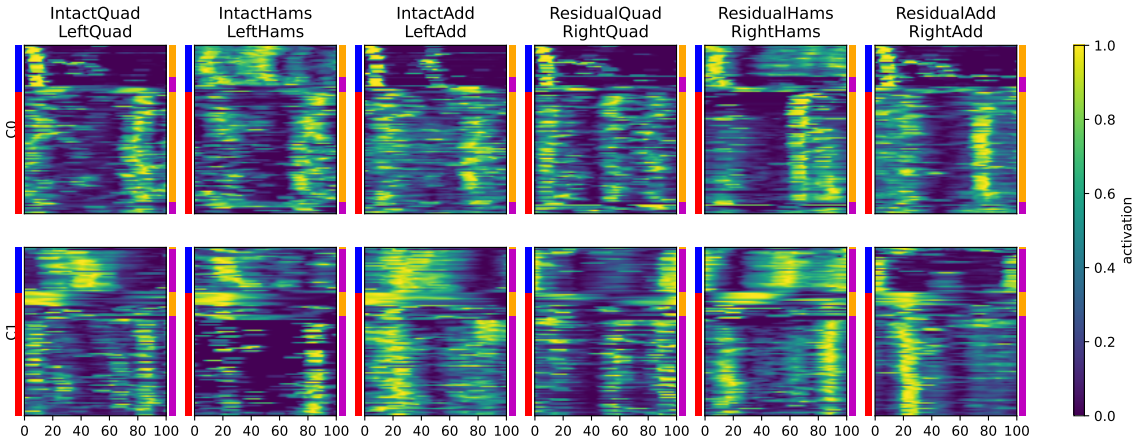
In Figure A7 are the second level clusters in the AE space constructed from the top level clusters in Figure 5.18. Similar to hierarchical clustering in the PC space, the strides within the clusters are more consistent than the strides in the higher level clusters. For example, the sub-clusters for C0 have distinct intact/left hamstrings behavior. Sub-cluster 0 of C0 has a major peak time around 40%, whereas in sub-cluster 1 there are two, more brief, major peak times around 20% and 50%. In Figure A8 are the 95% HDRs for the AE clusters. In cluster 0, sub-cluster 1, the intact/left quadriceps, intact/left adductors, and the residuum/right adductors have similar activity distributions. This suggests a strategy where these muscles might consistently co-activate.



(a) PCA Cluster 0 Sub-clusters

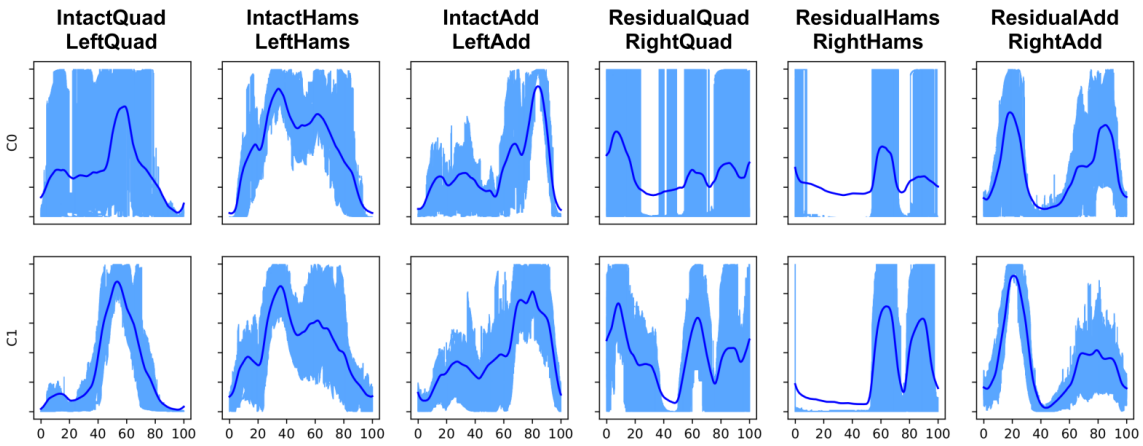


(b) PCA Cluster 1 Sub-clusters

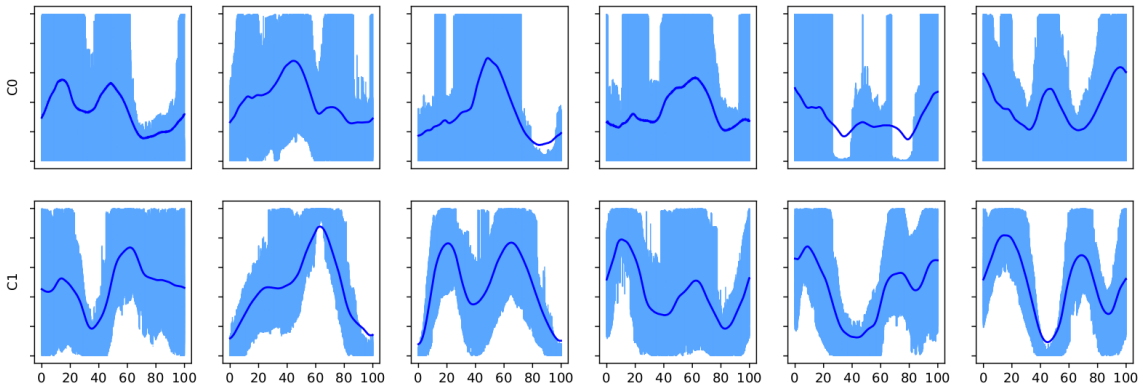


(c) PCA Cluster 2 Sub-clusters

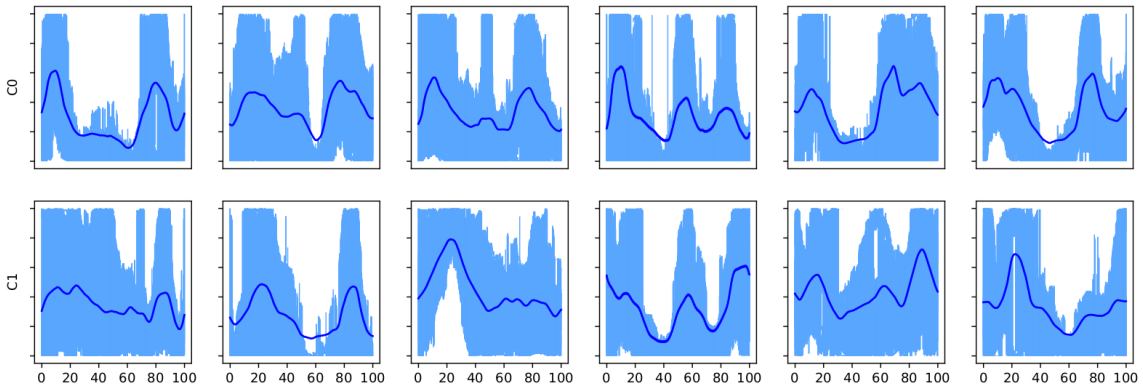
Figure A5: Lower level clusters in the PC space. (a) The sub-clusters from the top level cluster 0. (b) The sub-clusters from the top level cluster 1. (c) The sub-clusters from the top level cluster 2. The top level clusters are in Figure 5.18.



(a) PCA Cluster 0 Sub-clusters

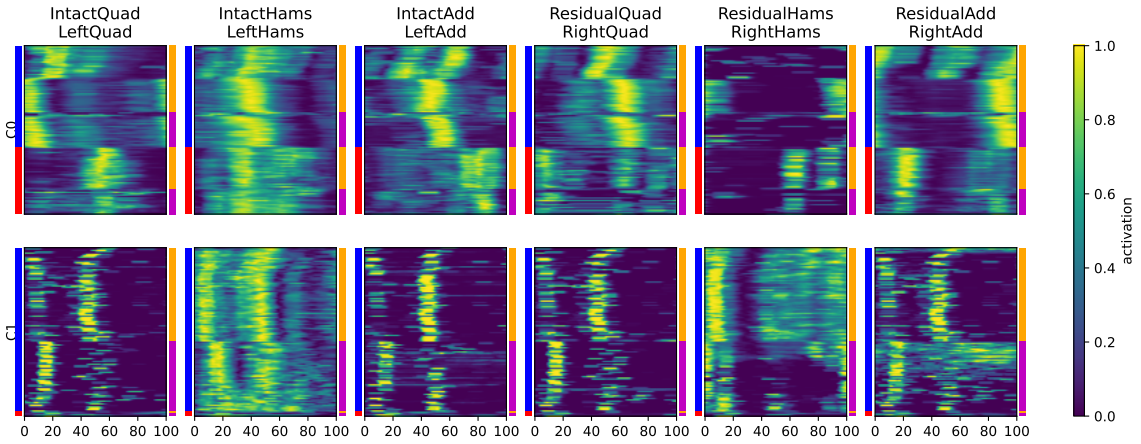


(b) PCA Cluster 1 Sub-clusters

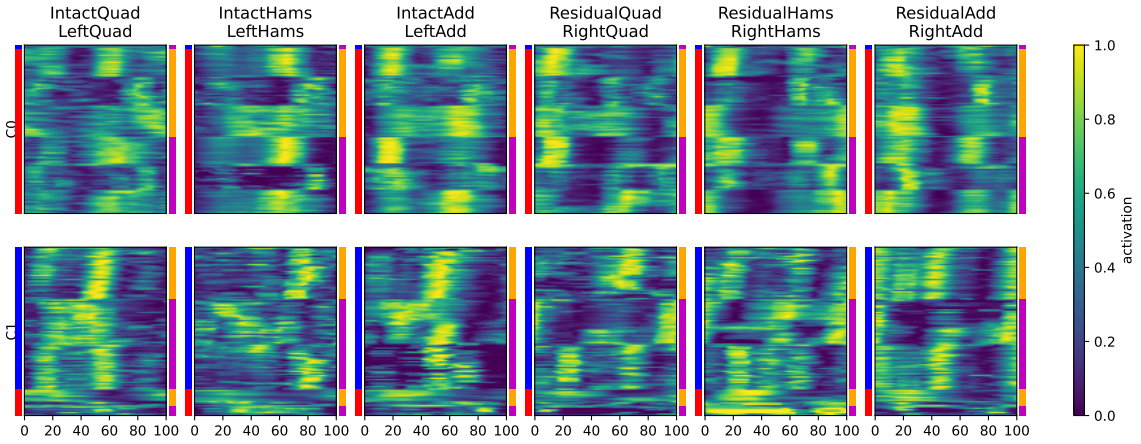


(c) PCA Cluster 2 Sub-clusters

Figure A6: 95% HDRs for the lower level clusters in the PC space.

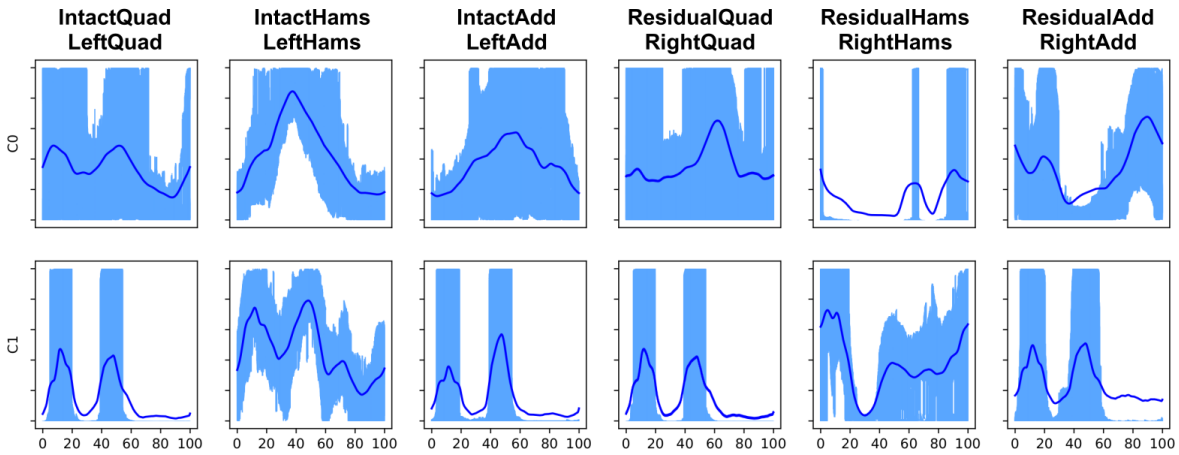


(a) AE Cluster 0 Sub-clusters

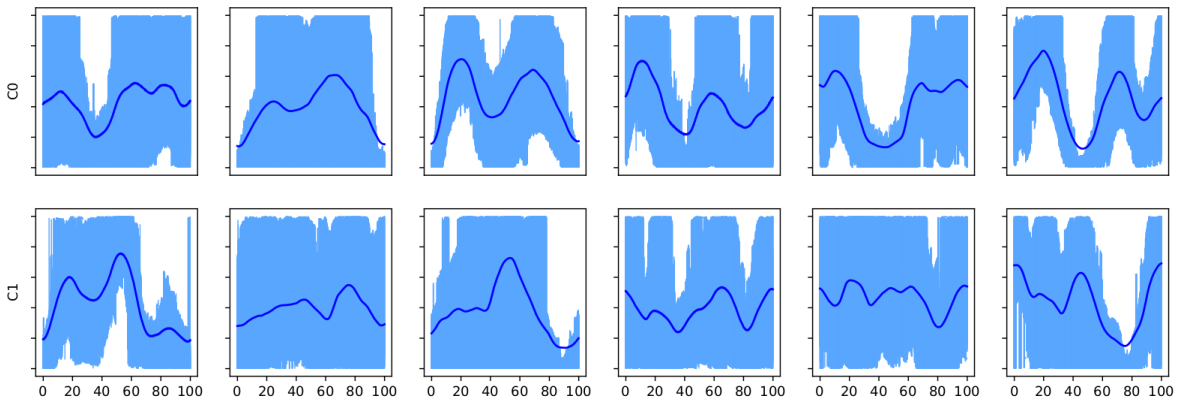


(b) AE Cluster 1 Sub-clusters

Figure A7: Lower level clusters in the AE space. (a) The sub-clusters from the top level cluster 0. (b) The sub-clusters from the top level cluster 1. The top level clusters are in Figure 5.18.



(a) AE Cluster 0 Sub-clusters



(b) AE Cluster 1 Sub-clusters

Figure A8: 95% HDRs for the lower level clusters in the AE latent space.

Bibliography

Abu-Faraj, Z., Harris, G., Smith, P., & Hassani, S. (2015). Human gait and clinical movement analysis. *Wiley Encyclopedia of Electrical and Electronics Engineering*, *12*, 1–34. https://doi.org/10.1002/047134608X.W6606.pub2

Adolph, K. E., Anderson, D. R., Bartz, D., Bateson, P. P. G., Bechtold, J., Benner, A. D., Bergman, L. R., Berkel, C., Bonner, S. B., Bornstein, M. H., et al. (2015). *Handbook of child psychology and developmental science: Theory and method*. Wiley Online Library.

Adolph, K. E., & Franchak, J. M. (2017). The development of motor behavior. *Wiley Interdisciplinary Reviews Cognitive Science*, *8*(1-2). https://doi.org/10.1002/wcs.1430

Adolph, K. E., Vereijken, B., & Denny, M. A. (1998). Learning to crawl. *Child Development*, *69*, 1299–1312. https://doi.org/10.1111/j.1467-8624.1998.tb06213.x

Akiyama, Y., Toda, H., Ogura, T., Okamoto, S., & Yamada, Y. (2018). Classification and analysis of the natural corner curving motion of humans based on gait motion. *Gait & posture*, *60*, 15–21.

Alamdari, A., & Krovi, V. N. (2017). Chapter two - A review of computational musculoskeletal analysis of human lower extremities. In J. Ueda & Y. Kurita (Eds.), *Human modeling for bio-inspired robotics* (pp. 37–73). Academic Press. https://doi.org/10.1016/B978-0-12-803137-7.00003-3

Altmann, A., Tolosi, L., Sander, O., & Lengauer, T. (2010). Permutation importance: A corrected feature importance measure. *Bioinformatics*, *26 10*, 1340–7.

Arac, A., Zhao, P., Dobkin, B. H., Carmichael, S. T., & Golshani, P. (2019). DeepBehavior: A Deep Learning Toolbox for Automated Analysis of Animal and Human Behavior Imaging Data. *Frontiers in Systems Neuroscience*, *13*. https://doi.org/10.3389/fnsys.2019.00020

Arlot, S., & Celisse, A. (2009). A survey of cross validation procedures for model selection. *Statistics Surveys*, *4*. https://doi.org/10.1214/09-SS054

Atri, R., Marquez, J. S., Murphy, D., Gorgey, A., Fei, D., Fox, J., Burkhardt, B., Lovegreen, W., & Bai, O. (2016). Investigation of muscle activity during loaded human gait using signal processing of multi-channel surface EMG and IMU. *2016 IEEE Signal Processing in Medicine and Biology Symposium (SPMB)*, 1–6. https://doi.org/10.1109/SPMB.2016.7846882

Bae, T. S., Choi, K., Hong, D., & Mun, M. (2007). Dynamic analysis of above-knee amputee gait. *Clinical Biomechanics*, *22*(5), 557–566. https://doi.org/10.1016/j.clinbiomech.2006.12.009

Bai, Y., & Gao, M.-Y. (2022). Effect of crawling training on the cognitive function of children with cerebral palsy. *International journal of rehabilitation research. Internationale Zeitschrift fur Rehabilitationsforschung. Revue internationale de recherches de readaptation*, *45*(2), 184–188. https://doi.org/10.1097/mrr.0000000000000526

Bao, X., Lucas, J., Sachdeva, S., & Grosse, R. (2020). Regularized linear autoencoders recover the principal components, eventually. *Advances in Neural Information Processing Systems*, *33*, 6971–6981. https://doi.org/10.48550/ARXIV.2007.06731

Bax, M., Goldstein, M., Rosenbaum, P., Leviton, A., Paneth, N., Dan, B., Jacobsson, B., & Damiano, D. (2005). Proposed definition and classification of cerebral palsy. *Developmental medicine and child neurology*, *47*(8), 571–576. https://doi.org/10.1017/s001216220500112x

Bell, M. A., & Fox, N. A. (1996). Crawling experience is related to changes in cortical organization during infancy: Evidence from EEG coherence. *Developmental psychobiology*, *29*(7), 551–561.

Bengio, Y., Courville, A., & Vincent, P. (2013). Representation learning: A review and new perspectives. *IEEE Transactions on Pattern Analysis and Machine Intelligence*, *35*(8), 1798–1828. https://doi.org/10.1109/TPAMI.2013.50

Bergstra, J., Bardenet, R., Bengio, Y., & Kégl, B. (2011). Algorithms for hyper-parameter optimization. *Proceedings of the 24th International Conference on Neural Information Processing Systems*, 2546–2554.

Berman, G. J. (2018). Measuring behavior across scales. *BMC biology*, *16*(1), 23. https://doi.org/10.1186/s12915-018-0494-7

Berrar, D. (2019). Cross-validation. In S. Ranganathan, M. Gribskov, K. Nakai, & C. Schönbach (Eds.), *Encyclopedia of bioinformatics and computational biology* (pp. 542–545). Academic Press. https://doi.org/https://doi.org/10.1016/B978-0-12-809633-8.20349-X

Besserve, M., Martinerie, J., & Garnero, L. (2011). Improving quantification of functional networks with EEG inverse problem: evidence from a decoding point of view. *Neuroimage*, *55*(4), 1536–1547. https://doi.org/10.1016/j.neuroimage.2011.01.056

Bishop, C. M. (2006). *Pattern recognition and machine learning*. Springer.

Boser, B. E., Guyon, I., & Vapnik, V. N. (1992). A training algorithm for optimal margin classifiers. *COLT '92*.

Bracewell, R. N. (1986). *The fourier transform and its applications* (Vol. 31999). McGraw-Hill New York.

Brattoli, B., Büchler, U., Dorkenwald, M., Reiser, P., Filli, L., Helmchen, F., Wahl, A.-S., & Ommer, B. (2021). Unsupervised behaviour analysis and magnification (uBAM) using deep learning. *Nature Machine Intelligence*, *3*(6), 495–506. https://doi.org/10.1038/s42256-021-00326-x

Britton, J. W., Hopp, J. L., Korb, P. J., Koubeissi, M. Z., Lievens, W. E., & Pestana-Knight, E. (2016). Electroencephalography (EEG): An Introductory Text and Atlas of Normal and Abnormal Findings in Adults, Children, and Infants. In E. K. St Louis & L. C. Frey (Eds.). Chicago: American Epilepsy Society. https://www.ncbi.nlm.nih.gov/books/NBK390354/

Butterworth, S. (1930). On the theory of filter amplifiers. *Experimental Wireless and the Wireless Engineer*, *7*, 536–541.

Champion, K., Lusch, B., Kutz, J. N., & Brunton, S. L. (2019). Data-driven discovery of coordinates and governing equations. *Proceedings of the National Academy of Sciences of the United States of America*, *116*(45), 22445–22451. https://doi.org/10.1073/pnas.1906995116

Chang, C.-C., & Lin, C.-J. (2007). Libsvm: A library for support vector machines. *ACM Transactions on Intelligent Systems and Technology*, *2*.

Cheyne, D. O., Kristeva, R., & Deecke, L. (1991). Homuncular organization of human motor cortex as indicated by neuromagnetic recordings. *Neuroscience Letters*, *122*, 17–20.

Chloca, F. (2018). Chapter 2 - the motor system. In P. Diez (Ed.), *Smart wheelchairs and brain-computer interfaces* (pp. 23–32). Academic Press. https://doi.org/10.1016/B978-0-12-812892-3.00002-9

Chorlian, D., Rangaswamy, M., & Porjesz, B. (2009). EEG coherence: Topography and frequency structure. *Experimental brain research. Experimentelle Hirnforschung. Expérimentation cérébrale*, *198*, 59–83. https://doi.org/10.1007/s00221-009-1936-9

Chouinard, P., & Paus, T. (2006). The primary motor and premotor areas of the human cerebral cortex. *The Neuroscientist : a review journal bringing neurobiology, neurology and psychiatry*, *12*, 143–52. https://doi.org/10.1177/1073858405284255

Clevert, D.-A., Unterthiner, T., & Hochreiter, S. (2016). Fast and accurate deep network learning by exponential linear units (ELUs). In *International conference on learning representations (ICLR)*.

Commuri, S., Day, J. D., Dionne, C. P., & Ertl, W. J. J. (2010). Assessment of pressures within the prosthetic socket of a person with osteomyoplastic amputation during varied walking tasks. *International Journal of Prosthetic sand Orthotics*, *22*(2), 127–137. https://doi.org/10.1097/JPO.0b013e3181cca6e0

Corbetta, D., Friedman, D., & Bell, M. A. (2014). Brain reorganization as a function of walking experience in 12-month-old infants: Implications for the development of manual laterality. *Frontiers in Psychology*, *5*. https://doi.org/10.3389/fpsyg.2014.00245

Crochiere, R. E., & Rabiner, L. R. (1988). Multirate processing of digital signals. In J. S. Lim & A. V. Oppenheim (Eds.), *Advanced topics in signal processing*. Prentice Hall.

Damiano, D. L. (1993). Reviewing muscle cocontraction. *Physical and occupational therapy in pediatrics*, *12*(4), 3–20. https://doi.org/10.1080/J006v12n04_02

Damiano, D. L. (2006). Activity, Activity, Activity: Rethinking Our Physical Therapy Approach to Cerebral Palsy. *Physical Therapy*, *86*(11), 1534–1540. https://doi.org/10.2522/ptj.20050397

Damiano, D. L. (2009). Rehabilitative therapies in cerebral palsy: The good, the not as good, and the possible. *Journal of child neurology*, *24*, 1200–1204. https://doi.org/10.1177/0883073809337919

Darainy, M., & Ostry, D. J. (2008). Muscle cocontraction following dynamics. *Journal of Orthopaedic Research*, *190*(2), 153–163. https://doi.org/10.1007/s00221-008-1457-y

De Luca, C., & Mambrito, B. (1987). Voluntary control of motor units in human antagonist muscles: Coactivation and reciprocal activation. *Journal of neurophysiology*, *58*(3), 525–542. https://doi.org/10.1152/jn.1987.58.3.525

Deisenroth, M. P., Faisal, A. A., & Ong, C. S. (2020). *Mathematics for machine learning*. Cambridge University Press. https://mml-book.github.io/book/mml-book.pdf

Démas, J., Bourguignon, M., Périvier, M., De Tiège, X., Dinomais, M., & Van Bogaert, P. (2020). Mu rhythm: State of the art with special focus on cerebral palsy [Cerebral

Palsy]. *Annals of Physical and Rehabilitation Medicine*, *63*(5), 439–446. https://doi.org/10.1016/j.rehab.2019.06.007

Dempster, A. P., Laird, N. M., & Rubin, D. B. (1977). Maximum likelihood from incomplete data via the EM - algorithm plus discussions on the paper. *Journal of the Royal Statistical Society: Series B (Methodological)*, *39*(1), 1–22. https://doi.org/10.1111/j.2517-6161.1977.tb01600.x

Dionne, C. P., Crawford, D. A., Day, J. D., & Ertl, W. J. J. (2017). Changes in residual limb anthropometrics and lift, carry and timed walking performance in men with transtibial amputation. *Journal of Prosthetics and Orthotics*, *29*, 50–53.

Dionne, C. P., Ertl, W. J. J., & Day, J. D. (2009). Physical therapy management of patients following an Ertl osteomyoplastic transtibial amputation procedure. *Journal of Prosthetics and Orthotics*, *21*(1), 64–70.

Dionne, C. P., Larosa-Aranda, M., Crawford, D. A., & Ertl, W. J. J. (2015). Work-related performance in men with traumatic osteomyoplastic or conventional transtibial amputation. *Orthopaedic Physical Therapy Practice*, *27*, 154–58.

Dionne, C. P., Regens, J. L., Day, J. D., Fagg, A. H., Bryant, D. J., Veirs, K. P., & Ertl, W. J. J. (2022). Gait performance at two speeds and carrying capacity by men with an osteomyoplastic transfemoral limb and comparable controls. *Journal of Prosthetics and Orthotics*, *34*(2), e109–e113. https://doi.org/10.1097/JPO.0000000000000352

Dogan, N., & Dogan, I. (2010). Determination of the number of bins/classes used in histograms and frequency tables: A short bibliography. *TurkStat, Journal of Statistical Research*, *07*, 77–86.

Eickhoff, S., & Müller, V. (2015). Functional connectivity. In A. W. Toga (Ed.), *Brain mapping* (pp. 187–201). Academic Press. https://doi.org/10.1016/B978-0-12-397025-1.00212-8

Elsworth-Edelsten, C., Bonnefoy-Mazure, A., Laidet, M., Armand, S., Assal, F., Lalive, P., & Allali, G. (2017). Upper limb movement analysis during gait in multiple sclerosis

patients. *Human Movement Science*, *54*, 248–252. https://doi.org/10.1016/j.humov.2017.05.014

Ertl, C. W., Ertl, J. P., & Ertl, W. J. J. (2010). The Ertl osteomyoplastic amputation. *The Academy Today*, *6*(2), 5–8. https://cdn.ymaws.com/www.oandp.org/resource/resmgr/docs/AT_archive/10mar_AT.pdf

Fagg, A. H., Ding, L., Kolobe, T. H. A., & Miller, D. P. (2012). Robot assistants for promoting crawling and walking [Last accessed October 2022]. http://www-symbiotic.cs.ou.edu/projects/cerebral_palsy/

Forman, C. R., Jacobsen, K., Karabanov, A., Nielsen, J., & Lorentzen, J. (2022). Corticomuscular coherence is reduced in relation to dorsiflexion fatigability to the same extent in adults with cerebral palsy as in neurologically intact adults. *European Journal of Applied Physiology*, *122*. https://doi.org/10.1007/s00421-022-04938-y

François, D., Wertz, V., & Verleysen, M. (2006). The permutation test for feature selection by mutual information. *ESANN Proceedings*, 239–244.

Frazier, P. I. (2018). A tutorial on bayesian optimization [arXiv]. https://doi.org/10.48550/ARXIV.1807.02811

Friston, K. J. (2011). Functional and effective connectivity: A review [PMID: 22432952]. *Brain Connectivity*, *1*(1), 13–36. https://doi.org/10.1089/brain.2011.0008

Garcia, V., Nielsen, F., & Nock, R. (2010). Hierarchical gaussian mixture model. *IEEE International Conference on Acoustics, Speech, and Signal Processing*, 4070–4073. https://doi.org/10.1109/ICASSP.2010.5495750

Garcia-Rill, E. (2015). Chapter 8 - the 10hz fulcrum. In E. Garcia-Rill (Ed.), *Waking and the reticular activating system in health and disease* (pp. 157–170). Academic Press. https://doi.org/10.1016/B978-0-12-801385-4.00008-2

Ghazi, M., Nash, M., Fagg, A., Ding, L., Kolobe, T., & Miller, D. (2016). Novel assistive device for teaching crawling skills to infants. In D. S. Wettergreen & T. D. Barfoot (Eds.). Springer International Publishing. https://doi.org/10.1007/978-3-319-27702-8_39

Goldberger, J., & Roweis, S. (2004). Hierarchical clustering of a mixture model. In L. Saul, Y. Weiss, & L. Bottou (Eds.), *Advances in neural information processing systems* (Vol. 17). MIT Press. https://proceedings.neurips.cc/paper/2004/file/36e729ec173b94133d8fa552e4029f8b-Paper.pdf

Goodfellow, I., Bengio, Y., & Courville, A. (2016). *Deep learning* [http://www.deeplearningbook.org]. MIT Press.

Graessle, E. (2018). Infant crawling orthosis and home program to strengthen a neurologically impaired upper extremity. *Journal of hand therapy : official journal of the American Society of Hand Therapists*, *31*(3), 411–415. https://doi.org/10.1016/j.jht.2017.05.014

Guevara, M. A., & Corsi-Cabrera, M. (1996). EEG coherence or EEG correlation? *International Journal of Psychophysiology*, *23*(3), 145–153. https://doi.org/10.1016/S0167-8760(96)00038-4

Harris, F. (1978). On the use of windows for harmonic analysis with the discrete fourier transform. *Proceedings of the IEEE*, *66*, 51–83. https://doi.org/10.1109/PROC.1978.10837

Harris, F., & Constantinides, A. (1991). Digital signal processing with efficient polyphase recursive all-pass filters. *International Conference on Signal Processing*.

Hinton, G. E., & Salakhutdinov, R. (2006). Reducing the dimensionality of data with neural networks. *Science*, *313*, 504–507.

Hodges, P. W., van den Hoorn, W., Wrigley, T. V., Hinman, R. S., Bowles, K.-A., Cicuttini, F., Wang, Y., & Bennell, K. (2015). Increased duration of co-contraction of medial knee muscles is associated with greater progression of knee osteoarthritis. *Manual Therapy*, *21*, 151–158. https://doi.org/10.1016/j.math.2015.07.004

Holsheimer, J., & Feenstra, B. (1977). Volume conduction and EEG measurements within the brain: A quantitative approach to the influence of electrical spread on the linear relationship of activity measured at different locations. *Electroencephalography and Clinical Neurophysiology*, *43*(1), 52–58. https://doi.org/10.1016/0013-4694(77)90194-8

Hong, J. H., & Mun, M. S. (2005). Relationship between socket pressure and EMG of two muscles in trans-femoral stumps during gait. *Prosthetics and Orthotics International*, *29*(1), 59–72. https://journals.sagepub.com/doi/pdf/10.1080/03093640500116764

Horst, F., Lapuschkin, S., Samek, W., Müller, K.-R., & Schöllhorn, W. I. (2019). Explaining the unique nature of individual gait patterns with deep learning. *Scientific reports*, *9*(1), 2391. https://doi.org/10.1038/s41598-019-38748-8

Huang, S.-C., Costa, G. D., Pisa, M., Gregoris, L., Leccabue, G., Congiu, M., Comi, G., & Leocani, L. (2020). The danger of walking with socks: Evidence from kinematic analysis in people with progressive multiple sclerosis. *Sensors (Basel)*, *20*(21). https://doi.org/10.3390/s20216160

Hudspeth, W. J., & Pribram, K. H. (1990). Stages of brain and cognitive maturation. *Journal of Educational Psychology*, *82*, 881–884.

Hunter, S. W., Batchelor, F., Hill, K. D., Hill, A.-M., Mackintosh, S., & Payne, M. (2017). Risk factors for falls in people with a lower limb amputation: A systematic review. *The Journal of Injury, Function, and Rehabilitation*, *9*(2), 170–180. https://doi.org/10.1016/j.pmrj.2016.07.531

Hyndman, R. J. (1996). Computing and graphing highest density regions. *The American Statistician*, *50*(2), 120–126.

Inuggi, A., Bassolino, M., Tacchino, C., Pippo, V., Bergamaschi, V., Campus, C., De Franchis, V., Pozzo, T., & Moretti, P. (2018). Ipsilesional functional recruitment within lower mu band in children with unilateral cerebral palsy, an event-related desynchronization study. *Experimental brain research*, *236*(2), 517–527.

Isaksson, A., Wallman, M., Göransson, H., & Gustafsson, M. G. (2008). Cross-validation and bootstrapping are unreliable in small sample classification. *Pattern Recognition Letters*, *29*(14), 1960–1965. https://doi.org/10.1016/j.patrec.2008.06.018

Jaegers, S., Arendzen, J., & de Jongh, H. (1995). Prosthetic gait of unilateral transfemoral amputees: A kinematic study. *Archives of Physical Medicine and Rehabilitation*, *76*(8), 736–743. https://doi.org/10.1016/s0003-9993(95)80528-1

Jaegers, S., Arendzen, J., & de Jongh, H. (1996). An Electromyographic Study of the Hip Muscles of Transfemoral Amputees in Walking. *Clinical Orthopaedics and Related Research*, *328*, 119–128.

Jolliffe, I. T., & Stephenson, D. B. (2011). Forecast verification : A practitioner's guide in atmospheric science.

Jonas. (2009). Violin plots for plotting multiple distributions (distributionplot.m) [Retrieved 1 July 2020 version 1.15.0.0]. https://www.mathworks.com/matlabcentral/fileexchange/23661-violin-plots-for-plotting-multiple-distributions-distributionplot-m

Kaas, J. H. (2015). Somatosensory cortex. In A. W. Toga (Ed.), *Brain mapping* (pp. 283–286). Academic Press. https://doi.org/10.1016/B978-0-12-397025-1.00223-2

Kahle, J. T., Highsmith, M. J., Kenney, J., Ruth, T., Lunseth, P. A., & Ertl, J. (2016). The effectiveness of the bone bridge transtibial amputation technique: A systematic review of high-quality evidence. *Prosthetics and orthotics international*, *41*(3), 219–226. https://doi.org/10.1177/0309364616679318

Kharb, A., Saini, V., Jain, Y., Dhiman, S., Tech, M., & Scholar. (2011). A review of gait cycle and its parameters. *IJCEM Int J Comput Eng Manag*, *13*.

Kingma, D. P., Mohamed, S., Rezende, D. J., & Welling, M. (2014). Semi-supervised learning with deep generative models. In Z. Ghahramani, M. Welling, C. Cortes, N. Lawrence, & K. Q. Weinberger (Eds.), *Advances in neural information processing systems* (Vol. 27). Curran Associates, Inc. https://proceedings.neurips.cc/paper/2014/file/d523773c6b194f37b938d340d5d02232-Paper.pdf

Kitago, T., & Krakauer, J. W. (2013). Motor learning principles for neurorehabilitation. *Handbook of clinical neurology*, *110*, 93–103.

Kleinberg, J. (2002). An impossibility theorem for clustering. *NIPS'02: Proceedings of the 15th International Conference on Neural Information Processing Systems*, 463–470.

Koeda, T., & Takeshita, K. (1998). Electroencephalographic coherence abnormalities in preterm diplegia. *Pediatric Neurology*, *18*(1), 51–56. https://doi.org/10.1016/S0887-8994(97)00155-0

Kolobe, T. H. A., & Fagg, A. H. (2019). Robot reinforcement and error-based movement learning in infants with and without cerebral palsy. *Physical Therapy*, *99*(6), 677–688. https://doi.org/10.1093/ptj/pzz043

Krashen, S. (1976). *Studies in neurolinguistias* (H. Witaker & H. Witaker, Eds.). Academic Press.

Kruschke, J. K. (2015). *Doing Bayesian Data Analysis: A Tutorial with R, JAGS, and Stan*. Academic Press / Elsevier.

Kukke, S. N., de Campos, A. C., Damiano, D., Alter, K. E., Patronas, N., & Hallett, M. (2015). Cortical activation and inter-hemispheric sensorimotor coherence in individuals with arm dystonia due to childhood stroke. *Clinical Neurophysiology*, *126*(8), 1589–1598.

Kulak, W., & Sobaniec, W. (2005). Quantitative EEG analysis in children with hemiparetic cerebral palsy. *NeuroRehabilitation*, *20*(2), 75–84. http://europepmc.org/abstract/MED/15920299

Kułak, W., & Sobaniec, W. (2003). Spectral analysis and EEG coherence in children with cerebral palsy: Spastic diplegia. *Przegla−d lekarski*, *60 Suppl 1*, 23–7.

LeCun, Y., Boser, B., Denker, J. S., Henderson, D., Howard, R. E., Hubbard, W., & Jackel, L. D. (1989). Backpropagation applied to handwritten zip code recognition. *Neural Computation*, *1*(4), 541–551. https://doi.org/10.1162/neco.1989.1.4.541

LeCun, Y., Bottou, L., Bengio, Y., & Haffner, P. (1998). Gradient-based learning applied to document recognition. *Proceedings of the IEEE*, *86*, 2278–2324. https://doi.org/10.1109/5.726791

Levac, D., Wishart, L., Missiuna, C., & Wright, V. (2009). The Application of Motor Learning Strategies Within Functionally Based Interventions for Children with Neuromotor Conditions. *Pediatric Physical Therapy*, *21*(4), 345–355. https://doi.org/10.1097/PEP.0b013e3181beb09d

Lindsley, D. B. (1939). A longitudinal study of the occipital alpha rhythm in normal children: Frequency and amplitude standards. *The Pedagogical Seminary and Journal of Genetic Psychology*, *55*(1), 197–213. https://doi.org/10.1080/08856559.1939.10533190

Mahalanobis, P. C. (1936). On the generalized distance in statistics. *National Institute of Science of India*, *2*(1), 49–55.

Mai, A., Commuri, S., Day, J. D., Dionne, C. P., Ertl, W. J. J., & Regens, J. L. (2012). Effect of prosthetic foot on residuum socket interface pressure and gait characteristics in an otherwise healthy male with transtibial osteomyoplastic amputation. *Journal of Prosthetics and Orthotics*, *24*, 211–220.

Mai, A., Commuri, S., Dionne, C. P., Day, J. D., Ertl, W. J. J., & Regens, J. L. (2013). Residual muscle contraction and residuum socket interface force in men with transtibial osteomyoplastic amputation. *Journal of Prosthetics and Orthotics*, *25*, 151–158.

Marcuse, L. V., Fields, M. C., & Yoo, J. J. (2016). 2 - The normal adult EEG. In L. V. Marcuse, M. C. Fields, & J. J. Yoo (Eds.), *Rowan's Primer of EEG* (Second Edition, pp. 39–66). Elsevier. https://doi.org/10.1016/B978-0-323-35387-8.00002-0

Marshall, P. J., & Meltzoff, A. N. (2011). Neural mirroring systems: Exploring the EEG mu rhythm in human infancy. *Developmental Cognitive Neuroscience*, *1*(2), 110–123.

Marshall, P. J., Saby, J., & Meltzoff, A. (2013). Infant brain responses to object weight: Exploring goal-directed actions and self-experience. *Infancy : the official Journal of the International Society on Infant Studies*, *18*. https://doi.org/10.1111/infa.12012

Massey, F. J. (1951). The Kolmogorov-Smirnov Test for Goodness of Fit. *Journal of the American Statistical Association*, *46*(253), 68–78. https://doi.org/10.1080/01621459.1951.10500769

Matousek, M., & Petersén, I. (1973). Automatic evaluation of EEG background activity by means of age-dependent EEG quotients. *Electroencephalography and Clinical Neurophysiology*, *35*(6), 603–612. https://doi.org/10.1016/0013-4694(73)90213-7

Meijer, E. J., Niemarkt, H. J., Raaijmakers, I. P. P. C., Mulder, A. M., van Pul, C., Wijn, P. F. F., & Andriessen, P. (2016). Interhemispheric connectivity estimated from EEG time-correlation analysis in preterm infants with normal follow-up at age of five. *Physiological Measurement*, *37*(12), 2286. https://doi.org/10.1088/1361-6579/37/12/2286

Microchip Technology. (1984). Atmel [Accessed 08 September 2022]. https://www.microchip.com/

Montavon, G., Braun, M. L., & Müller, K.-R. (2011). Kernel analysis of deep networks. *Journal of Machine Learning Research*, *12*(78), 2563–2581. http://jmlr.org/papers/v12/montavon11a.html

Morgan, C., Darrah, J., Gordon, A. M., Harbourne, R., Spittle, A., Johnson, R., & Fetters, L. (2016). Effectiveness of motor interventions in infants with cerebral palsy: A systematic review. *Developmental medicine and child neurology*, *58*(9), 900–909. https://doi.org/https://doi-org.ezproxy.lib.ou.edu/10.1111/dmcn.13105

Morgan, C., Novak, I., Dale, R. C., & Badawi, N. (2015). Optimising motor learning in infants at high risk of cerebral palsy: A pilot study. *BMC pediatrics*, *15*(30). https://doi.org/10.1186/s12887-015-0347-2

Nayak, C., & Anilkumar, A. (2022). EEG Normal Waveforms [PMID: 30969627]. Treasure Island (FL): StatPearls Publishing.

Nevalainen, P., Lauronen, L., Sambeth, A., Wikström, H., Okada, Y., & Pihko, E. (2008). Somatosensory evoked magnetic fields from the primary and secondary somatosensory cortices in healthy newborns. *NeuroImage*, *40*(2), 738–745. https://doi.org/10.1016/j.neuroimage.2007.09.075

Newson, J., & Thiagarajan, T. (2019). EEG Frequency Bands in Psychiatric Disorders: A Review of Resting State Studies. *Frontiers in Human Neuroscience*, *12*. https://doi.org/10.3389/fnhum.2018.00521

Paterson, S. J., Heim, S., Thomas Friedman, J., Choudhury, N., & Benasich, A. A. (2006). Development of structure and function in the infant brain: Implications for cognition, language and social behaviour. *Neuroscience & Biobehavioral Reviews*, *30*(8), 1087–1105. https://doi.org/10.1016/j.neubiorev.2006.05.001

Patino, A., Fagg, A., Kolobe, T., Miller, D., & Ding, L. (2017). Dynamic spatio-spectral patterns of rhythmic EEG in infants. *2017 8th International IEEE/EMBS Conference on Neural Engineering (NER)*, 621–624. https://doi.org/10.1109/NER.2017.8008428

Paulus, M., Hunnius, S., Elk, M., & Bekkering, H. (2012). How learning to shake a rattle affects 8-month-old infants' perception of the rattle's sound: Electrophysiological evidence for action-effect binding in infancy. *Developmental cognitive neuroscience*, *2*, 90–6. https://doi.org/10.1016/j.dcn.2011.05.006

Pedregosa, F., Varoquaux, G., Gramfort, A., Michel, V., Thirion, B., Grisel, O., Blondel, M., Prettenhofer, P., Weiss, R., Dubourg, V., Vanderplas, J., Passos, A., Cournapeau, D., Brucher, M., Perrot, M., & Duchesnay, E. (2011). Scikit-learn: Machine learning in Python. *Journal of Machine Learning Research*, *12*, 2825–2830.

Peirce, C. S. (1884). The numerical measure of the success of predictions. *Science*, *ns-4*(93), 453–454. https://doi.org/10.1126/science.ns-4.93.453.b

Pihko, E., Nevalainen, P., Vaalto, S., Laaksonen, K., Mäenpää, H., Valanne, L., & Lauronen, L. (2014). Reactivity of sensorimotor oscillations is altered in children with hemiplegic cerebral palsy: A magnetoencephalographic study. *Human brain mapping*, *35*(8), 4105–4117.

Plaut, E. (2018). From principal subspaces to principal components with linear autoencoders. https://doi.org/10.48550/ARXIV.1804.10253

Pomeroy, V., Aglioti, S. M., Mark, V. W., McFarland, D., Stinear, C., Wolf, S. L., Corbetta, M., & Fitzpatrick, S. M. (2011). Neurological principles and rehabilitation of action disorders: Rehabilitation interventions. *Neurorehabilitation and neural repair*, *25*(5), 33S–43S. https://doi.org/10.1177/1545968311410942

Rosa, M. (2015). Co-contraction Role on Human Motor Control. A Neural Basis. *Journal of Novel Physiotherapies*, *5*(248). https://doi.org/10.4172/2165-7025.1000248

Rosa, M., Marques, A., Demain, S., & Metcalf, C. (2013). Lower limb co-contraction during walking in subjects with stroke: A systematic review. *Journal of electromyography and kinesiology : official journal of the International Society of Electrophysiological Kinesiology*, *24*. https://doi.org/10.1016/j.jelekin.2013.10.016

Rumelhart, D. E., Hinton, G. E., & Williams, R. J. (1986). Learning representations by back-propagating errors. *Nature*, *323*, 533–536.

Sadeghi, H., Allard, P., Prince, F., & Labelle, H. (2000). Symmetry and limb dominance in able-bodied gait: A review. *Gait and Posture*, *12*, 34–45. https://doi.org/10.1016/S0966-6362(00)00070-9

Salamy, A., Eldredge, L., & Wakeley, A. (1985). Maturation of contralateral brain-stem responses in preterm infants. *Electroencephalography and Clinical Neurophysiology/Evoked Potentials Section*, *62*(2), 117–123. https://doi.org/10.1016/0168-5597(85)90023-1

Schmitt, L. C., & Rudolph, K. S. (2008). Muscle stabilization strategies in people with medial knee osteoarthritis: The effect of instability. *Journal of Orthopaedic Research*, *26*(9), 1180–1185. https://doi.org/10.1002/jor.20619

Schölkopf, B., Smola, A., & Müller, K.-R. (1998). Nonlinear component analysis as a kernel eigenvalue problem. *Neural Computation*, *10*(5), 1299–1319. https://doi.org/10.1162/089976698300017467

Seeley, M. K., Umberger, B. R., Clasey, J. L., & Shapiro, R. (2010). The relation between mild leg-length inequality and able-bodied gait asymmetry. *Journal of sports Science and Medicine*, *9*(4), 572–579. https://www.ncbi.nlm.nih.gov/pmc/articles/PMC3761822/

Seyedali, M., Czerniecki, J. M., Morgenroth, D. C., & Hahn, M. E. (2012). Co-contraction patterns of trans-tibial amputee ankle and knee musculature during gait. *Journal of NeuroEngineering and Rehabilitation*, *9*(29). https://doi.org/10.1186/1743-0003-9-29

Sharma, S. K., Yadav, S. L., Singh, U., & Wadhwa, S. (2017). Muscle Activation Profiles and Co-Activation of Quadriceps and Hamstring Muscles around Knee Joint in Indian Primary Osteoarthritis Knee Patients. *Journal of Clinical and Diagnostic Research*, *11*(5). https://doi.org/10.7860/JCDR/2017/26975.9870

Shaw, J. C. (1984). Correlation and coherence analysis of the EEG: A selective tutorial review. *International Journal of Psychophysiology*, *1*(3), 255–266. https://doi.org/10.1016/0167-8760(84)90045-X

Shlens, J. (2014). A tutorial on principal component analysis [Last accessed October 2022]. https://doi.org/10.48550/ARXIV.1404.1100

Shotande, M. O., Veirs, K. P., Day, J. D., Ertl, W. J. J., Fagg, A. H., & Dionne, C. P. (2022). Comparing temporospatial performance during brisk and self-paced walking by men with osteomyoplastic transfemoral amputation and controls using pressure and muscle activation peak times. *Frontiers in Rehabilitation Sciences*, *3*. https://doi.org/10.3389/fresc.2022.848657

Shotande, M. O., Veirs, K. P., Day, J. D., Ertl, W. J. J., Fagg, A. H., & Dionne, C. P. (in revision). Active recruitment of distal-most residual muscles in men with osteomyoplastic transfemoral amputation. *Gait & Posture*.

Šidák, Z. K. (1967). Rectangular confidence regions for the means of multivariate normal distributions. *Journal of the American Statistical Association*, *62*(318), 626–633. https://doi.org/10.1080/01621459.1967.10482935

Silverman, B. W. (1998). *Density estimation for statistics and data analysis*. Routledge. https://doi.org/10.1201/9781315140919

Singh, R. E., Iqbal, K., White, G., & Holtz, J. K. (2019). A review of EMG techniques for detection of gait disorders. IntechOpen. https://doi.org/10.5772/intechopen.84403

Smith, J. R. (1938a). The electroencephalogram during normal infancy and childhood: I. rhythmic activities present in the neonate and their subsequent development. *The Pedagogical Seminary and Journal of Genetic Psychology*, *53*(2), 431–453. https://doi.org/10.1080/08856559.1938.10533820

Smith, J. R. (1938b). The electroencephalogram during normal infancy and childhood: Ii. the nature of the growth of the alpha waves. *The Pedagogical Seminary and Journal of Genetic Psychology*, *53*(2), 455–469. https://doi.org/10.1080/08856559.1938.10533821

Smith, S. L., Allan, R., Marreiros, S. P., Woodburn, J., & Steultjens, M. P. M. (2019). Muscle co-activation across activities of daily living in individuals with knee osteoarthritis. *Arthritis Care & Research*, *71*(5), 651–660. https://doi.org/10.1002/acr.23688

Sohn, K., Lee, H., & Yan, X. (2015). Learning structured output representation using deep conditional generative models. *NIPS*.

Southerland, J. B. (2012). *Activity recognition and crawling assistance using multiple inexpensive inertial measurement units* [Master's thesis, University of Oklahoma]. Norman, Oklahoma.

Stroganova, T., & Orekhova, E. (2007). EEG and infant states. *Infant EEG and event-related potentials*, 251–287.

Taylor, B. C., & Poka, A. (2016). Osteomyoplastic transtibial amputation: The Ertl technique. *Journal of the American Academy of Orthopaedic Surgeons*, *24*(4), 259–265. https://doi.org/10.5435/JAAOS-D-15-00026

Thatcher, R. W., Walker, R. A., & Giudice, S. (1987). Human cerebral hemispheres develop at different rates and ages. *Science*, *236*(4805), 1110–1113. https://doi.org/10.1126/science.3576224

Thatcher, R. W. (1994). Psychopathology of early frontal lobe damage: Dependence on cycles of development. *Development and Psychopathology*, *6*(4), 565–596. https://doi.org/10.1017/S0954579400004697

Thatcher, R. W. (1998). A predator-prey model of human cerebral development. In *Applications of nonlinear dynamics to developmental process modeling* (pp. 87–128). Lawrence Erlbaum Associates.

Tukey, J. W. (1967). An introduction to the calculations of numerical spectrum analysis. *Spectral Analysis of Time Series*, 25–46.

Tuthill, J. C., & Azim, E. (2018). Proprioception. *Current Biology*, *28*, R194–R203.

van der Krogt, M. M., Delp, S. L., & Schwartz, M. H. (2012). How robust is human gait to muscle weakness? *Gait & Posture*, *36*(1), 113–119. https://doi.org/10.1016/j.gaitpost.2012.01.017

van der Maaten, L., Postma, E., & Herik, H. (2007). Dimensionality reduction: A comparative review. *Journal of Machine Learning Research - JMLR*, *10*.

van Elk, M., van Schie, H. T., Hunnius, S., Vesper, C., & Bekkering, H. (2008). You'll never crawl alone: Neurophysiological evidence for experience-dependent motor resonance in infancy. *Neuroimage*, *43*(4), 808–814.

Venables, B., & Ripley, B. D. (2002). Modern applied statistics with S. Springer. https://doi.org/10.1007/b97626

Webb, W. G. (2017). 2 - Organization of the Nervous System I. In W. G. Webb (Ed.), *Neurology for the speech-language pathologist* (Sixth Edition, pp. 13–43). Mosby. https://doi.org/10.1016/B978-0-323-10027-4.00002-6

Wentink, E. C., Preinsen, E. C., Rietman, J. S., & Veltink, P. H. (2013). Comparison of muscle activity patterns of transfemoral amputees and control subjects during walking. *Journal of NeuroEngineering and Rehabilitation*, *10*(87). https://doi.org/10.1186/1743-0003-10-87

Wiltschko, A. B., Johnson, M. J., Iurilli, G., Peterson, R. E., Katon, J. M., Pashkovski, S. L., Abraira, V. E., Adams, R. P., & Datta, S. R. (2015). Mapping sub-second structure in mouse behavior. *Neuron*, *88*(6), 1121–1135. https://doi.org/10.1016/j.neuron.2015.11.031

Wing, A. M. (1978). 7 - response timing in handwriting. In G. E. Stelmach (Ed.), *Information processing in motor control and learning* (pp. 153–172). Academic Press. https://doi.org/10.1016/B978-0-12-665960-3.50012-8

Winter, D. A. (1987). *The biomechanics and motor control of human gait*. University of Waterloo Press.

Winter, D. A. (1995). Human balance and posture control during standing and walking. *Gait & Posture*, *3*(4), 193–214. https://doi.org/10.1016/0966-6362(96)82849-9

Winter, D. A., & Yack, H. J. (1987). EMG profiles during normal human walking: Stride to stride and inter-subject variability. *Electroencephalography and clinical Neurophysiology*, *67*, 402–411.

Xiao, R., Qi, X., Patino, A., Fagg, A. H., Kolobe, T. H., Miller, D. P., & Ding, L. (2017). Characterization of infant mu rhythm immediately before crawling: A high-resolution EEG study. *NeuroImage*, *146*, 47–57. https://doi.org/10.1016/j.neuroimage.2016.11.007

Yuan, H., Ge, P., Du, L., & Xia, Q. (2019). Co-contraction of lower limb muscles contributes to knee stability during stance phase in hemiplegic stroke patients. *Medical Science Monitor: International Medical Journal of Experimental and Clinical Research*, *25*, 7443–7450. https://doi.org/10.12659/MSM.916154

Zhou, C., Ban, H., Zhang, J., Li, Q., & Zhang, Y. (2020). Gaussian mixture variational autoencoder for semi-supervised topic modeling. *IEEE Access*, *8*, 106843–106854. https://doi.org/10.1109/ACCESS.2020.3001184